EuroFlyer

An environmentally friendly regional aircraft with a propulsive fuselage entering into service in 2035

Bosma, S.B.M.	4077504	Meijburg, M.A.	4015525
Eggermont, A.A.L.A.X.A.V.	4112199	Morias, K.L.L.	4129547
Heuijerjans, R.	4080165	Oudenalder, F.S.C. van den	4084160
Kruijssen, F.	4081250	Peerlings, B.	4079388
Leest, S.A.	4109872	Zomeren, K.B. van	4010663

Final Report

Design Synthesis Excercise

TU Delft Delft University of Technology

Tutor: Dr. Rao, A.G. *Coaches*: Lv, P. (MSc) , Pröbsting, S. (MSc) , Zhao, X. (MSc)

Faculty of Aerospace Engineering

July 2, 2013

(This page is intentionally left blank)

Preface

Before you lies the Final Report concluding the EuroFlyer Project. This project is part of the Design Synthesis Exercise conducted at the faculty of Aerospace Engineering at Delft University of Technology. From April till July, 10 Bachelor students have committed themselves to design a new generation of aircraft for the year 2035. Succeeding the previously published Mid-Term Report, this deliverable acquaints the reader with the entire design process and results. Due to limited resources, it does not aim to attain a flawless result able to compete with contemporary standards in industrial practice. However, the goal of the EuroFlyer project is to prove that new innovative designs are worth examining and that the current generation of aircraft can be improved.

DSE Group 11 – EuroFlyer
July 2, 2013
Delft, The Netherlands

Acknowledgements

Now that the EuroFlyer design team has passed on to the penultimate stage of the Design Synthesis Exercise, we would like to express our gratitude to particular individuals. It is due their contributions, advice and insightful tips that we have been able to present with these innovative results.

First of all, various people have guided us through the entire project. Our gratitude goes to Dr. Arvind Gangoli Rao, for giving up the opportunity to conduct the EuroFlyer project. His expertise has constantly supported us in times of struggle.

We would like to express gratitude to our coaches Xiaojia Zhao, Stefan Pröbsting and Peijian Lv. They kept us on the right track from beginning to end. Especially Peijian Lv has assisted tremendously with various design optimisation problems regarding amongst others, Boundary Layer Ingestion.

Many other experts were consulted in the design process. In disciplines where our own knowledge was limited to make informed choices, Dr. Mostafa Abdalla, Dr. Ir. Leo Veldhuis, Dr. Ir. Dries Visser, Dr. Ir. Mark Voskuijl, Ir. Jan Hol and Ir. Nando Timmer have given insightful advice. Eddy van den Bos has greatly assisted us in creating elaborate drawings and three-dimensional renders, also allowing us to show the EuroFlyer to the world. With her expertise in technical communication, Drs. Regina Tange-Hoffman has thoroughly checked our work and pointed us to some possible improvements. Our gratitude goes out to all.

Furthermore, we would like to thank Dr. Jan van Toor at European Aeronautic Defence and Space Company (EADS) Innovation Works who inspired our design to a great extent and has given valuable feedback throughout the process.

Finally, the design team would like to thank the staff members of Delft University of Technology, and Ir. Joris Melkert in particular, for setting up this well-organised and educational Design Synthesis Exercise.

Contents

List of Figures

List of Tables

List of Abbreviations

AC	Alternating Current
ACARE	Advisory Council for Aeronautics Research in Europe
AGAPE	ACARE Goals Progress Evaluation
AMPR	Aeronautical Manufacturers Planning Report
ANSYS	Analysis System
APU	Auxiliary Power Unit
ASK	Available Seat Kilometre
ATM	Air Traffic Management
ATR	Aviations de Transport Regional
BGW	Basic Gross Weight
BLI	Boundary Layer Ingestion
BPR	Bypass Ratio
C2C	Cradle to Cradle
CAEP	Committee on Aviation Environmental Protection
CAD	Computer Aided Design
CAGR	Compound Annual Growth Rate
CATIA	Computer Aided Three-Dimensional Interactive Application
CER	Cost Estimation Relationship
CFD	Computational Fluid Dynamics
CFRP	Carbon Fiber Reinforced Plastics
CG	Centre of Gravity
CIS	Commonwealth of Independent States
CPR	Compressor Pressure Ratio
CNG	Compressed Natural Gas
CO_2	Carbon Dioxide
CRP	Contra-Rotating Propeller
CS	Certification Specifications
DC	Direct Current
DID	Deliverable Item Description
DOC	Direct Operating Cost
DOT	Design Option Tree
DSE	Design Synthesis Exercise
EADS	European Aeronautic Defence and Space Company
EAS	Equivalent Air Speed
EASA	European Aviation Safety Agency
ECS	Environmental Control System
EPNL	Effective Perceived Noise Level
ESDU	Engineering Sciences Data Unit
ER	Extended Range
FEM	Finite Element Method
FBS	Functional Breakdown Structure
FF	Form Factor
FFBD	Functional Flow Block Diagram
FM	Flight Model
GAMBIT	Geometry And Mesh Building Intelligent Toolkit
GC	Gantt Chart
GDP	Gross Domestic Product
HGW	High Gross Weight
HR	Human Resource
IAS	Indicated Air Speed
ICAO	International Civil Aviation Organisation
IOC	Indirect Operating Cost
ISA	International Standard Atmosphere
LCC	Low Cost Carrier / Life Cycle Cost
LNG	Liquefied Natural Gas
LR	Longer Range
MAC	Mean Aerodynamic Chord
MATLAB	Matrix Laboratory
MIT	Massachusetts Institute of Technology
MTOW	Maximum Take-Off Weight
MNS	Mission Need Statement
NACA	National Advisory Committee for Aeronautics
NASA	National Aeronautics and Space Administration
NO_x	Nitrogen Oxides
OEW	Operating Empty Weight
OBS	Organisational Breakdown Structure
OL	Operational Life
OPEC	Organisation of Petroleum Exporting Countries
PNL	Perceived Noise Level
POS	Project Objective Statement
PRM	Project Risk Management
PW	Pratt & Whitney
QFD	Quality Function Deployment
QM	Qualification Model
R&D	Research and Development
RDT&E	Research, Development, Testing & Evaluation
RAMS	Reliability, Availability, Maintainability & Safety
RDT	Requirements Discovery Tree
RJ	Regional Jet
RPK	Revenue Passenger Kilometre
RPM	Revolutions Per Minute
S&C	Stability & Control
SE	Systems Engineering
SHP	Shaft Horse Power
STD	Standard
SUGAR	Subsonic Ultra Green Aircraft Research
SWOT	Strengths, Weaknesses, Opportunities and Threats
TAS	True Air Speed
TAT	TurnAround Time
TRL	Technology Readiness Level
TSFC	Thrust Specific Fuel Consumption
ULD	Unit Load Device
US	United States
USD	United States Dollar
VALID	Verifiable, Achievable, Logical, Integral, Definitive
WAVG	Average Aircraft Weight
WBS	Work Breakdown Structure
WFD	Work Flow Diagram

List of Symbols

Latin Symbols

A	Area	m^2
a	Axis Location	m
a	Speed of Sound	m/s
A_{noise}	Airframe Noise	$EPNdB$
A_l	Area of the Longitudinal Stringers	m^2
a_x/g	Brake Factor on Dry Concrete	–
AR	Aspect Ratio	–
b	Wingspan	m
b	Half Cord Length	m
b	Number of Blades	–
B_w	Wing Span	ft
c	Chord Length	m
c	Specific Heat	J/kg
C	Cost	\$
c/V	Climb Gradient	–
$C^{\theta\theta}$	Flexibility Influence Coefficient	–
C_{aed}	Airframe Engineering and Design Cost	\$
C_{apc}	Aeroplane Production Cost	\$
C_D	Drag Coefficient	–
$C_{D_{Fuselage}}$	Drag Coefficient of the Fuselage	–
C_{D_0}	Zero Drag Coefficient	–
C_{D_i}	Induced Drag Coefficient	–
C_{D_p}	Pressure Drag Coefficient	–
C_{D_w}	Wave Drag Coefficient	–
C_{DR}	Horizontal/Vertical Tail Rolling Drag Coefficient	–
C_{dst}	Development Support and Testing Cost	\$
C_e	Engine Cost	\$
C_F	Friction Drag Coefficient	–
$C_{f_{lam_{xcr}}}$	Laminar Friction Coefficient up until the Transition Point	–
$C_{f_{turb_{xcr}}}$	Turbulent Friction Coefficient from the Transition Point	–
$C_{f_{turb_L}}$	Turbulent Friction Coefficient for the Complete Fuselage Length	–
$C_{f_{Fuselage}}$	Friction Coefficient of the Fuselage	–
$C_{f_{laminar}}$	Laminar Skin Friction Factor	–
$C_{f_{turbulent}}$	Turbulent Skin Friction Factor	–
C_{fin}	Financing Cost	\$
C_{fta}	Flight Test Aeroplanes Cost	\$
C_{fto}	Flight Test Operations Cost	\$
C_l	Two Dimensional Lift Coefficient	–
C_L	Three Dimensional Lift Coefficient	–
$C_{L_{T/O_{max}}}$	Maximum Lift Coefficient at Take-Off	–
$C_{L_{\alpha h}}$	Lift Coefficient Derivative w.r.t. Alpha of the Horizontal Tail	–
$C_{L_{A-h}}$	Lift Coefficient of the Aircraft Minus Horizontal Tail	–
$C_{L_{endurance}}$	Lift Coefficient for Maximum Endurance	–
$C_{L_{max,clear}}$	Maximum Clear Lift Coefficient	–
$C_{L_{max,landing}}$	Maximum Landing Lift Coefficient	–
$C_{L_{max}}$	Maximum Lift Coefficient	–
$C_{L_{Range}}$	Lift Coefficient for Maximum Range	–
C_{L_α}	Lift Coefficient Derivative w.r.t. Alpha	–
c_m	Moment Coefficient	–
$C_{m_{ac}}$	Moment Coefficient at the Aerodynamic Center	–
C_{man}	Manufacturing Cost	\$
C_{mat}	Material Cost	\$
C_p	Pressure Coefficient	–
C_p	Propeller Cost	\$
$C_{p_{air}}$	Specific Heat Constant Air	kJ/kgK
$C_{p_{cr}}$	Critical Pressure Coefficient	–
$C_{p_{gas}}$	Specific Heat Constant Gas Mixture	kJ/kgK
C_{p_0}	Zero Pressure Coefficient	–
C_{pro}	Profit	\$
$C_{program}$	Total Program Cost	\$
C_{RDTE}	Total RDT&E Cost	\$
C_R	Root Chord	m
C_t	Tip Chord	m
C_{tool}	Tooling Cost	\$
C_{tsf}	Test and Simulation Facilities Cost	\$
$cblade$	Blade Chord	m
CEF	Cost Escalation Factor	–
D	Drag	N
d	Diameter	m
dB	Decibels	–
d/l	Fineness Ratio	–
$d\epsilon/d\alpha$	Downwash Derivative w.r.t Angle of Attack	–
E	Young's Modulus	Pa
e	Oswald Factor	–
E_{batt}	Power Delivered by Batteries	W
E_{LNG}	Energy Delivered by LNG	W
$EPNdB$	Effective Perceived Noise Level	dB
E_{tot}	Total Energy Required	W
E_U	Energy Used	J
F	Shear Force	N
F_{cad}	CAD Correction Factor	–
F_{diff}	Difficulty Factor	–
F_{fin}	Financing Rate	–
F_{mat}	Material Selection Factor	–
F_{obs}	Observability Factor	–
F_{pro}	Profit Factor	–
F_{tsf}	Test and Simulation Facilities Cost Factor	–
FF	Form Factor	–
FF_{avg}	Average Form Factor	–
G	Shear Modulus	
G	Reduction in Induced Drag Coefficient Due to the Ground Effect	–
GMC	Geometric Chord	m
H	Humidity Factor	–
h	Height of the Wing w.r.t. The Ground	m
h_{OB}	Obstical Height at Take-Off	m
h_f	Height at Flare Distance	m
hcg	Location of the Centre of Gravity w.r.t. the Ground	m

I	Moment of Inertia	m^4
I_α	Mass Moment of Inertia per Unit Span	m^3
I_{xx}	Moment of Inertia	m^4
J	Second Polar Moment of Inertia	m^4
K_α	Spring Constant	–
k_{CO2}	Heat Conductivity Coefficient	–
K_{door}	Door Factor	–
K_{Lg}	Main Landing Gear Factor	–
K_{uc}	Flap Deflection Factor	–
K_{ws}	Fuselage Factor	–
L	Length of the Fuselage	m
l	Length	m
L/D	Lift over Drag Ratio	–
L_{shaft}	Shaft Length	m
L_A	Lift at Approach Speed	N
l_h	Length of the Horizontal Tail	m
l_m	Length of Main Landing Gear	m
l_n	Length of Nose Gear	m
LHV	Lower Heating Value of LNG	MJ/kg
M	Mach Number	–
m	Mass	kg
m	Mass per Unit Span	kg/m
M_∞	Free Stream Mach Number	–
m_{air}	Mass Flow Air	kg/s
M_{cr}	Critical Mach Number	–
m_{fuel}	Mass Flow Fuel	kg/s
m_{loss}	Loss of LNG due to Vaporation	kg
M_{max}	Maximum Moment	Nm
M_x	Moment at Position x	Nm
MAC	Mean Aerodynamic Chord	m
n	Number of Rotations per Second	–
N	Time to Initiate Rotation	t
n_{design}	Loading Factor	–
N_{pr}	Number of Propellers	–
N_{rdte}	RDT&E Production Volume	
$N_{stringers}$	Number of Stringers	–
N_r	Production Rate	$-/month$
n_s	Number of Main Gear Struts	–
N_z	Ultimate Load Factor	–
$nblade$	Number of Blades	–
$Noise_{total}$	Total Noise	dB
p	Pressure	Pa
P	Power	W
$P_{artificial}$	Artificial Power	W
P_{blade}	Blade Power	W
$P_{m_{dynamic}}$	Dynamic Loading Main Gear	Nm
$P_{m_{static}}$	Static Loading Main Gear	Nm
$P_{n_{dynamic}}$	Dynamic Loading Nose Gear	Nm
$P_{n_{static}}$	Static Loading Nose Gear	Nm
P_{noise}	Propulsive Noise	$_{EPNL}dB$
P_{sh}	Shaft Power	W
P_{shaft}	Shaft Power	W
P_{ss}	Roll Rate	rad/s^2
q	Dynamic Pressure	kg/ms^2
q	Conductive Heat Energy	J
q_{xy}	Shear Flow in the xy-Plane	Pa
q_S	Shear Flow due to Shear Force	Pa
q_T	Shear Flow due to Torsional Moment	Pa
r	Radius	m
r	Distance Noise Sender and Receiver	m
r_α	Radius of Gyration	–
R_{aed}	Airframe Engineering and Design Cost Rate	–
R_{e_m}	Labour Rate	–
R_{hub}	Radius of the Hub	m
R_{prop}	Radius of the Propeller	m
r_{tip}	Distance From the Centre of the Hub to the Tip	m
R_{tool}	Tooling Rate	–
R_{wf}	Wing Interference Factor	–
Re	Reynolds Number	–
Re_{xcr}	Critical Reynolds Number	–
Re_L	Reynolds Number of the Fuselage	m
Re_x	Reynolds Number of Point x	–
REI_{NOx}	Index Factor of NO_x	–
RoC	Rate of Climb	m/s

S	Wing Area	m^2
s	Time	s
$s_{landing}$	Landing Distance	m
$s_{Take-off}$	Take-Off Distance	m
S_{vt}	Surface Area of the Vertical Tail	m^2
S_{wet}	Wetted Surface Area	m^2
S_{wf}	Surface Area of the High-Lift Devices	m^2
s_a	Airborne Distance	m
S_f	Fusleage Surface	ft
s_g	Distance for Ground Roll	m
S_h	Horizontal Tail Surface	m^2
SHP_{TO}	Shaft Horsepower at Take-Off	hp
T	Torque	Nm
T	Thrust	N
T	Temperature	K
t	Time	s
t	Thickness	m
$t_{min_{circumferential}}$	Fuselage Skin Thickness Needed for Circumferential Stress	m
$t_{min_{longitudinal}}$	Fuselage Skin Thickness Needed for Longitudinal Stress	m
$T_{2\pi}$	Mimimum Turning Time	s
t_{min}	Minimum Skin Thickness	m
T_{rev}	Reverse Thrust	N
t_2	Time Necessary to Reach a Bank Angle of 30 deg	s
u	Approach Velocity	m/s
u_{LNG}	Energy Density of LNG	J/kg
U_D	Divergence Speed	m/s
U_F	Flutterspeed	m/s
u_j	Jet Stream Velocity	m/s
V	Velocity of the Aircraft	m/s
V_∞	Free Stream Velocity	m/s
$V_{stall_{landing}}$	Stall Speed at Landing	m/s
$V_{stall_{take-off}}$	Stall Speed at Take-Off	m/s
$V_{tire_{max}}$	Maximum Tire Operating Speed	m/s
V_{cr}	Cruise Velocity	m/s
$V_{Endurance}$	Speed for Maximum Endurance	m/s
V_{in}	Incoming Velocity	m/s
$V_{incomming}$	Incoming Free Stream Velocity as Seen by the Propeller	m/s
V_{LO}	Speed at Lift-Off	m/s
V_{Range}	Speed for Maximum Range	m/s
V_{stall}	Stall Speed	m/s
V_{tip}	Tip Speed	m/s
V_e	Exit Velocity	m/s
V_f	Speed at Flare Distance	m/s
V_h	Air Velocity over the Horizontal Tail	m/s
W	Weight	N
W/P	Power Loading	N/W
W/S	Wing Loading	N/m^2
W_{ampr}	AMPR Weight	N
W_{AVG}	Average Aircraft Weight	kg
W_{comp}	Compressor Work	J
$W_{compressive}$	Compressive Loading	N
W_{dg}	Design Gross Weight	lb
W_F	Fuel Weight	kg
W_{ff}	Fuel Flow Factor	–
$W_{fuselage}$	Fuselage Mass	lb
$\dot{W}_{gg}$	Work by the Free Turbine	J
W_{MTOW}	Maximum Take-Off Weight	kg
W_{OE}	Operational Empty Weight	kg
W_{PL}	Payload Weight	kg
$W_{tensile}$	Tensile Loading	
W_{TO}	Take-off Weight	N
W_f	Installed Fuel Flow	kg/s
x_α	Static Unbalance	m^2
x_{ac}	Position of the Aerodynamic Center	m
x_{cg}	Postion of the Centre of Gravity	m
x_{cr}	Transition Point	m
y	Distance to Neutral Line	m
y_D	Drag Moment Arm	m

Subscripts

m	Manufacturing Phase
r	RDT&E Phase

Greek symbols

α	Angle of Attack	deg
$\alpha_{overnose}$	Overnose Angle	deg
$\Delta C_{L_{max}}$	Change in Lift Coefficient with High-Lift Devices	–
$\Delta C_{l_{max}}$	Increased 2D Lift Coefficient Due to the High-Lift Devices	–
ΔV	Velocity Increment	m/s
δ	Boundary Layer Thickness	m
δ_{amb}	Ratio of Inlet Pressure	–
$\dot{m}$	Mass Flow	kg/s
$\dot{m}_{LNG}$	Fuel Flow LNG	kg/s
$\dot{m}_{NOx}$	NO_x Flow	kg/s
$\dot{P}$	Time Rate of Change of the Roll Rate	$1/s^2$
η_c	Combustion Efficiency	–
η_{fuel}	Fuel Efficiency	–
$\eta_{is,comp}$	Isentropic Compressor Efficiency	–
$\eta_{is,in}$	Intake Isentropic Efficiency	–
$\eta_{is,n}$	Nozzle Isentropic Efficiency	–
$\eta_{is,turb1}$	Isentropic Work Turbine Efficiency	–
$\eta_{is,turb2}$	Isentropic Free Turbine Efficiency	–
$\eta_{p,cc}$	Combustion Chamber Pressure Ratio	–
η_{mech}	Mechanical Efficiency	–
η_{th}	Thermal Efficiency	–
$\frac{\partial C_L}{\partial \alpha}$	Slope of the Lift Curve	–
γ	Specific Heat Ratio	–
$\gamma_{approach}$	Approach Angle	deg
κ	Specific Heat Ratio of Air	–
κ_g	Specific Heat Ratio of Gas	–
λ	Taper Ratio	–
Λ	Sweep	deg
$\Lambda_{hingeline}$	Sweep Angle at the Hingeline	deg
Λ_{LE}	Leading Edge Sweep Angle	deg
μ	Dynamic Viscosity of Air	
μ_r	Friction Coefficient	–
ω	Efficiency Factor for Prandtl Wing	–
ω_α	Uncoupled Natural Torsional Frequency	Hz
Φ_{des}	Design Bank Angle	rad
Φ_1	Reached Bank Angle with a Certain Roll Rate	rad
ρ	Air Density	kg/m^3
ρ_{sea}	Air Density at Sea Level	kg/m^3
σ	Normal Stress	Pa
$\sigma_{ultimate_{tensile_1}}$	Ultimate Tensile Stress	Pa
$\sigma_{tensile}$	Maximum Tensile Stress	Pa
σ_{VMS}	Von Mises Stress	Pa
σ_E	Critical Stress	Pa
σ_x	Normal Stress in x-direction	Pa
σ_y	Normal Stress in y-direction	Pa
σ_z	normal Stress in z-direction	Pa
τ_{xy}	Shaer Force in the xy-plane	Pa
τ_{yz}	Shear Force in the yz-plane	Pa
τ_{zx}	Shear Force in the zx-plane	Pa
θ	Elastic Twist	rad
Θ_{amb}	Ratio of Inlet Temperature	–
θ_{OB}	Angle of Flight Path Between Take-off and Obstical Hight	rad

List of Deliverables

Deliverable	*Present*	*Chapter/Appendix*
Baseline Report		
Functional Flow Diagram	✓	3
Functional Breakdown Structure	✓	3
Sustainable Development Strategy	✓	5
Market Analysis	✓	6
Technical Risk Assessment	✓	16
Resource Allocation & Budget Breakdown	✓	17
Mid-Term Report		
Communication Flow Diagram	✓	4
Aerodynamic Characteristics Estimate	✓	9
Stability & Control Characteristics Estimate	✓	12
Sensitivity Analysis	✓	16
Verification & Validation Procedures	✓	18
Final Report		
Aircraft System Characteristics	✓	8, 9, 10, 11
Structural Characteristics	✓	8, 9, 10
Material Characteristics	✓	8, 9
Performance Analysis	✓	15
Configuration/Layout	✓	16
RAMS Characteristics	✓	16
Cost Breakdown Structure	✓	17
Compliance Matrix	✓	19
Project Gantt Chart	✓	C

Task Division

Below, the task division of the final report can be found. Note that this list serves only as an indication and for a more detailed overview of the executed tasks of every group member, please refer to the logbook.

Task	*Executed by*
General	
Preface	Bram
Acknowledgements	Bram
Introduction	Bram, Frouke
Summary	Sebastian
Conclusion	Frederick
Adapt Baseline Report & Mid-Term Report Deliverables	Bram
CATIA	Robbert, Koen & Frederick
LaTeX	Frouke
Review & Quality Check	All Team Members
Design Tasks	
Fuselage	Frederick & Robbert
Propulsion	Steven, Sebastian & Marit
Wing	Frouke & Koen
Energy	Kailey & Bram
Noise	Steven
Performance Analysis	Kailey & Robbert
Subsystem Integration & Optimalisation	Arnault-Quentin
Family Concepts	Kailey
Control & Stability	Sebastian & Frouke
Cost Analysis	Bram & Kailey
RAMS Characteristics	Kailey
Recommendations	Bram

Summary

The Advisory Council for Aviation Research and Innovation in Europe (ACARE) has set challenging goals to push engineers even further in the race to design a new generation of aircraft. The EuroFlyer project aims to take a head start by meeting goals previously thought optimistic while ensuring a realistic and feasible design entering service in 2035.

With the goal of pushing boundaries to aim for new frontiers, the EuroFlyer required a 75% decrease in carbon dioxide (CO_2) emissions and a 90% decrease in Nitrogen Oxides (NO_x) emissions with respect to the Embraer E170 on a similar mission. Furthermore a 10 dB noise emission reduction with regard to the Chapter 4 goals of the International Civil Aviation Organisation (ICAO) is to be accomplished. Although the economy has been plagued with drawbacks and a large recession, the air transport market has proven resilient. A profound market analysis pinpointed a profitable market gap in the future European regional air transport segment. With oil prices on the rise and the demand for low cost carriers increasing, airliners are seeking efficient aircraft to maintain their margin of profit. To satisfy this accumulating demand, the EuroFlyer is designed to carry 81 passengers over a range of 1500 km with a minimum flight speed of Mach 0.65. In addition, the aircraft has to possess the ability to operate on regional airports while complying with regulations and providing a safe and comfortable travel environment.

To meet these challenging requirements, an innovative design is proposed implementing several promising enhancements. The first novel feature is the revolutionary propulsive system achieving a propulsive efficiency of 99.8% by utilizing the boundary layer ingestion theory. Two large slowly contra-rotating fuselage mounted propellers ingest the low energy fuselage wake, leading to a higher propulsive efficiency. The second feature is the implementation of a fail-safe hybrid power train consisting of an electrical engine in combination with a Liquefied Natural Gas (LNG) powered turboprop and Auxiliary Power Unit (APU). Furthermore, the increased fuselage fineness ratio allows spacious installation of the drive train in addition to improved aerodynamic and structural properties. Finally, a slender clean wing design with spiroid wingtips reduces drag to a minimum. The implemented technologies show potential of possibly surpassing the projects conservative expectations in the future.

The presented design satisfies almost all key requirements and is estimated to weigh 27,840 kg, to consume 34.6 GJ of energy and to deliver 3.3 MW. The unequal amount of blades reduces noise emission substantially. In addition, the technique of trailing edge blowing is applied to the vertical tail. The horizontal tail is lowered with the purpose of further reducing propeller noise. The energy supply is divided between batteries and LNG, providing 17.5% and 82.5% of the total energy, respectively. The fuselage is sized at 20.37 m in length and has a diameter of 4.7 m. The wings span 36 m covering a surface of 65.18 m^2. Throughout the design process, a realistic approach is adopted to ensure aircraft performance with entry into service in 2035.

CHAPTER 1

Introduction

Sustainable development is hitting headlines around the globe, pushing aircraft industry to new solutions while still answering the ever increasing standards and requirements set by consumers. The ACARE has set challenging goals to reduce CO_2 emissions by 75%, NO_x emissions by 90% and noise emissions by 50% by the year 2050 [1]. In addition to rising demand of regional air transport in Europe, a solution is intensively sought after. With the goal of satisfying this demand and pushing creativity, the team was assigned to design an aircraft, named EuroFlyer, which fulfils the given requirements and enters service in 2035.

This Final Report marks the end of the Design Synthesis Exercise (DSE) 2013. As a concluding work, it provides a detailed overview of the steps taken in the final design process of the EuroFlyer aircraft. This report consists of 20 chapters which are although not expressly indicated as such, subdivided in three parts.

The first part covers the project and product background and discusses how the design team has progressed up to this point. Chapter 2 defines the mission, in Chapter 3, the Functional Breakdown Structure (FBS) and Functional Flow Block Diagram (FFBD) are discussed. Team Organisation and Planning follows in Chapter 4, after which the background of the EuroFlyer concept design is discussed in terms of a Sustainable Development Strategy (Chapter 5) and a Market Analysis (Chapter 6). In Chapter 7, the various concepts that were considered in the conceptual design stage are discussed and the final concept is selected.

The second part discusses the detailed design of the aircraft. First the fuselage is designed in Chapter 8, next follows the wing design (Chapter 9). This part concludes with a determination of the required energy and sizing the energy storage system in Chapter 11, after the design of the propulsion system has been discussed in Chapter 10.

The final part continues with an analysis of the stability and control characteristics in Chapter 12, noise emissions (Chapter 14) and flight performance (Chapter 15). Chapter 13 discusses the iterative process and shows how both the aircraft and its various subsystems are optimised, whereas Chapter 16 gives an overview of the final design, discusses Reliability, Availability, Maintainability & Safety (RAMS) characteristics and risk, shows the results of a sensitivity analysis and elaborates on the possibility of creating an entire aircraft family. Chapter 17 aims to compute the cost of the aircraft, after which the design is verified and validated in Chapter 18. A conclusion follows in Chapter 20, after which Chapter 21 ends the report with a set of recommendations for the continuation of the EuroFlyer design project.

CHAPTER 2

Mission Definition

With the aviation industry being larger than ever before, mission optimised aircraft are increasingly important. These aircraft are optimised for their range, velocity and number of passengers, resulting in lower fuel consumption and thus less operational costs. In any economy, cost reduction is an on going important process. Additionally, the environment becomes increasingly important. Concepts using biofuels and alternative power sources result in reduced fuel emissions and have lowered the overall cradle-to-cradle environmental impact. Chapters 5 and 6 further elaborate on the need for this mission.

Investigating the majority of aviation traffic movements shows an increasing growth in the short-haul flights which continue throughout the following decades [2]. The market is analysed in further detail in Chapter 6. From this the EuroFlyer is defined as a short-haul small capacity aircraft usable on the European market.

The Advisory Council for Aeronautics Research in Europe (ACARE) has formulated goals to reduce CO_2 emissions by 75%, NO_x emissions by 90% and noise emissions by 50% for the year 2050. To realise those reductions a whole new generation of aircraft is required.

With this information, the EuroFlyer mission and now a mission need statement and a project objective statement can be defined.

Mission Need Statement

To ensure future profitability of air transport and continue increasing sustainability in air travel an aircraft for the intra-European market needs to be designed with increased propulsive efficiency and lowered fuel consumption also meeting the ACARE goals set for emissions and noise.

Project Objective Statement

Design an environmentally friendly low passenger capacity short range aircraft using the propulsive fuselage concept which can carry around 80 passengers with a range of at least 1500 km in the year 2035, by 10 Bachelor students of TU Delft in 10 weeks time [3].

CHAPTER 3

Functional Breakdown Structure and Functional Flow Block Diagram

Before one starts thinking how the Mission Need Statement (MNS) and Project Objective Statement (POS) can be achieved, it is important to fully understand what the system is expected to do to satisfy the customer. In this chapter, the functions of the EuroFlyer are investigated and derived, as they describe the required behaviour of a system. In order to provide a logical sequence and a detailed operational sequence of the functions of the EuroFlyer, the Functional Breakdown Structure (FBS) & Functional Flow Block Diagram (FFBD) are presented.

3.1 Functional Breakdown Structure

The FBS, shown in Appendix A, provides a baseline of functions and their subsequent sub-functions in order to get an understanding of the total operation of the EuroFlyer. In addition, the FBS serves as a basis for the development of contingency procedures. All functions that must be performed by the EuroFlyer need to be identified and linked to requirements. Due to the fact that the FBS has an influence on the requirements and vice versa, an iterative process is required. The FBS is divided into three main functions: design, production and operation.

3.2 Functional Flow Block Diagram

The FFBD, shown in Appendix B, shows the detailed operational sequence for the EuroFlyer and the connection between the individual functions. These functions are divided into three main levels: before lift-off, flight and after touchdown. The functions of the EuroFlyer end with the end of flight cycle which can be seen as the beginning of a new flight. The before lift-off phase ends at the point when the EuroFlyer is airborne, whereas the after touchdown level starts as soon as the wheels of the aircraft touch the ground. The individual functions are connected by arrows showing the logical sequence between them. In order to describe the functions in more detail, some of them are shown in sub-levels, illustrating the exact procedure to perform the task. The production functions identified in the FBS are not elaborated on by means of a FFBD, since this is not the main focus of this project.

CHAPTER 4

Team Organisation & Planning

This chapter covers the team organisation and provides an insight into the task division. Firstly, the Organisational Breakdown Structure (OBS) will be treated, followed by the Human Resource (HR) allocation. Finally, the project planning will be discussed.

4.1 Organisational Breakdown Structure

The organisation of the EuroFlyer group consists out of four positions: a chairman, an administrative position, a reporting position and a systems engineering position. This is illustrated in Fig. 4.1.

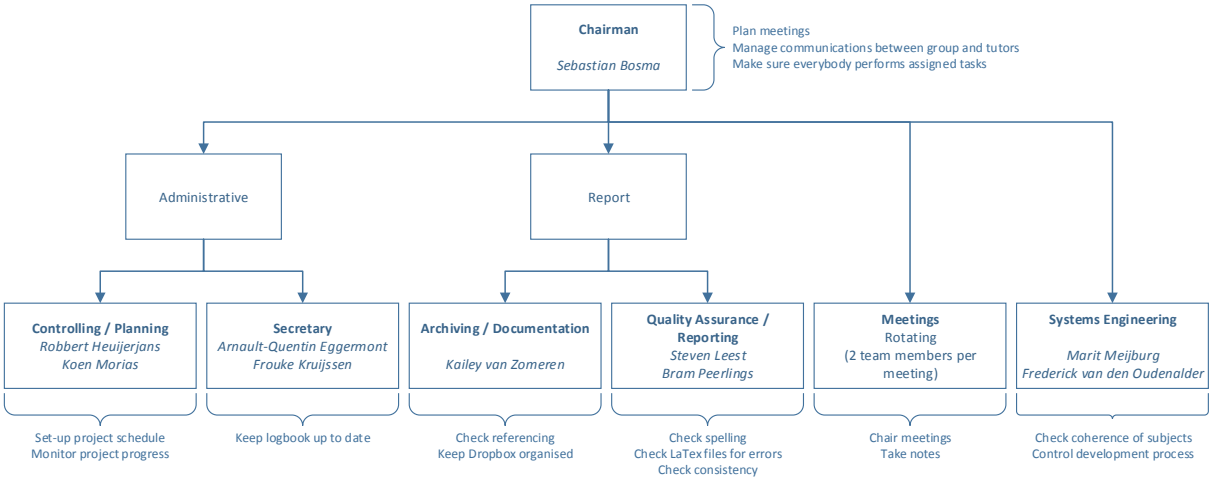

Figure 4.1: Organisational Breakdown Structure

In the following, every function is assigned to a group member and is further elaborated on. The allocation of the team members for every function was influenced by the results of a Belbin Test. Sebastian Bosma is assigned to fulfill the chairman position and is responsible for the communication between the group and various stakeholders. The secretary position is divided between two group members, being Arnault-Quentin Eggermont and Frouke Kruijssen. This task includes making minutes during the internal group meetings and to keep the logbook up to date. The controlling and planning function is executed by Robbert Heuijerjans and Koen Morias. This function focuses on the project progress with respect to the scheduled time. The quality assurance/reporting task will be executed by Steven Leest and Bram Peerlings which consists out of checking project for errors, spelling and consistency. The archiving/documentation task, which includes organising all the references used throughout the documents and to keep the documentation structured, will be executed by Kailey van Zomeren. Finally, the systems engineering task will be executed by Marit Meijburg and Frederick van den Oudenalder. The main focus of this task is to check the coherence between the different engineering disciplines. Throughout the project, the task of chairing and making minutes during the meetings is alternating between all team members.

4.2 Human Resource Allocation

The engineering tasks for the EuroFlyer project are divided into six disciplines as shown into Fig. 4.2. All the team members are working on the same design, which means that there has to be intensive communication between the different disciplines at all times, as they are all closely related. This also means that the allocated members might took the lead in design challenges, but were certainly not the only people working on problems in these design areas.

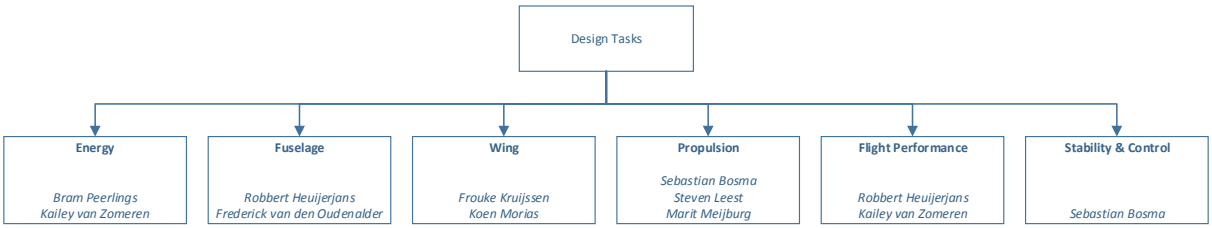

Figure 4.2: Human Resource Allocation

4.3 Team Procedures

To ensure continuous progress and that every group member was aware of all the developments in the project, certain procedures with respect to communication and documentation were defined.

In order to keep track of the progress of all the team members, three small meetings were held daily. The first one at the start of each day (9 am) in which the morning schedule was discussed. After lunch break (1:30 pm), a second meeting , to evaluate the progress made in the morning. At the end of the day (5:30 pm), the last meeting was held to update the team on every member's work that day and what he or she expected to be working on the next day. Also it was discussed whether the team was still on track. Furthermore, two meetings per week with the supervisor and coaches were held. These meetings were usually scheduled on Monday at 10 am and Wednesday at 4 pm, but varied due to irregular week schedules. During these meetings, the supervisor and coaches were informed on the project's developments and feedback and advice was given to the team.

CHAPTER 5

Sustainable Development Strategy

Since its origins the aviation industry has been growing. This resulted in the fact that the environmental impact became a crucial aspect during the design process. A more sustainable development approach is required to face the associated increasing emissions. Sustainable Development is defined as "meeting the needs of the present without compromising the ability of future generations to meet their own needs", according to the World Commission on Environment and Development [4]. This approach is nothing new for the aviation industry. Over the past 40 years fuel efficiency improved with almost 70%, reducing the amount of emissions significantly [5]. Recent studies showed that switching to new sustainable biofuels can reduce CO_2 emission by 72% in the aviation sector [6].

Subsonic aircraft in flight contribute to climate change in four ways, emitting carbon dioxide, oxides of nitrogen, water vapour and particulates. The CO_2 emissions are the most significant and best understood of these four. CO_2 emissions due to aviation is only a small percentage (2%) of the total global level. As can be seen in Fig. 5.2, a large growth in CO_2 emissions is expected if the technology level stays constant (displayed by the grey area). This forecast and the increasing social awareness on the global warming has raised the bar to reduce those emissions to the yellow projected area in Fig. 5.2 [5].

Other aircraft emissions enlarge the environmental impact significantly. Nitrogen oxide emissions effectively form ozone in the upper troposphere locally. High altitude emissions result in greater concentrations of ozone. Nitrogen also reduce levels of methane, which is also a greenhouse gas [7]. Water vapour produced by aircraft engines will under certain conditions form water droplets, creating condensation trails that also contribute to global warming due to the resulting increased cloud formation. Particulates (soot and sulphate) have the least significant effect, but all aircraft powered by combustion engines will release some amount of soot [8].

The total climate impact of aircraft emissions in the form of radiate forcing is possibly as much as 4.9% [9]. Turboprop aircraft have two significant benefits over jet aircraft regarding climate impact. They burn less fuel per passenger mile and they fly at lower altitudes, where there are less concerns on trails and ozone production. An overview of the amount of kilogram CO_2 emitted per passenger mile for several means of transport can be found in Fig. 5.1. Short distance is defined for trips under 20 miles for bus and train.

ACARE has set standards to reduce CO_2 emissions with 75%, the NO_x emissions with 90% and the noise emissions with 50% by the year 2050 [1]. The aircraft industry needs to change their design methodology towards a more sustainable approach to come up with new aircraft and propulsions systems, to comply with these emission standards. The EuroFlyer project requires a reduction of CO_2 emissions by 75% compared to the Embrear E170. In addition, noise should be reduced to 10 dB less than the standards described in ICAO Chapter 4. A new innovative and sustainable approach is needed to meet these goals with new aircraft.

In order to address these problems, it is important to define the origin of the emissions. Gas emissions are mainly originated from the propulsion system and the APU, whereas noise is generated in the propulsion system, the APU and on the airframe.

Propulsion systems used to contribute the most to noise. However over the last few years technology reduced

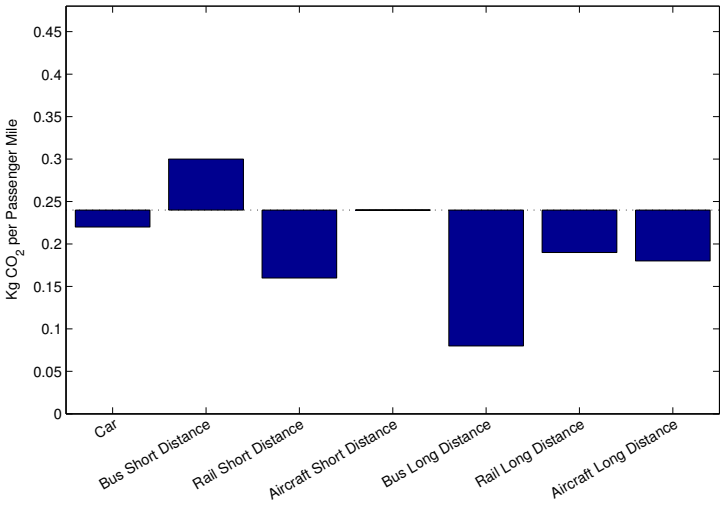

Figure 5.1: Emitted Amount of CO_2 for Different Means of Transport [10]

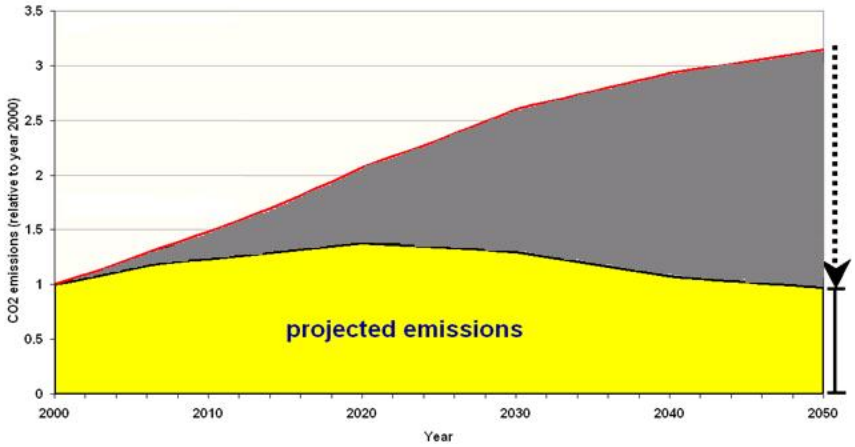

Figure 5.2: Roadmap for Future Emissions of CO_2 in Aviation [5]

this proportion, so that the airframe is the highest noise source nowadays [11]. Further reduction of the noise should be accomplished by limiting the noise created by the airframe. Most of the noise of the airframe is caused by the high lift devices (flaps and slats) and the landing gear [11]. These subsystems disturb the flow, directly resulting in the creation of vibrations. Reducing the noise further consists of finding innovative solutions for both the airframe and propulsion system.

Reducing the gas emissions, especially CO_2 and NO_2, can be easily done by burning less fossil fuels or even better by not burning any fossil fuel at all. The latter can be achieved by using an electrical energy source, which is an innovative solution for the future, but might not be feasible by 2035. Reduction in the amount of fuel used can be achieved in multiple ways. The propulsion system is of big importance, as the efficiency depends on the chosen propulsion system. For instance, a propulsive fuselage can increase the propulsion efficiency. Other possibilities can be found by reducing the required power. The thrust can be reduced by using new efficient aerodynamics shapes, high lift devices or by using a low drag fuselage. Another option is decreasing structural mass by the use of new materials such as composites. Finally, filtering these exhaust gasses might be a solution. Therefore meeting the gas emission goals of ACARE can be done in many ways.

A sustainable development approach should not be limited to new innovative concepts, it can be found as well in the production process. The selection of recyclable material or using the Cradle to Cradle (C2C) principle will result in less waste and disposal. For instance, using composites is beneficial because it will result in a lighter structure mass, but are hard to recycle. By now it may be clear that are many ways for the aviation industry to operate in a sustainable responsible way.

CHAPTER 6

Market Analysis

In the past ten years, the economy has been faced with some of most market affecting events, such as the great recession. Although the economy remains unstable and the events have had close relationships with the aircraft industry, the air transport business continues to thrive [12]. This resilience proves the importance of air travel in our society and is also a good market property which can be exploited when forecasting. These forecasts are an indispensable tool to ensure the success of a new type of aircraft, as this is largely assessed based on its sales. Forecasts can help predict in whether the market demands in the targeted market segments will be of profitable size and what parameters characterize these demands. In this process, market analysis is often defined as three-dimensional, differentiating between *customer*, *function* and *technology*.

To ensure that the product that is being designed does indeed satisfy future demand, a market analysis needs to be performed. First, literature studies were performed on the three dimensions by examining different twenty-year forecasts [2, 12, 13, 14, 15], made available by various aircraft manufacturers. With the extracted information and retrieved data, the amount of units demanded in 2035 was predicted. A preliminary cost estimation was performed in [16], a more accurate will be conducted in Chapter 17.

6.1 Function and Customer

As different customers require different product functions, the first two dimensions, function and customer, are closely related in this project and are therefore combined. The first step was to look into market customers as well as the different continents. Next, the expected market for implementation was evaluated in order to find the biggest functional developments predicted for 2035. This was executed by separately looking into passenger needs and aircraft carrier needs.

6.1.1 Continental Markets

When investigating the demand in different continents, one development clearly has the headline in all market outlooks. As it happens, an impressive relative growth is expected from developing economies. Embraer forecasts that world air transport demand in 2029 will reach levels close to 2.7 times higher than in 2009. China will lead this increase with an average annual Revenue Passenger Kilometre (RPK) growth rate of 7.3% over the next 20 years followed by Latin America, Asia Pacific and Russia/Commonwealth of Independent States (CIS), each with rates of around 6% per year. Africa will grow 5.1% and mature economies such as North America and Europe by about 3.2% and 4.2%, respectively [15]. However what must be kept in mind is that these are percentages. If the actual RPK sizes are illustrated, one can see in Fig. 6.1 that Europe will be the most profitable continent of the world by 2029.

Airbus' forecast of the largest airflows (see Fig. 6.2) in the year 2030 shows similar trends to the Embraer forecast. Again, it can be distinguished that the large air traffic regions will be Europe, North America and China. Now it can even be precised that domestic flights in these three regions, merging Central and Western Europe as one region, account for more than 30% of air travel in even shares. When looking at deliveries of regional aircraft forecast, the largest orders are expected to originate from Pacific Asia, North America and Europe. Airbus' estimates are presented in Table 6.1.

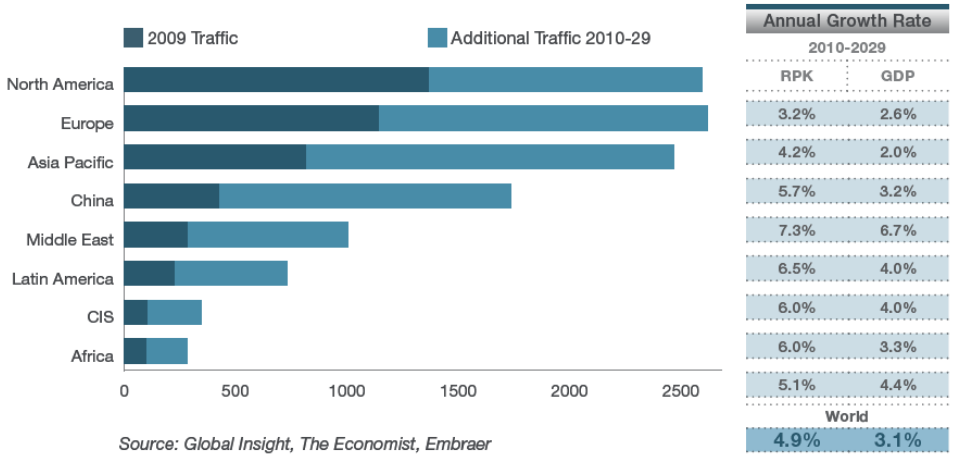

Figure 6.1: Projected Traffic and Economic Growth 2010 - 2029, Billion RPK by Region [15]

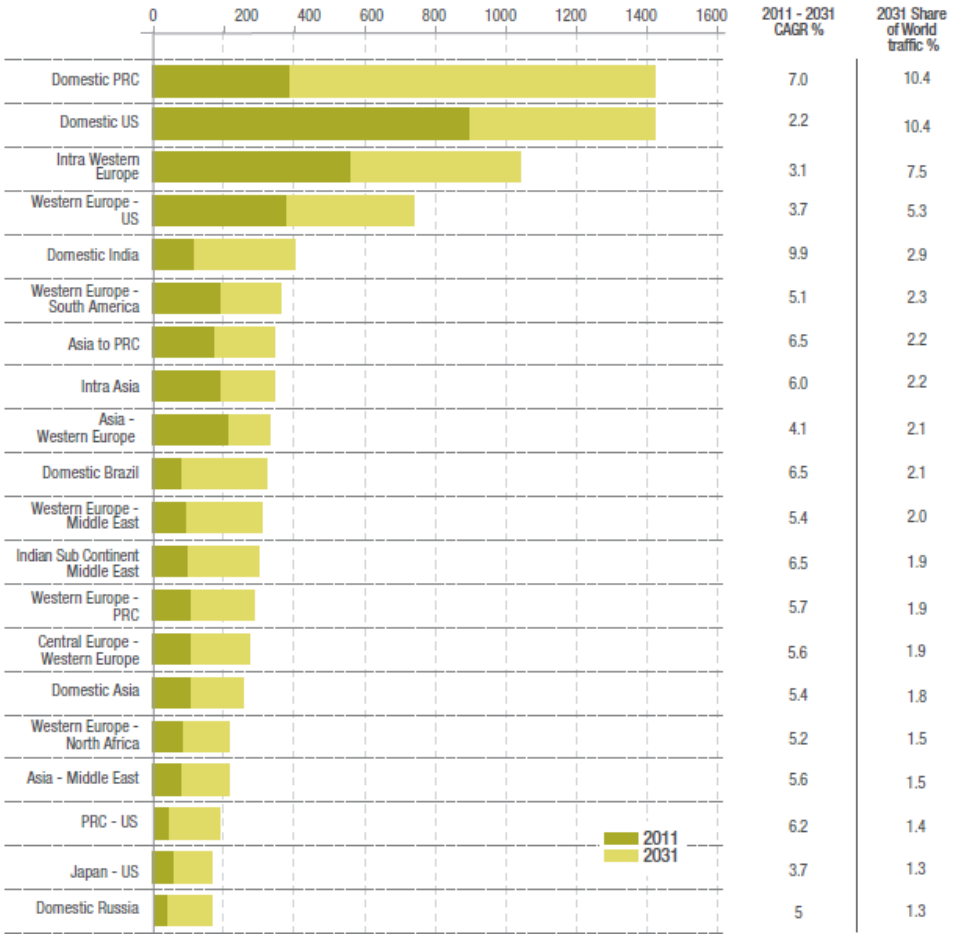

Figure 6.2: Largest 20 Traffic Flows in 2031, by RPK (Billion) [12]

Table 6.1: New Passenger Aircraft Deliveries by Region [12]

	Africa	*Asia-Pacific*	*CIS*	*Europe*	*Latin America*	*Middle East*	*North America*	*World*
2012 - 2021	413	4,505	492	2,815	1,004	1,007	2,580	12,816
2022 - 2031	544	5,113	737	2,886	1,081	899	3,271	14,531
2012 - 2031	957	9,618	1,229	5,701	2,085	1,906	5,851	27,347
	4%	35%	4%	21%	8%	7%	21%	100%

It seems that the European market is an appropriate choice for the product to be developed. This is due to high future demand and earnings in addition to low market implementation and entry costs. Now a more in-depth look is necessary into what the specific demand of the customers in the European market is.

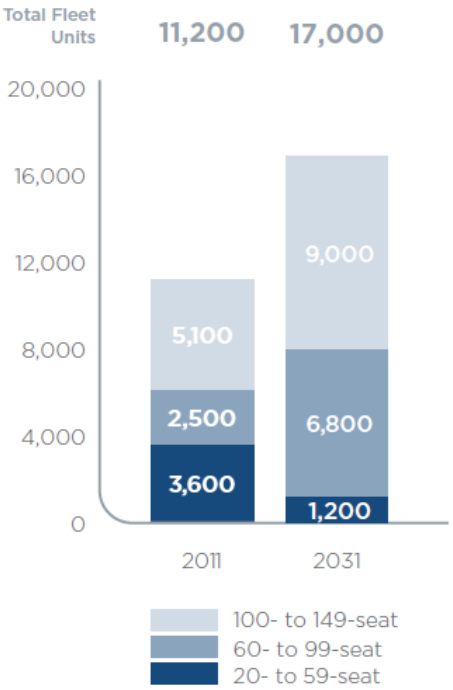

Figure 6.3: Total Fleet Units in 2011 and 2031 [15]

6.1.2 European Market

There are two aircraft performance indicators which are driving the demand. One is the amount of seats, which is driven by aircraft carrier needs, and the second is range, which is a demand coming from air travellers. First, looking into the amount of seats, Bombardier forecasts a large increase in the demand for aircraft with 60 to 99 seats which will consist of the delivery of 5600 new units including replacement [2]. The total fleet size growth is illustrated in Fig. 6.3.

Next, the second aspect, range of aircraft, was investigated. In the segment of regional carriers, the average length flown in Europe augmented from 384 statute miles to 390 statute miles in the period from 2000 to 2010 [2]. Linear regression yields a 0.6 miles per year increase, resulting in a forecast estimating an average distance flown of 400 miles or 640 km by the year 2030. From these flights, the longest flights with still interesting shares in the amount of air traffic will be around 1400 - 1800 km. These distances are connections from London, Amsterdam and Berlin to Madrid, for example.

6.1.3 Other Markets

Briefly remembering that in the forecast of the largest airflows, domestic North American flights and domestic Chinese flights, each had more than a 10% share as well, it could be interesting to investigate possible implementation of the product in those markets as well without having to make larger changes to the design. Chinese markets however are demanding for larger capacity aircraft in combination to medium range as opposed to regional distances which this project focuses on. On the other hand, the North American market is quite similar to the European segment differing only slightly in range. In the United States, the largest and driving air traffic market in North America, average trip length has experienced a similar rise compared to Europe, from 296 statute miles in 2000, to 464 statute miles in 2010 and even to 468 statute miles as of the first half of 2011 [2]. Linear regression yields a 16.3 miles per year increase, forecasting 795 miles or 1273 km by the year 2030. Keeping this data in mind when designing, the products' application could almost be doubled in size.

6.2 Technology

The last dimension characterizing markets is technology. In this relatively short project there will not be sufficient time to design, test and implement completely new concepts, therefore existing and conceptual technology will be used and combined. However, there are a few important developments on the technology front that should be mentioned. At the moment there are two crucial demand driven requirements that are pushing for technological innovation in future aircraft design: stricter regulations on emissions and rising oil prices. In Chapter 5, a closer

look was taken into the regulations on emissions. An interesting point to realize relative to emissions is that the targeted market is the most inefficient market segment. Fig. 6.4 depicts the energy consumed per Available Seat Kilometre (ASK). From this, it can be concluded that the largest gains can be obtained in the targeted regional market segment. The second requirement is imposed by aircraft carriers who have seen the continuous rise in kerosene prices, as illustrated in Fig. 6.5, decrease their profits [17]. Fig. 6.6 shows the rise in fuel share of total operating costs. Although there was a big oscillation in fuel price in 2008 - 2009, the fuel price is expected to continue to increase, following the trend of the past ten years. This is because the oscillation was mainly due to unique events. First, the threatening embargo of a few of the countries within the Organisation of the Petroleum Exporting Countries (OPEC) and the United States (US) demand for supplies caused the price to increase to an unprecedented level. Then, the US sell off of reserves, predicted reduction of European demand, a strong Euro and the fall of the Lehman brothers sent the price tumbling back down. This kind of events cannot be forecast, so an average has to be assumed.

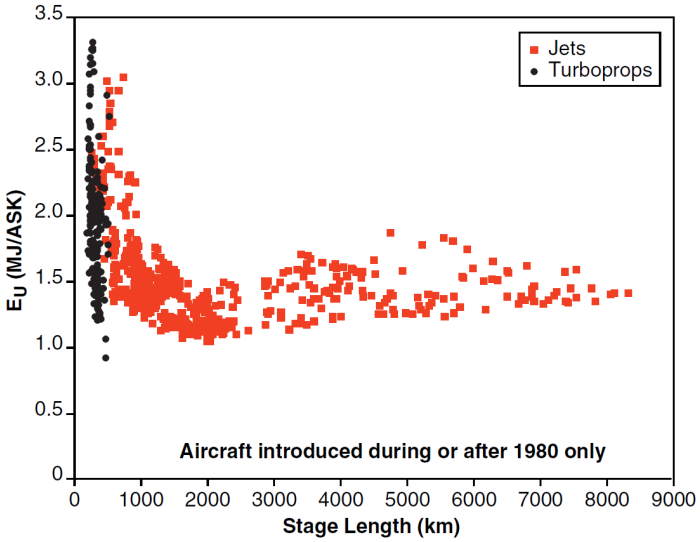

Figure 6.4: Energy Consumed per Available Seat Kilometre [18]

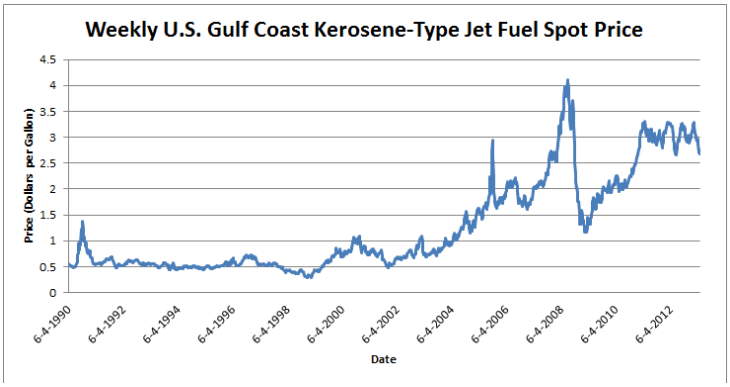

Figure 6.5: Weekly U.S Gulf Coast Kerosene-Type Jet Fuel Spot Price [19]

Another development is the competition of the high speed train network, where topographic characteristics permit it. There has been a lot of attention going to this development, especially with the recent large investments in the Chinese high speed railway network. However, Airbus forecasts that "high speed rail and air transport might face competition on some market segments. But, due to the main performance characteristics and differences between surface and air transport large segment markets will remain well separated. Air transport networks still have the potential to respond to modal competition" [12]. The predictions also stipulated that for distances over 1000 km, air travel would maintain an undeniable upper hand. In Europe, air travel will have a 70% market share for distances of around 1000 km, increasing asymptotically and reaching almost 100% at about 1500 km [12].

Closely related to the high speed train network competition is the subject of an aircraft biggest advantage: speed. Although it may seem like a bad idea to reduce this advantage by lowering speed, National Aeronautics and

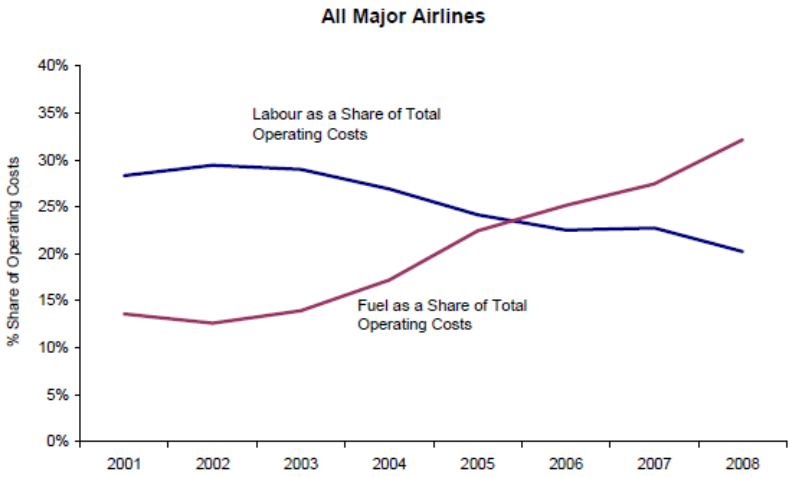

Figure 6.6: Fuel as a Share of Total Operating Costs [17]

Space Administration (NASA) argues in its market analysis for the Subsonic Ultra Green Aircraft Research (SUGAR) project [6] that the advantages of slower air travel will outweigh the disadvantages. The main advantage is that slower flight can make aircraft notably more efficient, therefore reducing fuel costs and ultimately ticket costs. This would make air travel more attractive to consumers outweighing the now slighter smaller travel time difference. NASA predicts that optimum flight speeds for medium and large aircraft will respectively be between Mach 0.7 and 0.8. Projecting these flight speeds to regional aircraft, an optimum flight speed of approximately 0.61 to Mach 0.64 is found. When looking at NASA categorisation an aircraft with 80 passengers would be in the largest section of regional aircraft, bordering on medium when looking at a range of 1500 km. Therefore for the sketched scenario a cruise speed of Mach 0.65 would seem a good first estimation.

The last development in the technological dimension is the growing market share of turboprops. ATR specified that the confidence in the turboprop market potential is dramatically growing and the company is expecting a 25% increase in turboprop market share between 2019 - 2029 [13]. In the forecast beyond 2030 which is elaborated in Section 6.3, more attention will be given to this subject.

6.3 2030 and Beyond

The reference market outlooks used unfortunately do not provide scenarios for the future beyond 2030. As the EuroFlyer is intended to be launched in 2035, at first sight these forecasts only provide an indication for the market potential. However, when the global trends spotted in these analyses are projected forward and the current regional fleet is investigated, the team trusts to be able to provide at least a qualitative scenario about the market that EuroFlyer will be entering in 25 years time. Based on the current fleet, projected market growth and retirement rate, some quantitative estimates are also made.

6.3.1 Trends

As stated above, the team assumes the most important global trends to continue for many years beyond 2030. First of these is a sustained growth of the Gross Domestic Product (GDP). Amongst others, this has been roughly constant at an average of 3% per year, measured over 40 years [2]. Additionally, two drivers that will get more and more important in the future are oil prices and the associated ecological footprint of the airline industry. The best known example of this is the emission of carbon dioxide, but the ACARE has also set stringent goals on reduction of nitrogen oxides and aircraft noise [1]. This will, in the teams opinion, lead to better utilisation of available aircraft (gradually increasing the average load factor) and will cause operators to turn to more sustainable aircraft sooner than projected. Besides these well-established driving factors, new influences are gradually becoming more important. In Western Europe one can think of the increasing role that a high-speed rail network can play [2, 12]. Globally, emerging markets in Asia and Africa cannot be denied as significant growth drivers.

6.3.2 Fleet Analysis

To be able to relate the above to the market potential of the EuroFlyer project, the current regional market was analysed. This market was said to stretch from aircraft seating 60 to 90 passengers. The research was focussed on the most important aircraft in this category, listed as [[20]]:

- ATR 72 – 70 seats
- Bombardier CRJ700 – 70 seats & CRJ900 – 86 seats
- Bombardier Dash 8 Series 400, formerly DHC-8 400 – 70 seats
- Embraer E170 – 70 seats & E175 – 78 seats
- Fokker 70 – 79 seats

The complete results of this analysis are shown in Appendix D; the most important figures are repeated here. According to the data [21], 1843 units of the above aircraft types are currently operated around the globe. On average, these aircraft are 7.5 years old, with the oldest still in operation having reached the age of 25. Not surprisingly, given a positive order backlog, the newest in this fleet has just been delivered to the customer. In this exact same market, Embraer counted 1805 units [15]. The difference can be explained by the fact that the Embraer count is from 2009. Also, it has to be noted that only the most important aircraft in this category are counted, and it therefore might not include some minor players.

When this market segment is split up between propulsion methods, the differences between the analysis by the group and by Embraer are a little larger [15]. The latter mentions 740 turboprops as of 2009 (ATR 72 and DHC-8 400), whereas own research has shown there to be 900 in operation. This is almost completely explained by the fact that since 2009, 170 ATR's have been produced. Looking at jets, the group counts 943 units, whereas Embraer shows 1065 [15]. This variance is explained by, as mentioned previously, the focus of the group's research, in which aircraft with a very low market share were not considered. On average, turboprops are a few months older than their jet powered counterparts.

Growth

Based on this current (60- to 90-seat) fleet, Embraer expects the 2029 fleet to have grown to 5030 units, of which 4325 will be new deliveries [15]. In the 60- to 99-seat market, Bombardier sees room for 5600 deliveries [2]. Combined with a 2011 fleet of 2500 aircraft, of which 1300 will retire in the next two decades, the 2031 fleet will consists of about 6800 aircraft. ATR [13] is a little less specific with their outlook, but sees room for 1250 new turboprops seating 61 to 90 passengers. From this, however, they are able to conclude a growing confidence in the turboprop market potential. Boeing is less positive, with a little over 2000 regional jets to be delivered between now and 2030 [14], Airbus sees room for approximately 1700 new single-aisle aircraft up to 100 seats, but unfortunately does not specify a lower limit to the number of seats available in the aircraft considered [12].

It cannot be missed that the different forecasts have produced quite different results. Airbus and Boeing, which do not (or only barely) cater to the regional market, estimate growth towards larger single-aisle jets (such as their 737 and A320-families). Embraer and Bombardier are closer together, especially when it is taken into account that 90- to 100-seaters are also included in the latter forecast. Adjusting for this assuming a linear distribution, 75% of 5600 deliveries (4200 units) will be aircraft seating 60 to 90 passengers. ATR deviates from these numbers again, although it specifically mentions turboprop regional aircraft. The team has decided to average all these different numbers, weighing Bombardier's and Embraer's marginally more (a factor of 1.1), to get to a combined forecast of 3120 aircraft deliveries, of which 40% (approximately 1250 units) is assumed to be turboprops aircraft.

Retirement

Now growth has been considered, it is worthwhile to look at fleet replacement. Avolon, an international aircraft leasing company, spots that the retirement age of regional aircraft is increasing [22], as shown in Figs. 6.7 (a) and (b). Whereas at present, most of these aircraft are jets with a high operating cost, Avolon agrees that in the future, the market share of turboprops will increase [22]. As these are cheaper to operate, the economic life is lengthened and carriers will be not so eager to replace these machines early on. As can be read from the graphs, the mean retirement age is 12.1 years and is assumed to shift to 18.3 years in 2021. It is not unthinkable that around 2030, this average retirement age will have increased further, up to 23 to 25 years[1].

[1] Unfortunately, no data for regional propeller aircraft could be found. Given their lower operational cost, it is assumed that these machines are retired later than their jet-powered counterparts. This is taken into account in the estimation for 2030.

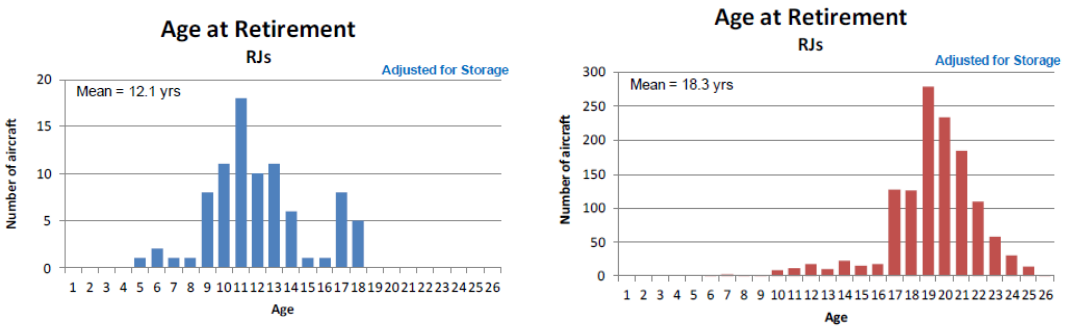

(a) 2012

(b) 2020

Figure 6.7: Regional Jet Age at Retirement [22]

As any market analyst will confirm, the aviation industry is highly cyclical. Based on the period of these cycles on the average retirement age, it can be argued that the market potential available today, will be available by 2035 as well. The team has decided the future to be too uncertain to analyse long-term future industry growth or decline at this stage. Therefore, it assumed that the number of aircraft to be delivered in 2012 to 2031 will be equal to the number of regional aircraft to be delivered in 2032 to 2051: 3120 in total, split 40/60 between (turbo)props and jets. If this again follows a normal distribution, most aircraft will be delivered by 2040.

6.3.3 Conclusions and SWOT-Analysis

If the EuroFlyer is scheduled to make it first flight in 2035 and sees the program launched a few years earlier, the team is confident that the aircraft is available in time for regional airlines to consider in their fleet replacement plans. Given the added efficiency of propeller-driven aircraft, the team considers it most likely that the industry will continue to grow, ensuring the market potential established. Based on simple analyses, it is expected that somewhat over 3000 aircraft (split 40/60 between turboprops and jets) will be delivered to this entire market between 2032 and 2051. This number holds for the global industry, whereas the team sees most opportunities in the European (and possibly North-American) market.

In order to assess the attractiveness of the European market for the EuroFlyer, a (Strengths, Weaknesses, Opportunities and Threats (SWOT) analysis is performed. All strengths, weaknesses, opportunities and threats mentioned below can be visualized in a SWOT-diagram, as shown in Table 6.2.

Table 6.2: SWOT-Analysis of the European Market

Strengths	*Weaknesses*
High demand for aircraft type Much to improve, current aircraft outdated	Not tending to 'next-future' markets (2050 +)
Opportunities	*Threats*
Sustainable image Ability to start EuroFlyer-family Trendsetting in emerging markets Interesting to Low Cost Carriers (LCC)	Modal shift (esp. rail network) Cluttered airports Cluttered airspace

CHAPTER 7

Concept Selection

Starting out with a mission, a set of constraints and having identified a market potential, the EuroFlyer design team has progressed through various stages to be able to present its final work in this report. The most notable step made concerns the concept selection. In the previously published Mid-Term Report, the design team has moved from an extensive Design Options Tree (DOT) to three proposed designs [16]. Using a weighted trade-off process, one of these was selected most promising and was taken into the detailed design phase. A short overview of the aforementioned process is given in this chapter. Sections 7.1, 7.2 and 7.3 present the various concepts considered. The trade-off criteria and results are shown in Section 7.4, with a more elaborate description of the detailed design phase following in Section 7.5.

7.1 Novel Concept

The first concept, dubbed novel concept because of its futuristic layout, is a low-wing aircraft with a set of two contra-rotating propellers mounted at the rear of the fuselage. The fuselage is, although cylindrical, wider and shorter than normal, to increase structural efficiency and to create a larger boundary layer. This boundary layer is ingested by the propellers, increasing propulsive efficiency. Power will be provided by a hybrid system, combining LNG and high-tech Lithium-air (Li-air) batteries. A conventional tail configuration was found to ensure optimal stability and control characteristics, as well as a convenient structural integrity solution for the EuroFlyer.

As mentioned previously, this novel concept ultimately stems from an extensive DOT. Various subsystems were considered in more detail, such as the fuselage shape, wing, energy source, propulsion system and tail configuration. For further details on these separate trade-offs, the team refers to aforementioned Mid-Term Report [16].

7.2 Conventional Concept

As the name suggest, the conventional concept is more down-to-earth than the novel concept presented above. It is based on a reference aircraft, the ATR 72-500, which has been carefully adapted to suit the different mission needs. The result is a low-wing and conventional tail aircraft with an extraordinarily wide fuselage, seating all passengers and providing room for the landing gear (previously stored in separate fairings). The turboprop engines featured on the original ATR design are replaced by two high bypass ratio turbofans, increasing efficiency and reducing fuel burn and both noise and greenhouse emissions. The latter are further reduced by using LNG as fuel, replacing the kerosene today. Fig. 7.1a shows a schematic top view of this concept.

With all these design changes, the team is confident of having adapted the aircraft to such an extent that all EuroFlyer mission requirements are met. For further elaboration on the changes made to the original aircraft and their projected consequences, the reader is referred to the Mid-Term Report [16].

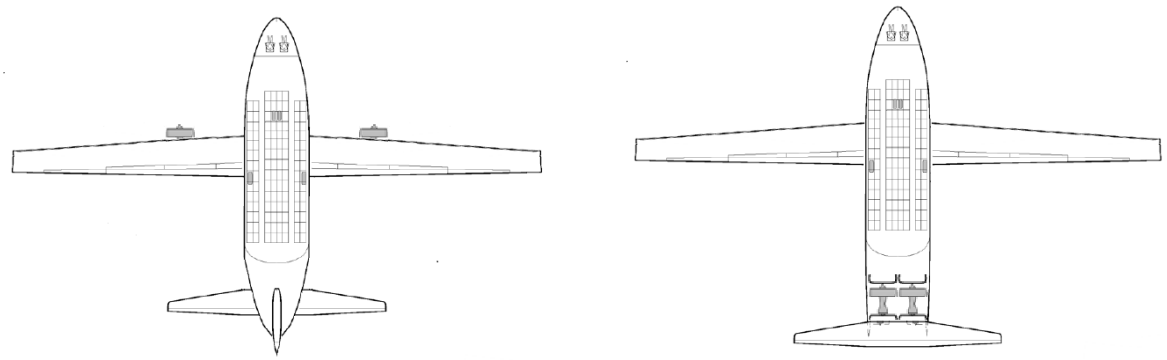

(a) Schematic Top View of the Conventional Concept

(b) Schematic Top View of the Π-tail Concept

Figure 7.1: Concepts Derived from the ATR 72-500

7.3 Π-tail Concept

For the Π-tail concept, the team elaborated on the conventional concept presented in the previous section. With one important change, the aircraft has moved away from the ATR design even further. To increase the total efficiency, the two turbofan engines have been moved to the top of the aft fuselage, such that the principles of Boundary Layer Ingestion could be applied. A direct consequence of this is the redesigned tail section. Previously featuring a conventional tail, this has changed into a Π-shaped tail, essentially a T-tail with two vertical stabilizers. The engines are mounted in between, as can be also seen from Fig. 7.1b.

7.4 Trade-Off

Choosing between these concepts was no easy task. Of course, all have some weaker points, but all also have equally valuable advantages. The conventional concept might be conservative and not high-tech, but seems much more likely to be introduced by 2035 than the novel concepts. The three concepts were carefully graded on these and other trade-off criteria, which are presented below. The list also includes the applied weighting factor and a short explanation of the criteria considered.

- **Emissions (10)**
  Sustainability is and has been a main focus in aviation. A reduction in fuel emission is one of the most important goals of the EuroFlyer project. Therefore the criterion emissions was appointed highest possible weighting factor. This should ensure that the concept chosen has the highest likelihood of achieving the desired performance.
- **Fuel Efficiency (8)**
  Another heavily weighted criterion is the fuel efficiency. With fuel prices on the rise and fuel resources running out in the future, airlines are looking towards ever more fuel efficient aircraft. All three concepts will be compared looking at the efficiency of the total propulsive system and operational empty weight to estimate the energy necessary to carry the payload.
- **Feasibility (8)**
  The EuroFlyer is projected to enter service in 2035. However, some of the concepts use subsystems and expected efficiency gains which are still under development or only theoretically proven. Feasibility assesses if all the integrated subsystems are expected to be ready, available and constructible before 2035.
- **Noise (7)**
  A reduction of 10 dB during take-off and landing as compared to the current ICAO Chapter 4 regulations is set as a design requirement for the EuroFlyer. The noise generated during take-off and landing is originating from various sources. The variables with the highest contribution to the noise are the high-lift devices, engine types and engines location. Some of the stakeholders have great interest in reducing the noise, explaining the high weighting factor.
- **Reliability, Availability, Maintainability and Safety (6)**
  Airlines operating EuroFlyer aircraft will do this to generate a profit. The cost related to the maintenance of the design, the turnover time and the availability of the design are therefore highly important for the customer.

- **Aerodynamic Efficiency (6)**
  An increased aerodynamic performance of an aircraft results in an overall higher efficiency. Metrics as lift-to-drag ratio were used to judge the performance of the concept aircraft.
- **Stability & Control (6)**
  When comparing the three design concepts Stability & Control (S&C) is an important criterion, as all aircraft should be safe to operate. As it is difficult to already determine the stability characteristics of an aircraft with the information known at the concept selection stage, an estimate is provided through logical reasoning. To grade the concepts on this criterion, positions of subsystems which have a large contribution to weight and the position of the lift surfaces are taken into account. It is especially noteworthy that a lower score on this criterion does not indicate an uncontrollable aircraft, but would rather indicate (predicted) smaller margins for the centre of gravity.
- **Complexity (5)**
  Complexity of a system will rapidly increase costs and is therefore important to customers. This fact holds for design, assembly but also for maintenance.
- **Sales Prospective (4)**
  The aviation market has shown that airliners are sceptic about adopting new aircraft designs in their fleet. This is accounted for with this trade-off criterion.
- **Family Concepts (3)**
  In addition to cost, possibilities to develop family aircraft are favourable to optimise the design potential and customer needs. New aircraft with similar missions can be designed with relatively low costs compared to an entirely new design.

For each criterion, grades between -2 and +2 were awarded. These, in addition to the final scores, are shown in Table 7.1 below.

Table 7.1: Concept Selection Trade-Off

		Scores with Weighting Factor		
Criterion/Concepts	*Weighting Factor*	*Novel Concept*	*Π-Tail Concept*	*Conventional Concept*
Fuel Emissions	10	18.0	-1.0	-10.0
Fuel Efficiency	8	8.0	8.8	-4.0
Feasibility	8	-7.2	-4.8	8.0
Noise	7	4.9	7.0	-2.8
RAMS	6	0.0	1.2	7.2
Aerodynamic Efficiency	6	10.2	4.2	-4.2
Stability and Control	6	-4.8	-1.8	7.8
Complexity	5	-5.0	-3.5	6.0
Sales Prospective	4	-0.8	-0.4	4.8
Family Concepts	3	1.2	2.1	4.2
Total Score		24.5	15.3	17.0

With a total of 24.5 points, the novel concept turns out to be the most promising design. The conventional concept comes second (with 17 points), the Π-tail concept, scoring 15.3 points, is the least promising design option. Hence, the novel concept is chosen as the concept with which the detailed design phase will start. As these total scores greatly depend on the weighting factors chosen, a sensitivity analysis was performed. The weighting factors were varied around the baseline (shown in the Table 7.1) with -2 or +2, and the total scores were computed for all these possible combinations. There also, the novel concept obtained the highest score.

7.5 Detailed Design

Although the team undeniably has gone a long way from the first brainstorms and design option trees to the concept presented above, it does not stretch any further than the conceptual design phase. Having selected the Novel concept as the starting point to the detailed design performed in the last half of the DSE, the team has looked into the aircraft in more detail. The findings are presented in the next chapters and show the final design of the fuselage, wing, propulsive system, energy storage and S&C. After that, the performance is analysed on various topics, such as flight performance and noise.

As with any engineering problem, the process of designing the EuroFlyer in detail has been highly iterative. This is further detailed in Chapter 13, but when continuing to read it is highly advised to keep this process in mind. That means that values that are presented in and at the end of the upcoming chapters are final values, obtained after the iterative process is completed, unless stated otherwise.

CHAPTER 8

Fuselage

This chapter presents the detailed fuselage design of the EuroFlyer. In Fig. 8.1, a road map can be found which displays the basic structure of this chapter. Firstly, the fuselage layout is determined. Secondly, the Environmental Control System (ECS) is discussed. Next, the overall geometry of the fuselage is established. After this, a preliminary structural analysis of the fuselage is provided and finally, the methodology to obtain the landing gear main parameters is described.

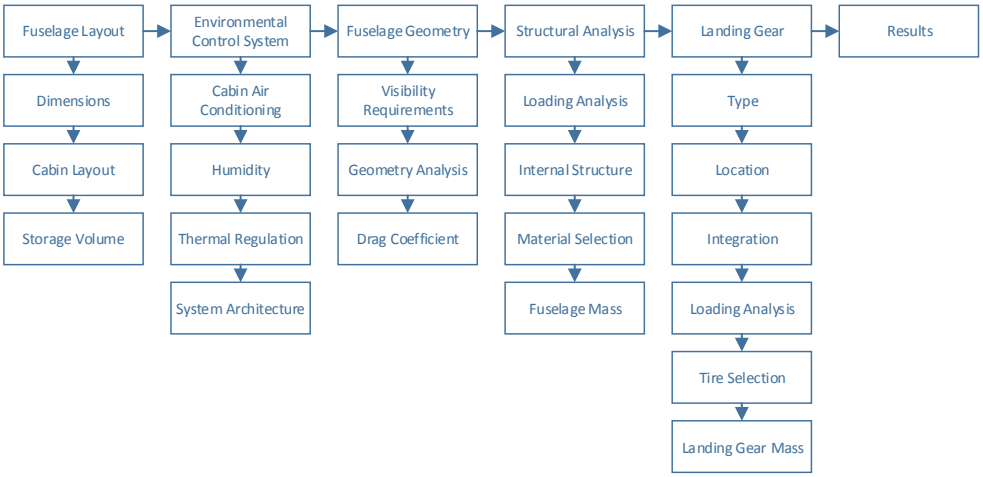

Figure 8.1: Fuselage Road Map

8.1 Layout

In this section, the dimensions of the fuselage are determined. Here the driving parameters for increasing the boundary layer area, fuselage length and diameter, are investigated. Secondly, the cabin layout of the fuselage is established for two different seating configurations. In the last section the cargo storage volume is estimated.

8.1.1 Dimensions

Since the main design parameters of the fuselage are the length and diameter, the first step in the detailed design of the fuselage consists out of examining which of these parameters is the most dominant in terms of increasing the boundary layer area. Since the EuroFlyer strives to make optimal use of Boundary Layer Ingestion (BLI), an initial sizing using the area of the boundary layer as a key parameter is performed. Here, the boundary layer thickness is approximated using thin plate turbulent boundary layer theory [23]. Due to the fact that the

boundary layer area is a function of the length and the diameter of the fuselage, it is crucial to determine which parameter has the most influence. In order to investigate this, a three-dimensional plot showing the boundary layer area as a function of fuselage diameter and length, as shown in Fig. 8.2a, is made.
As expected, it can be seen in Fig. 8.2a that the larger the fuselage diameter or length, the larger the area of the boundary layer. However, what is of interest, is which one is the most dominant factor for a reasonable fuselage length and diameter. When looking at the slopes of Fig. 8.2b and Fig. 8.2c, it can be seen that for a fuselage diameter of approximately five metres, the diameter is the driving factor for increasing the boundary layer area. After that point, it is more efficient to use a longer fuselage to increase the boundary layer area.

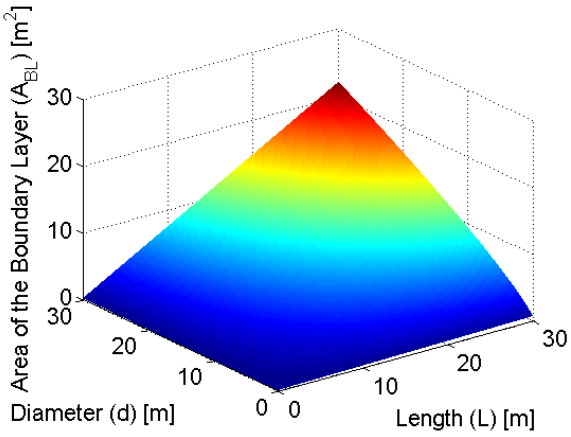

(a) As a Function of Fuselage Length and Diameter

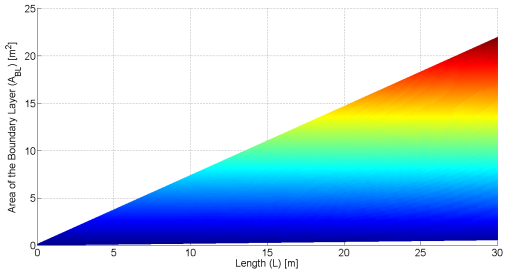

(b) As a Function of Fuselage Length

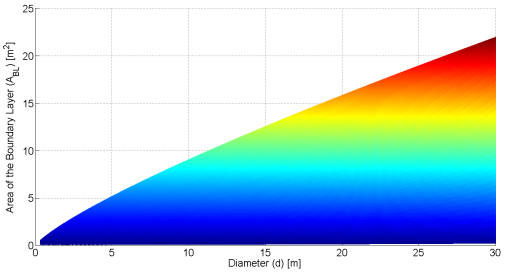

(c) As a Function of Fuselage Diameter

Figure 8.2: Area of the Boundary Layer as a Function of Fuselage Length and Diameter

The next step in the fuselage design process is to determine the actual size of the fuselage. The general approach is an inside out approach which means that first the seating configuration is chosen and the resulting fuselage length and diameter follow from this configuration.

In order to determine the size of the fuselage, important parameters and their dimensions for the internal layout of the fuselage, shown in Table 8.1, are derived from CS-25 regulations.

Table 8.1: Internal Layout Parameters

Parameter	*Value*	*Unit*
Seat Pitch (Economy)	0.8128	m
Seat Pitch (Business)	0.9652	m
Seat Width (Economy)	0.4572	m
Seat Width (Business)	0.4572	m
Aisle Width	0.381	m
Aisle Height	1.524	m
Flight Deck Margin	2.54	m
Cockpit Length including the Nose	3.5	m
Tailcone Length	3.5	m
Side Margin	0.23	m
Galley Volume per Passenger	0-0.03	m^3
Lavatories (per 40-50 Passengers)	1	–
Luggage Volume per Passenger	0.044	m^3

Earlier this section, it was observed that for a fuselage diameter under five metres, the diameter has a larger influence than the length on the boundary layer area. Thus, the fuselage sizing starts by defining the seating configuration in the form of adjacent seats. Due to the current trend and popularity of low cost carriers, the fuselage is sized for a pure economy class configuration. In order to obtain flexibility, a length margin of two metres is taken into account during the sizing of the fuselage length. This margin accounts for galleys, toilets and minor seating configuration changes. The values given in Table 8.1 are used to determine the seating configuration parameters. Furthermore, the so called fineness ratio which is the diameter over the length ratio is used as an additional criterion as it serves as a basis for the drag estimation of the fuselage. In Table 8.2, five proposed seating configurations are presented.

Table 8.2: Proposed Seating Configurations

Seating Configuration	*3x3*	*2x2x2*	*2x3x2*	*2x4x2*	*2x2x2x2*	*Unit*
Fuselage Diameter	3.822	4.242	4.699	5.156	5.576	*m*
Fuselage Length	21.998	21.998	20.374	18.75	18.75	*m*
Fineness Ratio (d/l)	0.1737	0.1928	0.2306	0.275	0.2974	–

From Table 8.2 it can be seen that the 2x3x2 configuration is the most beneficial for the EuroFlyer to meet the given requirements. This is due to the following reasons. As discussed previously, the driving parameter for the boundary layer area is the fuselage diameter. However, it is also argued that a too large fuselage diameter is not very convenient due to several reasons. A too large diameter would mean that a large propeller is required to efficiently make use of BLI. Secondly, the passenger comfort would decrease during manoeuvres, as the outer passengers are located further away from the centre-line of rotation. Also, it can be seen that the fineness ratio of the 2x3x2 configuration is quite close in comparison to today's aircraft to the optimal fineness ratio of 0.3 in order to reduce the drag coefficient [24].

Another point of importance is the emergency exits. As stated in Corke [25], two type I and one type III emergency exits are required at each side of the fuselage. The dimensions for such emergency exits are 122 *cm* x 61 *cm* and 91 *cm* x 51 *cm*, respectively. These exits have been located at the front, middle and aft section of the fuselage. The front and aft exit on the port side of the aircraft are used during regular loading and unloading operations. Due to the twin aisles configuration, the time required for these operations is reduced and thus the turnaround time is decreased.

Just as the number of exits, the amount of windows is also regulated by CS-25 regulations. These state that for the fuselage length of the EuroFlyer, a minimum of 13 windows on each side of the fuselage is required. From a structural point of view, the window edges are curved to decrease stress concentrations located at each corner. For safety reasons, the type III exit accommodates one window, located in the middle of the cabin.

8.1.2 Cabin Layout

With the given seating configuration, fuselage length and diameter, exit locations and extra facilities such as toilets and galleys, the fuselage layout and seating plan can be established as shown in Fig. 8.3a. It can be seen that the cabin contains 84 seats, 81 for airline customers and 3 for flight attendants. Furthermore, the aircraft contains two galleys and two lavatories at the front and back of the cabin respectively. Fig. 8.3b displays an alternative cabin layout, which includes a business class section at the front of the cabin. This configuration has room for 12 passengers in business class, 67 in economy class and 3 flight attendants. This option allows airliners to change seating configurations according to their customers preferences and needs.
The next major step in the fuselage design is the detailed sizing of the cross-section of the fuselage. As can be seen in Fig. 8.4, the different dimensions of the fuselage cross-section are provided. Even though most short range aircraft do not use cargo containers, the cargo hold is still compatible with standard type A and type B Unit Load Devices (ULD) [25].

The fuselage dimensions, shown in Fig. 8.4, are summarised in Table 8.3 for convenience.

8.1.3 Storage Volume

As Fig. 8.3a and Table 8.3 show, the diameter of the fuselage is sufficiently large to provide a high storage volume, as well as a large head room for the passengers. The total volume beneath the cabin was approximated to be 76.52 m^3, by using a trapezoidal approximation. However, the volume available for cargo will be lower since the fuel system, energy system and wing box required for operation will be placed within this volume. In

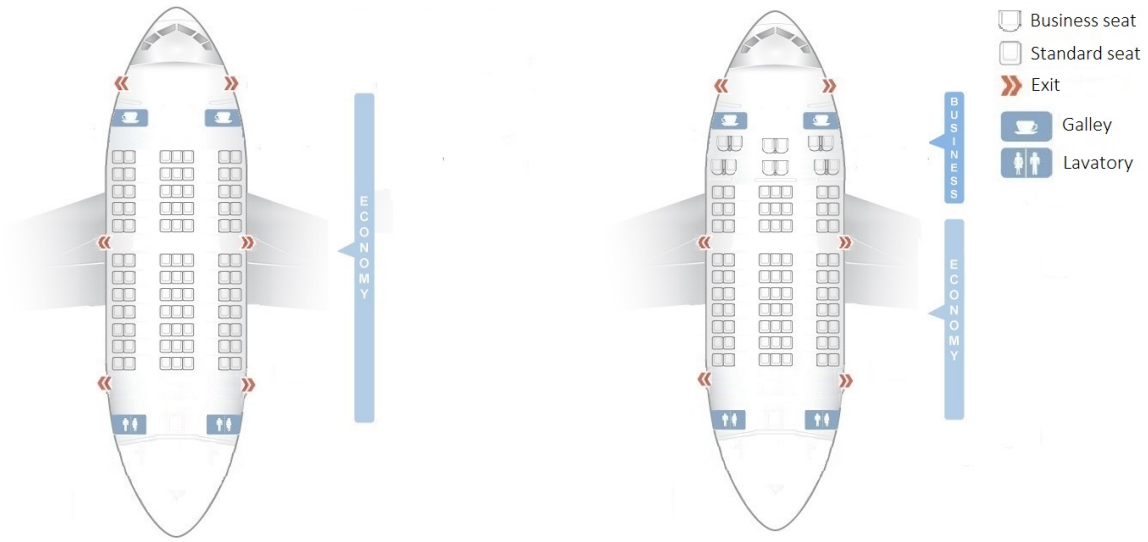

(a) Economy Class only

(b) Economy and Business Class

Figure 8.3: Seating Configurations

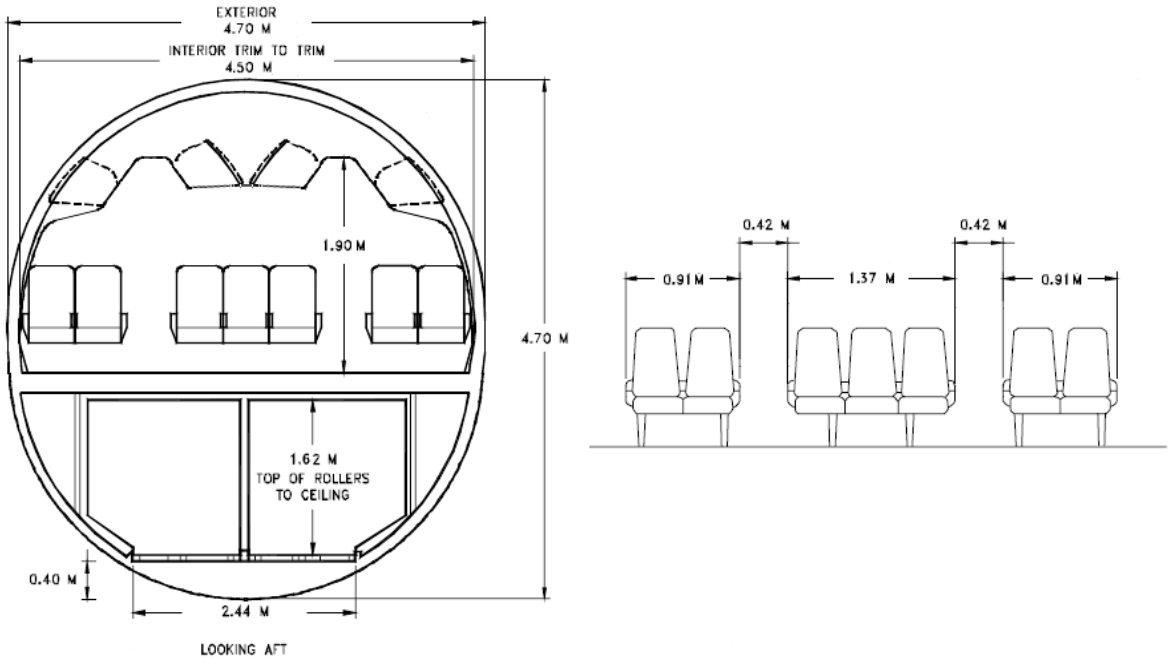

(a) Cabin Cross Sectional View

(b) Seating Configuration

Figure 8.4: Interior Fuselage Dimensions

Table 8.3: Dimensions of the Fuselage Cross-Section

Element	*Dimension*	*Unit*
Thickness of Passenger Floor	0.1	*m*
Thickness of Cargo Floor	0.1	*m*
Headroom	1.65	*m*
Aisle Height	1.90	*m*
Height of Cargo Floor	0.4	*m*
Height of ULD	1.62	*m*
Container Clearance Margin	0.08	*m*

this stage, the fuel tanks are estimated to contain a volume of approximately 7 m^3, the battery container is sized for a volume of 10 m^3 and the wing box for approximately 5.5 m^3. When subtracting these numbers from the

total available cargo hold volume, approximately 54 m^3 is available for cargo storage. However, the location and integration of the landing gear, which will be discussed in Section 8.5.3, may further decrease the cargo storage volume.

8.2 Environmental Control System

To ensure passenger comfort, the EuroFlyer is equipped with an ECS. Its purpose is to maintain a comfortable atmosphere during flight. The ECS usually focuses on the internal part of a vehicle. Therefore, this section will only discuss the internal aircraft environment. In addition cabin air conditioning, humidity levels, temperature and the air cycle method are described in this section.

8.2.1 Cabin Air Conditioning

The air conditioning system must provide comfortable cabin conditions (22 $\pm$ 2 $°C$, 95 $\pm$ 5 kPa, 50-70 % humidity) [26]. These conditions have to be maintained during all flight phases. This means that the air conditioning system must provide ventilation, pressurisation, heating, cooling, humidification, dehumidification and disinfection. Due to these tasks, the air conditioning system is the second most power-consuming system of the aircraft [26]. Therefore approximately five percent of the total energy is accounted for operating the onboard systems, including the ECS.

The complete cabin air is refreshed 20 times per hour. With the cabin pressure set at 8000 ft and a cabin volume of approximately 58.09 m^3 a mass flow of 0.31 kg/s is required. Since cabin air is originated from the main compressor this mass flow is taken into account when sizing the compressor. This is further discussed in Section 8.2.4. This amount of air enters the cabin through grilles present in the cabin. Air exits the cabin through additional grilles located near the floor and finally, the air exits through an outflow valve in the bottom part of the fuselage (see Fig. 8.5).

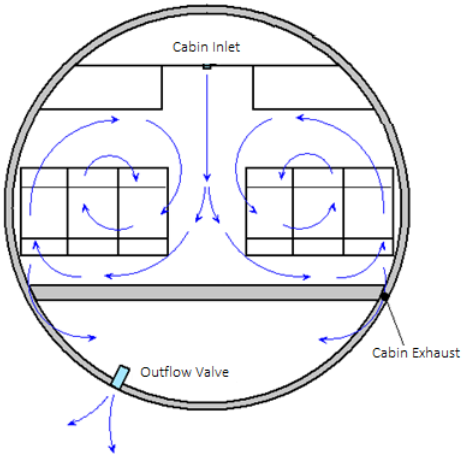

Figure 8.5: Cabin Air Flow [27]

8.2.2 Humidity

As mentioned earlier, human comfort requires a relative humidity of 50-70%. However, such high levels can not be maintained on board of an aircraft. The main reason for this is due to condensation which can affect metals and stimulate micro-organism growth. Therefore, the relative cabin humidity is kept within the 10-20% range. At cruise altitude, the outside air humidity levels are very low, thus during cruise it is easy to maintain such low levels without the presence of passengers. However, when passengers are present, the water vapour released by breathing increases the air humidity. During loading and unloading operations, the ECS must first dehumidify the fresh air introduced into the cabin in order to avoid damaging the aircraft. Another reason for regulating air humidity is that after 3-4 hours of exposure to 10% humidity, passengers might experience discomfort [26].

The EuroFlyer strives to maintain a relative humidity of 20 to 60%. However, this depends on the material used for constructing the fuselage. Regarding humidity levels, composites offer a significant advantage. Composites

are not as sensitive to water vapour as metals, which allows for operation at higher humidity levels. This in turn leads to a substantial improvement in flight experience [28].

8.2.3 Thermal Regulation

From a temperature point of view, there are two main requirements, one related to human comfort and the other to avionics. The cabin temperature should be regulated between 18 and 26 °C without any thermal shocks. In order to provide the optimal atmosphere for avionics, the cabinets must be kept within 30 to 70 °C [26].

Thermal design is driven by two extreme cases. The first case is the worst cooling case. This means that the aircraft is at a hot, humid location with its doors closed, its engines running and filled with passengers. In this situation, the cooling system should be able to cool the cabin down from 47 to 21 °C in less than 30 minutes [26].

The second case is the worst heating case. In this situation, the aircraft is completely empty and located at a cold humid place with its doors opened, engines off and running on APU power. For this case, the systems should be able to heat the aircraft from -40 to 24 °C within 30 minutes [26].
The ECS is designed to cope with both extreme cases. Therefore, the EuroFlyer is able to operate successfully in different environments where the temperatures differ significantly.

8.2.4 System Architecture

The EuroFlyer takes air from the main compressor, also known as bleed air, for pressurisation and air ventilation purposes. This air is run through two heat exchangers in order to cool the air before it can enter the cabin. After the first heat exchanger, the air is compressed again before it runs through the second heat exchanger. Afterwards, air is expanded through a turbine and is mixed with hot bleed air to reach the 10 to 35 °C needed to keep the cabin air at around 22 °C at all times [26]. A simplified form of the system architecture is shown in Fig. 8.6.

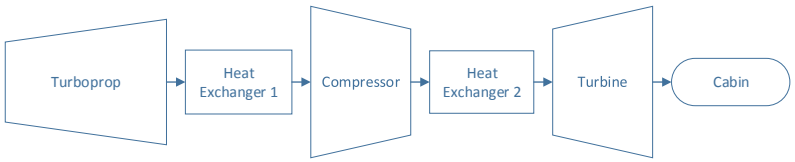

Figure 8.6: Air Flow Architecture

8.3 Geometry

Since the overall dimensions and interior layout have been determined, the precise geometry of the fuselage can be established. This section first identifies the visibility requirements regarding fuselage design. Then, it elaborates on the performed geometry analysis. Finally, the drag coefficient corresponding to the chosen geometry is calculated.

8.3.1 Visibility Requirements

Before the baseline geometry can be developed, a few important factors have to be taken into consideration. Firstly, the pilots need to have is an unobstructed forward view [29]. In order to achieve this, a minimum over-nose angle, $\alpha_{overnose}$ is required. This angle is defined as the angle between the horizontal and a line running through the pilot's eye, down to the point of highest visual obstruction, see Fig. 8.7. The required over-nose angle depends on the approach angle, $\gamma_{approach}$, and the approach velocity, $V_{approach}$. The approach angle is defined as follows [25].

$$\gamma_{approach} = sin^{-1}\left(\frac{-D}{W}\right) \tag{8.1}$$

The approach velocity can be approximated to be 1.3 times the landing stall velocity with extended high lift devices [25]. With these values in mind, the over-nose angle can be computed by using Eq. 8.2.

$$\alpha_{overnose} = \gamma_{approach} + 0.177 \cdot V_{stall} \tag{8.2}$$

In this equation, V_{stall} is in m/s and $\alpha_{overnose}$ and $\gamma_{approach}$ are in degrees. Using Eqs. 8.1 and 8.2, the L/D ratio of 17.61 and a landing stall speed of $51.7 m/s$, the over-nose angle is calculated to be 9.1 deg.

Another visual requirement is the over-side vision angle, $\alpha_{overside}$. This angle represents the angle between a horizontal line through the pilot's eye down to the highest visual obstruction on the side of the fuselage, see Fig. 8.7. For commercial aircraft and general aviation, this angle is 35 deg [25].

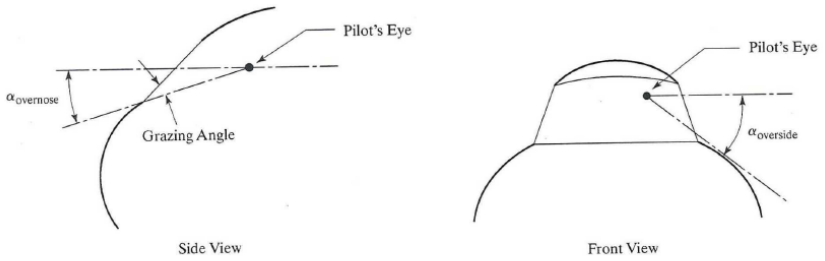

Figure 8.7: Representation of Pilot Vision Parameters [25]

8.3.2 Geometry Analysis

Two different shapes are evaluated and the final shape is chosen according to its aerodynamic performance. Each design's aerodynamic performance is monitored by making use of Computational Fluid Dynamics (CFD). In order to obtain these results, the fuselage geometry is defined in 2D using Computer Aided Three-Dimensional Interactive Application (CATIA), the meshing is performed in Geometry And Mesh Building Intelligent Toolkit (GAMBIT) version 2.4.6 and finally the CFD analysis is performed using ANSYS FLUENT version 14.5.

In Fig. 8.8 a graphical representation of both shapes is displayed. As can be seen in this figure, only the nose of both geometries differs. The tailcone section of both fuselage shape is identical. The first shape, referred to as the the baseline shape, is displayed in Fig. 8.8a. The second shape where the geometry of the nose has been altered is displayed in Fig. 8.8b. From this point on, this geometry is referred to as the altered nose concept.

(a) Baseline Geometry

(b) Altered Nose Geometry

Figure 8.8: Analysis of Evaluated Fuselage Shapes

For each geometry, the lift, drag, and moment coefficients are obtained. From this analysis, the effect of a different type of nose on the aerodynamic characteristics can be derived. As an example, Fig. 8.9 displays the velocity profile and pressure distributions for both geometries.

From these velocity profiles and pressure distributions the lift, drag and moment coefficient per geometry are obtained. In Table 8.6 these lift, drag and moment coefficients are displayed for both geometries.

Table 8.4: Aerodynamic Characteristics per Geometry

Parameter	*Baseline*	*Altered Nose*	*Unit*
Lift Coefficient	$-7.581 \cdot 10^{-3}$	$-2.478 \cdot 10^{-3}$	–
Drag Coefficient	$1.889 \cdot 10^{-2}$	$9.956 \cdot 10^{-3}$	–
Moment Coefficient	$4.816 \cdot 10^{-1}$	$3.088 \cdot 10^{-1}$	–

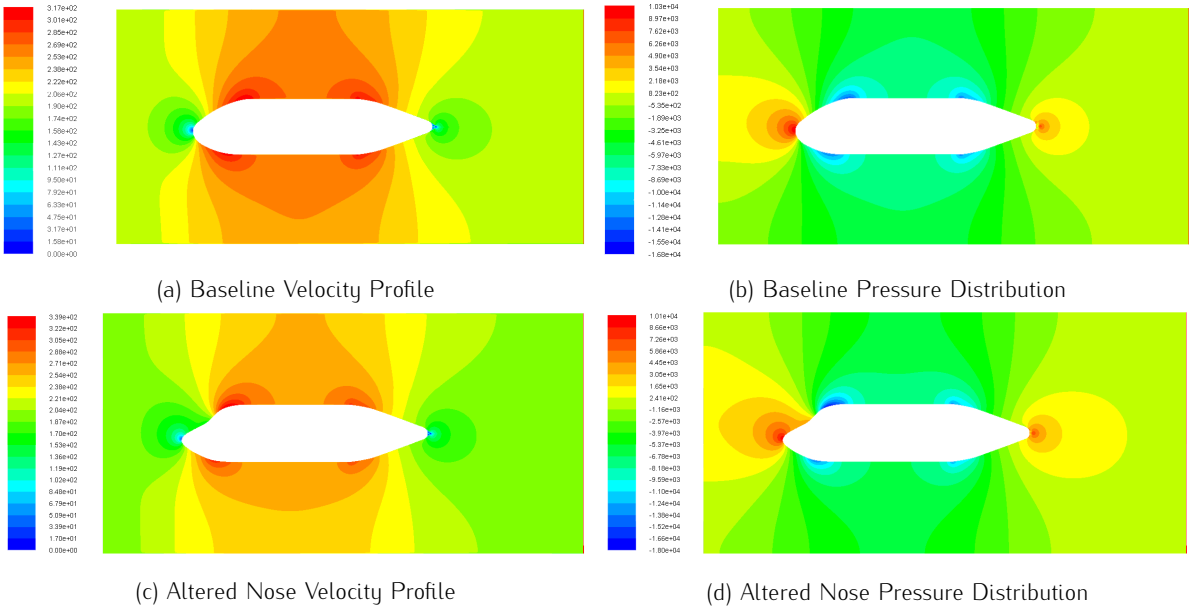

(a) Baseline Velocity Profile

(b) Baseline Pressure Distribution

(c) Altered Nose Velocity Profile

(d) Altered Nose Pressure Distribution

Figure 8.9: Velocity Profile and Pressure Distribution Analysis for the Baseline and Altedered Nose Geometry

When looking at the drag coefficients provided in this table it can quickly be noted that, in terms of drag, the altered nose geometry is superior. When considering the visibility requirements as stated in Section 8.3.1, the conventional nose also comes with advantages over the altered nose. Thus is due to the fact that the "dent" automatically increases the pilots over-nose angle.

8.3.3 Drag Coefficient Estimation

In this section, the procedure for the drag coefficient estimation of the fuselage of the EuroFlyer is described.

As the boundary layer changes from laminar to turbulent over the fuselage length, the drag significantly increases. Therefore, one has to account for laminar and turbulent skin friction coefficient. Since the point where this transition occurs must be known, the design team consulted literature to estimate the location of this point. According to Corke [25], it is assumed that the location of the transition point, x_{cr}, from laminar to turbulent flow, is at 5% of the fuselage length. This assumption is valid for a fuselage which has distinct shaped nose where in general transition takes place.

The general formula to determine the drag coefficient of the fuselage is provided by Eq. 8.3, which is shown below.

$$C_{D_{Fuselage}} = C_{f_{Fuselage}} \cdot FF \cdot \frac{S_{wet}}{S} \cdot R_{wf} \tag{8.3}$$

In Eq. 8.3, S represents the wing area and is determined in an iterative approach. The value for the wetted area of the fuselage is found using Computer Aided Design (CAD). The form factor, FF, is averaged from four different methods as proposed by Gur et. al. [30]. The wing interference factor, R_{wf}, can be read from Fig. 8.10, shown below [31], by knowing the Reynolds number and Mach number.
The skin friction coefficient of the fuselage, $C_{f_{Fuselage}}$, is determined using Eq. 8.4.

$$C_{f_{Fuselage}} = C_{f_{turb_L}} - \frac{x_{cr}}{L} \cdot C_{f_{turb_{x_{cr}}}} + \frac{x_{cr}}{L} \cdot C_{f_{lam_{x_{cr}}}} \cdot 1.16 \tag{8.4}$$

In Eq. 8.4, $C_{f_{turb_L}}$, $C_{f_{turb_{x_{cr}}}}$ and $C_{f_{lam_{x_{cr}}}}$ are the turbulent skin friction coefficient for the complete fuselage length, the turbulent and laminar skin friction coefficients until the transition point, respectively. The correction factor 1.16 is sugested by Corke [25] in order to correct the flat plate skin friction coefficient for the nose. The turbulent skin friction coefficient, $C_{f_{turbulent}}$ can be determined with Eq. 8.5, as provided below.

$$C_{f_{turbulent}} = \frac{0.455}{(log_{10}Re_x)^{2.58} \cdot (1 + 0.144 \cdot M^2)^{0.65}} \tag{8.5}$$

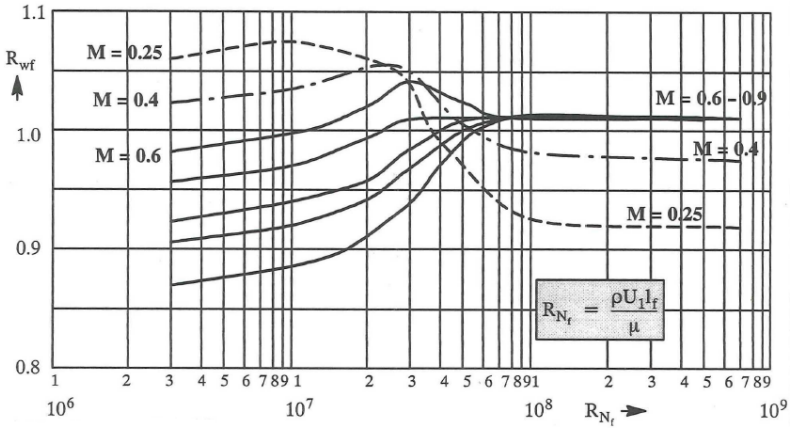

Figure 8.10: Interference Factor of the Wing as a Function of Reynolds Number [31]

The skin friction coefficient is calculated at the Reynolds number for the complete fuselage length and for the transition from laminar to turbulent. The calculation of both Reynolds numbers are presented in Eqs. 8.6 & 8.7, respectively.

$$Re_L = \frac{\rho \cdot V \cdot L}{\mu} \tag{8.6}$$

$$Re_{x_{cr}} = \frac{\rho \cdot V \cdot x_{cr}}{\mu} \tag{8.7}$$

The laminar skin friction coefficient until the transition point is calculated with Eq. 8.8.

$$C_{f_{laminar}} = \frac{1.382}{\sqrt{Re_{x_{cr}}}} \tag{8.8}$$

Using Eq. 8.3 to Eq. 8.8, the fuselage drag coefficient of the EuroFlyer is estimated to have a value of 0.0106.

8.4 Structural Design

In this section, the fuselage structure is designed. The main purpose of the fuselage structure is to transfer and withstand loads which occur during different phases of the flight profile. First, the shear force and the bending moment as a function of fuselage length are determined, followed by the sizing of the internal structure of the fuselage. Then, the material is selected and finally the mass of the fuselage is estimated.

8.4.1 Shear and Bending Moment Analysis on the Fuselage

In order to determine the required skin thickness of the fuselage, the maximum bending moment and the internal pressure need to be calculated. The maximum moment can be determined by modelling the fuselage as a beam with concentrated and distributed loads acting on it [25]. The beam is assumed to be simply support at the aerodynamic centre where the resultant lift force acts. In Fig. 8.11, the idealised fuselage structure and the loads acting on it are shown.

From Fig. 8.11, the shear force and bending moment as a function of fuselage length can be determined. Since at the start of the nose and at the end of the aft part of the fuselage, the shear force and moment must be zero, the most convenient start to analyse the structure is either at the nose or at the aft part of the fuselage. By making multiple cuts, the shear force and bending moment diagrams can be determined which are shown in Fig. 8.12a and Fig. 8.12b, respectively.
From Fig. 8.12b, the maximum moment acting on the fuselage structure can be deduced. From this value, the skin thickness can be sized by using Eq. 8.9 and by realising that the maximum tensile stress is located at the top of the fuselage.

$$\sigma_{tensile} = \frac{M_{max} \cdot d}{2 \cdot I} \tag{8.9}$$

Using the thin walled approximation for the moment of inertia in Eq. 8.10 and including the load factor of 2.5 which is further discussed in Chapter 15, the thickness of the skin can be determined with Eq. 8.11 [25].

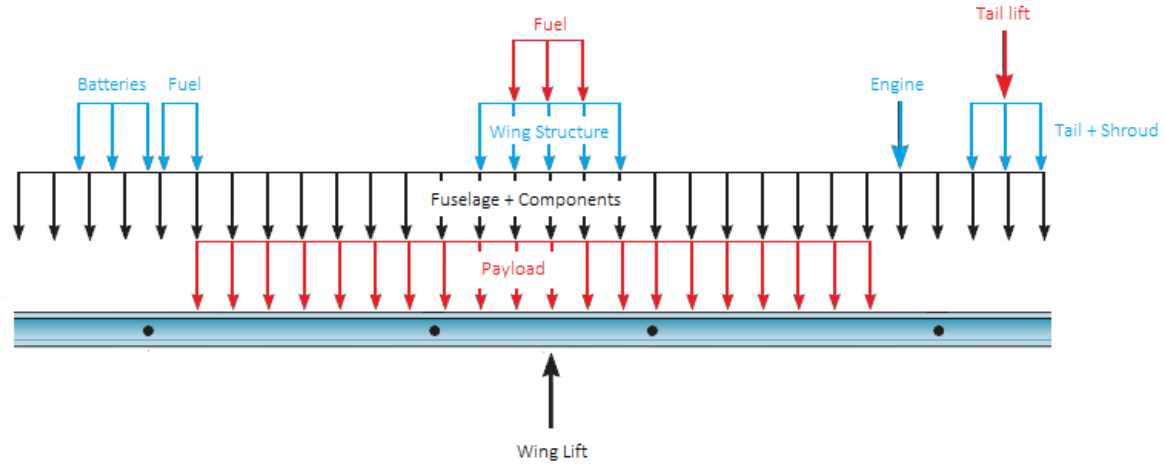

Figure 8.11: Distributed Load Acting on the Idealised Fuselage Structure

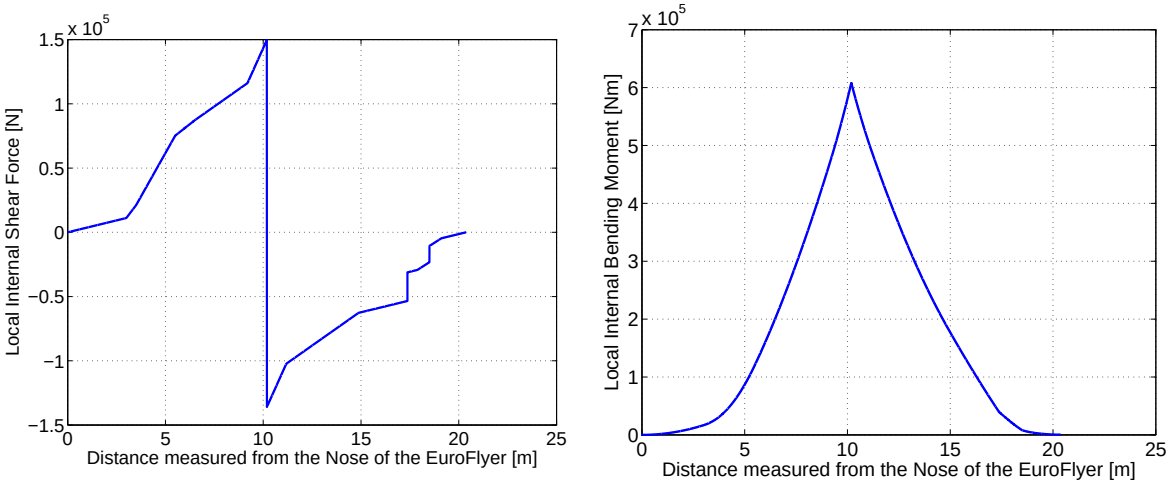

(a) Shear Force Diagram

(b) Bending Moment Diagram

Figure 8.12: Fuselage Loading Diagrams

$$I = \frac{8\pi \cdot d^3 \cdot t_{min}}{2} \tag{8.10}$$

$$t_{min} = \frac{8 \cdot M_{max} \cdot n}{\pi \cdot \sigma_{tensile} \cdot d^2} \tag{8.11}$$

However, the minimum thickness is also influenced by the internal pressure. The cabin pressure is dictated by the CS-25 regulations which state that the internal pressure in the cabin should be at least equivalent to the outside pressure of 8000 ft [32]. As the cruise altitude is at 29527.6 ft, the cabin has to be pressurised, introducing another load on the skin of the fuselage. Since the circumferential stress due to pressure is two times larger than the longitudinal stress, both cases have to be checked for obtaining the minimum thickness of the fuselage skin.

Summarizing, the skin thickness is obtained by Eqs. 8.12 and 8.13, respectively, which are provided below and the thickest skin is used for the fuselage.

$$t_{min_{longitudinal}} = \frac{8 \cdot M_{max} \cdot n}{\pi \cdot \sigma_{tensile} \cdot d^2} + \frac{p \cdot d}{4 \cdot \sigma} \tag{8.12}$$

$$t_{min_{circumferential}} = \frac{p \cdot d}{2 \cdot \sigma} \tag{8.13}$$

8.4.2 Sizing of the Internal Structure

The next step in the sizing of the internal structure consists out of determining the amount of longitudinal and circumferential stiffeners which take the compressive and tensile load respectively.

As the structural design of the fuselage is kept to a basic level only, the determination of the required amount of stiffeners is based on reference data. For this, the book 'Airframe Structural Design' [33] is consulted which lists the longitudinal stringer spacing as a function of fuselage radius. Using a linear regression analysis and knowing the diameter of the fuselage, a spacing of 0.19 m is found. Dividing the perimeter of the fuselage by the pitch, the total amount of stringers is calculated to be 78. Making the approximation that a common ratio between the pitch of the longitudinal and circumferential stringers is 2, the circumferential stringer pitch of 0.38 m is found. As the fuselage length is determined to be 20.37 m, the total number of circumferential stringers is found as 53 .

Since the number of stringers is known, the required moment of inertia of the stringers can be determined in order to resist the compressive loading in the structure. The main criterion for compressive loading is dictated by the column buckling of the longitudinal placed stringers. Using the Euler formula for buckling, with a value of 1 for C, explained by the fact that the circumferential stringers are assumed to be free to twist and bend [25], and rewriting it for the critical stress, Eq. 8.14 can be found [25].

$$\sigma_E = \frac{C \cdot \pi^2 \cdot E}{(L/\rho)^2} \tag{8.14}$$

The actual stress taken by the longitudinal stringers should be lower than the allowable buckling stress divided by the loading factor, as Eq. 8.15 shows [25].

$$\sigma < \frac{\sigma_E}{n} \tag{8.15}$$

Ultimately, the formulas given above can be combined into the following relation, Eq. 8.16 [25].

$$\sigma_{max} \cdot \frac{L^2}{I} < \frac{C \cdot \pi^2 \cdot E}{n \cdot A} \tag{8.16}$$

The maximum compressive stress due to the bending moment occurs at the bottom part of the fuselage. This value is used for the determination of the moment of inertia of the longitudinal stringers. As 78 longitudinal stringers are used, the moment of inertia can be determined by consulting Corke who suggests using symmetry for the calculation. The formula for the moment of inertia is provided in Eq. 8.17.

$$I = A_l \cdot \sum y^2 \tag{8.17}$$

When assuming the centre line of the fuselage as the centroid and using only the right half plane for the moment of inertia calculation the following equation can be found.

$$I = 2 \cdot A_l \cdot r^2 \cdot \left[\sum_{i=1}^{N_{stringers}} cos^2(i \cdot \pi/(2 \cdot N_{stringers})) \right] \tag{8.18}$$

Combining the previous results gives a relation for the required moment of inertia, as Eq. 8.19 shows.

$$I_l > \frac{L^2 \cdot n \cdot 0.026316 \cdot M_{max}}{r \cdot C \cdot \pi \cdot E} \tag{8.19}$$

The most common shapes for stringers are circular, rectangular tubes or hat shaped stringers [25]. The circular tubes are difficult to manufacture and therefore these are not used for the internal structure of the fuselage. The rectangular stringers are too heavy in relation to their moment of inertia contribution and thus they are discarded as well. As the hat shaped stringers provide more attachment points in comparison to the 'S' stringer shape and they are reasonably easy to manufacture, these stringers are used for the EuroFlyer structure.

8.4.3 Material Selection

From the previous analysis it was found that the driving design factors for the material selection are the ultimate tensile strength and the Young's Modulus. As the design should be as light as possible, the material will be selected according to its specific ultimate strength and specific stiffness. In addition, it is important to realize that the cost of the aircraft should be in within reasonable range and therefore, the price is also included in the material selection.

The specific relations of the weight of the material with respect to the ultimate strength and Young's Modulus are derived as follows. The tensile stress is defined by Eq. 8.20.

$$\sigma_{tensile} = \frac{F}{A} \tag{8.20}$$

Knowing that the volume is equal to length times width times thickness and using the density of the material gives the following relation for the weight for tensile loading, as provided in Eq. 8.21 [25].

$$W_t = \frac{F \cdot L \cdot \rho}{\sigma_{tensile}} \tag{8.21}$$

If the applied load is the same, a comparison between different materials can be made based on the following relation, Eq. 8.22 [25].

$$\frac{W_{tensile_1}}{W_{tensile_2}} = \frac{\rho_1 \cdot \sigma_{ultimate_{tensile_1}}}{\rho_2 \cdot \sigma_{ultimate_{tensile_2}}} \tag{8.22}$$

Using the same argumentation, a relation for compressive loading can be made which is given by Eq. 8.23 [25].

$$\frac{W_{compressive_1}}{W_{compressive_2}} = \frac{\rho_1 \cdot E_2^{1/3}}{\rho_2 \cdot E_1^{1/3}} \tag{8.23}$$

Knowing these relations, two graphs using CES EduPack 2013 Version 12.2.13, shown in Figs. 8.13 & 8.14 can be made which show commonly used materials in the aerospace industry. Metals and alloys are shown in a red shading and the composites material group is shaded in grey. The scale on the abscissa and ordinate are logarithmic and the slope of 1 in Fig. 8.13 and of 1/3 in Fig. 8.14 are shown by multiple dotted lines. The upper limit for the material price is set to 100 €/kg, eliminating certain materials leaving them grey in the graph. In addition, the materials below the bold line show marginal performance with respect to the loading requirements which is indicated by grey filled circles. A final restriction in the material selection is that for composites only isotropic layups are considered.

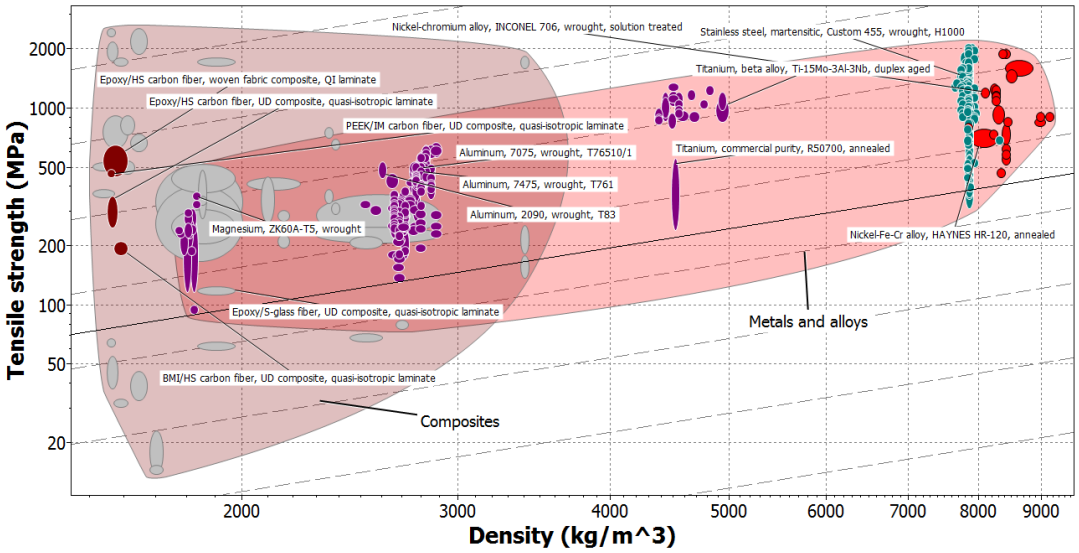

Figure 8.13: Tensile Strength as a Function of Density

In Fig. 8.13, the tensile strength is plotted against the density. The closer the material is to the top left side of the graph, the better the performance with respect to lightweight design. Also, material on the same dotted line show the same performance with respect to tensile loading and minimizing weight. As can be seen in Fig. 8.13, woven fabric carbon fibre with an epoxy resin and a quasi-isotropic layup is the best material for the tensile loading.

In Fig. 8.14, the Young's Modulus is shown as function of the density of the material. Again, the more the material is located in the top left corner of the graph, the better the performance. It can be seen that PEEK carbon fibre and epoxy carbon fibre show good performance with respect to compressive loading. However, from this graph it also becomes apparent that aluminium and titanium are better in terms of compressive loading.

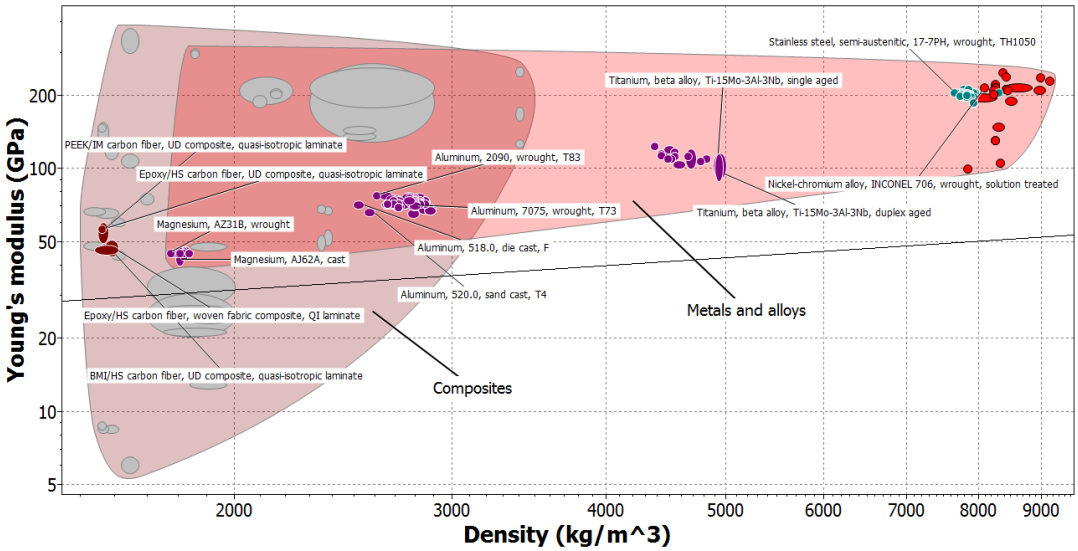

Figure 8.14: Young's Modulus as a Function of Density

Realising that composites have superior fatigue properties with respect to metals and consulting Fig. 8.13 and Fig. 8.14, it can be seen that Carbon Fibre Reinforced Plastics (CFRP) using an epoxy resin is the material of choice for the EuroFlyer fuselage skin. As the material properties for a quasi-isotropic layup of the fibres (0°, 90°, +45°, -45°) can be obtained with CES EduPack, the minimum required skin thickness can be calculated using Eqs. 8.12 and 8.13. The resulting thickness includes a loading factor of 2.5 and a safety factor of 1.5. The required moment of inertia for the stringers can now be calculated using Eq. 8.19, as the Young's Modulus is known.

8.4.4 Fuselage Mass

In this section, a first estimation of the fuselage structural mass is provided. The method used to estimate this weight as described by Raymer [34]. The equation used is described below.

$$W_{fuselage} = 0.3280 \cdot S_f^{0.302} \cdot (N_z \cdot W_{dg})^{0.5} \cdot K_{door} \cdot K_{Lg} \cdot (L/D)^{0.1} \cdot L^{0.25} \cdot (1 + K_{ws})^{0.04} \tag{8.24}$$

Please note that the equation to compute K_{ws} is shown in Eq. 8.25. This parameter depends on the taper ratio, wingspan, sweep angle and fuselage structural length.

$$K_{ws} = \frac{0.75(1 + 2\lambda)}{(1 + \lambda)} \frac{B_w \tan \Lambda}{L} \tag{8.25}$$

Substituting Eq. 8.25 into Eq. 8.24 leads to Raymer's equation to estimate the fuselage mass. When using the values found during the iterative process, a fuselage mass of 2937 kg is found. However, since the fineness ratio of the EuroFlyer differs significantly from today's commercial aircraft, this value should only be used as a first approximation, not as a final value. Also keep in mind that this estimation does not take into account any material choice.

8.5 Landing Gear Sizing

The focus of this section lies on the landing gear design. The landing gear system, configuration, loading, tires, and mass will be sized in this section. The methodology is described and final values are given for each parameter. As input parameters, the final iteration values were used.

8.5.1 Type

First, the landing gear system has to be chosen. Retractable systems are generally used for aircraft that fly faster than 77.2 m/s (150 kts) [27]. As the cruise speed of the EuroFlyer is above this speed, a retractable landing gear is used. Next, the landing gear type is determined. After consulting literature, the conventional tricycle landing gear configuration evidently turns out to be the most suitable for the EuroFlyer [27]. The Nose Landing Gear (NLG) consists out of two tires to reduce the chance of a fatal tire blow out. The number of tires for the main gear is based on the loading per tire and is discussed in Section 8.5.6.

8.5.2 Location

The most common location for the main landing is close to the centre wing box. The wing and centre of gravity positions follow from a Class II weight estimation and stability and control analysis of the aircraft. When these locations are known, and the assumptions is made that the Main Landing Gear (MLG) is located 20 cm behind the wing, the aircraft can be analysed for longitudinal stability. Fig. 8.15 displays the two criteria related to landing gear height. First the longitudinal tip over criterion, displayed by angle A, and secondly the clearance criterion, displayed by angle B [24]. Each of these criteria provides a required landing gear height. A maximum height comes forth from the tip over criterion, while the clearance criterion provides a minimum height. The methods to obtain these heights are explained below, starting with the tip over criterion.

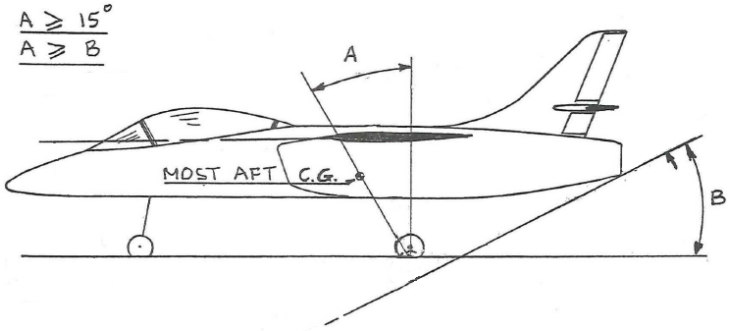

Figure 8.15: Longitudinal Landing Gear Layout Requirements for Tricycle Configuration [31]

When the wing location and thus the MLG location is known, the aircraft can be checked for compliance with its tip over requirements. By using trigonometric relations and an angle A of 15 deg, the maximum landing gear height is obtained. Please note that this criterion has to be fulfilled for both the most forward and aft centre of gravity location. Where in this case, the most aft centre of gravity is the crucial of the two. If the MLG location does not comply with this criterion, it has to be moved aft or the centre of gravity forward.

For the take-off clearance criterion, an angle B of minimum twelve degree has to be satisfied. Since the EuroFlyer has a shroud at the aft of the fuselage, it can lead to clearance complications and therefore the landing gear height has been sized for an angle B of 14 deg. If the outer diameter of the shroud and the horizontal length between the MLG and the aft of the shroud are known, the height of the landing gear can once again be computed by using trigonometric relations.

Now that both criteria related to landing gear height have been evaluated, a maximum and minimum landing gear height known for the centre of gravity, wing and shroud locations. Within these boundaries, the landing gear height can be sized. For the values found during the final iteration a landing gear height of 1.74 m is found. This value complies with both criteria regarding longitudinal stability.

The next step in the process to in determine the distance between the MLG and the NLG. Fig. 8.16 shows the relation between the wheelbase and the fuselage length. This wheelbase length is the distance between the NLG and MLG. The wheelbase is determined with help of Fig. 8.16, and a reasonable estimation for the nose gear location is found. Using a total wheelbase value of ten metres, the distance between the NLG and the centre of gravity is obtained. This value has been chosen in accordance with the nose wheel loading which is described in Section 8.5.4.

Another criterion which has to be satisfied is the lateral tip over criterion. As can be seen in Fig. 8.17, the angle Ψ has to be equal to or more than 25 deg. This ensures that the aircraft will not perform any fatal rolling movements during its ground operations.

By consulting reference aircraft, a first estimate for this length is obtained. Fig. 8.18 displays the trackwidth length in relation to the MTOW (Maximum Take-Off Weight) [31].

From Fig. 8.18, a track width of approximately six metres can be found for a MTOW of 27840 kg. When computing the track width according to the criterion displayed in Fig. 8.17, an angle Ψ of 29.2 deg is found for an track width of 5 metres. Please note that for this computation, the centre of gravity is assumed to be in the centre of the fuselage cross-section. Comparing this value to the value found from reference aircraft, it can be concluded that this value is within close proximity of operational aircraft track lengths.

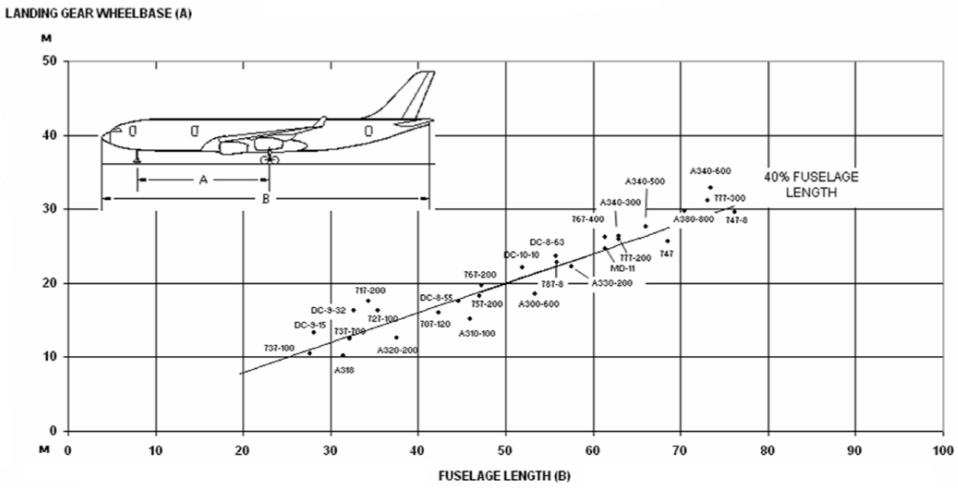

Figure 8.16: Reference Aircraft Wheelbase Length with respect to Fuselage Length [31]

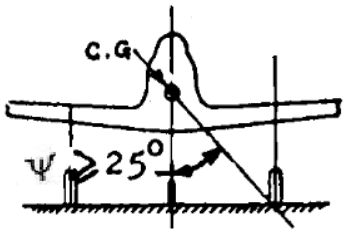

Figure 8.17: Lateral Tip Over criterion for Tricycle Configuration [35]

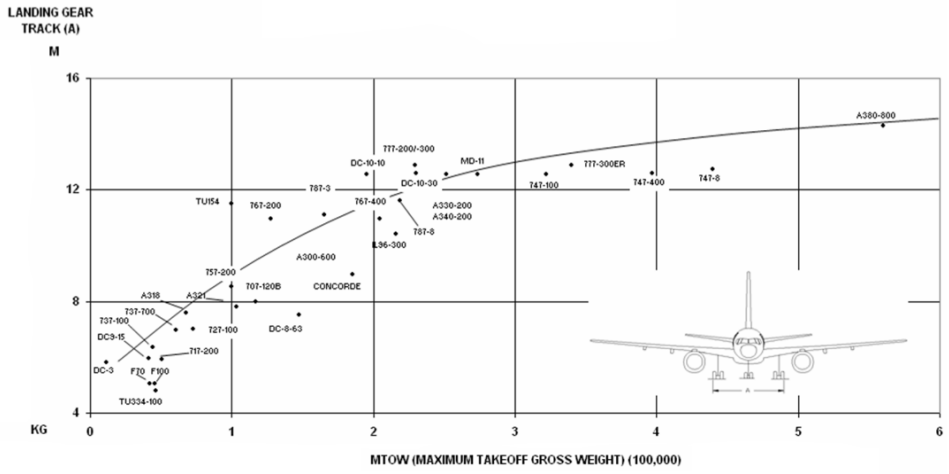

Figure 8.18: Reference Aircraft Trackwidth with Respect to Maximum Take-Off Weight [31]

8.5.3 Integration

Due to the lateral stability criterion, the undercarriage will have to be placed on either the wings or inside the fuselage. Since locating the MLG in the wing leads to complications with the wing box, the undercarriage is located behind the wing inside of the fuselage. The landing gear deploys outwards in order to satisfy the lateral stability criterion. Such a deployment, instead of deploying it forward or backward increases the undercarriage stiffness. For this configuration to work, the MLG requires a pivot point. Due to this, it can be stored inside the fuselage since the effective strut length is decreased. A graphical representation of this system can be seen in Fig. 8.19. This displays the deployed MLG of the British Aerospace 146 aircraft, also known as the BAe 146 [36].

The undercarriage location comes with certain advantages. Firstly, since the landing gear is not connected to the wing, the air flow over the wing is undisturbed. Secondly, the further aft the MLG, the more stable the aircraft is regarding tip over requirement.

Figure 8.19: British Aerospace 146 Deployed Fuselage Mounted Main Landing Gear [37]

8.5.4 Static Loading Analysis

For tricycle configurations, the main and nose gear static loading can be computed by using Eqs. 8.26 and 8.27. In these equations, n_s represents the number of main gear struts. In this case, the first iteration assumes a value of two for this parameter.

$$P_{n_{static}} = \frac{W_{TO} \cdot l_m}{l_m + l_n} \tag{8.26}$$

$$P_{m_{static}} = \frac{W_{TO} \cdot l_m}{n_s(l_m + l_n)} \tag{8.27}$$

For good steering qualities, eight to fifteen percent of the MTOW should be statically loaded on the nose gear [27]. However for the current parameters and landing gear location 37% of the MTOW is loaded on the NLG. This is due to the fact that the MLG can not be located in the wing, and thus has to be placed further back. Due to the relatively short fuselage, placing the NLG further forward in order to decrease the static loading is only possible to a certain extend.

8.5.5 Dynamic Loading Analysis

The dynamic loading experienced by the landing gear can be expressed by Eqs. 8.28 and 8.29 [27]. In order for the tires to be FAR-25 certified and to account for growth in airplane weight, the dynamic load per tire is multiplied by 1.07 and 1.25, respectively.

$$P_{n_{dynamic}} = \frac{W_{TO}(l_m + \frac{a_x}{g \cdot hcg})}{(l_m + l_n)} \tag{8.28}$$

$$P_{m_{dynamic}} = \frac{W_{TO}(l_n + \frac{a_x}{g \cdot hcg})}{(l_m + l_n)} \tag{8.29}$$

Extra parameters used in these equations are specified as follows.

- $a_x/g = 0.35$ for dry concrete with simple brakes
- $a_x/g = 0.45$ for dry concrete with anti-skid brakes

Since the dynamic loading is higher than the static loading the tires will be sized in accordance to the dynamic loading. This dynamic loading for the NLG and MLG are 11510 lb and 15176 lb respectively. However, in order to select the appropriate tires, the maximum tire operating speed has to be determined first. This can be determined by using Eqs. 8.30 and 8.31. Here the assumption is made that the take-off and landing speed are equal to 1.05 times their specific stall speed.

$$V_{tire_{max}} = 1.1 \cdot 1.05 \cdot V_{stall_{take-off}} \tag{8.30}$$

$$V_{tire_{max}} = 1.1 \cdot 1.05 \cdot V_{stall_{landing}} \tag{8.31}$$

Since the lift coefficient for take-off and landing are 2.1 and 2.5 respectively, the stall speed will be higher for take-off. At sea level, the stall speed for take-off will be 57 m/s. Substituting this value in Eq. 8.30 will lead to a $V_{tire_{max}}$ value of approximately 66 m/s (147.7 mph). Now that both the maximum dynamic load per tire and operating speed are known, the tires can be selected in accordance the tire data as provided in Roskam [31].

8.5.6 Tire Selection

For the MTOW, landing gear location and centre of gravity location which came from the iteration, the tires can be chosen. The nose gear will make use of two tires where each one is subjected to a 11510 lbs load. The main landing gear consists out of four tires which are each subjected to a 15176 lbs load. Consulting literature, the following tire selection was performed, as shown in Tab. 8.5.

Table 8.5: Tire Parameters

Parameter	*Nose Gear Tire*	*Main Gear Tire*	*Unit*
Rated Load	12500	16200	lb
Operating Speed	230	217	mph
Size	24x8.0-13	25.5x8-14	$inch$
Ply Rating	18	20	–
Weight	28.3	39.5	lb

8.6 Results

For convenience all major parameters from this Chapter are summarised in Table 8.6. These were obtained after several iterations were performed. Please note that not all parameters used are stated here. For more information and the methodology behind the values, please refer to the beginning of Chapter 8.

Table 8.6: Fuselage Parameters

Parameter	*Value*	*Unit*
External Geometry		
Fuselage Diameter	4.699	m
Fuselage Length	20.374	m
Fineness Ratio	0.2306	–
Internal Geometry		
Seating Configuration	2x3x2	–
Maximum Number of Seats	84	–
Number of Exits	6	–
Number of Windows	30	–
Available Storage Volume	54	m^3
Aerodynamic/Structural Specification		
Fuselage Drag Coefficient	0.0106	–
Minimum Fuselage Skin Thickness	0.93	mm
Minimum Required Moment of Inertia for the Stringers	$4.87 \cdot 10^7$	mm^4
Fuselage Structural Mass	2937	kg
Landing Gear		
Landing Gear Height	1.74	m
Landing Gear Track Width	5.0	m
Landing Gear Wheelbase	10	m
Main Landing Gear Location (from nose)	12.0	m
Nose Landing Gear Location (from nose)	2.0	m
Number of Nose Tires	2	–
Number of Main Tires	4	–
Nose Landing Gear Mass	277	kg
Main Landing Gear Mass	1028	kg
Tire Selection		
Nose Tire Diameter	0.61	m
Main tire Diameter	0.65	m
Nose Tire Width	0.20	m
Main Tire Width	0.20	m
Nose Tire Maximum Operating Speed	102.82	m/s
Main Tire Maximum Operating Speed	97.01	m/s
Nose Tire Maximum Static Loading	8269	lb
Main Tire Maximum Static Loading	11178	lb
Nose Tire Maximum Dynamic Loading	11510	lb
Main Tire Maximum Dynamic Loading	15176	lb

CHAPTER 9

Wing

This chapter presents the detailed wing design of the EuroFlyer. The road map of this chapter can be found in Fig. 9.1. Firstly, an appropriate aerofoil is selected according to the maximum wing loading and the Maximum Take-Off Weight, determined in Chapter 13 [16]. Next step is to determine the optimal parameters to design an optimal wing planform according to the requirements and mission needs. Afterwards the aerodynamic characteristics of the wing are calculated. Then, wing is structurally analysed to ensure the feasibility of the proposed design. Finally the results are summarised in the last section.

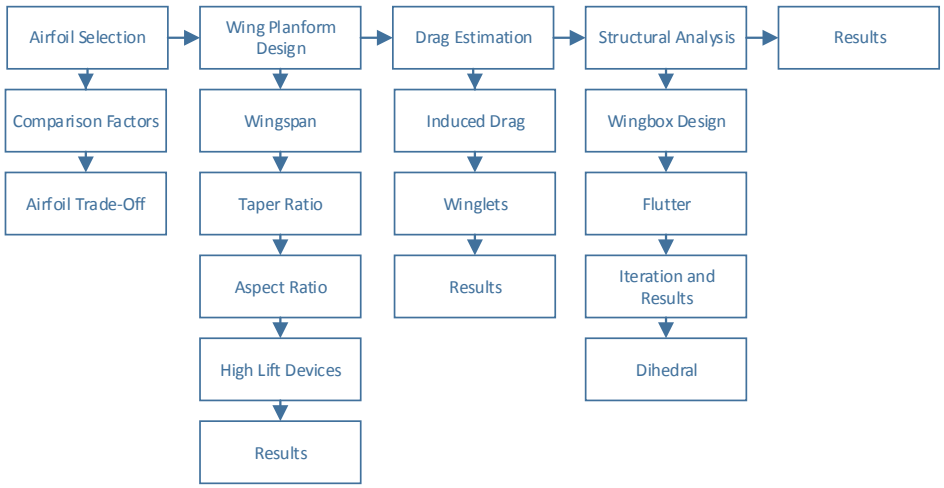

Figure 9.1: Wing Road Map

9.1 Aerofoil Selection

From the design point and the estimated Maximum Take-Off Weight, some preliminary aerodynamic characteristics were derived. The design lift coefficient is calculated to be 0.49 for a MTOW of 27840 kg and a maximum wing loading of 4190 N/m^2. These characteristics need to be achieved at Mach 0.65 at 9000 m, an altitude which results in an airspeed of 197.6 m/s. The maximum lift coefficient in clean configuration should be at least 1.3 in order to prevent the need for heavy high lift devices. The clean wing without any flaps or slats has a $C_{L_{max}}$ value of 1.73 determined using the computational tool XFLR5 [38]. With this information, an appropriate aerofoil can be selected.

9.1.1 Comparison Factors

The aerofoil selection is performed using data obtained from Abbott and Von Doenhoff (A & vD) and the computational tools XFLR5 and JavaFoil [38, 39]. However, due to different methods used and assumptions made in the computational tools, the actual aerodynamic characteristics of the aerofoils often differ from the experimental data. In order to give an accurate estimate of the aerofoil characteristics, the computational data is compared to the experimental. Comparison factors are defined to scale the computational towards the experimental data.

The aerofoils NACA 63_2-415, NACA 63_2-615, NACA 65_2-415 and NLF-0416 are considered after a first analysis. The characteristics of these aerofoils are simulated in XFLR5 and compared to experimental data, obtained from Abott and Von Doenhoff [39]. Comparison factors are defined for the C_D, $C_{L_{max}}$ and α_{max} values of all the aerofoils at Reynolds numbers of 3, 6 and 9 million. These values are extrapolated to a Reynolds number of 12 million, the estimated Reynolds number in cruise, to reduce the induced error in the computational values. All the mentioned values and factors can be found in Table 9.1.

Table 9.1: Aerodynamic Values and Comparison Values

		$Re = 3 \cdot 10^6$			$Re = 6 \cdot 10^6$			$Re = 9 \cdot 10^6$			$Re = 12 \cdot 10^6$		
Aerofoil	*Parameter*	*XFLR5*	*A & vD*	*Factor*	*XFLR5*	*A & vD*	*Factor*	*XFLR5*	*A & vD*	*Factor*	*XFLR5*	*Value with Factor*	*Factor*
NACA 63_2-615	C_D	0.0049	0.0053	1.08	0.0053	0.0052	0.98	0.0053	0.0048	0.90	0.0069	0.0055	0.80
	$C_{L_{max}}$	1.51	1.46	0.97	1.63	1.56	0.96	1.69	1.67	0.99	1.79	1.78	0.99
	α_{max}	20	13.5	0.68	19	14.25	0.75	20	15	0.75	20.8	17.2	0.83
NACA 63_2-415	C_D	0.0050	0.0055	1.11	0.0043	0.0052	1.21	0.0043	0.0049	1.14	0.0039	0.0047	1.22
	$C_{L_{max}}$	1.7	1.55	0.91	1.82	1.64	0.90	1.89	1.66	0.88	2.00	1.73	0.86
	α_{max}	19.0	13.9	0.73	20.0	15.2	0.76	20.0	16.0	0.80	21.0	18.0	0.86
NACA 65_2-415	C_D	0.0047	0.0050	1.06	0.0038	0.0042	1.11	0.0037	0,0042	1.14	0.0044	0.0053	1.20
	$C_{L_{max}}$	1.71	1.45	0.85	1.76	1.58	0.90	1.82	1.62	0.89	1.95	1.82	0.93
	α_{max}	19	16.34	0.86	20	17.4	0.87	22	16.5	0.75	22	14.7	0.67
NLF-0416	C_D	0.0053	0.0060	1.14	0.0051	0.0058	1.14	0.0053	0.0057	1.08	0.0048	0.0051	1.06
	$C_{L_{max}}$	1.76	1.71	0.97	1.88	1.84	0.98	1.94	1.90	0.98	2.00	1.98	0.99
	α_{max}	16	13.8	0.86	17	15.5	0.91	17.5	15.6	0.89	16	14.9	0.93

9.1.2 Trade-Off

Now that the aerodynamic characteristics are known, a trade-off between the four selected aerofoils is performed. The trade-off will be based on the three parameters extrapolated in the previous section, being the drag coefficient C_D, the maximum lift coefficient $C_{L_{max}}$ and the maximum angle of attack α_{max}. As the most important parameter is the drag coefficient during cruise, this parameter has a weighting factor of 3, compared to 1 for both the maximum lift coefficient and the maximum angle of attack. The grading scale runs for -2 to 2. In this scale a score of -2 defines the lowest scores and 2 defines the highest possible score. The trade-off can be found in Table 9.2. The selected aerofoil is the NACA 63_2-415.

Table 9.2: Aerofoil Selection Trade-Off

Aerofoil / Criterion	C_D	$C_{L_{max}}$	α_{max}	*Total Score*
Weighting Factor	*3*	*1*	*1*	
NACA 63_2-615	0	0	0	*0*
NACA 63_2-415	2	-1	1	*6*
NACA 65_2-415	1	1	-2	*2*
NLF-0416	1	2	-2	*3*

9.2 Planform Design

In this section, the wing planform will be designed. The aerofoil is determined and from this two-dimensional aerofoil a three dimensional wing is created. The goal is to design a wing with the lowest drag as possible and to insure the wing weight stays within an acceptable range. The final wing surface was determined by means of an iterative process in Chapter 13 and equals 65.18 m^2 for a lift coefficient of 0.50 at a MTOW of 27840 kg.

9.2.1 Wingspan

An important parameter when designing the wing planform, is the maximum allowable wingspan. One of the key requirements of the project is that the aircraft should be able to operate at regional airports. The Airbus A320 is a good reference aircraft regarding this requirement. Its wingspan is 34.10 m [40], and according to the ICAO Airport Reference Codes, this is a Class 3 aircraft [41]. The maximum allowable wingspan for a Class 3 aircraft

is 36 m, this value is set as the maximum allowable wingspan for the EuroFlyer.

9.2.2 Taper Ratio

The optimum taper ratio was determined using the computational tool XFLR5. The drag estimation of XFLR5 is not accurate enough to use the drag coefficients, but the trend due to changes is reliable. Different taper ratios were analysed with the above mentioned parameters. Leading edge sweep was set to zero degrees in order to increase laminarity over the wings. The different taper ratios are plotted in Fig. 9.2 against the lift over drag ratio, L/D, of the wing. The wing surface and the lift coefficient are constants for this plot. It can clearly be seen that the optimal taper ratio is in between 0.3 and 0.4. The maximum value is obtained at a taper ratio of 0.30, shown by the dotted line.

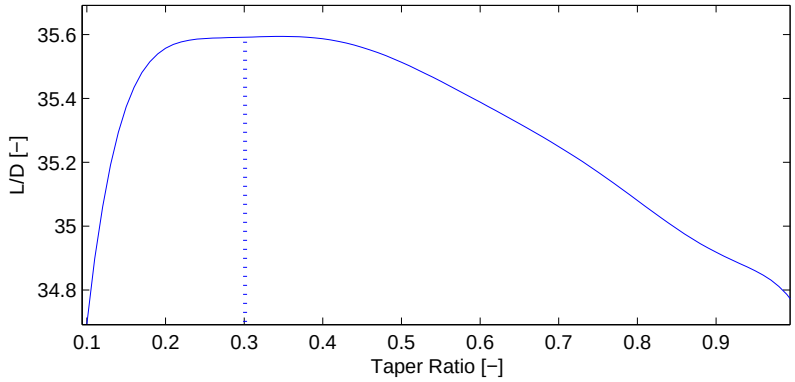

Figure 9.2: Optimal Taper Ratio for Constant S and C_L

9.2.3 Mach Critical and Sweep

With the followings two equations the critical Mach number can be determined.

$$C_p = \frac{C_{p,0}}{\sqrt{1 - M_\infty^2}} \tag{9.1}$$

$$C_{p_{cr}} = \frac{2}{\gamma M_{cr}^2}\left[\left(\frac{1 + \left[\frac{(\gamma-1)}{2}\right] M_{cr}^2}{1 + \left[\frac{(\gamma-1)}{2}\right]}\right)^{\frac{\gamma}{\gamma-1}} - 1\right] \tag{9.2}$$

In Eq. 9.2 γ stands for the heat capacity ratio, which is 1.4 for air. Plotting these equations as function of the Mach number, one can find the intersection of the two curves. The intersection point is the critical Mach number. In Fig. 9.3 the two curves are plotted and the critical Mach number in case of zero sweep equals 0.6522, which is above the cruise Mach number, therefore no sweep is required. This is also beneficial for the amount of laminar flow on the wing, which will heavily influence the drag characteristics of the wing, as will be discussed in Section 9.3.

9.2.4 Aspect Ratio

Finally the aspect ratio (AR) needs to be determined. In Fig. 9.4 the total wing drag coefficient is plotted against aspect ratio for the cruise conditions of the EuroFlyer, neglecting the effect of the winglets. One can conclude that the higher the aspect ratio is, the lower the wing drag coefficient will be. This is the main reason for designing the wing with an aspect ratio as high as possible. Furthermore, for propeller aircraft, an increasing aspect ratio has positive consequences on the climb rate and climb gradient of propeller aircraft. A drawback is a heaver design and possible aero elastic effects [42]. The weight penalty and aero elastic effects are taken into account and will be discussed in Section 9.4. Given the wing surface, maximum wingspan and the taper ratio, the optimal aspect ratio is 19.88.

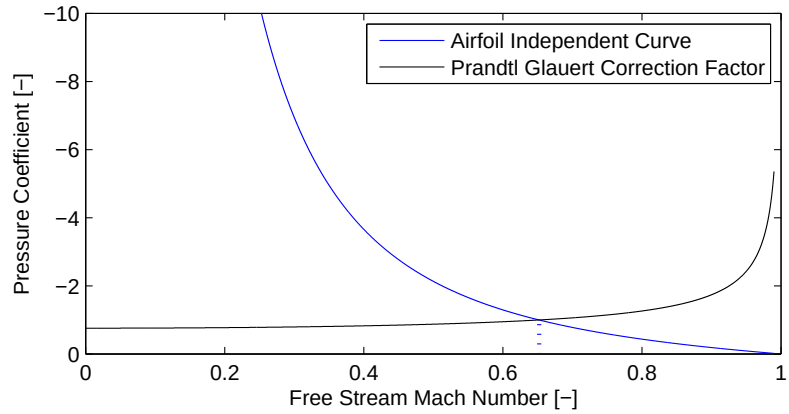

Figure 9.3: Critical Mach Number Determination

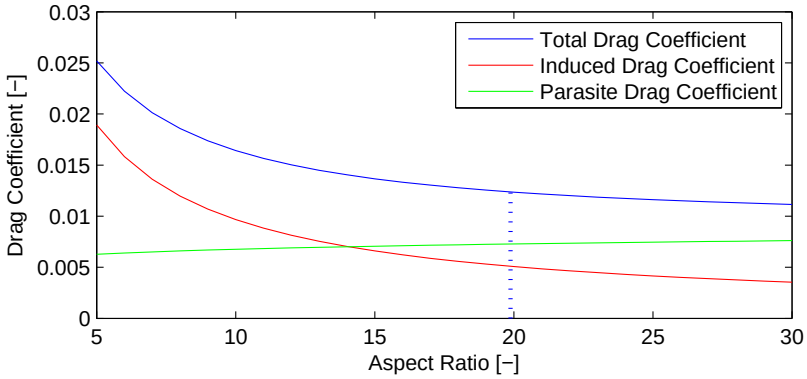

Figure 9.4: Influence of Aspect Ratio on the Wing Drag Coefficients

9.2.5 High Lift Devices

In order to fulfil the take-off and landing requirements [16] and to come up with a feasible high lift device design, the landing requirements were set to a landing distance of 1500 m and a maximum landing coefficient of 2.5. The aircraft needs to have a maximum take-off lift coefficient $C_{L_{T/O,max}}$ of 2.1. In Section 9.1.1 the induced error of this program was corrected with a comparison factor. Therefore, a correction factor of 0.85 is used to get the right $C_{L_{max}}$ value.

The maximum increase in lift coefficient $\Delta C_{L_{max}}$ of the wing can be calculated using Eq. 9.3 [43]. In this equation, $\Delta C_{l_{max}}$ is the increase in lift coefficient C_l of the aerofoil with extended flap compared to the aerofoil in normal configuration. The ratio of wetted area over the reference area is given by $\frac{S_{wf}}{S}$. The wetted area represents the area of the wing equipped with high lift devices. The parameter $\Lambda_{hingeline}$ represents the sweep of the hinge-line of the high lift device.

$$\Delta C_{L_{max}} = 0.9 \Delta C_{l_{max}} \frac{S_{wf}}{S} cos(\Lambda_{hingeline}) \tag{9.3}$$

A broad spectrum of high lift devices is used nowadays. The highest $C_{l_{max}}$ values, can be achieved by more complicated high lift devices. However, when high lift devices become more complicated, they become heavier as well. Therefore, the least complicated high lift device, delivering the required $\Delta C_{L_{max}}$, is the best to use: the Fowler flap. The Fowler flap has a $C_{l_{max}}$ of $1.3 \cdot \frac{c'}{c}$ [43]. In order to generate the maximum lift coefficient of 2.5, the high lift devices should cover 41% of each wing. The Fowler Flaps starts at approximately 13% spanwise of each wing, which means at 2.34 m from the fuselage, and ends at 57% of the span. The exact geometry of the wing and the high lift devices is visualised in Fig. G.2 in Appendix G.

9.2.6 Results

The final wing planform is fixed, knowing these above mentioned parameters. The geometry of the wing can be found Appendix G. All the parameters and their associated variables are summarised in Table 9.3. Note that wing tip technology will be discussed in Section 9.3 and that the dihedral angle will be determined based on the tip deflection on ground, obtained from the structural analysis in Section 9.4.

Table 9.3: Wing Planform Parameters

Parameter	*Value*	*Unit*	*Parameter*	*Value*	*Unit*
Wing Surface	65.18	m^2	Wingspan	36.00	m
Aspect Ratio	19.88	–	Sweep Angle LE	0	rad
Mean Aerodynamic Chord	1.98	m	Reynolds Number	$12 \cdot 10^6$	–
Geometric Chord	1.81	m	Taper Ratio	0.3012	–
Root Chord	2.7830	m	Tip Chord	0.8382	m
Max. Clean Lift Coefficient	1.7	–	Max. Landing Lift Coefficient	2.5	–
High Lift Device	*Single Fowler Flaps*				

9.3 Drag Estimation

The determination of the drag force of the wing is an essential part of the aircraft design process, as it directly affects the overall aircraft performance. The main equation for estimating the drag of the wing is given in Eq. 9.4. The parasite drag coefficient C_{D_0} is caused by the resistance of moving a body through a medium such as air. The induced drag coefficient C_{D_i} is in turn given by the second term and is the drag associated by the lift generation of the wing.

$$C_D = C_{D_0} + C_{D_i} \tag{9.4}$$

9.3.1 Parasite Drag

The parasitic drag coefficient C_{D_0} is often defined as the sum of the skin friction coefficient C_F, the form drag coefficient C_{D_p} and the wave drag coefficient C_{D_w}, as shown in Eq. 9.5. The sum of the skin friction and the form drag coefficient is often defined as the profile drag coefficient C_{D_F}. The interference drag is not taken into account, as this value has already been accounted for in the fuselage drag estimation in Section 8.3.3.

$$C_{D_0} = C_{D_F} + C_{D_w} = C_F + C_{D_p} + C_{D_w} \tag{9.5}$$

First the profile drag will be determined. The skin friction originates from the presence of retarded flow in the proximity of the wing surface, also known as the boundary layer. Most of the boundary layer is turbulent. However, for the NACA 63_2-415 aerofoil in subsonic conditions, laminar flow is assumed up to ten percent of the chord length. For laminar flow the skin friction of a flat plate can be calculated with Eq. 9.6, while for turbulent flow Eq. 9.7 can be used [44]. In these equations, Re is the Reynolds number given by Eq. 9.8. In this last equation, ρ represents the air density, V is the airspeed and l is the characteristic length, as percentage of the chord. Finally μ is the dynamic viscosity of the fluid, a parameter obtained from the International Standard Atmosphere (ISA).

$$C_{f_{lam}} = \frac{1.328}{Re^{\frac{1}{2}}} \tag{9.6}$$

$$C_{f_{turb}} = \frac{0.074}{Re^{\frac{1}{5}}} \tag{9.7}$$

$$Re = \frac{\rho \cdot V \cdot l}{\mu} \tag{9.8}$$

The profile drag includes pressure drag and the skin friction as mentioned earlier. Pressure drag depends on the form of a body. It occurs in case adverse pressure gradients exist near the trailing edge on the wing, resulting in flow separation. The profile drag coefficient can be estimated with the use of form factors, FF. A form factor represents the drag correction due to thickness and pressure drag. A broad spectrum of form factors are available and described by Gur et al. [30]. These form factors have differences up to 20%. As these difference have an high influence on the drag characteristics, the average value of the form factors defined by Hoerner, Torenbeek, Edet, Nicolai, Kroo and Shevell is used to perform the calculations.

$$C_{D_F} = FF_{avg} \cdot C_{f_{skin}} \cdot \frac{S_{wf}}{S_{ref}} \tag{9.9}$$

Wave drag appears at airspeeds higher than the critical Mach number M_{cr}, due to the presence of shock waves. In Section 9.2.3 it was shown that the critical Mach number is higher than the cruise Mach number. As there is no supersonic velocities on the wing, the wave drag is zero and can be neglected.

9.3.2 Induced Drag

The induced drag is the drag produced by the wing when generating lift. In order to produce lift, the direction of the flow is redirected by the wing, causing drag. This drag can be calculated using the lifting line theory as in Eq.9.10. The design lift coefficient, C_L, is estimated to be 0.5. The aspect ratio, AR, is found to be 19.88. The Oswald Factor, e, is determined by using Eq. 9.11 [45].

$$C_{D_i} = \frac{{C_L}^2}{\pi \cdot AR \cdot e} \tag{9.10}$$

$$e = \frac{1}{\left(1 + 0.12M^6\right)\left[1 + \frac{0.142 + f(\lambda)\ AR\ \left(10\frac{t}{c}\right)^{0.33}}{cos(\Lambda_{.25})} + \frac{0.1(3N_e+1)}{(4+AR)^{0.8}}\right]} \tag{9.11}$$

$$\text{with } f(\lambda) = 0.005\left(1 + 1.5\,(\lambda - 0.6)^2\right) \tag{9.12}$$

In the above equation the Mach number M equals the cruise Mach number of 0.65. The value of the aspect ratio is determined earlier. The ratio t/c is the maximum thickness of the aerofoil and is equal to 0.15 for the NACA 63_2-415 aerofoil. The sweep angle at quarter chord length $\Lambda_{.25}$ is -0.027. The taper ratio λ is determined in Section 9.2.2 to be optimal with a value of 0.3012. Finally there are no engines on top of the wing surface, setting N_e to zero. This leads to an Oswald factor of 0.77. Now the induced drag coefficient C_{D_i} turns out to be 0.0051 using Eq. 9.10.

9.3.3 Winglets

The induced drag can be significantly reduced with the use of wing tip technology, such as a winglet. The most promising technology in the field of winglets is the spiroid wing tip see Fig.9.5. According to Guerrero et al. [46] the induced drag can be reduced by 28% at a lift coefficient of 0.40 and by 35% at a lift coefficient of 0.55 using spiroid winglets. However, this value was decreased to a more conservative value of ten percent in the calculations, as this technology is only in an early stage and more investigation is required to prove this high beneficial reduction in reality. Taking the reduction of ten percent into account in Eq. 9.10, the induced drag is equal to 0.0046.

Figure 9.5: Spiroid Wing Tip

9.3.4 Results

An overview of all the obtained wing drag coefficients are summarised in Table 9.4.

Table 9.4: Wing Drag Parameters

Parameter	*Symbol*	*Value*	*Unit*
Parasite Drag Coefficient	C_{D_0}	0.0073	-
Induced Drag Coefficient	C_{D_i}	0.0046	-
Total Drag Coefficient	C_D	0.0119	-

9.4 Structural Design

This section discusses a preliminary structural sizing of the wing, in particular the wing box. As mentioned before, the wing of the EuroFlyer features an aspect ratio of 19.88. Given the fact that current commercial aircraft have a considerably lower value for this parameter, one can easily understand that the structural design of such an high aspect ratio wing could potentially be an issue. The normal and shear stresses along the span will be

considerably higher compared to a wing with a lower aspect ratio. Furthermore, aerodynamic flutter has to be taken into account as this resonating oscillation could result in a catastrophic in-flight failure.

This section aims to demonstrate the feasibility of the proposed wing rather than providing a detailed design of the complete wing box. Firstly, a structural design is proposed once the internal shear forces and bending moments distributions along the wingspan have been determined. Next, flutter is addressed and the wing box design is adjusted to prevent these phenomena in flight.

9.4.1 Wing Box

In this section, the proposed wing design will structurally be analysed and a wing box structure which is able to cope with the different load cases will be presented. The wing is not only subjected to a shear force and bending moment distribution along the span, but as there is an offset between the centre of pressure and shear centre of the wing box and the wing is generating a constant pitch down moment around the aerodynamic centre, the cross-section is also subjected to a torsional moment. The cross-section considered for the structural design is shown in Fig. 9.6. All dimensions are proportional to the local chord length, in order to reduce the overall wing weight. Both the top and bottom skin are assumed to have identical thickness, resulting in a fixed location of the neutral line and thus simplifying the structural analysis to a great extent. As the front and rear spar feature a different thickness, the shear centre location is varying along the wingspan.

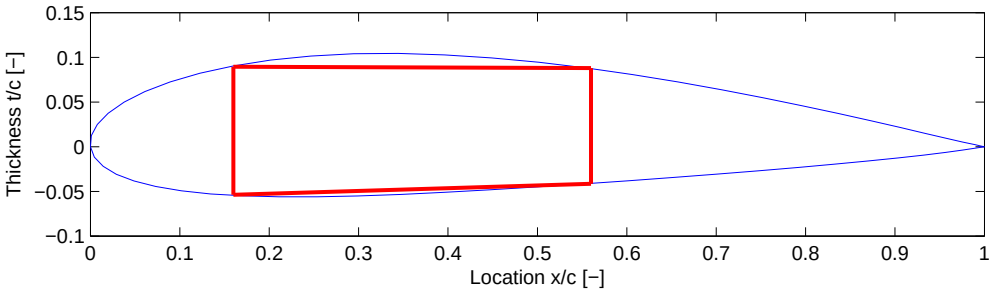

Figure 9.6: Wing Box Location in the Cross-Section

Before establishing the shear force and moment diagrams, it is important to note that some simplifying assumptions have been made in this preliminary sizing. Firstly, there will be assumed that no stringers are present and that whereas it is common to design the structure such that the skin will carry only the shear stresses and the stringers will take up the normal stresses due to bending. For a preliminary sizing however, where the main focus is to show the feasibility of the high aspect ratio wing within a reasonable mass budget, this assumption is valid. Secondly, there is opted for a structural idealisation by means of a finite number of booms, which greatly reduces the time budget required for the analysis. This implies that skin thickness is set zero and the boom areas are adjusted to account for the area of the skin. Furthermore, it is assumed that the beam is made of a specified composite material with isotropic properties, beam deflections under the applied loads are negligible, plain cross-sections remain plain and that no axial constraints exist at the ends.

Now that the cross-section has been defined and the assumptions have been stated, the distribution of the internal shear force, bending moment and torsional moment along the span can be determined. Assuming that lift distribution is directly proportional to the local chord length and the wing loading will be multiplied with an overall safety factor of 3.75, to account for the ultimate load factor of 2.5 and material degradation factor of 1.5, the shear force and bending moment diagrams can be established by means of force and moment equilibrium. These are shown in Figs. 9.7a and 9.7b. Due to symmetry, only half of the wingspan is shown.

From these distributions, the resulting normal and shear stress distribution can be derived. Eq. 9.13 and Eq. 9.14 shows how the bending moment and shear flow is related to the normal and shear stress respectively. The shear flow q_{xy} accounts both for the component originating from the shear force, q_S, and the one from the torsional moment, q_T. To take into account both the normal and shear stress at a given location, one can compute the Von Mises Stress, σ_{VMS}. By doing so, one gets an idea about the total stress state at that specific location and it allows to observe if yielding (in case of a metal) or failure (in case of a composite material) occurs. The Von Mises stress can be found by evaluating Eq. 9.15. In this case however, due to the absence of two normal stresses and shear stresses in the remaining directions, this equation can significantly be reduced.

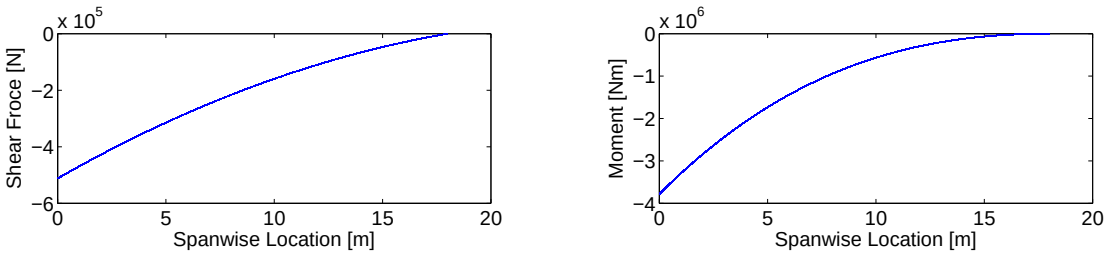

(a) Shear Force Diagram (b) Bending Moment Diagram

Figure 9.7: Internal Shear Force and Bending Moment Diagrams

$$\sigma_z = \frac{M_x \cdot y}{I_{xx}} \tag{9.13}$$

$$\tau_{xy} = \frac{q_{xy}}{t} = \frac{q_S + q_T}{t} \tag{9.14}$$

$$\sigma_{VMS} = \sqrt{\tfrac{1}{2}\left[(\sigma_x - \sigma_y)^2 + (\sigma_y - \sigma_z)^2 + (\sigma_z - \sigma_x)^2\right] + 3\left[\tau_{xy}^2 + \tau_{yz}^2 + \tau_{zx}^2\right]} = \sqrt{\sigma_z^2 + 3\tau_{xy}^2} \tag{9.15}$$

$$m = \rho \cdot A \cdot b \tag{9.16}$$

The wing box dimensions are varied in an iterative process until the maximum Von Mises stress equals 350 MPa, the assumed ultimate strength of the composite material. The resulting Von Mises stress distribution over the wing box is shown in Fig. 9.8. Table 9.5 contains the values of the Von Mises Stress as well as the corresponding dimensions of the skin, front and back spar for three distinct locations along the span. Once these values are known, Eq. 9.16 can be used to estimate the mass of the wing box. Here A represents the average of all cross-sectional areas along the wingspan and ρ is the material density, which is assumed to have a value of 1600 kg/m^3. Substituting the obtained wing box dimensions, a wing box mass of 2557.2 kg can be found.

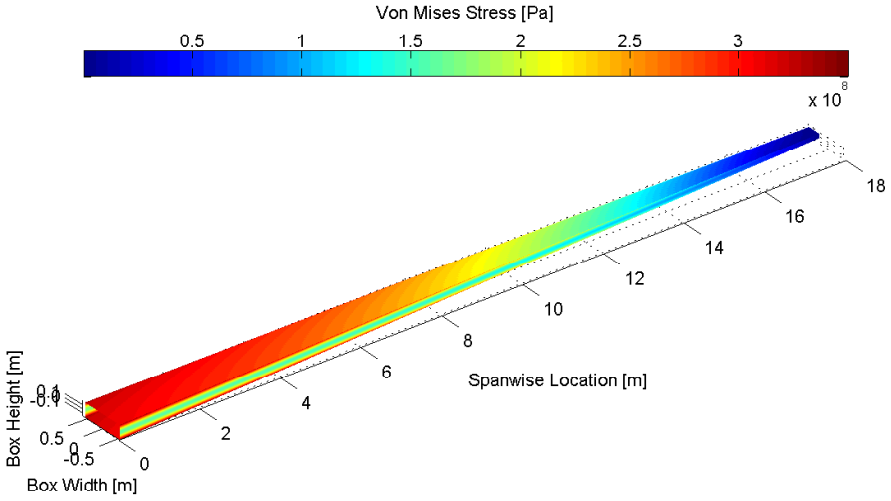

Figure 9.8: Von Mises Stress Distribution over the Wingbox

Table 9.5: Wing Box Parameters

	Skin		Front Spar		Rear Spar	
Parameter	*Thickness [mm]*	σ_{VMS} *[MPa]*	*Thickness [mm]*	σ_{VMS} *[MPa]*	*Thickness [mm]*	σ_{VMS} *[MPa]*
Root	31.4	323.8	19.5	349.6	4.50	348.7
Mid-Span	20.5	236.4	12.7	262.5	2.90	261.6
Tip	9.50	173.6	5.90	281.4	1.40	278.2

9.4.2 Flutter

When designing a wing box, several failure modes can be identified. Aside from the evident failure modes, bending and compression, two aero elastic phenomena need to be investigated, namely flutter and divergence. Within the scope of our project these failure modes are too complex for a thorough investigation, however to confirm the feasibility of the design a simplified approximation can be made.

The first motion which is assessed is flutter. Flutter is a dynamic motion which is characterised by rapid flapping of the wingtips. The airspeed U_F at which flutter becomes a diverging vibration can be computed with a simplified two dimensional model with two degrees of freedom (Fig. 9.9b).

The second motion, divergence, is a static motion. Over the length of the span the wing will get a moment induced angle, θ (Fig. 9.9a). Due to this increased angle of attack, the lift and moment of the section will increase, again leading to a larger twist angle. The divergence speed U_D is defined as the speed at which this twist exceeds the structural limits and the wing fails [47].

The wing box needs to be designed such that both limit speeds are larger than the designs dive speed, equal to 1.5 times cruise speed. This so that the aircraft can perform emergency manoeuvres without wing failure as this would result in a worsened situation allowing no chance of recovery.

When calculating the static flutter, both the flutter speed and the divergence speed, the typical cross section of the wing is the assessed profile. The typical cross section of the wing is the cross section at 75% of the wing. In this case the stiffness of the wing will be modelled by a spring (Fig. 9.9). In Table 9.5 the typical cross section and the values needed in order to calculate the flutter and divergence speed are visible [47].

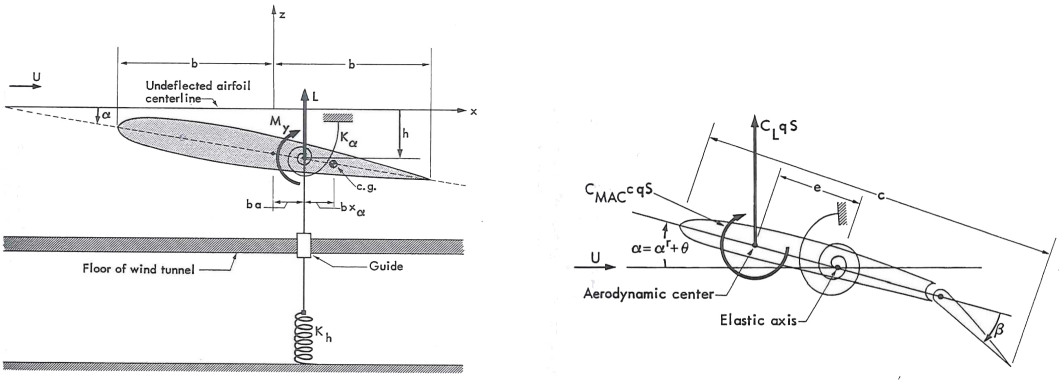

(a) Calculation Divergence Speed [47]

(b) Calculation Flutter Speed [47]

Figure 9.9: Aerofoil Segments to Calculate Flutter Speed and Divergence Speed

Flutter Speed

The flutter speed can be calculated using Eq. 9.17, where r_α and ω_α are given by Eqs. 9.18 and 9.19 [47].

$$\frac{U_F}{b\omega_\alpha} = \sqrt{\frac{m}{\pi\rho b^2}\frac{r_\alpha^2}{[1+2(a+x_\alpha)]}} \tag{9.17}$$

$$r_\alpha = \sqrt{\frac{I_\alpha}{mb^2}} \tag{9.18}$$

$$\omega_\alpha = \sqrt{\frac{K_\alpha}{I_\alpha}} \tag{9.19}$$

Divergence Speed

The calculation of the divergence speed is done using Eq. 9.20.

$$U_D = \sqrt{\frac{1}{C^{\theta\theta}\left(\frac{\partial C_L}{\partial \alpha}\right)\left(\frac{\rho}{2}\right)Se}} \tag{9.20}$$

Where $C^{\theta\theta}$ is equal to Eq. 9.21 [47].

$$C^{\theta\theta} = \frac{\theta}{T} \tag{9.21}$$

9.4.3 Iteration and Results

With all the failure modes defined, the wing box can be sized so that it can withstand all conditions. The sizing of the wing box is an iterative process where the lightest solution is sought where all requirements are met. Considering the high aspect ratio generating high loads and importance of reducing weight, an appropriate material had to be selected. The only material which proved capable of fulfilling the requirements was carbon fibre reinforced polymer.

This composite provides the possibility to custom design every section with respect to the loads it has to carry. This customisation is done by selecting the amount of layers with carbon in 0° direction and the amount of layers with carbon in 45° direction. Layers in 0° direction are efficient at counteracting the bending moment which results in compressive stress in the skins. Layers in 45° direction are effective in supporting torque loading. With this in mind one can play with the composition of the skin. To simplify the calculations the composition is assumed identical throughout the wing box, as this computation has the sole goal of proving feasibility of the high aspect ratio. In reality, the wing box weight will be significantly lower after detailed component design where composition and thickness of the skin are optimally varied over the wingspan.

The iteration is done in a specific order to minimise weight. Throughout the iteration skin thickness are assumed constant over the wing box for simplification purposes. In first instance the wing box is designed to be able to cope with the bending moment. With the resulting thicknesses, both aero elastic cases are assessed. Spars are then thickened until the flutter and divergence requirements are satisfied. Once they are satisfied the bending moment failure mode is recomputed and the top and bottom skin are minimised. With the new cross-section the aero elastic cases are reassessed. This loop is repeated until the values are constant.

After the iteration a final wing box design satisfying all requirements was found. The parameters of this wing box are summarised in the Table 9.6. In next steps of the design process, skin thickness and material composition should be varied. In addition the wing box is currently modelled only with skins, however in real life stringers and stiffeners will also be applied. Taking into account these later design choices the wing box weight can be lowered substantially.

9.4.4 Dihedral

The dihedral angle plays a role in two characteristics: ground clearance of the wing and roll stability of the aircraft. First the ground clearance criteria is assessed by computing what angle is necessary for the wing to not deflect passed the root height under its own weight. By taking the average area moment of inertia and modelling the weight of the wing as a distributed load, a first approximation of the deflection can be made using Eq. 9.22.

$$\delta = \frac{9.81 \cdot W_{tip} \cdot L^2}{24EI}(3L^2) + \frac{9.81 \cdot (W_{root} - W_{tip}) \cdot L}{120EI}(4L^3) \tag{9.22}$$

The dihedral angle is computed by taking the arctangent of the deflection over the half wingspan. This results in a necessary dihedral angle of $2.9193 \cdot 10^{-4}$ deg, or approximately 0. Therefore a dihedral angle is chosen based on benefits in roll stability. However the flight dynamics analysis required to determine the optimal dihedral angle is out of the scope of this project and will be determined in later stages of the design process.

9.5 Results

The final results of the wing obtained in this chapter, are summarised in Table 9.6.

Table 9.6: Wing Parameters

Parameter	*Value*	*Unit*
Aerofoil		
Aerofoil Number	$NACA63_2$-415	–
Wing Planform		
Wing Surface	65.18	m^2
Wing Span	36.00	m
Aspect Ratio	19.88	–
Sweep Angle LE	0	rad
Taper Ratio	0.3012	–
Root Chord	2.7830	m
Mean Aerodynamic Chord	1.98	m
Reynolds Number	$12{\cdot}10^6$	–
Cruise Lift Coefficient	0.5	–
Max. Clean Lift Coefficient	1.7	–
Max. Landing Lift Coefficient	2.5	–
High Lift Device	Single Fowler Flaps	
Aerodynamics		
Oswald Factor	0.77	–
Induced Drag Coefficient	0.0046	–
Parasite Drag Coefficient	0.0073	–
Total Drag Coefficient	0.0119	–
Winglets	Spiroid	
Structural Analysis		
Top Skin Thickness	0.028	m
Bottom Skin Thickness	0.028	m
Front Spar Thickness	0.041	m
Rear Spar Thickness	0.0103	m
Fibre Direction: +/- 45 °	51	%
Fibre Direction: 0/90°	49	%
Wing Box Weight	3572	kg
Dihedral	0	deg

CHAPTER 10

Propulsion

One of the most innovative aspects of the EuroFlyer is the propulsive system. The revolutionary hybrid power system, which is further explained in Chapter 11, powers two large slow Contra Rotating Propellers (CRP) integrated at the aft of the fuselage. These adjustments were performed to maximize efficiency with better propeller characteristics and by implementing the BLI principle. These implementations have additional consequences for the power train. In order to power two propellers with different energy sources, a complicated but failproof power train is required. The EuroFlyer resolves this problem by simultaneously running a turboprop engine, APU and an electrical engine with the necessary safety measures.

In this chapter the design process and results of the propulsive system are discussed. This includes basic propeller parameter optimization, engine design, shaft sizing and propulsive system architecture design. The roadmap of this chapter can be found in Fig. 10.1.

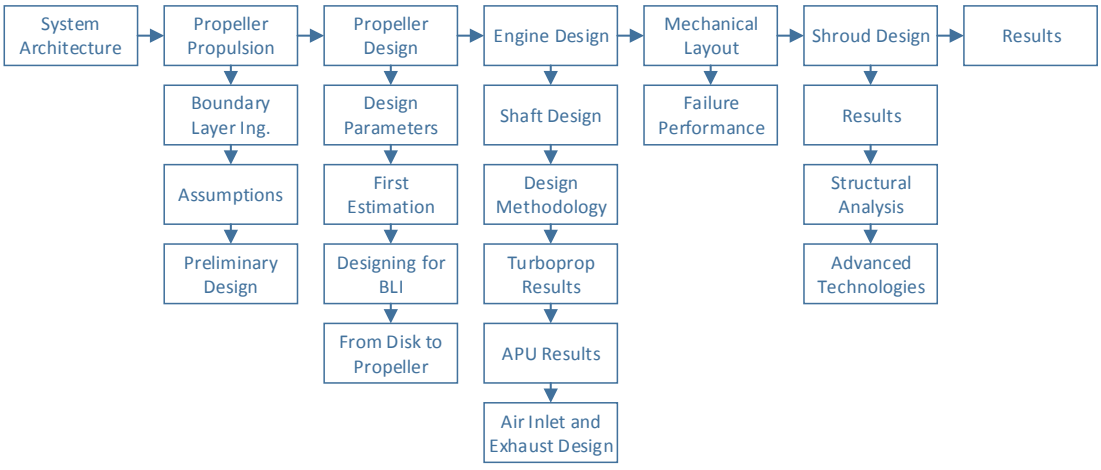

Figure 10.1: Propulsion Road Map

10.1 System Architecture

Many requirements for the EuroFlyer design are dictated by regulations set by the European Aviation Safety Agency (EASA), as published in their Certification Specifications for Large Aeroplanes [32]. There are important requirements set on the configuration of the propulsive system, to prevent further damage in case of partial failure. At first, the proposed hybrid solution seems to automatically tackle these problems as the LNG- and

battery-fed systems are inherently independent systems. However, due to the large weight associated with the electrical system, it is not feasible to split the energy and power requirements in equal parts. Having one of the two propellers run only half the time is no option either. Hence, the LNG-system does not only have to provide continuous power to one of the propellers, it is also partially powering the other. That would normally result in a mechanically coupled system (which cannot be certified), but as can be seen from the schematic layout shown in Fig. 10.2, the team has come up with a solution that would comply with the regulations. In reality the propellers are placed on the same horizontal axis, but for clarity they are shown next to each other.

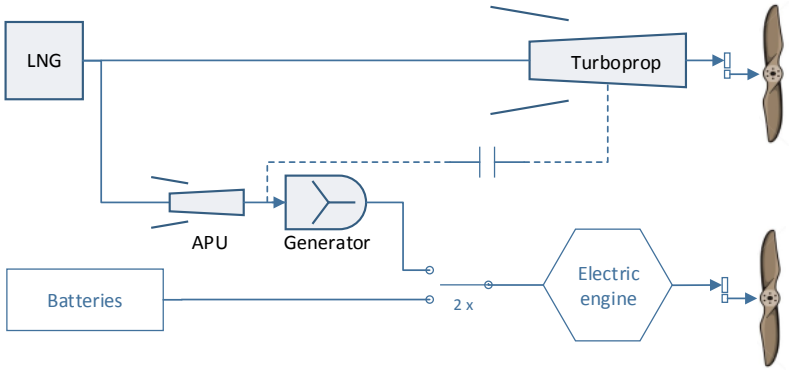

Figure 10.2: Selected Propulsive System Configuration

In this layout, the LNG is used as fuel for both a turboprop and a gas generator. The turboprop is connected to the drive shaft of one of the propeller disks. The other propeller is driven by an electric engine that draws its power from the battery pack and the generator. The generator receives power from another gas turbine engine (APU). This gas generator is slightly smaller than the turboprop and will also supply power to all electrical systems. A switch has been added between the turboprop and the generator to assure sufficient power to the on-board systems in the case that the APU turboprop fails.

10.2 Propeller Propulsion

The thrust from a propeller is derived by the addition of small velocity changes to a large mass of air, therefore the efficiency increases rapidly with increasing flight speed [48]. However, at higher subsonic Mach numbers the performance of the propellers suffers, mainly as a result of the adverse changes of pressure distribution on the blade due to compressibility effects. Therefore, a limit to the Mach number exists at which propellers may efficiently be employed. Modern propellers employed by high speed propeller aircraft use wide chord, multiple, swept blades rotating relatively slowly and can be usefully used up to a Mach number of about 0.7, although a Mach number between 0.6 and 0.65 is a more frequent design point [49].

Propellers may be designed to achieve their highest efficiency at various Mach numbers depending upon the required application. The adjustment of blade pitch on an individual propeller enables relatively high efficiency to be achieved over a range of speeds. At Mach numbers between 0.3 and 0.65 an efficiency of 85 to 90% is commonly realised [50].

The propulsive system of the EuroFlyer consists out of two CRP, surrounded by a shroud. This configuration has the advantage that the required pressure ratio to generate a specific amount of thrust can be distributed over two propeller stages, resulting in a lower loading per stage as compared to a single propeller.

The overall pressure ratio of the CRP is distributed over both propellers. From this, two approaches can be derived on how the propulsive system may be designed. The first approach is to opt for a system where the overall pressure is higher than that of a comparable conventional propulsive system generating an equal amount of thrust. This leads to lower rotational speeds for the CRP engine set-up as compared to the rotational speed of a conventional single propeller. The higher pressure ratio implies that for an equal amount of thrust, the propeller diameter must be reduced, leading to lower propeller and hub weight. The smaller fan diameter also results in an overall engine drag reduction. The lower rotational speed, and hence lower tip speed of the propellers results in a lower noise emission.

The second approach is not to increase the pressure ratio as compared to a conventional propeller. For the contra rotating propeller, this leads to even lower rotational speeds and pressure ratios for both propeller stages. Since the total pressure ratio is not increased, the size (or area) of the propeller will be the same for the given thrust requirements. The lower rotational speed implies that the aircraft can cruise at higher Mach numbers and the required lift coefficients with suitable critical Mach numbers are more feasible to be reached. This concept results in the largest reduction in fuel consumption since a propeller with a larger diameter generally operates more efficient [51]. Because of the strict emission requirements set for the EuroFlyer the second design approach is followed.

10.2.1 Boundary Layer Ingestion

One of the most prominent fuel saving methods implemented in the EuroFlyer is the BLI phenomenon. BLI in the context used here means taking fuselage boundary layer fluid through the engine for the purpose of improving fuel efficiency. In a conventional aircraft configuration the fuselage wake momentum deficit is balanced by the engine wake momentum excess. The benefit of BLI comes from re-energizing this fuselage wake by the engines, allowing lower energy waste. Fig. 10.3 gives an overview of the two situations.

With podded engines the flow entering the engine is at free stream velocity. The engine accelerates the flow of a velocity u_{jet}, such that the created moment excess balances the momentum deficit due to the drag of the airframe, $D_{airframe}$. In the theoretical case where 100% of the boundary layer is ingested, and the flow is perfectly accelerated to the free stream velocity, it can be observed that there is a perfect momentum balance. The difference in energy input between the two situations occurs because, with a given thrust force, less power needs to be added to a flow that enters the engine with a lower velocity [51]. The loading of the blades will be designed in such a way that the BLI effect is optimized, while still keeping realistic blade parameters.

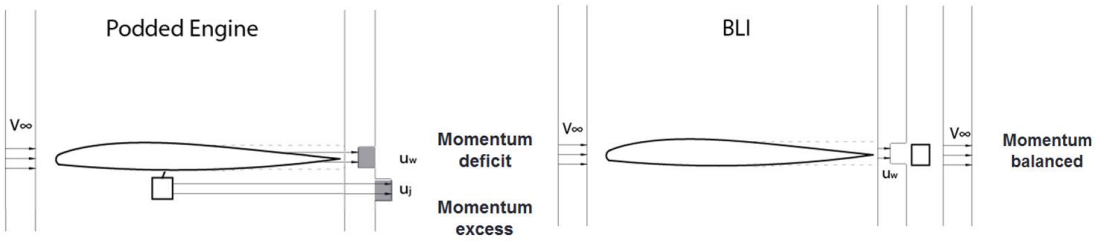

(a) Podded (b) BLI

Figure 10.3: Difference Between a Podded Engine and BLI

10.2.2 Assumptions

To understand the performance of the propeller and relate this performance to simple initial design parameters, the actuator disk theory is applied [52]. With this theory the propeller is modelled as a continuous disk instead of a finite number of propeller blades. This theory has the following assumptions.

- The rotation imparted to the flow is neglect
- Assume the flow outside the propeller stream tube has constant stagnation pressure
- Assume that the flow is steady. Smear out the moving blades so they are one thin steady disk that has approximately the same effect on the flow as the moving blades
- Across the actuator disk, assume that the pressure changes discontinuously, but the velocity varies in a continuous manner.

From a certification point of view the Shaft Horse Power (SHP) over both shafts driving the two propellers may not deviate too much from one another. This way, the propellers should be able to generate a sufficient amount of thrust, given that the airspeed is lowered, in the case that either one of the engines fails. However, this also brings difficulties when designing the contra-rotating propellers and their energy source.

In particular, determining the optimal pressure ratios for both propellers poses a large problem as the first propeller is located just in front of the second propeller. Therefore, the inlet velocity of the second propeller will

be higher than the inlet velocity of the first propeller. Because of the working principle of a propeller, this implies that the second propeller is unable to produce the same amount of thrust, as the SHP is equal over both shafts.

In order to cope with this problem, it is assumed that the rise in total pressure caused by the first propeller can be seen by the second propeller as a rise in static pressure only. This implies that the second propeller sees the same inlet velocity, u_0, as the first propeller. With this assumption the two contra rotating propellers may be modelled by a single actuator disk in the preliminary design phase.

Furthermore it is assumed that due to the presence of the shroud around the propellers, the Prandtl tip loss may be neglected. This ignores the tip loss concerning the blade tip, thereby increasing propulsive efficiency, which approximately models a shrouded rotor.

10.2.3 Preliminary Design

Theoretically the most efficient propeller is a slowly rotating propeller with a large diameter [49]. Since a large diameter will provide the highest efficiency, the largest propeller diameter which complies with the CS-25 ground clearance regulations is selected. The ground clearance is a function of the landing gear positioning; after iteration the maximal propeller diameter has been set 3.7 metres, as an additional clearance is required for the shroud.

As the propulsive system will be optimized for cruise operations, the required thrust will be calculated at true airspeed cruise velocity and altitude. From the preliminary sizing however, the weight to power ratio was calculated based on the take-off performance of the EuroFlyer. Therefore it is necessary to assure that the propulsive system optimized for cruise conditions is capable of also generating the required take-off thrust. At the end of the design phase this will be verified. In the final iteration, a total drag during cruise of 16714 N was determined. This implies that since the propulsive system will be design for cruise conditions, also 16714 N of Thrust has to be produced.

With the thrust known, a model of the propulsive system may be constructed. Combining the required thrust with the local ambient pressure and the diameter of the propeller, a pressure ratio over the two contra rotating propellers of 1.002 is found. Applying the assumption that the rise in total pressure after the first propeller is caused by an increase in static pressure only, the pressure ratio of the two propellers is 1.001.

10.3 Propeller Design

In this section, the propeller design process is thoroughly explained. Propeller propulsion systems are complicated systems where still a lot of research is done on how to optimise the efficiency of such propulsors. In addition, due to the EuroFlyer performance's close correlation to the efficiency of BLI, it has to be investigated how the system can be designed to optimally benefit BLI. To do so, the following approach is opted for and is documented accordingly.

To begin with, design parameters are chosen and boundaries are set to these values. Next, a first estimation is made using free stream actuator disk theory. The incoming velocity is then modelled according to the boundary layer profile and the actuator disk are modelled element wise and a necessary shaft power is computed which will function as input in the engine design. The actuator disk is then translated to propeller blades. During the whole process, the design parameters are continuously verified on boundary violation. A schematic representation of the propeller design process is provided by Fig. 10.4. Here, for clarity, the steps explained in every subsection of this paragraph are marked accordingly.

10.3.1 Design Parameters

As initial input in the design process for the propulsive system, certain constrains will be placed on several parameters in the same manner as the propeller diameter has already been specified earlier.

Starting with the tip speed, the effective velocity seen by the propeller tip may not exceed Mach 0.88 during cruise [48]. This limit has been determined as the Mach number from when compressibility effects may no longer be ignored.

Despite that a propeller only suffers relatively small efficiency losses, even when the flow goes supersonic, a tip velocity of more than Mach one will produce unacceptable noise levels. Since the noise requirements on the EuroFlyer are most important during take-off, the tip Mach number during take-off may not exceed 0.72 Mach

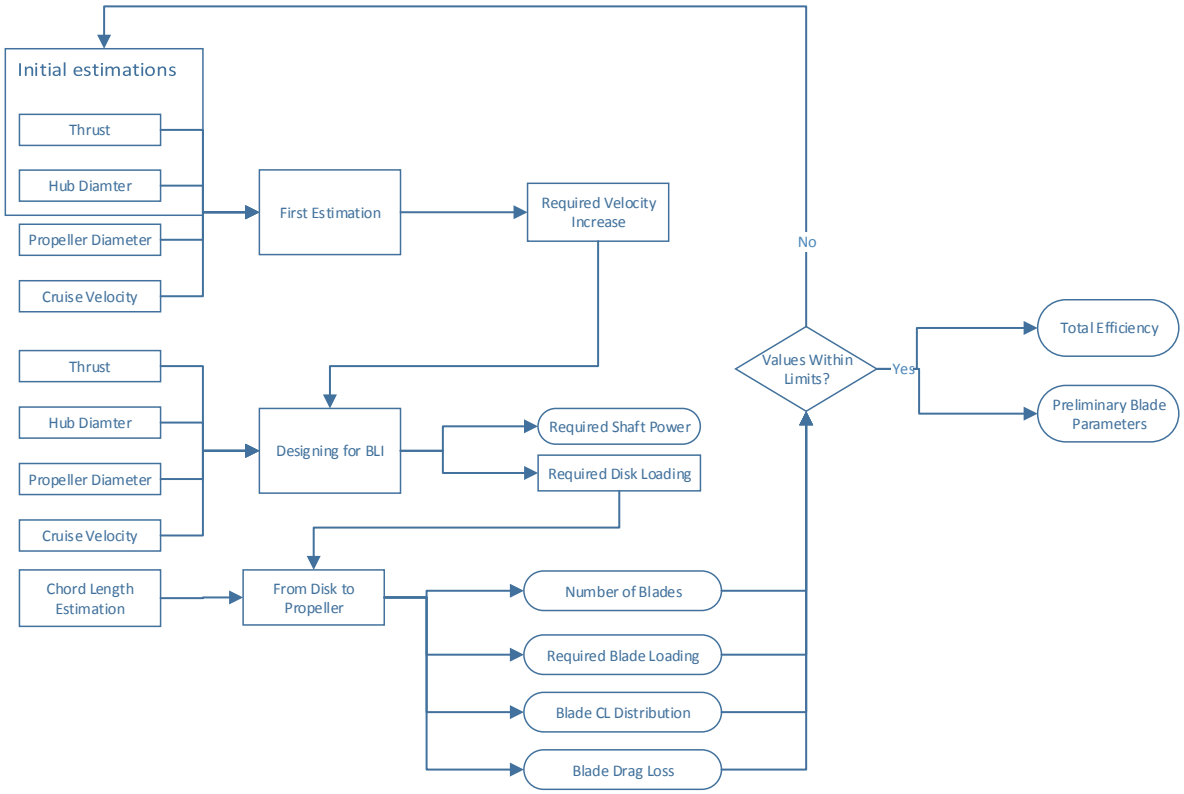

Figure 10.4: Propeller Design Flow Chart

[53] to suppressed noise production. The effective velocity of the wing tip is the vector addition of the cruise velocity and the rotational velocity of the wing tip, resulting in Eq. 10.1.

$$V_{tip} = \sqrt{V_{cr}^2 + (\pi \cdot 2r_{tip} \cdot n)^2} \tag{10.1}$$

Here r_{tip} is the distance from the centre of the hub to the tip and n the number of revolutions per second.

With the propeller tip velocity known, the revolutions per minute (RPM) of the propeller may be selected. The RPM of the propeller influences the tip velocity and the aerofoil characteristics of the propeller, for a given amount of thrust. From a noise point of view, the lower the propeller RPM the less noise will be emitted. This however is especially relevant during take-off, but will also be considered for cruise conditions to reduce both ground- and cabin noise. For this reason the RPM of the propeller will be lowered to a value where the required lift coefficients, and corresponding drag coefficients, over the blade are still in acceptable limits.

With limits set on RPM, the required thrust, V_{tip} and the propeller diameter and the limits of the pressure ratio over both propellers known, the propeller may be modelled. In the following section the methodology of the sizing of the propeller is described. At the end, after several iteration rounds of the whole aircraft, the final values for the above named parameters will be given.

10.3.2 First Estimation

In the following subsection the process of generating the initial estimation for the propeller parameters will be described. For this phase the inputs were the limits set on the parameters described in Section 10.3.1, the outputs are the initial parameters of the actuator disk. In this phase a constant input velocity profile is used; the boundary layer is not yet taken into account.
Fig. 10.5 provides an overview of the simplified initial model according to the Actuator Disk Theory. The convenience of the this model is that an even pressure distribution over the disk is assumed.
To prepare the calculations to account for BLI, it was attempted to generate a disk loading such that the velocity profile behind the disk was constant. This implies that the thrust generated over the radius of the disk must be

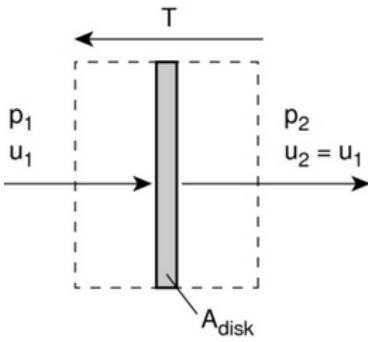

Figure 10.5: Schematic Overview of the Propeller, Modelled According to the *Actuator Disk Theory*

constant. This in term results in a required propeller loading. With Eq. 10.2 [51] the required velocity increase before and after the propeller can be calculated when the actuator disk theory is applied.

$$T = \rho \frac{\pi}{4} D^2 \left(V_\infty + \frac{1}{2} \Delta V \right) \Delta V \tag{10.2}$$

In this equation ΔV is the velocity increment that must be given to the free stream in order to generate the required thrust of 16714 N. However, since part of the actuator disk theory states that half of the velocity increase occurs before the disk, due to suction, and the other half of the velocity increase after the disk. This in term leads to the relation given in Eq. 10.3 [51].

$$V_{atblade} = V_\infty + \frac{1}{2} \Delta V \tag{10.3}$$

This is an important relation as now the incoming free stream velocity as seen by the propeller can be calculated. Specifying this velocity has great influence on the propeller and blade properties. With this incoming velocity specified, it is now possible to go into more detail.

10.3.3 Designing for Boundary Layer Ingestion

When designing for BLI, a velocity profile behind the propeller similar as in Fig. 10.6 should be strived for. To adopt the BLI principle in the design of the propulsive system, an incoming boundary layer velocity profile is required. This incoming velocity profile is initially modelled using the Blasius formula. However, at the aft of the fuselage, the boundary layer seen by the propeller will have become turbulent due to the high Reynolds number. The Blasius formula is therefore scaled to represent a turbulent boundary layer profile which is steeper and reaches 95% of the free stream velocity in less distance from the skin. The scaling is then verified to the profile resulting from ANSYS FLUENT, with the limiting offset set to five percent. The result can be seen in Fig. 10.6, note that the straight line in the centre of the outgoing velocity profile originates from the exhaust velocity.

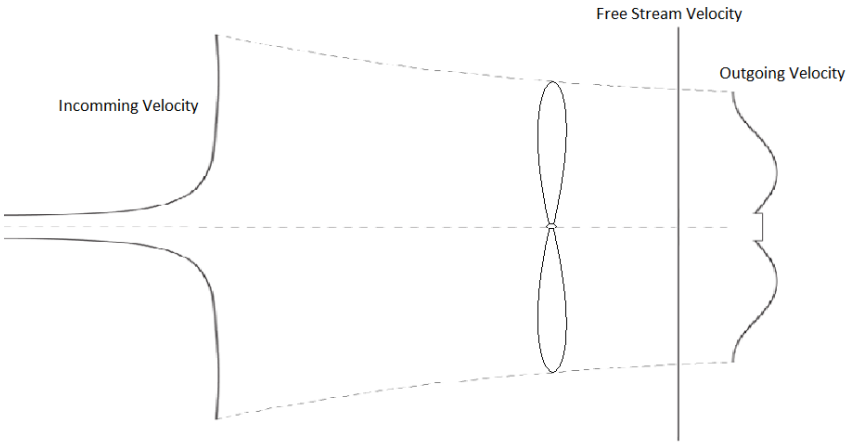

Figure 10.6: Schematic Overview of the Velocity Profile Before and After the Propeller

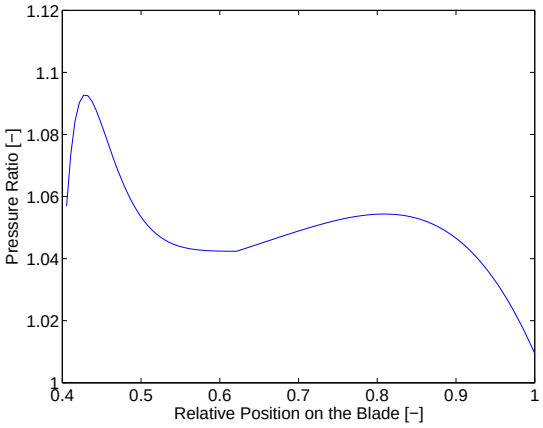

(a) Final Blade Loading per Blade

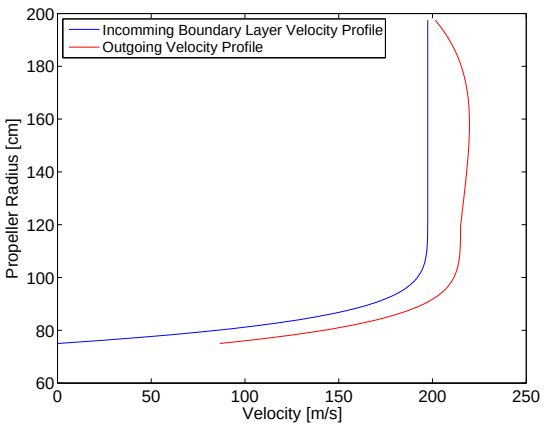

(b) Velocity Profiles behind the Propellers

Figure 10.7: Final Blade Loading and Velocity Profiles Before and After the two Contra-Rotating Propellers

Furthermore, the outgoing velocity profile also has to be modelled. This is done according to the loading profile sought after. Important efficiency gains can be obtained by doing this optimally. Typically, propellers are best gradually loaded increasing to a maximum loading at 0.8-0.85% of the blade length. However the design team hopes to gain efficiency by propelling boundary layer, so a suggestion was done to mirror the optimal loading of a conventional propeller. Nevertheless only the first section of the propeller is functioning in boundary layer and the rest is still propelling free stream air.

With this in mind a novel loading distribution combining both ideas is developed. After testing all three profiles through the whole design process and verifying that their required blade lift coefficients are within reasonable limits, the novel loading distribution is found to be the most efficient and is adopted which results in an efficiency of 99.8% compared to 95% without BLI. This load distribution is depicted in Fig. 10.7a. With the outgoing velocity the shaft power is then computed element-wise along the span with Eq. 10.4.

$$P_{shaft} = \int_{R_{hub}}^{R_{prop}} \rho\pi \left(\left(r + \frac{\delta r}{2} \right)^2 - \left(r - \frac{\delta r}{2} \right)^2 \right) \cdot (V_{in} + 0.5\Delta V)^2 \cdot \Delta V \delta r \tag{10.4}$$

10.3.4 From Disk to Propeller

From the actuator disk model, a realistic propeller can be designed. First the required amount of blades is computed to then calculate the necessary lift coefficient and chord of every element following the blade element theory, depicted in Fig. 10.8. To begin with, the amount of blades can be calculated by rewriting Eq. 10.5 where b is the number of blades. Here, the blade power is chosen to be 5.2 W/m^2 based on highly loaded reference propellers [53].

$$P_{blade} = \frac{4P}{\pi b D^2} \tag{10.5}$$

Normally, before the blade lift coefficient, C_l, and chord, c, can be calculated, three important losses in efficiency should be taken into account: compressibility loss, tip loss and blade drag loss. However, in the EuroFlyer's case, the first two can be neglected as tip velocities will not exceed the blade critical Mach number avoiding compressibility losses and as the propeller will be enclosed by a shroud tip losses are negligible as well. Finally, blade drag efficiency loss can be computed using Eq. 10.6 where C_d is approximated with respect to the average necessary lift coefficient. The total efficiency can then be computed with Eq. 10.7. An artificial required thrust is then found and the whole process is reiterated. If the amount of blades increases, the process has to be reiterated once more taking into account the additional drag loss.

$$P_{artificial} = \frac{P_{shaft}}{1 - \frac{n_{blade} \cdot C_d \cdot \left(R_{prop} - R_{hub}\right) \cdot c_{blade}}{\pi \cdot \left(R_{prop}^2 - R_{hub}^2\right)}} \tag{10.6}$$

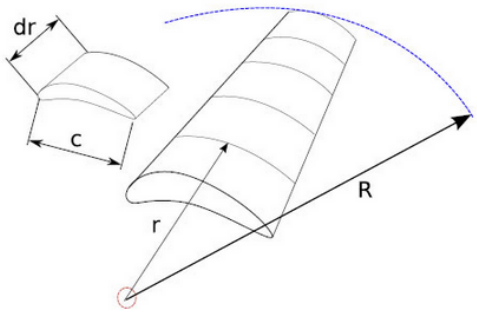

Figure 10.8: Schematic Overview of the Propeller, Modelled According to the *Blade Element Theory*

$$\eta = \frac{T \cdot V}{P_{artificial}} \tag{10.7}$$

With the artificial required thrust increments, a blade chord and C_l can be selected for every element by rewriting the following formula. Here, V_e is the effective velocity seen by the blade.

$$T = \frac{1}{2} \cdot \rho \cdot b \int_{0.75}^{1.9} \cdot V_e^2 \cdot c \cdot C_l \cdot dr \tag{10.8}$$

The final blade dimensions can then be checked if they are realistic, in particular if the C_l values are obtainable with the effective Mach number of the blade element. Table 10.2 summarizes the characteristics of the propeller. Also, in Fig. 10.9 the required lift coefficient over the span of the propeller blade is shown, here the chord dimensions are selected such that the lift coefficients are within acceptable limits [54].

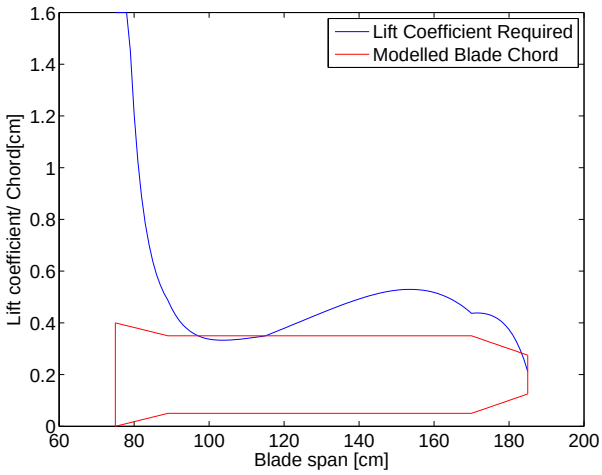

Figure 10.9: Schematic Overview of the Lift Coefficient over the Blade Span

Fig. 10.10 shows a rendering of the propeller system. The next step in the propulsion design process is the sizing of the engine. Section 10.4 will elaborate on the method employed.

10.4 Engine Design

The next step in the design process of the propulsion system is the design of the power train. As mentioned before, the EuroFlyer will integrate a revolutionary hybrid power system. To obtain high fuel efficiency of the aircraft, it is essential that the engines are designed precisely. The powertrain will consist of three engines, two LNG powered engines and an electrical engine. As electrical engines are scalable with consistent efficiencies and outside the field of expertise of the team, the design of the electrical engine will be left for a later design stage. On the other hand the LNG powered engines are sensitive to power output and require sizing. In the EuroFlyer design, the required output led to the decision to utilize two turboprops, where one will function as APU. This section will discuss the sizing of these engines and the integrated system.

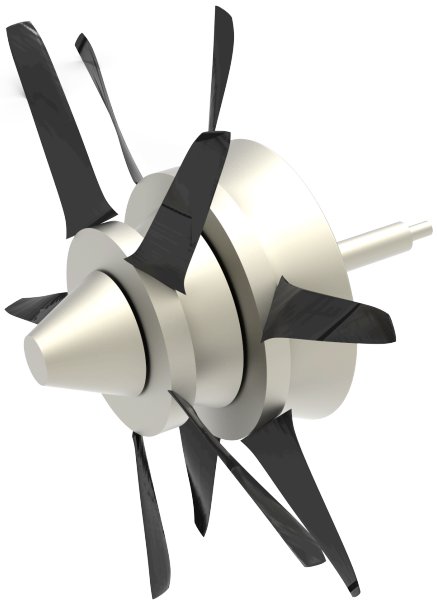

Figure 10.10: Artist Impression of the Propeller System

10.4.1 Shaft Design

As the propulsive system is an unprecedented system the weight and dimension sizing based on statistical data is not possible. Fortunately for some components, such as the shaft, a good approximation can be made with a few simple structural equations. Closely related to the shaft design is the design of the exhaust, which will also be explained in this subsection.

First, the load cases of the shaft are defined. Three critical failure modes are identified, starting with torsional failure. To make sure the shaft can carry the applied load, the torsional rigidity needs to be found. This can be done using Eq. 10.9. This value depends on the torque applied, the shear force in the shaft and the radius of the shaft.

$$J = T \cdot R_{shaft}/\tau \tag{10.9}$$

Next, the column buckling was found with Eq. 10.10. By looking at the trust provided by the propellers, the length of the shaft and the Young Modulus.

$$I = \frac{\frac{Thrust}{2} \cdot 4 \cdot L_{shaft}^2}{4 \cdot \pi^2 \cdot E} \tag{10.10}$$

The last failure mode the shaft needs to withstand is the compressive loading. The compressive yield stress can be found with Eq. 10.11. Which also depends on the trust, like the column buckling, but also depends on the area of the shaft. Since failure is not allowed for any of these three cases, the shaft should be designed so it can carry all the loads, including a safety factor.

$$\sigma = \frac{Thrust}{2 \cdot \pi \cdot \left(R_{shaft}^2 - (R_{shaft} - t)^2)\right)} \tag{10.11}$$

The length of the shaft is determined in the allocation of space to all subsystems and was found to be one metre. Next, the shaft diameter is chosen, which should be larger than the exhaust and smaller than the hub with a 30 cm margin to account for necessary systems such as pitch control. This resulted in a diameter of 50 cm for the outer concentric shaft.

For the shaft titanium was opted for as material because of the beneficial strength to weight ratio and possible high operating temperatures. With these design choices, a necessary thickness of 1.6 and 2.0 mm was calculated for the outer and inner shaft respectively. Here, a load factor of 6 and safety factor of 1.5 are already taken into account in these values. However experience proves that due to visual discomfort of such thin shafts and the importance of a fail proof shaft that extra thickness is always added. So, for simplicity a shaft thickness of one centimetre is chosen for both concentric shafts. This results in a total shaft mass of 147.1 kg.

10.4.2 Design Methodology

The properties at every stage of the engine are calculated using the isentropic relations and equations for work and thrust. The turboprop and APU will be dual stage engines with a third turbine to power the shaft. However for simplicity it is modelled as a single stage engine, as it is assumed that technology will be at a level where the performance of a current single stage and a future twin stage engine is equal. During the description of the engine model the reference points as depicted in Fig. 10.11 are addressed accordingly. The airflow conditions change from ambient at point zero before entering the compressor stages at point two. The pressure loss and temperature increase are computed with the isentropic relations.

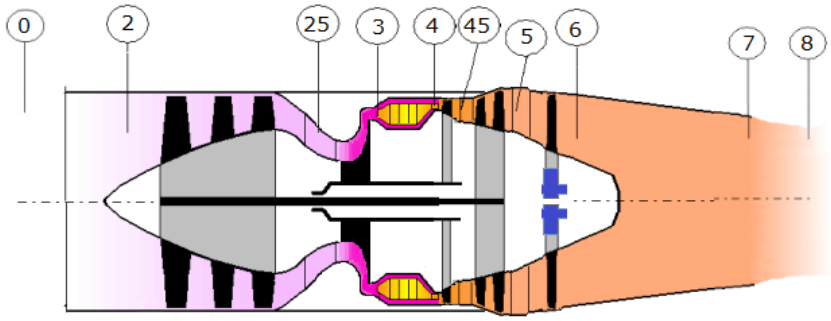

Figure 10.11: Engine Overview

By applying Eq. 10.12 the temperature after the compression stage is found. After this stage $0.59 kg/s$ of compressed bleed air is withdrawn with the purpose of refreshing cabin air and blowing air through the struts and vertical tail plane (Section 10.6). It is verified that the combustion chamber does not exceed the limit temperature of $1500K$ [55]. With the application of Eqs. 10.13 and 10.12 and by calculating the work performed by the compressors with Eq.10.14 the pressure and temperature at location five are found.

$$\frac{T_a}{T_b} = 1 + \frac{1}{\eta_{is}} \left[\frac{p_a}{p_b}^{\frac{\kappa}{\kappa-1}} - 1 \right] \tag{10.12}$$

$$\dot{m}_{fuel} = \frac{m_{air} \cdot Cp_{gas} \cdot \Delta T}{LHV \cdot \eta_{cc}} \tag{10.13}$$

$$\dot{W}_{comp} = \dot{m}_{air} \cdot Cp_{air} \cdot (T_{30} - T_{20}) \tag{10.14}$$

As a twin spool engine is selected, the work required to compress the air at the compressor stages has to be delivered by the turbines. An additional turbine is added to provide the required shaft power. Using Eq. 10.15 the required work that has to be done by this turbine is calculated. The conditions of the turbine stages are accordingly calculated with Eqs. 10.14 and 10.12.

$$\dot{W}_{gg} = \dot{m}_{gas} \cdot Cp_{gas} \cdot T_{50} \left[1 - \frac{p_0}{p_{50}}^{\frac{\kappa_g - 1}{\kappa_g}} \right] \tag{10.15}$$

It was verified that the nozzle is unchoked and that the exhaust thrust is minimized to obtain maximum propulsive efficiency. This will be explained in the following section.
Finally, the fuel efficiency can be calculated using Eq. 10.16.

$$\eta_{fuel} = \frac{\dot{W}_{gg}}{\dot{m}_{fuel} \cdot LHV} \tag{10.16}$$

10.4.3 Turboprop Results

To optimize the efficiency of the propulsive system, it is desirable to suppress the thrust generated by the turboprop as much as possible as the CRP have a significantly higher propulsive efficiency than the exhaust velocity thrust. To achieve this, a near zero pressure and velocity difference is opted for. With the strict fuel flow requirements and a maximum temperature in the combustion chamber, the optimal turbine entry temperature, thermal efficiency, thrust and shaft power can be deduced from the plots displayed in Fig. 10.12. These plots represent every possible combination of engine parameters and the associated engine characteristics.

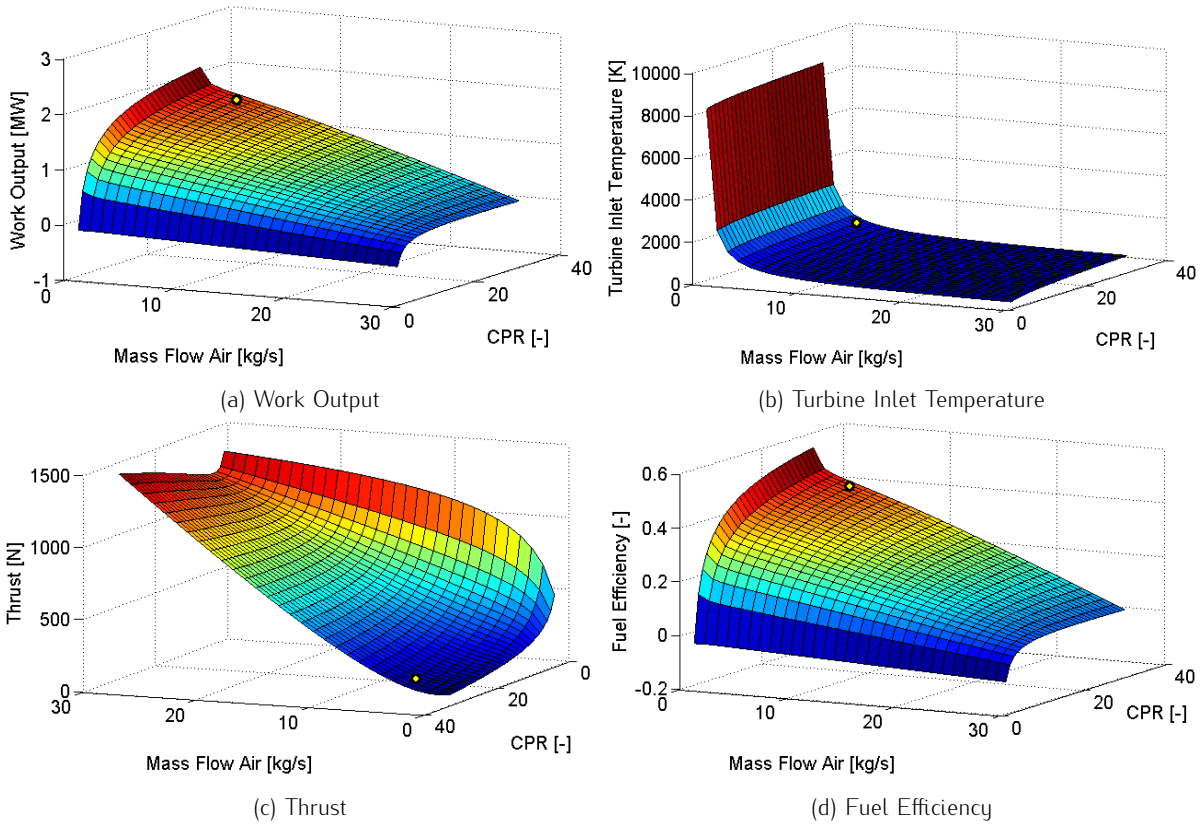

(a) Work Output

(b) Turbine Inlet Temperature

(c) Thrust

(d) Fuel Efficiency

Figure 10.12: Engine Parameters as a function of Air Mass Flow and Compressor Pressure Ratio

Using a twin spool turboprop engine allows for high pressure ratios and increased efficiencies. However in the EuroFlyer design the airflow is a limiting parameter as the engine inlet is complex and limited in size. Finally, based on the combination of work output and fuel efficiency, the optimal engine was chosen. A short summarising table describing the turboprop characteristics can be found in Table 10.2 and the complete set of engine specifications are included in Appendix F. For take-off performance, the fuel flow can be increased to 0.095 kg/s to generate the desired power output of 2.2 MW as discussed in Chapter 11.

10.4.4 APU Results

The APU gas turbine sizing process is very similar to that of the turboprop engine described in Section 10.4. Where the in- and outputs differ, the computation method remains the same. By distributing the fuel flow equally, the total fuel efficiency is maximised. As a result the APU is allowed the same mass fuel flow as the turboprop engine. The pressure ratio of the twin spool engine is 17 consisting of an axial compressor with pressure ratio of 4.25 and a radial compressor with a ratio of 4. A summarising description of the APU can be found in Table 10.2.

The electrical engine is to provide the same shaft power as the turboprop, namely half of the total power required. Electric engine development is making giant leaps in technology, allowing for a relatively small engine with a large power output. Different possibilities exist with varieties in power-to-weight ratios and RPM. One particularly interesting engine is a 4 MW naval engine manufactured by Siemens [56]. Masson states that similar engines in terms of power and efficiency are very much possible and available [57].

10.4.5 Air Inlet and Exhaust Design

The amount of air the turboprop and the APU require is relatively small compared to other engines allowing the inlets to be integrated into the fuselage, just after the wing. This position is beneficial because the wing has already disturbed the boundary layer in that region, minimising the disturbance in boundary layer for the propellers. The inlets can be connected with each other by opening up the connecting section for safety reasons. The inlets can be viewed in Fig. 10.13.

With the shaft design fixed the exhaust design can now be executed. An exhaust leaves from each fuel powered engine, the turboprop and APU, and join smoothly just before the concentric shafts. The exhaust then runs through the full length of the shafts to propel the exhaust air parallel to the velocity. The radius of the exhaust was computed to be 16 *cm*. Chevrons are a newly used method on turbofan engines which allow silent mixing of the cold outer air and the hot exhaust fumes [58].

10.5 Mechanical Layout

A topview of the propulsive system and all its components is shown in Fig. 10.13 as located in the aft fuselage. The two gas turbines are flanked by two fire shields each, to prevent damage to the other components. The gas turbines are located at the same height, positioned near the fuselage centre line. The turboprop provides all the shaft power for the second set of propeller blades. The free turbine in the engine translates the power through a gearbox to a drive shaft. The electrical engine is placed above the APU as seen from behind, driving the outer propeller shaft through a gearbox. The generator is located below the APU and turboprop and is directly connected to the APU. The generator can also be powered by the turboprop by means of a clutch in case of APU failure. The electric engine is powered by the generator and the batteries.

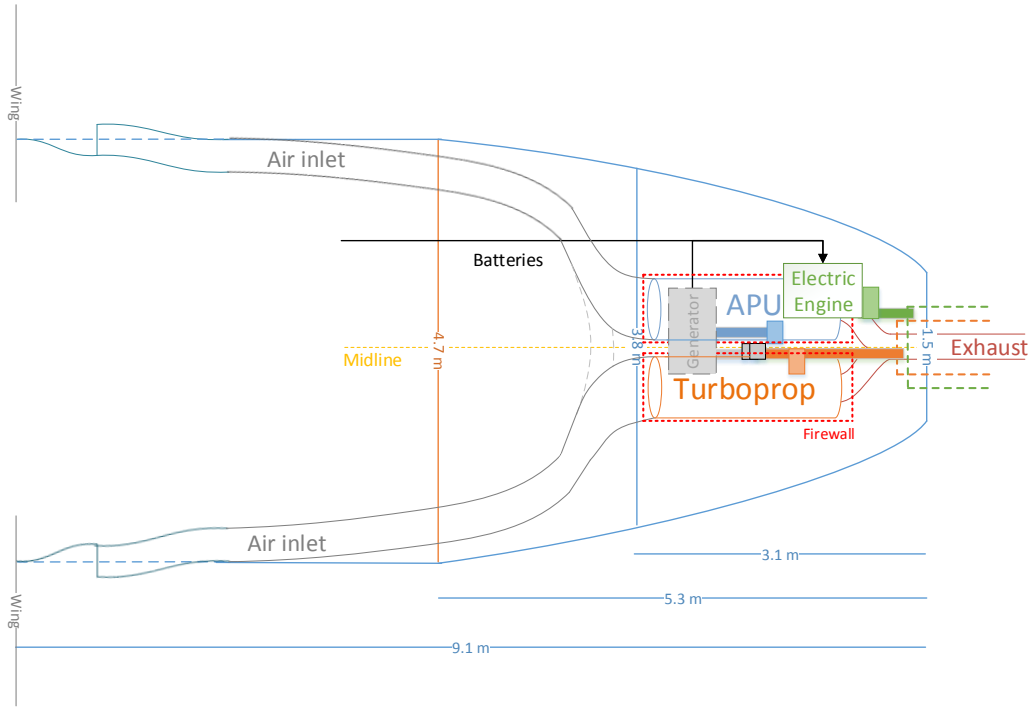

Figure 10.13: Top View of the Propulsive System in the Fuselage Rear Section

10.5.1 Failure Performance

Safety regulations demand an acceptable separation of systems in terms of mechanics, electronics and a physical separation. Analysing the failure performance of the propulsion system, it can be seen that no single component failure can shut down the entire system. In the unlikely case that one of the engines or the APU or one of their main components is unable to function, the other shaft and attached power source will still provide sufficient power to ensure a safe landing.

The turboprop and drive shafts are not connected to the electrical system unless the clutch to the generator is enabled. The electric engine system in turn is not dependent upon or connected to the turboprop system, save for the electric engine starter on the turboprop. An extra advantage of the distinctly different systems is that it is very unlikely that one (external) cause will result in failure of both. As for physical separation, several fire-proof walls will be integrated around the gas turbines along with adequate structural support and attachments.

10.6 Shroud Design

In this section, there will be focused on the design of the shroud, surrounding the contra-rotating propeller. The shroud is not only included to reduce the noise emissions due to blockage of the sound waves, it also affects the propeller performance by reducing the losses at the blade tip. However, its wetted surface increases the overall aircraft drag and its structural integration is not evident. Therefore, the design team considers it relevant to perform an in depth analysis of the influence of the presence of the shroud on the propulsive subsystem to enable an objective decision whether a shroud is desirable for the EuroFlyer. Lazareff compares in his paper the propulsive efficiency of a freestream and shrouded propeller at various flight speeds [59]. This is illustrated in Fig. 10.14. One can observe that shrouded propellers are characterized by a higher propulsive efficiency at low flight speeds. This changes however at Mach numbers approximately higher than 0.3, as the drag of the shroud becomes more significant and induces a reduction in propulsive efficiency. From Mach 0.65 onwards however, the propulsive efficiency of a freestream propeller rapidly drops due to compressibility effects on the blade tips. Given the cruise Mach number of the EuroFlyer, one can thus conclude that the addition of a shroud will not affect the propulsive efficiency during cruise. Nevertheless, in order to allow the EuroFlyer to meet the stipulated noise reductions during take-off and landing, a shrouded propeller design was opted for, even though the structural integration is not straightforward. This section will proceed with the determination of main shroud characteristics, such as the shroud dimensions and drag.

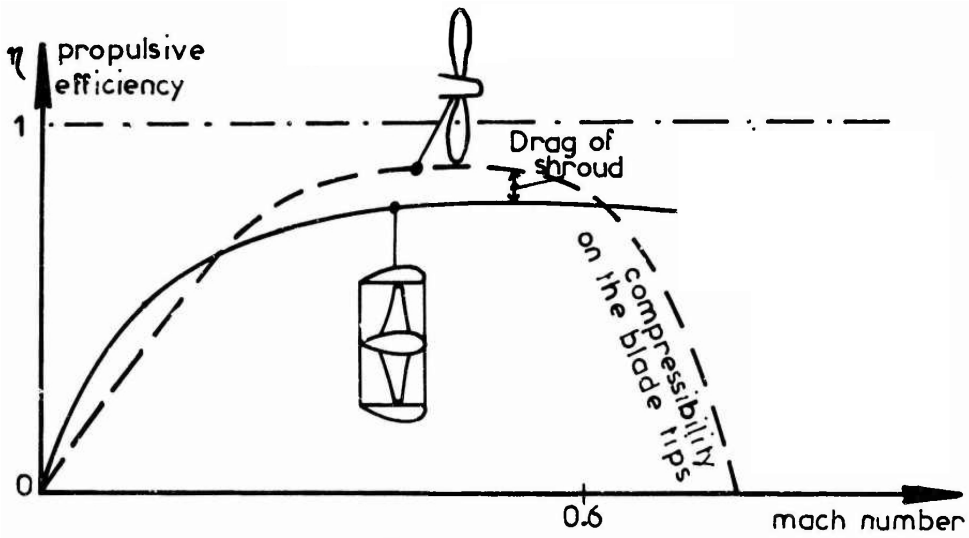

Figure 10.14: Effect of Shroud on Propulsive Efficiency

10.6.1 Shroud Parameters

Using a similar method to that of the wing and tailplane drag estimations, the appropriate friction and drag coefficients were calculated for the shroud by modelling it as a circular wing with a symmetric aerofoil. The shroud length is estimated to be 1.2 *m* based on the propeller geometry, propeller offset, tail plane lengths and exit area. The type of aerofoil decided upon is half of the NACA 0012, the inner side of the aerofoil is cut off from the camber line. This ensures benefits of an aerofoil in terms of drag while lowering its thickness and skin friction coefficient [59]. The skin friction coefficient is calculated in a similar manner as the wing by means of Eqs. 9.7 and 9.8. The most essential shroud characteristics are united in Table 10.1.

Table 10.1: Shroud Parameters

Parameter	*Value*	*Unit*
Shroud Length	1.2	*m*
Thickness Ratio	6%	%
Skin Friction Coefficient	0.0017	–
Total Shroud Drag	1008.1	*N*

10.6.2 Advanced Technologies

Some novel technologies are implemented on the shroud to contribute to noise reduction or improve overall efficiency. To temporarily alter the propeller exit velocity for example, the shroud exit area is adjustable by means of a shroud flap. This may be beneficiary in certain flight conditions such as take-off, but also compressibility effects can be postponed [59]. As the shroud forms the boundary between the faster flowing air propelled by the propeller and the more slowly flowing free stream air, the implementation of chevrons is suggested to reduce the noise generated by the shroud.

Chevrons are serrations at the trailing edge of a nozzle. By serrating the trailing edge of the shroud the low frequency noise is reduced as the rate of mixing between the two airflows is increased [58]. A by-product of the enhanced mixing ratio is the production of large amount of high-frequency noise. High frequency sound levels are much easier damped by atmospheric attenuation than lower frequency sound levels. The addition of chevrons in the shroud design will lead to a reduction in cruise emitted noise, allowing more silent flight which is especially beneficial during night flights.

The design of chevrons is mainly a function of the velocity difference between the inner and outer flows specified as V_{diff}/V_{mix}; the acoustic benefit can be related to this parameter. The chevrons are especially efficient when this ratio is higher than 0.8. The chevrons of the EuroFlyer will be operating at a ratio of approximately 0.05. Research shows that for a normalized velocity difference of 0.1, a noise reduction of 1.5 EPNdB is realisable. Here it was experimentally proven that a total of eight serrations provided the largest reduction in emitted noise for the velocity difference ratio of the EuroFlyer. For a low normalized velocity difference it was shown that this number of serrations is the optimal.

10.7 Results

This paragraph provides a brief overview of the final values of the propulsive system parameters after iteration of the final design.

Table 10.2: Propulsion Parameters

Parameter	*Value*	*Unit*
Propeller		
Blade Length	1.1	m
Hub Diameter	1.5	m
Rotational Speed	11.67	RPS
Tip Mach Number	0.79	–
Number of Blades First propeller	5	–
Number of Blades Second Propeller	6	–
Propeller Efficiency	99.8	%
Improved Efficiency due to BLI	4.3	%
Shaft Power	3.30	MW
Inner Shaft Thickness	1	cm
Outer Shaft Thickness	1	cm
Turboprop Engine		
Work Free Turbine	1.66	MW
Mass Flow Fuel	0.075	kg/s
Mass Flow Air	5	kg/s
Fuel Efficiency	0.432	–
Thermal Efficiency	0.385	–
APU Engine		
Work Free Turbine	1.69	MW
Mass Flow Fuel	0.075	kg/s
Mass Flow Air	5	kg/s
Fuel Efficiency	0.439	–
Thermal Efficiency	0.444	–

CHAPTER 11

Energy

Due to stringent requirements on emissions of carbon dioxide CO_2 and NO_x, the EuroFlyer team has carefully investigated various options of storing energy. Earlier in the design process, the trade-off proved a hybrid energy system as most favourable, combining LNG with high-tech Li-air batteries [16]. Then, the required amount of energy was estimated using reference data. Having progressed in the design process, it is now time to turn to more advanced methods. This chapter shows and explains this exact methodology, ending in a presentation of the results obtained.

To simplify the iterative process, extensive use was made of the MATLAB programming suite. Fig. 11.1 shows the program setup.

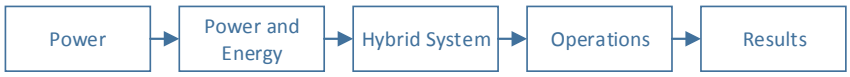

Figure 11.1: Energy Road Map

The steps taken are presented chronologically in the next sections. Section 11.1 explains the method used to find the required power, Section 11.2 details how this energy is stored and divided between LNG and the batteries. Some operational aspects are outlined in the remainder of the chapter, Section 11.3.

11.1 Power and Energy

Previously, the required amount of energy was determined by considering the fuel consumption of various reference aircraft [16]. For this more detailed analysis, a different approach was taken. This was further elaborated in Chapter 10. The value for the maximum power found, 3.3008 MW, forms the basis of all further calculations. Based on the NASA N+3 mission profile, as depicted in Fig. 11.2, the mission is split up in various phases and power settings for each phase are estimated. Next, the total flight time is split between these phases. With both power and time known, the energy is computed. Table 11.1 shows the values used in this process.

Some values might require some clarification. Flight times for take-off, climb out, climb to cruise, descent and landing have been assumed based on aforementioned mission profile. The flight phase hold only appears in the part of the flight where reserves are used, and is set to 10 minutes (given in the mission profile). Taxi time is indicated as 4 minutes for taxi in and 4 minutes for taxi out and is summed in Table 11.1. This does not appear in the reserve phase for obvious reasons. The mission cruise phase follows from subtracting all mission flight times (excluding taxi) from the total mission flight time, based on range and average speed. The reserve cruise phase flight time is found using a similar method, with the total reserve flight range (climb out up to and including descent) set at 200 nautical miles (370 km).

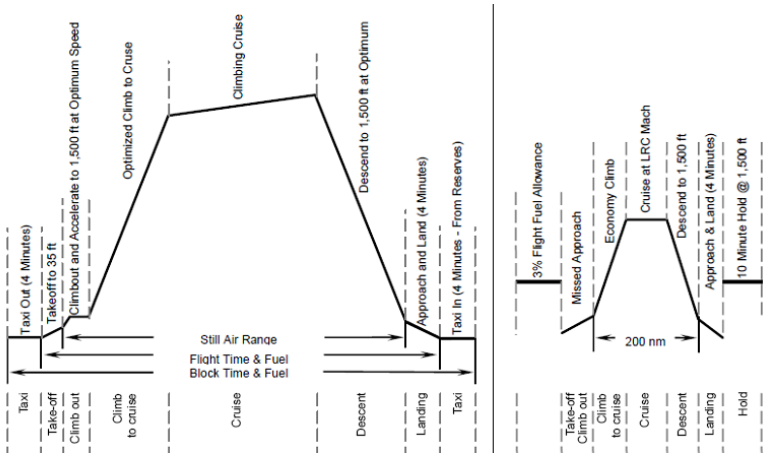

Figure 11.2: NASA N+3 Mission Profile [3]

Table 11.1: Flight Phase Division, Indicating Power Setting and Flight Time

Flight phase	*Power setting [-]*	*Flight time [s]*	
		Mission	*Reserve*
Take-off	1	60	60
Climb out	0.95	120	60
Climb to cruise	0.85	800	200
Cruise	0.75	(A)	(B)
Hold	0.75	0	600
Descent	0.65	800	400
Landing	0.75	240	240
Taxi	0.5	480	0

Two important factors cannot be forgotten. Firstly, there is a three percent flight fuel allowance, which is taken into account by multiplying all mission flight phase durations with 1.03. Secondly, a margin of five percent is taken into account (over the entire flight) to account for the energy consumption by on-board electrical systems [31].

11.2 Hybrid System

As indicated in earlier work [16], the EuroFlyers hybrid system will be sized to precisely meet the emission requirements, set at a 75% reduction in CO_2 and a 90% reduction in NO_x as compared to the Embraer E170 on a comparable mission. That aircraft uses a total of 4387.5 kg of kerosene to transport its payload over 1500 km [60].

Reaction of hydrocarbons can be found with Eq. 11.1, which can be converted to Eqs. 11.2 and 11.3. From these equations, it was found that for one kilogram of burnt kerosene, 3.11 kg of CO_2 is produced. For LNG, this value is a little lower, at 2.75 kilogram $C0_2$ per kilogram LNG. Based on these values and the required reduction, the maximum LNG weight can be determined, which in turn results in a maximum energy fraction to be supplied by burning LNG.

$$C_xH_y + \left(x + \frac{y}{4}\right) O_2 + 3.76 \left(x + \frac{y}{4}\right) N_2 \longrightarrow xCO_2 + \frac{y}{2}H_2O + 3.76 \left(x + \frac{y}{4}\right) N_2 \tag{11.1}$$

$$\text{Kerosene:} \quad C_{12}H_{26} + 18.5O_2 + 69.56N_2 \longrightarrow 12CO_2 + 13H_2O + 69.56N_2 \tag{11.2}$$

$$\text{LNG:} \quad CH_4 + 2O_2 + 7.52N_2 \longrightarrow CO_2 + 2H_2O + 7.52N_2 \tag{11.3}$$

Where CO_2 emissions are reduced by 75% by just reducing the amount of fuel burned, finding the NO_x reduction needs another approach. Calculating the exact NO_x emitted is more challenging as it depends on many different parameters, such as temperature, pressure, fuel flow and altitude. In addition, LNG is new to the aviation industry meaning that there are almost no reference aircraft. In order to provide a good estimation, a method for computing aircraft emissions suggested by NASA is used [61]. As this method is based on aircraft using kerosene, a correction factor is applied (reducing NO_x emissions by 60%) [62].

This approach starts with the input of the different fuel flows, during all flight stages. Known values are taken from literature, others are interpolated or estimated based on power setting. With these fuel flows, a fuel flow factor can be found using Eq. 11.4. This is used to find its corresponding Reference Emission Index (REI) needed to compute the NO_x emission per amount of fuel burned. In this equation, δ_{amb} and Θ_{amb} are the ratio of inlet temperature and ambient pressure.

$$W_{ff} = \frac{W_f}{\delta_{amb}} \cdot \Theta_{amb}^{3.8} \cdot e^{0.2M^2} \tag{11.4}$$

After this, the NO_x per kilogram of LNG is calculated with Eq. 11.5, where REI_{NO_x} is the REI coefficient and H depends on the humidity, pressure and temperature of the airflow. Multiplying the outcome of this formula with the fuel flow and duration of the flight phase, the emitted NO_x of every phase can be found. Summing all flight phases yields the total amount of nitrogen oxides emitted.

$$\dot{m}_{NO_x} = REI_{NO_x} \cdot e^H \cdot \left(\frac{\delta_{amb}^{1.02}}{\Theta_{amb}^{3.3}} \right)^{0.5} \tag{11.5}$$

The most critical emission requirement is chosen being the leading one. Based on that, the maximum amount of LNG that can be burnt is found. Subtracting this value from the total required amount of energy gives an indication of the amount of energy that the batteries have to supply.

Based on the power requirement defined above, the total amount of energy required to perform the mission and possible diversions is 34.602 GJ. The CO_2 reduction was found to be most driving design requirement and results in a split of 17.5% energy in batteries, the other 82.5% in LNG. In terms of energy, this means that over 28 GJ is supplied by LNG, and approximately 6 GJ is carried in a battery pack.Implying that the requirement of 75% emission reduction is just met. For NO_x, the EuroFlyer will perform even better than required. When performing the same calculation for the Embraer E170 a reduction of 92% was found for the EuroFlyer.

Batteries

Working from this latter value, the weight of the battery system is computed. For Lithium-air batteries, a (cell) specific energy of 4.86 MJ/kg is determined [63, 64, 65, 66, 67]. Also, it is assumed that the batteries have an efficiency of 95%, which might increase due to the high temperature superconductors the design team is planning to use [68]. To preserve battery performance, the team has chosen to de-charge the batteries to only 63%, reducing the effective specific energy. An interesting complication is formed by the fact that Lithium-air batteries gain weight during de-charge, as the air is drawn from the ambient. This weight increase is already incorporated in the aforementioned specific energy, but for further reference, the weight difference is computed as well.

As indicated above, these values only comprise the battery cells. Although these are the only parts that store energy, various additional components are required to make the system work. These include a battery management system, a casing, and additional subsystems. Based on the current state of the art, where the cells take up 40% of the battery weight [69], it is assumed that by 2035, the split is 50:50 [68]. Hence the mass computed above is doubled to account for this. Combining this with the gravimetric density (assuming this is equal for cells and related components), the volume of the system can be found.

Combining the energy requirement with the effective specific energy of the Lithium-air batteries, the total system mass is found to be 4159 kg, of which 119 kg is air mass that is gained during flight. The total system will require a storage volume of 3.51 m^3.

LNG

In the previous section, the amount of allowable LNG was found, taking in to account the reduction of CO_2 and NO_x compared with the Embraer E170. As this is known, the effective energy gained by LNG can be found as well as the power required from the batteries. Next to that more specific sizing can be done, resulting in detailed weights and volumes of the system which are needed for further iterations.

To compute the effective energy, the total mass of LNG has to be multiplied with its energy density and the efficiency factor, as can be seen in Eq. 11.6. For LNG an energy density of 53.6 MJ/kg is found, where the total efficiency of the system is carefully predicted. Nowadays, efficiencies are around 40%, where the design team sees an increase over the following years and is expect to reach 50% by the year 2035. Using this in the following equation results to the effective energy. The energy required can be found by simply subtracting both values, as shown in Eq. 11.7.

$$E_{LNG} = \dot{m}_{LNG} \cdot u_{LNG} \cdot \eta \tag{11.6}$$

$$E_{batt} = E_{tot} - E_{LNG} \tag{11.7}$$

With this required energy, the batteries are sized, which is explained previously. Here it is also found that the battery mass increases when the battery is discharging. To cope with this effect, part of the LNG will be stored close to the batteries, where the rest will be close to the centre of gravity. This reduces the chance of unwanted gravity shifts during flight. Note that the amount of fuel stored close to the battery will have the same mass as the increase in mass of the battery, thereby keeping the total weight as constant as possible.

During flight, LNG will be stored in fuel tanks which will cool itself. This cooling system will be elaborated later on, but first the amount of volume needed has to be computed. This can easily be done, using the gravimetric density of the fuel, 440 kg/m^3 and adding a safety factor of ten percent. Next to that, the design team found that a spherical tank would be the best solution. Since this shape has the smallest outer area for a given volume, the LNG will experience minimum heat exchange with its surroundings. However, for this reason it is impossible to store fuel in the wings but due to the large fuselage volume, this does not cause any problems. With the shape of the fuel tank and the volume of LNG known, tanks can be sized and focus shifts to the cooling system.

The LNG will be stored at 103 K in an isolated tank, which consists out of two thin layers aluminium separated by a layer of CO_2. Using Eq. 11.8 one can compute the heat transfer of the system [70]. Here k is the thermal conductivity, A the total area, t the thickness, s the time lapse in seconds and ΔT the temperature difference between the fuel and its surroundings. Note that only the layer of CO_2 is considered as isolation, since aluminium can be ignored due to its high thermal conductivity and the small thickness. After that, the thickness of the CO_2 layer is optimised, by looking at the total mass of the tank (increasing for a thicker isolation layer) and the amount of extra fuel needed to cool the system.

$$q = k_{CO_2} \cdot A \cdot \frac{\Delta T}{t} \cdot s \tag{11.8}$$

Just as nitrogen, LNG will be cooled using a similar process. To make this process work, the pressure inside the tank needs to remain constant and the LNG will be stored around its boiling point. Hence it tends to evaporate, once heat is added due to the temperature difference with the surroundings. However, this phase transformation requires a high amount of energy namely 525.48 kJ to evaporate one kilogram of LNG. During the whole flight, a little less than 5 MJ heat was added from the surrounding.
By simply dividing the total amount of heat added by the heating value of the phase change of LNG, as can be seen in Eq. 11.9, the total amount of LNG that will be vaporized can be computed and was found to be 9.5kg. As was stated earlier in the paragraph, the LNG needs to be stored at a constant pressure. This means that the vaporized gas should be removed from the tank, which slightly complicates the system.

$$m_{loss} = \frac{q}{c} \tag{11.9}$$

Even when vaporized, the natural gas is still at a very low temperature. Aiming to reduce emissions, this gas is not simply emitted into the atmosphere. As the mass of the dissipated LNG will be limited [71], the team has calculated that it is possible to store this gas. When the aircraft lands at an airport, the gas can be extracted and be turned into LNG again. However, before the natural gas is stored, it is used to help cooling the high temperature superconducting wiring connecting the battery packs and electric engine. As the natural gas is still at a very low temperature, it is perfectly suitable for this purpose.

As explained above, 28.55 GJ of energy has to be contained in the LNG system. Given the specific energy, this can be translated into a mass of 1248.2 kg, of which 119 kg will be located in the front tank (to compensate the weight increase of the batteries for stability and control reasons) and 1119.7 kg will be stored in a main tank. Clever readers might note that 199 and 1119.7 does not add up to 1248.2. The remaining 9.5 kg is evaporated during flight. The tanks have been optimized to be as light as possible, varying the amount of LNG burnt off and the insulating properties. For the front tank, a gap of 8 cm separates the two tank walls; for the centre tank, this distance increases to 10 cm. In total, the tanks have an inner radius of 41.4 and 87.4 cm and weigh approximately 4.4 and 18.9 kg. If airliners prefer to increase the operational range of their EuroFlyer aircraft without having to reduce the payload weight, larger or extra tanks can be installed. Due to the low weight of these components, the team has chosen not to elaborate on this any further.

11.3 Operations

Especially on short haul flights, turnaround times are crucial to make a profit. The time spent on the ground makes the difference between being able to operate three or four daily flights, and in turn to split costs over - in the EuroFlyer case - 240 or 320 people. In these precious moments, passengers get off and on the aircraft, the

cabin is cleaned, food and drink reserves are filled up and, most important in this chapter, the aircraft's energy sources are replenished. As the EuroFlyer will be powered by a combination of LNG and batteries, this process is a little less straight forward compared to conventional airliners.

Re-fuelling the LNG tanks is not going to raise major difficulties. The largest problem is that the fuel has to remain in its liquid state during the entire process. However, LNG can be used to cool itself (as explained previously), reducing the need for external cooling mechanisms. As also explained above, extra fuel is taken on board to use for this cryogenic cooling process. When aircraft are re-fuelled a long time before their departure, additional boil-off LNG is required. All in all, it is assumed that this process will not take more time than is currently necessary to re-fuel a regional aircraft.

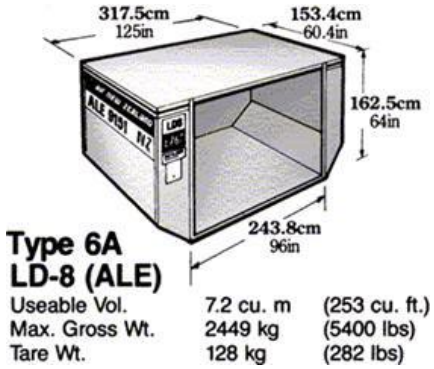

Figure 11.3: Dimensions of LD-8 Unit Load Device [27]

Charging batteries would definitely take longer than the 20 to 60 minutes aircraft are on the ground [72]. As an alternative solution, a strategy is conceived in which batteries are not recharged while in the aircraft, but are simply taken out and replaced by charged ones. To facilitate the unloading and loading of battery packs, these are placed in standard-sized Unit Load Devices (ULD's). These are sized based on the dimensions and weight of the battery system.

As was mentioned earlier, the total volume of the battery pack is a relatively small amount: only 3.51 m^3. The weight is more substantial, at 4160 kg. Given the large volume available in the cargo hold, the weight is considered the driving requirement, as reinforcing other ULD's would result in non-uniformity and higher cost. One model of container is particularly suitable for these requirements: an LD-9 ULD has a usable volume of 10.2 m^2 and a max gross weight of 4624 kg, which includes 220 kg of structural weight for the container itself. Looking at the dimensions leads to the conclusion that the selected container fits in the cargo hold. Loading and unloading might be more difficult, as this would require a cargo door of 162.5 cm high and, more importantly, 317.5 cm wide. Next to that, unloading the whole battery at once causes a large shift in the centre of gravity.

For these reasons, the battery packs will be split up in two separate containers. Two LD-8 containers can be used when both containers carry the same amount of batteries, their dimensions are shown in Fig. 11.3 [27]. Now the door sizes can be reduced to 162.5cm height and 153.4cm width.

11.4 Results

Table 11.2 provides an overview of the values found for the final design of the EuroFlyer.

Table 11.2: Energy Parameters

Parameter	*Value*	*Unit*
Energy Required	34.6	GJ
LNG Mass	1248	kg
% of Energy	82.5	
Battery Mass	4159	kg
% of Energy	17.5	
Container Type	6A LD-8	
Container Mass	128	kg
Total System Mass	5663	kg

CHAPTER 12

Stability and Control

For a non-aerospace engineer, an aircraft's requirement to fly seems to be solely to possess a wing and a tail. However the required precision of the complicated system to operate controls and ensure stability is often forgotten or severely underestimated. This chapter explains the design choices made to provide this essential requirement of the EuroFlyer. It is structured according to the procedure as follows: first the weight estimation is discussed, followed by the loading and tail sizing. Finally, the design of the control surfaces is stipulated.

12.1 Weight Estimation

The first step in ensuring stability and control (S&C) of an aircraft in a conceptual design phase is to perform a precise class II weight estimation. With this estimation an initial centre of gravity location is determined, in addition to its corresponding limits based on the payload loading.

12.1.1 Class II

Before it is possible to perform a class II weight estimation, a class I weight estimation is done based on reference aircraft. By means of a multi-variable linear regression a first estimate of the EuroFlyer operational empty weight (OEW) and MTOW were found to be 27840 and 35000 kg respectively [16]. Implementing those values into a class II weight estimation a precise weight distribution can be determined.

A class II weight estimation is based on a statistical method which estimates system and component weights of the aircraft. There are several published methods which can be chosen. In the design process of the EuroFlyer, a method provided by Raymer [34] was employed. As the equations are based on statistical analysis, other weight estimations will be required for novel implementations. These new estimations are addressed in the corresponding chapters and sections. Once all the weights have been determined a new MTOW is found and inputted into the estimation. This iterative process is repeated until the input MTOW is equal to the output MTOW. This is done in parallel to updating the wing size by determining a new wing surface based on the wing loading. This iteration is part of the larger iteration discussed in Chapter 13.

12.1.2 Loading Diagrams

In addition to sizing the weight of all systems and components, they are located as well. Furthermore the passenger, or payload, positions will be defined. The systems are placed by sizing them and allocating space available under the fuselage. Likewise the passengers are located according to the seating configuration as presented in Chapter 8. As the EuroFlyer has an unconventionally high engine weight at the aft of the aircraft, it is important that this weight is sufficiently counteracted to result in a more distributed load. Fortunately batteries and other systems can be placed more forward in the aircraft. Once the centre of gravity locations and weights are known, loading diagrams can be constructed. A detailed overview of all the centre of gravity locations is presented in Table 12.1.

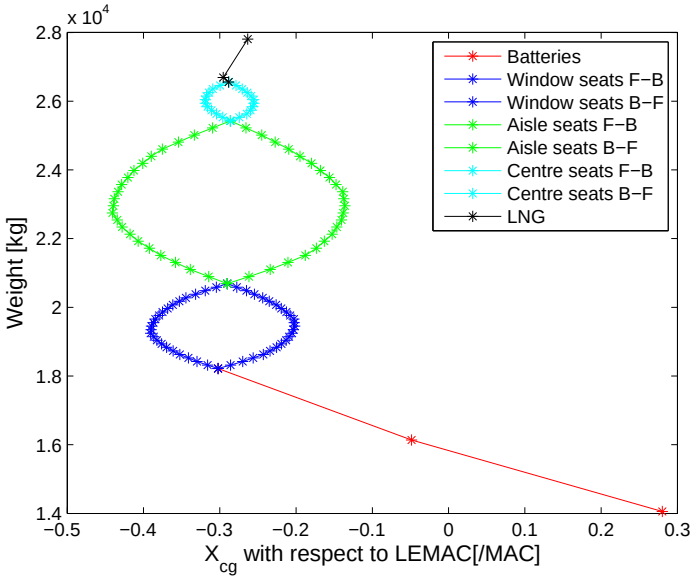

Figure 12.1: Loading Diagram

Loading diagrams plot the shift in centre of gravity as the aircraft is loaded. The following loading procedure was adopted for the EuroFlyer. First the batteries are replaced by loaded units, one-by-one, next the passengers are loaded and lastly the Liquefied Natural Gas is refuelled. This order was chosen as the switch in batteries is an important procedure where it is undesirable to have passengers boarding at the same time as it could make the area slightly hectic elevating chances of human error. The batteries are switched one-by-one, however if necessary both can be removed without tip over occurring. Tanking and boarding of passengers happen simultaneously in reality, however for ease of computation passengers are boarded first. This order is beneficial for the temperature at which LNG needs to be stored. The boarding procedure of passengers is assessed in two directions, namely front-to-back and back-to-front. Passengers are divided into 3 groups, window seats, aisle seats and centre seats, which are boarded accordingly. The loading diagrams are presented in Fig. 12.1. From these, the extreme load cases for the stationary and flight case can be determined, -44% to -6% and -44% to -14% respectively. These load cases are expressed with respect to the leading edge of the mean aerodynamic chord as percentage of the mean aerodynamic chord.

12.2 Tail

To provide stable and controllable flight an aircraft needs to be able to counteract all forces and moments in every extreme load case. The most efficient way to do this is by using a tail. Therefore it is essential that in a conceptual design phase it can be proven that the tail necessary to render an aircraft stable and controllable is feasible. This section addresses the tail configuration, and horizontal- and vertical tail sizing.

12.2.1 Configuration

With the eccentric propulsive design of the EuroFlyer, the tail configuration has great impact on performance. In the trade-off process explained in Chapter 7, a conventional tail with a bottom strut to protect the propeller from ground strikes was chosen. Although other more unconventional tails might provide some additional benefits in performance, the structural complexity and unpredictability of those concepts drove the EuroFlyer to the current configuration. Nevertheless, to minimize performance losses some alterations need to be made.

The most affected aspect by the tail configuration in the EuroFlyer is noise. As a propeller will be rotating at high speeds closely behind the tail, sudden pressure differences occur as the propeller hits through the wake of the tail. One way to notably diminish these sound levels is by making the striking angle between the prop and tail surface differ from 0 degrees as much as possible. Implementing this idea, the horizontal tail surface was lowered to the bottom of the fuselage at that location.

However this solution only solves half of the problem as the vertical tail and bottom strut are still producing a wake parallel to the propeller blades. Decentralizing these would produce an uneven loading with respect to roll and would destabilize the system. To solve this complication the EuroFlyer implements the technique of

blowing. Blowing consists of filling the wake with energized or propelled bleed air from an engine compressor by means of a slit near the trailing edge. Studies have shown that the most efficient noise reduction occurs by filling approximately 60% of the wake [73]. To estimate how much mass flow needs to be energized, the wake area is approximated by computing the boundary layer thickness. When estimating the wake area, only the boundary layer where the velocity is reduced to less than 95% of the free stream velocity was taken into account. Eq. 12.1 was applied to calculate the total boundary layer thickness after which the boundary layer profile was modelled with the approximation also used for propulsion. The resulting bleed air mass flow required is 0.28 kg/s. This value was taken into account when sizing the engines and inlet.

$$\delta = \frac{0.37x}{Re_c^{1/5}} \tag{12.1}$$

12.2.2 Horizontal Tail

Consequently to determining the ultimate load cases, the horizontal tail can be sized to provide sufficient control and stability in these extreme scenarios. The first step in this process is the generation of a stability and control plot which can be seen in Fig. 12.2. The plotted functions for stability and control are derived from the stable flight situation. This derivation results in two equations, Eqs. 12.3.The first is for stability and the latter for controllability. The coefficients in these equations were computed using the method presented in the Systems Engineering & Aerospace Design course at the Aerospace Faculty of the TU Delft [74]. In computing these coefficients a first estimation of the horizontal tail surface is made based on reference aircraft. This estimation is then adjusted to the value which is obtained from the plot. This value is deduced by finding the minimum horizontal tail surface for which the centre of gravity range is within the stable and controllable range. This range is the area to the left of the stability line and to the right of the controllability line (see plot Fig. 12.2).

The horizontal surface is iterated until the optimum is achieved. In this process a couple design choices had to be fixed. A taper ratio of 0.4 was chosen. This low taper ratio has induced drag benefits and is still large enough to provide and support sufficient lift without complicated structural designs. An aspect ratio of 6.63 is chosen which is slightly higher than current aircraft but relative to the main wing aspect ratio is a realistic value [75]. Furthermore a lift coefficient of -0.6 was chosen. For simplified analysis a symmetric profile was selected, the NACA 0012. The iteration resulted in a surface area of 9.97 m^2 and a wingspan of 8.13 m. Including the fuselage diameter at this location this turned out to be 9.63 m.

$$x_{cg} = x_{ac} + \frac{C_{L_{ah}}}{C_{L_\alpha}}\left(1 - \frac{d\varepsilon}{d\alpha}\right)\frac{S_h l_h}{S\bar{c}}\left(\frac{V_h}{V}\right)^2 \tag{12.2}$$

$$C_m = C_{m_{ac}} + C_{L_{A-h}}\left(\frac{x_{cg} - x_{ac}}{\bar{c}}\right) - \frac{C_{L_h} S_h l_h}{S\bar{c}}\left(\frac{V_h}{V}\right)^2 \tag{12.3}$$

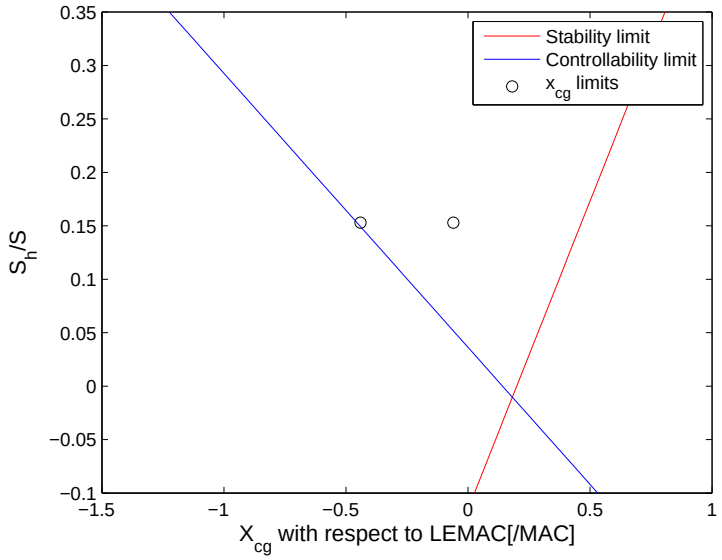

Figure 12.2: Stability and Control Limits

12.2.3 Vertical Tail

Conventionally the vertical tail is designed to counteract the engine out yawing moment. However in the case of the EuroFlyer, the propulsive system cannot produce a yawing moment and the shroud will also conteract yawing motions effectively. Resulting in the fact that the vertical tail can be designed significantly smaller. The propulsive system does however induce a rolling moment in case of one engine failure. This moment can however be counteracted efficiently by the wings and ailerons. The driving requirement is then to ensure that the tail in combination with the rudder can provide the necessary controllability to turn the aircraft. As a first assumption vertical tail volume coefficients were assessed and a value of 0.03 was chosen. This is a common value for single prop driven aircraft [74]. The height was chosen based on reference aircraft to be 4.07 m; including the fuselage the total height is equal to 4.82 m. Identical to the horizontal tail a taper ratio of 0.4 was chosen. The resulting surface is 9.37 m^2.

12.3 Control Surfaces

Now that the tail has been designed, control surfaces need to be sized. This section discusses the sizing of the rudder, ailerons and elevators to ensure the EuroFlyer's compliance with manoeuver regulations.

12.3.1 Rudder

A standard turn rate for light aircraft is defined as three degrees per second or 180 degrees in a minute. To size the rudder the assumption is made that without banking this turn rate can be achieved. This is simulated with a horizontal force exerted by the rudder, making the aircraft turn. This turn rate is necessary at loiter altitude, defined as 1500 m. Computing the necessary force, the vertical tail needs to produce, a lift coefficient of 0.237 is established. To obtain this value a rudder with a deflection of ten degrees is implemented which results in a lift coefficient of 0.6 over the affected area. From these values it is deducted that the rudder needs to affect 39.6% of the area. This should be feasible without affecting the area in front of the propeller. If this is not the case then the vertical tail has to be resized or redesigned until this is possible. The mentioned values satisfy this requirement.

12.3.2 Ailerons

In order to define the size of the ailerons, the time required to obtain a certain bank angle has to be determined. Since the MTOW of the aircraft is 27840 kg, the aircraft is categorised as a class II [76]. Also, since the aircraft is a passenger transport aircraft the acceptability is level 1 [76]. A class II level 1 aircraft should take maximum 1.8 seconds to achieve a bank angle of 30 deg.

The time required to reach a bank angle of 30 deg can be calculated using Eq. 12.4. In this equation $\dot{P}$ is the time rate of change of the roll rate.

$$t_2 = \sqrt{\frac{2\Phi_{des}}{\dot{P}}} \tag{12.4}$$

$\dot{P}$ can be calculated using Eq. 12.5, where it can be seen that the time rate of change is an equation of the roll rate against the reached bank angle.

$$\dot{P} = \frac{P_{ss}^2}{2\Phi_1} \tag{12.5}$$

When working out the equations, the ailerons are sized at a surface of 3.1 m^2. With this surface, the time required to reach a bank angle of 30 deg is 1.74 s, which is lower than the maximum of 1.8 s.

12.3.3 Elevators

From the stability and control plot it can be observed that only during manoeuvres the lift coefficient of -0.6 is necessary. To increase the critical Mach number above cruise Mach number the horizontal tail was set at an angle of -2.5 degrees and a leading edge sweep of 35 degrees was applied. This sweep is also beneficial for control as the arm of the horizontal stabilizer with respect to the centre of gravity is larger. To obtain the lift coefficient needed during manoeuvres, elevators are added to the horizontal tail. These elevators are sized to deflect 12 degrees and start at 80% of the chord to obtain a lift coefficient of -0.968 over the area affected. This concluded that the area the elevators needed to affect was 46.3% of the horizontal tail surface.

In Fig. 12.3 a render of the entire tail configuration including control surfaces is depicted.

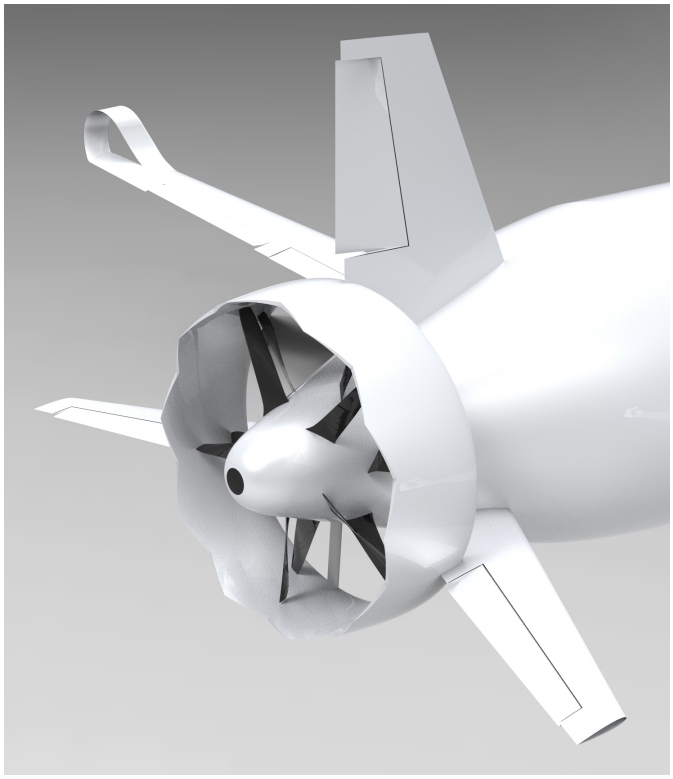

Figure 12.3: Artist Impression of the Integrated Tail with Control Surfaces

Table 12.1: Centre of Gravity Locations

System	*c.g. Location w.r.t. Nose [m]*	*Mass [kg]*
Instruments	1	186
Nose Landing Gear	2	257
Avionics	2.5	903
Crew Weight	3.5	515
Electrical	5	464
Battery Weight	5	4160
Fuel Weight Front	6	129
Payload	9	8137
Furnishings	9	1619
Anti-Ice	9.5	29
Fuselage	10	2937
Wing	10.5	2700
Fuel Weight Middle	10.5	1120
Flight Controls	10.5	345
Horizontal Tail	18.5	196
Vertical Tail	18.5	194
Main Landing Gear	11.8	993
Hydraulics	11.8	113
Fuel System	14	126
Engine Group	15	1148
Engine Controls	16	27
Starter	16	38
APU	16	924
Handling Gear	18	4
Air Conditioning	19	276
Shroud	19	200

CHAPTER 13

Subsystem Integration & Optimisation

In Chapter 9 to 11, the design methodology of the fuselage, wing, power train and energy system has been described. Once these individual subsystems have been decomposed into components and elements and each of these has been sized according to the specified requirements, the various subsystems will be integrated in the synthesis phase. Due to the complexity of the overall system, the many relationships that exist between the different elements force the design team to use an iterative approach before the final design can be obtained. This process is known to be very time consuming, but it allows the design team to optimise the overall system performance. This chapter discusses the various steps taken in the subsystem integration and optimisation, including the establishment of the N^2 chart and the definition of the parameters to be optimised. Finally, the results of the iterative process are discussed.

13.1 Interface Definition

In order to simplify the iterative process and the optimisation of each individual subsystem, an N^2 chart is established. Such a chart is a tool to visualise a system's subsystems and which information is exchanged between these. One can also refer to this as interface definition, as an N^2 chart indicates the borders of various subsystems and their relations. It is a square matrix which has all the subsystems on the diagonal and the interaction between them in the other cells, where outputs are horizontal and inputs are vertical. It is of crucial importance to perform this interface definition before the start of the trade-off, as it clearly indicates the relationships and interdependencies of various subsystems. In Fig. 13.1, an N^2 chart is depicted showing the iterations done in this preliminary design phase. In order to use the available resources as efficiently as possible, there is opted to initially only consider the first four elements on the diagonal, being Weight Estimation, Aerodynamics, Propulsion System and Energy. After this first loop has been completed, the controllability and stability of the EuroFlyer will be evaluated. Eventually, the complete iterative process will be run once again to verify the obtained result.

13.2 Subsystem Optimisation

Before the actual iterative process can be started, one needs to define which parameters have to be optimised. One of the most important parameters which has not been specified in the mission definition is the cruise altitude, as every individual subsystem is directly influenced by the local atmospheric conditions. In addition, the wing aspect ratio is a parameter which the design team can make use of in order to increase the aircraft performance. Therefore, it can be understood that the first step in the iterative process consists of determining the cruise altitude and aspect ratio. In order to be fully aware of the effect of varying these parameters for a fixed MTOW, one could opt for a qualitative analysis of the lift over drag ratio. This is often used as a measure of the aerodynamic efficiency of an aircraft and is therefore a good parameter to optimise. Secondly, given the fact that the amount of LNG for the EuroFlyer is limited and that all the remaining energy needs to be carried in Lithium-air batteries, the shaft power required is preferably minimised. Fig. 13.2a and 13.2b depict the variation of lift over drag ratio and shaft power required with altitude respectively. One can observe that both higher altitudes and aspect ratios are beneficial to reduce the energy system mass and increase the overall aerodynamic efficiency.

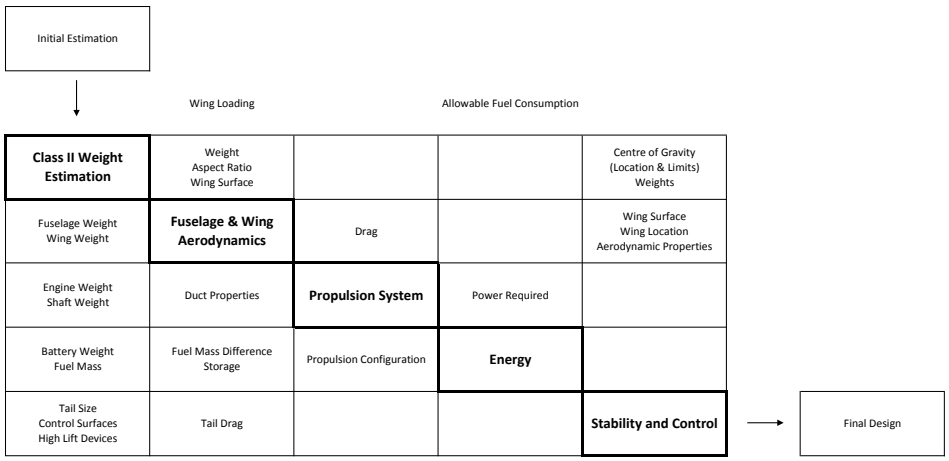

Figure 13.1: Interface Definition for the Iterative Process

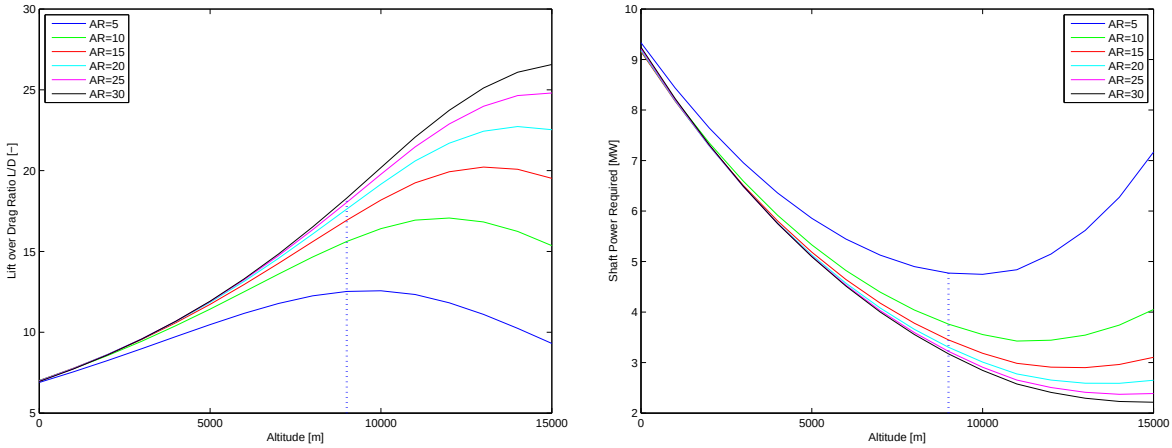

(a) Lift over Drag Ratio

(b) Shaft Power Required

Figure 13.2: L/D and Shaft Power Required as a Function of Altitude and Aspect Ratio

One must take into account however that due to the use of propellers, the aircraft cruise altitude is limited by the propeller performance at elevated altitude [77]. After a preliminary investigation on the feasibility of the propeller blade design and decrease in propulsive efficiency, the design team opted to set the cruise altitude at 9000 m. Figure 13.2a reveals that in order to have the cruise speed located right in the middle of the drag bucket, an aspect ratio of less than 5 would be required. For the same cruise altitude however, a higher aspect ratio not only increases the lift over drag ratio but also reduces the power required significantly. It is important to note that the benefit from increasing the aspect ratio diminishes the higher this property becomes, as the lift over drag ratio and power required only marginally reduce between 20 and 30 at the chosen cruise altitude.

Nevertheless, this decrease in power required might still considerably reduce the overall energy system mass. On the other hand, other parameters such as the wing mass are known to increase with increasing aspect ratio, due to the higher force and moment distributions along the span [43]. In order to provide the design team more insight into this matter, a plot as shown in Fig. 13.3 can be established. The aspect ratio of current (civil) aircraft is determined by the intersection of the wing and fuel mass, as the fuel reduces with increasing aspect ratio while the wing mass increases [43]. For the hybrid energy system of the EuroFlyer however, the energy system and wing mass curves intersect at an aspect ratio of 31, which is considerably higher than what is currently used for commercial aircraft. Figure 13.3 reveals however that the minimal total mass can be achieved by selecting an aspect ratio of 27. Still, the feasibility of such high aspect ratio for commercial flight is doubtable, given the fact that struts or any other additional load carrying members are undesirable. As the requirement stipulating that the EuroFlyer should be able to operate at regional airports limits the wingspan to 36 m, the design team opted to set this maximum wingspan in order to maximize the aspect ratio [41]. By doing so, with the given wing loading of 4190 N/m^2 the aspect ratio will be the highest achievable one for a specific MTOW.

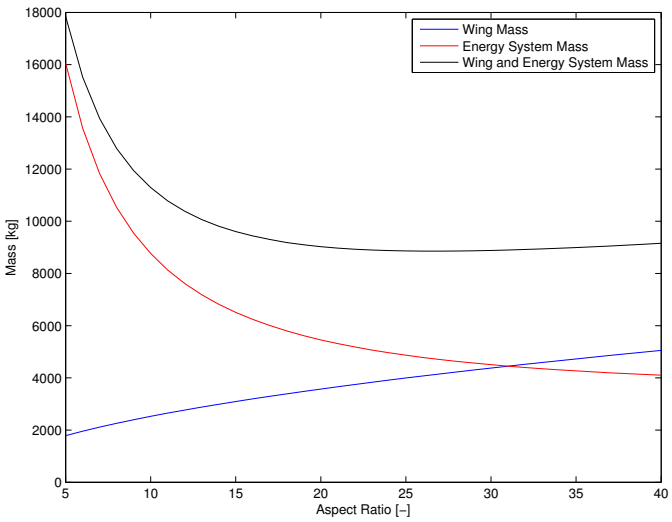

Figure 13.3: Variation of Wing and Energy System Mass with Varying Aspect Ratio

13.3 Results

Once the parameters to be optimised are defined, the iterative process can be started. As discussed before, the cruise altitude in this iteration will be fixed at 9000 *m* due to diminishing propeller performance and increasing sensitivity of the atmospheric layers at more elevated altitudes. Furthermore, the wingspan is set to a value of 36 *m* in order to be able to operate at regional airports. The N^2 chart, as shown in Fig. 13.1, summarizes the iterative process and shows which variables are being varied in every loop. The final iteration required 32 iterations before convergence was reached. The final values are listed in Table 13.1. As can be observed, the obtained aspect ratio of 19.88 does not equal the optimal aspect ratio of 27. However, despite this offset, the lower aspect ratio only results in a 2% increase in the combined mass of the wing and energy system. In order to validate the obtained values and thus enhance the credibility of the proposed design, these were compared to reference aircraft such as the ATR 72-500. As an offset in MTOW of just 23.7% has been calculated, the obtained values enjoy the full confidence of the design team.

Table 13.1: Iteration Results

Parameter	*Value*	*Unit*
Maximum Take-Off Weight	27840	*kg*
Battery Mass	4160	*kg*
Total Drag Force	16704	*N*
Shaft Power Required	3.3	*MW*
Aspect Ratio	19.88	–

CHAPTER 14

Noise

This chapter provides an overview of the noise emissions during various operations of the EuroFlyer. First, a brief literary review on the theory of airframe and propulsive system noise is provided. Due to the fact that the prediction and modelling of aircraft noise is extremely difficult, an estimation of the aircraft noise emissions is made by means of noise predicting software of the Engineering Sciences Data Unit (ESDU). Then it is verified whether these predictions will meet the requirements regarding noise emissions of the EuroFlyer. Finally, an overview of implementable noise reduction methods and systems are given.

14.1 Introduction to Aircraft Noise

A sound wave can be modelled as changes in air pressure; therefore, the wave carries a certain amount of energy with it in the direction of propagation. Sound waves are created at a source and will propagate through a medium until observed by the final observer. For an aircraft, the main sources of noise originate from the airframe and the propulsive system. The scale most often used for aircraft noise measurement is the Effective Perceived Noise Level (EPNL) scale. It involves a correction factor that adds to the Perceived Noise Level (PNL) when there are discrete tones in the noise spectrum. The EPNL accounts for duration and presence of discrete frequency tones. It also includes a correction obtained by integrating the PNL over a 10 second time interval. The fact that peoples' perception of noise varies logarithmically with sound intensity is also a reason why noise reduction is a challenge. According to requirements 4.3.1-4.3.3, the noise levels have to be reduced by around 10 dB, relative to ICAO Chapter 4 noise limit regulations. This implies that the sound intensity has to be reduced by approximately 90% [78].

As stated earlier, the main sources of aircraft noise are the airframe and the propulsive system. Airframe noise is caused by airflow over aircraft surfaces. The noise level emitted by the airframe is dependent on the aircraft configuration. In aerodynamically clean configurations, less noise is emitted when compared to landing or take-off configurations. The components responsible for the airframe noise can be split up into five main contributors [78, 79] which are listed below:

- Trailing-edge noise
  In a clean configuration, the main source of the noise due to the presence of the wing is the noise generated at the trailing edge. A trailing-edge in a fluctuating flow field generates an unsteady vortical wake.
- Slats/flap coves
  Recirculating flow behind the leading-edge causes a turbulent bubble to form in the cove of the slat, generating sound of a broadband nature. A similar phenomenon occurs in the cove of the flap.
- Flap side-edge noise
  The noise induced by the flaps is a large contributor to the landing and take-off noise. The noise is caused by the pressure jump across the upper and lower surfaces of the flap, this in term creates a recirculating flow around the side edge. The shear layer of this flow detaches at the side of the flap and rolls up to a single vortical structure.
- Main- and nose landing gear
  A vortex force is generated behind the landing gear due to unsteady flow separation caused by the different

structural components. Because of the unfavourable placing of the landing gear, the vertically radiated noise has to be scaled as part of the noise is reflected downward by the airframe panels. Therefore, the landing gear has a large contribution to airframe noise.

- Horizontal- and vertical tail surfaces
  The noise generation of the tail is similar to that of the leading edge of the wing; the main noise source of the tail is already listed above.

Most of the fluctuating lift and drag generating components, which generate aircraft noise, are associated with the contributions listed above. Here, it may be noted that despite the fact that the fuselage does produce some lift, it is not adopted in the list of main sources of noise production. This is due to the fact that the noise of the fuselage may be considered negligible at a measurement point in the far downstream. In addition, to reduce the noise of the EuroFlyer no slats are installed, reducing that noise component to zero.

The air induced by the propeller of the EuroFlyer will be of turbulent nature due to effects as atmospheric turbulence, the ingestion of the boundary layer and the vertical- and horizontal tail that are located in front of the propellers. The blades then experience fluctuating forces which in turn produce fluctuating levels of discrete frequency and broad-band noise. Aerodynamically induced noise from an aircraft using a propeller as propulsive system may be split up into two main components. First there is discrete frequency component, which occurs at a fixed frequency interval, the rotational noise. Then there is a broad-band component, the vortex noise [80, 81]. Dependent on the frequency region either one of the noise sources is dominant, rotational noise is usually dominant at low frequency and vortex noise at higher frequencies. The rotational noise is the main contributor to the fluctuating levels of discrete frequency and broad-band noise mentioned earlier. The phenomenon of blade slap is also categorised as rotational noise. Blade slap originates from the interaction between the propeller blades and a concentrated vortex created by the preceding blade and interruptions in free stream air prior to meeting the propeller blade. The last source of blade slap will be neglected for the noise predictions made later.

14.2 ICAO Chapter 4

One of the key requirements set for the EuroFlyer is related to the noise emission. The requirement states that the EuroFlyer shall reduce its noise emission by 10 dB according to the standards defined in ICAO Chapter 4. Therefore, before the noise emissions of the EuroFlyer are modelled, first the noise limits will be specified.

The noise limits are set at three specific locations named the Lateral measurement point, the Fly-Over measurement point and the Approach measurement point. These three points are visualised in Fig. 14.1. The Lateral measurement point is defined as the point on a line parallel to and 450 m from the runway centre line, where the noise level is maximum during take-off, Fig. 14.1a. The Fly-over measurement point is the point on the extended centre line of the runway and at a distance of 6500 m from the start of roll, Fig. 14.1b. Finally, the approach reference noise measurement point is the point on the extended centre line of the runway which is 2000 m from the threshold. This corresponds to a position 120 m vertically below the 3° descent path originating from a point 300 m beyond the threshold [82]. The limits of noise emission at these points are defined as: 94 dB for the Lateral measurement point, 89 dB for the Fly-Over measurement point and 98 dB for the Approach measurement point. For the EuroFlyer, these limits are approximately 84 dB, 79 dB and 88 dB, respectively. In addition, the following rules also have to be fulfilled in order to meet the ICAO Chapter 4 requirements.

- The maximum permitted noise levels shall not be exceeded at any of the measurement points
- The sum of the differences, the cumulative margin, at all three measurement points between the maximum noise levels and the previously set maximum noise levels shall not be less than 10 $EPNdB$;
- The sum of the differences at any two measurement points between the respective maximum noise levels and the previously mentioned maximum noise levels shall not be less than 2 $EPNdB$.

Whether the EuroFlyer complies with these requirements is computed in the next section.

14.3 Model

The program used to model the noise emissions of the EuroFlyer is based on the ESDU Royal Aeronautical Society airframe- and propeller noise prediction software. For both software packs it is necessary to enter geometrical and performance related parameters of the aircraft.

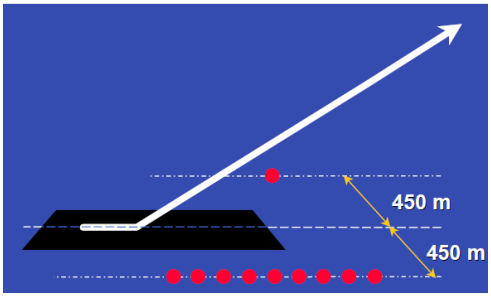

(a) Lateral Measurement Point

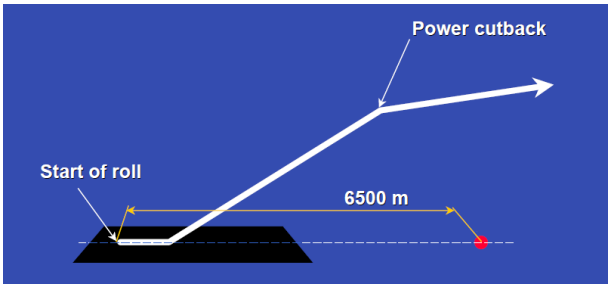

(b) Fly-Over Measurement Point

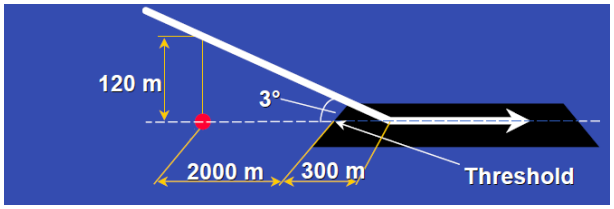

(c) Approach Measurement Point

Figure 14.1: Visualisation of the ICAO Chapter 4 Noise Measurement Points, the Red Dots indicating the Measurement Points

In order to estimate the airframe noise, the ESDUpac A9023 and B9023 software packages are used [79]. The prediction method used by this software is semi-empirical and follows the procedure proposed by Fink [83] with changes to directivity and spectral functions based on recent data. Each airframe component has its own directivity function, $D(\phi_f, \theta)$), and spectrum function, $F(Sr)$. Also, the motion of the source is accounted for by the Doppler frequency factor, $(1 - M\cos\theta)$, and source amplification factor $(1 - M\cos\theta)^4$. These predictions do not account for atmospheric attenuation, ground reflection and lateral attenuation [79]. After giving the input of the aircraft geometry and operating conditions, the program returns the noise generation predictions of the airframe components listed earlier in this chapter. By means of validation, the accuracy of the software is determined to be within 3 dB at maximum.

The prediction of the propulsive system induced noise is performed with the ESDUpac A1105, B1105, MB1105 and MG1105 software [80]. These predictions are based on the propeller noise emissions methods developed by Hanson & Parzych [81]. The program computes monopole and dipole noise for propellers. Here reflections from surfaces and ground vortex effects caused by proximity of the ground to the propeller are not taken into account as their influence is negligible. For the propulsive system, the source frequency is also modified by the Doppler effect to the received frequency. Contrary to the airframe noise, this program also copes with atmospheric conditions with zero wind. An accuracy of ± 2.5 dB at maximum is claimed to be achieved, based on validation.

To combine the results of both the airframe and propulsive system, Eq. 14.1 is used to calculate the total noise emission.

$$Noise_{total} = 10 \cdot \log_{10}\left(10^{A_{noise}/10} + 10^{P_{noise}/10}\right) \tag{14.1}$$

In Eq. 14.1, A_{noise} is the airframe induced noise and P_{noise} is the noise generated by the propulsive system. When combining these two noise sources through Eq. 14.1, the total aircraft noise is found. Here it is assumed that the two sources, the airframe and the propulsive systems, radiate independently from one another and that the noise caused by the interactions between the two sources is negligible. The shroud of the EuroFlyer is not taken into account because of limitations of the software packages and due to the fact that experimental results of [84] show that the shroud does not affect the noise at measurement points significantly. Specifically, in this paper the Fly-Over measurement point was investigated. This can be explained by the fact that lower frequencies are much harder to damp than higher frequencies. When looking at the 5-bladed propeller rotating at 700 RPM, a simple hand calculation shows a main frequency band of 58.3 Hz and wavelength of 5.8 m. Therefore it is assumed that the noise damping effects of the shroud are negligible.
In the next three paragraphs, the results of the computations are given and evaluated.

14.3.1 Lateral Measurement Point

The lateral noise is measured just after take-off, at the moment of maximum engine power settings. Here, the maximum engine power setting is set at the screen height of 35 ft or 10.7 m. In addition, the landing gear is already retracted, the flaps are extended and the flight velocity has been determined to be 55.76 m/s. The resulting noise pattern is given in Fig. 14.2.

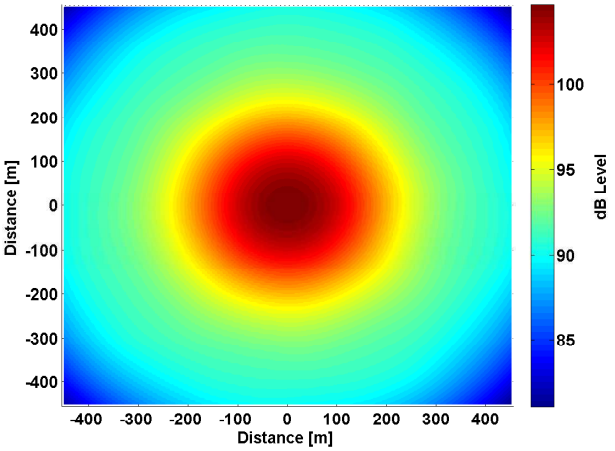

(a) Frontal View of the Lateral Continuous Sound Intensity Level Pattern

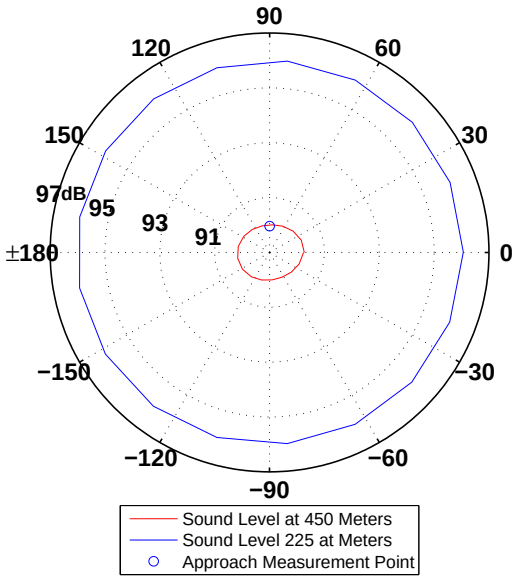

(b) Lateral Discrete Sound Intensity Level

Figure 14.2: Visualisation of the Noise Emissions of the EuroFlyer during Take-Off. In both Graphs the Sound Intensity Level is plotted against the distance to the Aircraft.

As can be seen in Fig. 14.2a, the noise radiation pattern is very circular. This can be explained by the fact that during take-off, the engine noise is dominant over the airframe noise. The airframe noise is also significantly reduced because the landing gear is retracted and the EuroFlyer does not have slats installed on the wings. As stated earlier, slats are a large part of the airframe noise in conventional aircraft. From Fig. 14.2b the sound level at the measurement point can be concluded to be 90 dB which is 6 dB more than the requirement of 84 dB. This implies that noise reduction techniques have to be implemented in order to reduce the noise during take-off.

14.3.2 Fly-Over Measurement Point

After take-off, the fly-over noise is measured. Here the aircraft is still climbing, but at a lower engine power setting. The noise is measured at a distance of 1167 m from the aircraft, this is the theoretically obtained altitude by subtracting the take-off distance from the 6500 m measurement point distance, and multiplying the result with the vertical speed over the horizontal speed ratio. The resulting plots are given in Fig. 14.3.

Here, the EuroFlyer is emitting a small amount of noise: 77.2 dB which is 1.8 dB under the required 79 dB. This is mainly the result of the high climbing performances combined with a short take-off distance of the EuroFlyer. Therefore, the distance between the measurement point and the EuroFlyer is much larger when compared to conventional aircraft. According to the pattern given in Fig. 14.3a, the propeller noise is still dominant over the airframe noise. However, the margin between these two sources is smaller when compared to the take-off measurement point from Fig. 14.2a. This is expected since the power setting of the engine has been lowered.

14.3.3 Approach Measurement Point

During approach, the situation becomes different from the previously treated measurement points. The landing gear is deployed and the flaps are at full deflection. The aircraft is flying at 52 m/s with a low engine setting. For the final measurement point, the resulting plots are given in Fig. 14.4.

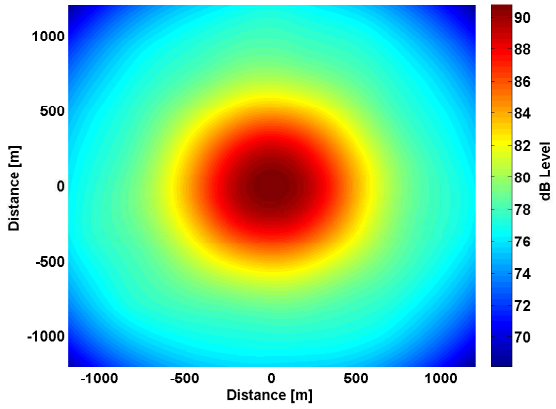

(a) Frontal View of the Fly-Over Continuous Sound Intensity Level Pattern

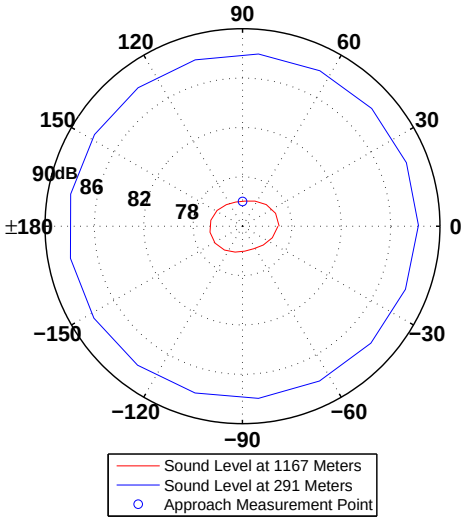

(b) Fly-Over Discrete Sound Intensity Level

Figure 14.3: Visualisation of the Noise Emissions of the EuroFlyer during Fly-over. In both Graphs the Sound Intensity Level is plotted against the Distance to the Aircraft.

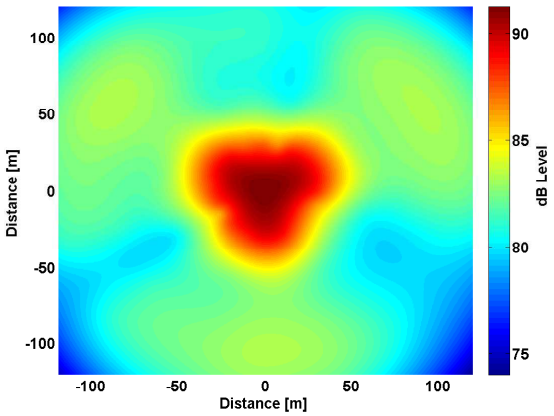

(a) Frontal View of the Approach Continuous Sound Intensity Level Pattern

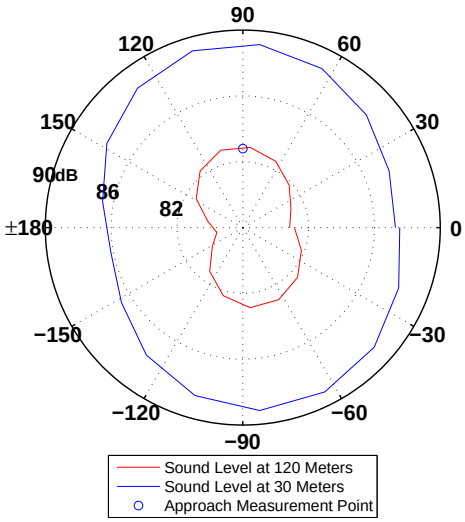

(b) Approach Discrete Sound Intensity Level

Figure 14.4: Visualisation of the Noise Emissions of the EuroFlyer during Approach. In both Graphs the Sound Intensity Level is plotted against the Distance to the Aircraft.

In Fig. 14.4a, the landing gear can easily be distinguished as the lower peak at the bottom of the aircraft. Also, the wings and even the tail are made out of this noise pattern. The more distinct recognition can be reasoned by the airframe noise being the dominant source of the aircraft. Because of the clean wing configuration, no engines and no slats, the aircraft is only emitting 83 *dB*, 5 *dB* under the maximum of allowable emission of 88 *dB*.

14.4 Noise Reduction Techniques

The previous paragraphs showed the noise emissions of the EuroFlyer at the three relevant measurement points. Two of these measurement points do meet the ICAO Chapter 4 criteria because of the clean configuration, short take-off distance and good climbing performances. From the measurement point figures, the propulsive system of the EuroFlyer may be regarded as largest contributor of the total aircraft noise. Implementing methods to reduce the propeller noise emissions will thus have the greatest effect on the overall noise profile. In this paragraph an attempt will be made to predict the effects on noise emissions by implementing various promising noise reduction techniques to both the airframe and propulsive system.

14.4.1 Airframe

Starting off with the trailing-edge noise. Currently the trailing-edge produces at maximum 88.8 dB at 30 m during Approach. A promising method to reduce this number is based on theoretical work in aeroacoustics by Fink et al. from 1980 [85]. With this method, the airframe trailing edges are acoustically treated by deploying brushes to reduce the aerofoil self-noise. By means of experiments on a scale model, a noise reduction of 4 dB was demonstrated [86]. Other researches achieve a noise reduction in the order of 2 to 10 dB [87].

The decision of not installing flaps on the leading edge already has a significant influence on the total airframe noise. The EuroFlyer does utilise flaps, resulting in the generation of flap cove noise. Since the noise generating turbulence originates from the vortex captured in the flap cove, a streamlined cove-cover provides a solution to reducing the turbulence in this area by preventing the vorticity to penetrate into the slot flow. With this cover, a broadband noise reduction of up to 5 dB has been experimentally shown [88].

Flap side-edge noise can be reduced by implementing side-edge fences. A flap side-edge fence is a simple device attached to the side surface of the flaps. By making sure that the fence protrudes into the flow on the lower side of the flap, the local flow structure is altered whilst it is made sure that the overall lift characteristics of the flap are not affected. By altering the flow structure, a downward shift of the dominant frequency of the peaks is forced [89]. For noise induced exclusively by flap side-edge, a reduction of around 4 to 5 dB can be achieved [88, 89].

In Figs. 14.2a, 14.3a and 14.4a, the landing gear can easily be identified from its high levels of noise emission. The landing gear emits such high noise levels because it is a complex 3-dimensional cluster of noise sources: vortex shedding off struts, wake-flow interaction between components and shear layer interaction with downstream bay rim [90]. Designing a low noise emitting landing gear configuration can thus evoke great improvements. Much research has been done in this field, and the landing gear fairings are becoming more adequate. By means of CFD and full scale mock-up wind tunnel testing, results within 5 to 7 dB decrease have been realised [85].

The sound pressure level of the airframe noise sources scale with $1/r^2$ and u^n. In these relations r is the distance between the source and the observer, u is the approach velocity and the exponent n is a factor dependent on where the corresponding sound wave stems from [86]. These relations imply that when flying at lower speeds near the measurement points, the noise level at the observer is lower. In addition, the noise may be reduced by landing further into the runway to keep the aircraft at a higher altitude when crossing the airport perimeter. As both methods depend on the approach speed of the aircraft, reducing the approach speed will reduce the noise emissions exponentially. This noise reduction method is applicable to all sources of airframe noise.

14.4.2 Propulsive System

In addition to reducing the airframe noise, several improvements may be implemented in the propulsive system in order to reduce the propulsive system noise. Since the propeller is the main source of the noise emitted by the propulsive system, this paragraph will be focused on techniques to reduce the propeller noise.

One of the most determining factors in the propeller noise is the tip Mach number [91]. Reducing the tip Mach number leads to significantly reduced propeller noise emission. The tip Mach number can be lowered in various of ways. The method with least impact for reducing the noise is by means of introducing a single or double sweep of the propeller blade. The blade may be swept away from the free stream velocity or from the rotational velocity part. Measurements showed that with a rather extreme sweep of 52°, a noise reduction of 5.2 dB at Fly-Over can be achieved [92].

The propeller blade spacing affects the frequency distribution of the propeller rotational noise components. For a multi-bladed propeller, the noise can be described to be generated by summation of the sound pressure signal of each individual blade. According to [93], in the case of asymmetrically space blades, identical waveforms interfere as a function of their displacement in phase and thus their geometrical location. This will lead to an altered propeller noise radiation in the spectral content and directivity. By means of experiments and the theory previously described, a noise reduction of 3 dB was achieved [92, 93], with a similar tip Mach number compared to the EuroFlyer.

Finally, another method to reduce the propeller induced noise emission which do not require a complete redesign of the propulsive system is adding serrations to the leading edge. Serrations in the trailing edge of the propeller blade mitigate noise, since they extend the presence of a more varied range of turbulence length scales, reducing the effect of the interference from pressure fluctuations at the blade leading edge [94, 95]. Experiments have

shown a possible blade noise reduction of 2-3 *dB*.

14.5 Results

This section provides a brief overview whether the EuroFlyer is able to meet the noise related requirements. It was already shown that, for the fly-over and the approach, the EuroFlyer is emitting even less noise than required. To pass the noise requirement, however, the lateral noise must be reduced by 6 *dB*.

Since the propeller is so dominant during take-off, the 6 *dB* reduction can be achieved by only implementing the previously mentioned propeller noise reduction methods. Here, the option of serrated blades and a tip sweep of 26° provide a sufficient noise reduction of 6.11 *dB*, after applying Eq. 14.1. It might prove to be necessary to implement more of the above named methods to account for the assumptions and the limitations of the used software package. The final results are given in Table 14.1. With the implementation of a few noise reduction methods, the EuroFlyer is able to satisfy all requirements of the ICAO Chapter 4, with an additional noise reduction of 10 dB.

Table 14.1: Noise Analysis Results

Measurement Point	Maximum Allowable Noise Emission	Achieved Noise Emission	Margin
Lateral	84 dB	83.9 dB	0.1 dB
Fly-over	79 dB	77.2 dB	1.8 dB
Approach	88 dB	83 dB	5 dB

	Result	Decibels
	Cumulative Margin	36.9 dB

CHAPTER 15

Performance Analysis

This chapter elaborates on the performance of the EuroFlyer. A road map for the performance analysis is shown in Fig. 15.1. Firstly, the accelerated performance is described, using the method from J. Anderson [96]. Secondly, the cruise performances in normal flight and in case of engine failure are discussed. After having calculated the turning performance, the climb performance of the aircraft is determined. Then, the loading diagrams and the payload-range diagram of the EuroFlyer are shown. Finally, the results of the performance analysis are summarized.

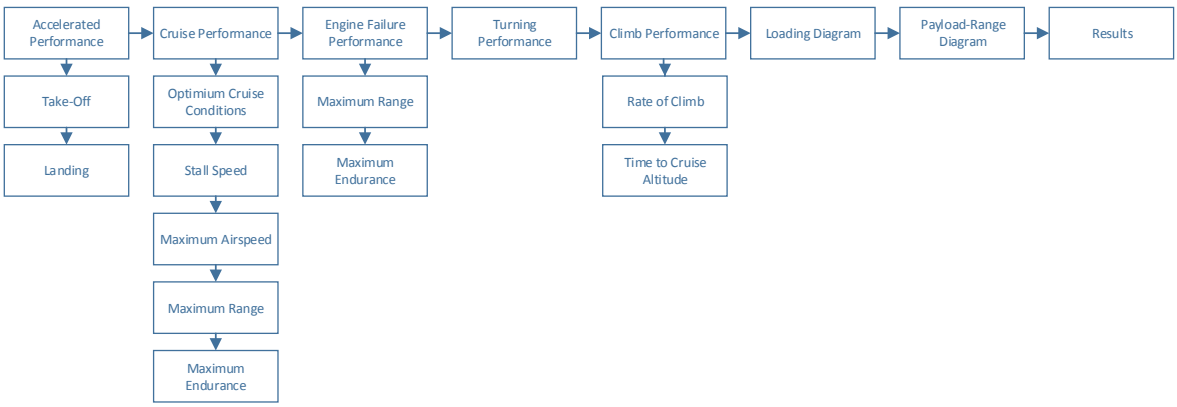

Figure 15.1: Performance Analysis Road Map

15.1 Accelerated Performance

This section elaborates on the take-off performance, followed by the landing performance of the EuroFlyer.

15.1.1 Take-Off

The take-off of an aircraft is a performance problem of accelerated nature. In detail, the take-off distance consists out of the ground roll, s_g, which is the distance from the start of the take-off until the aircraft lifts into the air and some extra ground distance s_a which is required to pass over a 35 ft obstacle height as stated in CS-25 [96, 32]. The general take-off procedure with the corresponding distances is shown in Fig. 15.2.
In general, the speed required for liftoff, V_{LO}, is 1.1 times the stall speed [97]. According to Anderson [96], for a propeller configuration, the power available is reasonably constant. Hence, during ground roll, the thrust can be calculated with Eq. 15.1.

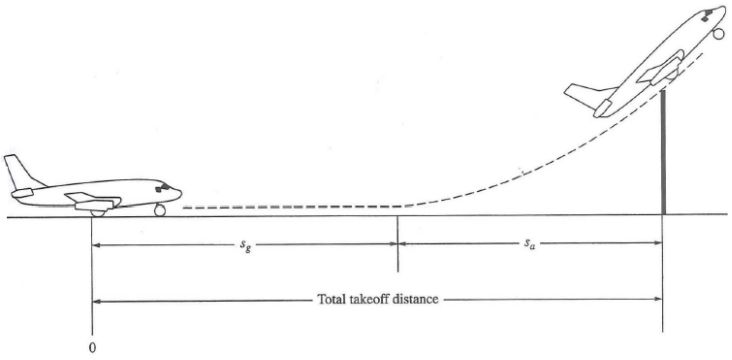

Figure 15.2: Take-Off Distance

$$T = \frac{P}{V_\infty} \tag{15.1}$$

The drag coefficient must be adjusted to account for the additional drag of the extended landing gear and the reduction of drag due to the presence of the ground effect. The increase in drag due to the extended landing gear can be approximated by Eq. 15.2 as stated in Aircraft Performance [97].

$$\Delta C_{D_0} = \frac{W}{S} \cdot K_{uc} \cdot m^{-0.215} \tag{15.2}$$

In Eq. 15.2, K_{uc} is a factor to account for the flap deflection, since the landing gear drag is decreases for a flap deflection [96]. The reduction in the induced drag coefficient due to the ground effect can be determined by Eq. 15.3 [98].

$$G = \frac{(16 \cdot \frac{h}{b})^2}{1 + (16 \cdot \frac{h}{b})^2} \tag{15.3}$$

In Eq. 15.3, h is the height of the wing with respect to the ground and b is the wingspan. The distance for ground roll can be determined by Eq. 15.4 as mentioned by J. Anderson [96].

$$s_g = \frac{1}{2 \cdot g \cdot K_A} \cdot ln(1 + \frac{K_A}{K_T} \cdot V_{LO}^2) + N \cdot V_{LO} \tag{15.4}$$

In Eq. 15.4, K_A is represented Eq. 15.5 and K_T by Eq. 15.6. These two parameters are calculated at an airspeed equal to 0.7 times the lift-off velocity.

$$K_A = -\frac{\rho_\infty}{2 \cdot \frac{W}{S}} \cdot (C_{D_0} + \Delta C_{D_0} + (k_1 + \frac{G}{\pi e A R}) C_L^2 - \mu_r C_L) \tag{15.5}$$

$$K_T = (\frac{T}{W} - \mu_r) \tag{15.6}$$

In Eq. 15.5, k_1 is one third of $1/\pi ARe$. According to Raymer [34], the lift coefficient at ground roll can be safely assumed to be 0.1. However, it is important to realize that this value depends on the deployment of the high lift devices and will increase during the rotation phase. The friction coefficient, μ_r is assumed to be 0.04 which is a typical value for dry concrete with no brakes applied [96]. In Eq. 15.4, N represents the time between the initiation of rotation and actual lift-off which is three seconds for large aircraft [34].

The airborne distance of the take-off can be determined using Fig. 15.3. The radius can be calculated using Eq. 15.7 where the load factor is determined with an airspeed which is 1.15 times the stall speed.

$$R = \frac{1.15 \cdot V_{Stall}^2}{g \cdot (n - 1)} \tag{15.7}$$

The airborne distance can be calculated using Eq. 15.9 by knowing the angle which is determined using Eq. 15.8.

$$\theta_{OB} = cos^{-1}(1 - \frac{h_{OB}}{R}) \tag{15.8}$$

$$s_a = R \cdot \sin(\theta_{OB}) \tag{15.9}$$

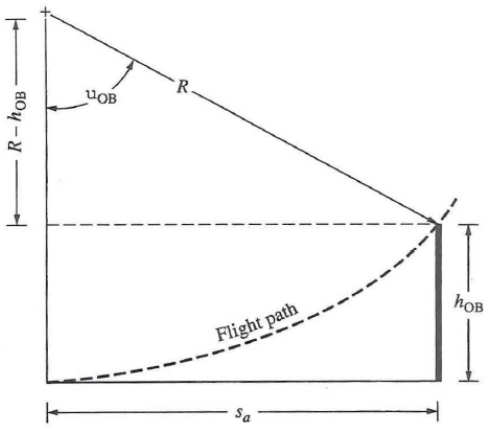

Figure 15.3: Take-Off Airborne Distance

The total take-off length is found by adding the airborne distance and the ground roll distance, shown in Eq. 15.10.

$$s_{Take-Off} = s_a + s_g \tag{15.10}$$

15.1.2 Landing

The landing distance of the aircraft consists out of three phases, being the approach distance, s_a, the flare distance, s_f and ground roll, s_g. This is shown in Fig. 15.4 for more clarity. From Fig. 15.4, the approach distance can be obtained using trigonometry and by knowing the height of the screen, as shown in Eq. 15.11.

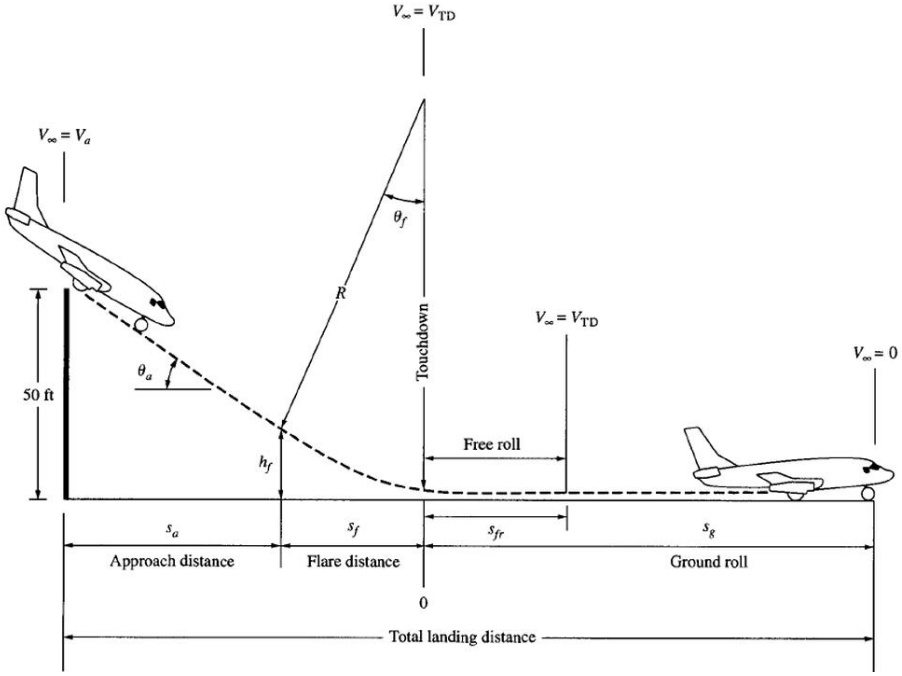

Figure 15.4: Landing Distance [96]

$$s_a = \frac{15.24 - h_f}{\tan(\theta_a)} \tag{15.11}$$

As stated in Chapter 8, the approach angle was found to be -0.051 degrees. Again, using Fig. 15.4, the flare distance is calculated using Eq. 15.12.

$$s_f = R \cdot \sin\theta_a \tag{15.12}$$

The radius, R, is determined by means of Eq. 15.13.

$$R = \frac{V_f^2}{g \cdot (n-1)} \tag{15.13}$$

Where the load factor is determined at the flare speed which is equal to 1.23 times the stall speed. The ground distance is calculated using Eq. 15.14.

$$s_g = N \cdot V_{TD} + \frac{1}{2 \cdot g \cdot J_A} \cdot ln(1 + \frac{J_a}{J_T} \cdot V_{TD}^2) \tag{15.14}$$

Here, N is the time increment for the free roll and a value of three seconds is common for large aircraft [34]. The velocity at touchdown, V_{TD}, is assumed to be 1.15 times the stall speed. J_T accounts for reverse thrust and the friction coefficient, as Eq. 15.15 shows. However, no reverse thrust is used, so T_{rev} is set to zero and the value for μ_r is set to 0.4 since the brakes are applied, as suggested by [96].

$$J_T = \frac{T_{rev}}{W} + \mu_r \tag{15.15}$$

The symbol J_A is calculated by using Eq. 15.16.

$$J_A = -\frac{\rho_\infty}{2(W/S)} \cdot (C_{D_0} + \Delta C_{D_0} + (k_1 + \frac{G}{\pi e A R}) C_L^2 - \mu_r C_L) \tag{15.16}$$

In Eq. 15.16, k_1 is one third of $1/\pi ARe$ and the lift coefficient is assumed to be 0.1, as discussed previously. Combining the three landing distances, the total landing distance is obtained via Eq. 15.17.

$$s_{Landing} = s_a + s_f + s_g \tag{15.17}$$

15.2 Cruise Performance

This section assesses the cruise performance of the EuroFlyer. As the cruise phase is the most important phase of the mission, it is definitely worthwhile to consider in this performance analysis. First the drag and lift over drag ratio will be analysed at cruise altitude. Afterwards the stall speed and maximum velocity are determined. Finally the airspeeds, at which the aircraft should fly to obtain its maximum range and maximum endurance are calculated.

15.2.1 Optimum Cruise Conditions

Figure 15.5 illustrates the variation of the drag force and lift over drag ratio as a function of Mach number at the cruise altitude of 9000 m. As can be observed in Fig. 15.5a, the parasitic drag increases with increasing flight speed while the induced drag decreases. By adding these two components, the total drag is found to decrease until a freestream Mach number of 0.424, where an extremum is reached. This minimal value is also referred to as the drag bucket. As the EuroFlyer has a minimum cruise Mach number of 0.65, the drag generated by the EuroFlyer is found to be 32% higher than this minimum value. The same trends can be identified in the lift over drag ratio, a measure for the aerodynamic efficiency of the aircraft. This is shown in Fig. 15.5b.

The reason that the aircraft in cruise is not perfectly in the drag bucket is that at this altitude and velocity, the highest lift over drag ratio is obtained at the current design point. The ratio L/D can be increased by flying at a lower airspeed or by flying at a higher altitude. Unfortunately, flying at a lower airspeed is not allowed by the minimum cruise requirements and flying at an higher altitude is restricted by the engine's performance. Due these restrictions, the current design point can be considered as the optimal.

15.2.2 Stall Speed

The stall speed of the EuroFlyer is determined using Eq. 15.18. The maximum lift coefficient in clean configuration and both the density at sea level and at cruise altitude are used to calculate the stall speeds at sea level and cruise altitude respectively.

$$V_{min} = \sqrt{\frac{2 \cdot W}{S \cdot \rho \cdot C_{L_{Max_{Clean}}}}} \tag{15.18}$$

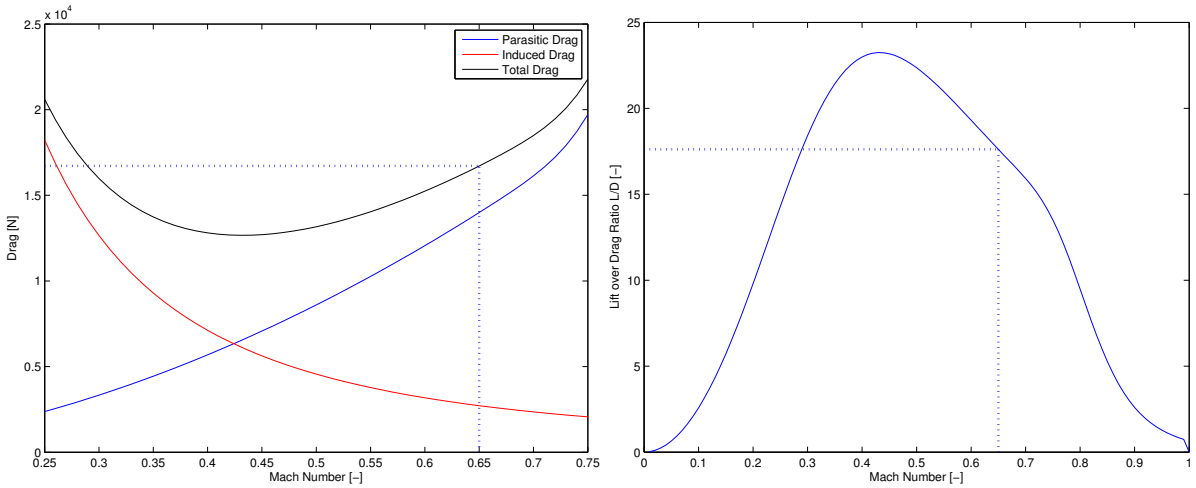

(a) Drag

(b) L/D ratio

Figure 15.5: Drag and L/D ratio as Function of Mach Number at Cruise Altitude

15.2.3 Maximum Airspeed

The maximum airspeed at cruise altitude can be obtained by knowing the maximum thrust the propulsion unit can deliver and setting it equal to the drag. Using simple algebra, Eq. 15.19 can be obtained which gives a relation for the drag coefficient.

$$C_D = \frac{C_L \cdot T}{W} \tag{15.19}$$

The relation of the drag coefficient is then plugged into the lift drag polar shown in Eq. 15.20.

$$C_D = C_{D_0} + \frac{C_L^2}{\pi A R e} \tag{15.20}$$

This results into a quadratic equation which is solved for the lift coefficient. Next, this value is inserted in Eq. 15.21 and the maximum speed at cruise altitude is obtained.

$$V = \sqrt{\frac{2 \cdot W}{S \cdot \rho \cdot C_L}} \tag{15.21}$$

15.2.4 Speed for Maximum Range

The optimal lift coefficient in order to obtain the maximum range is determined by minimising the drag of the aircraft. This is achieved by differentiating the lift over drag ratio with respect to the lift coefficient, hence maximising it. This is shown in Eq. 15.22 [99].

$$C_{L_{Range}} = \sqrt{C_{D_0} \cdot \pi \cdot AR \cdot e} \tag{15.22}$$

The corresponding speed for the maximum range is calculated using Eq. 15.23 [99].

$$V_{Range} = \sqrt{\frac{W \cdot 2}{S \cdot \rho \cdot C_{L_{Range}}}} \tag{15.23}$$

15.2.5 Speed for Maximum Endurance

The maximum endurance can be calculated by minimizing the drag over velocity ratio [99]. This is obtained by maximizing the lift coefficient over the square of the drag coefficient. The resulting lift coefficient for maximum endurance is shown in Eq. 15.24 [99].

$$C_{L_{Endurance}} = \sqrt{\frac{1}{3} \cdot C_{D_0} \cdot \pi \cdot AR \cdot e} \tag{15.24}$$

The speed is given in Eq. 15.25 [99].

$$V_{Endurance} = \sqrt{\frac{W \cdot 2}{S \cdot \rho \cdot C_{L_{Endurance}}}} \tag{15.25}$$

15.3 Engine Failure Performance

Only recently, aircraft are allowed to fly over large oceans without having more than of two engines. This was simply due to unreliable engines, which had a relative high chance of failure. Now that the reliability is increasing, various new aircraft are allowed to fly over seas, with only two engines. In addition, aerodynamics shapes keep evolving into more efficient forms leading to higher gliding performance.

In this section, the performances during an engine failure will be analysed by looking at the maximum range and maximum endurance of the EuroFlyer. Note that the speeds found in Sections 15.2.4 and 15.2.5 are equal to the speeds used in this section.

15.3.1 Maximum Range

When all the engines of the EuroFlyer fail, the aircraft is no longer able to provide trust and is forced to make an emergency landing. It is, therefore, important to know the distance the EuroFlyer can cover, to find a suitable airport to land. The most efficient airspeed was already found, but to maintain at the same airspeed the aircraft has to overcome the corresponding drag. In such an event, by using the equation of motion, the gliding angle can found as is shown in Eq. 15.26 [100]. Here P_a is zero, $P_r = (D \cdot V)$ should be as low as possible, meaning that the drag should be minimum, and V was found earlier. Using these values, Eq. 15.26 can be rewritten to Eq. 15.27, which gives a gliding angle for the longest range. When this is known, the maximum range can be found with Eq. 15.28.

$$P_a - P_r = \frac{W}{2 \cdot g} \cdot V \cdot \sin(\gamma) = W \cdot RoC \tag{15.26}$$

$$\gamma = \arcsin\left(C_D / C_L\right) \tag{15.27}$$

$$Range = \frac{H}{\arctan \gamma} \tag{15.28}$$

15.3.2 Maximum Endurance

The maximum endurance corresponding to the maximum amount of time the EuroFlyer can stay airborne, when both engines are inoperative. Normally, however, the aircraft is allowed to land as soon as possible. Nevertheless, it will still be computed for completeness, where first the Rate of Climb (RoC) was found with Eq. 15.26. For the longest range, different P_r and V values are used. P_r can be found with Eq. 15.29 [100] and the airspeed was calculated in Section 15.2.5. At last, dividing the altitude by the computed RoC will result in the maximum endurance.

$$P_r = W \cdot \sqrt{\frac{2 \cdot W \cdot C_D^2}{S \cdot \rho \cdot C_L^3}} \tag{15.29}$$

15.4 Turning Performance

To make sure that the EuroFlyer can reach its destination, it has to be able to perform a suitable turn. In section, the turn performance is elaborated, by looking at the steepest turn, minimum turn radius and the minimum turn time. The steepest turn occurs at the maximum load factor, which was found to be 2.5 in Section. 15.6.

The minimum turn radius which is also referred to as the tightest turn, can be found using two conditions that depend on the airspeed and load factor. The first condition represents the stall condition, since the lift vector (L') pointing upwards should be equal to the weight of the aircraft as can be seen in Fig. 15.6a. Therefore, the lift (L) can be found using Eqs. 15.30 and 15.31, which can be rewritten into Eq. 15.32 [100].

$$L = n \cdot L' \tag{15.30}$$

$$L = 0.5 \cdot \rho \cdot V^2 \cdot S \cdot C_L \tag{15.31}$$

$$V = \sqrt{\frac{2 \cdot n \cdot W}{S \cdot \rho \cdot C_L}} \tag{15.32}$$

The corresponding minimum range is obtained by leaving n as a variable. Using the different load factors and their corresponding airspeed values, obtained from Eq. 15.32, result in a minimum range, shown in Eq. 15.33, while still satisfying the minimum amount of lift needed. This is illustrated by the purple line displayed in Fig. 15.6b. However, these load factors vary until a value of six which will never occur during the mission of the EuroFlyer. This leads to the second condition, where different load factors are used (1.15, 1.41 and 2) corresponding to different bank angles (30, 45 and 60 deg), respectively. Leaving these factors constant, while the airspeed is kept as a variable, leads to the other three lines shown in Fig. 15.6b. Note that the Euroflyer should satisfy both conditions; the minimum turn radius cannot lie below one of these lines.

$$R = \frac{V^2}{g \cdot \sqrt{n^2 - 1}} \tag{15.33}$$

Now, the minimum turn radius can be easily found for the different bank angles, by looking at the intersections between the lines. As expected, a higher load factor leads to a lower turn radius. With the obtained relationship between the airspeed and radius, the minimum turning time can be found with Eq. 15.34.

$$T_{2\pi} = \frac{2 \cdot \pi \cdot R}{V} \tag{15.34}$$

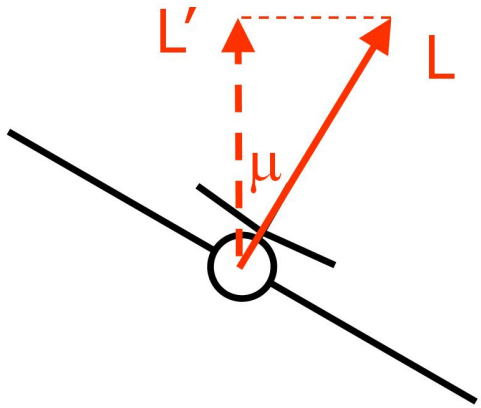

(a) Visualisation of the Lift Force During a Turn

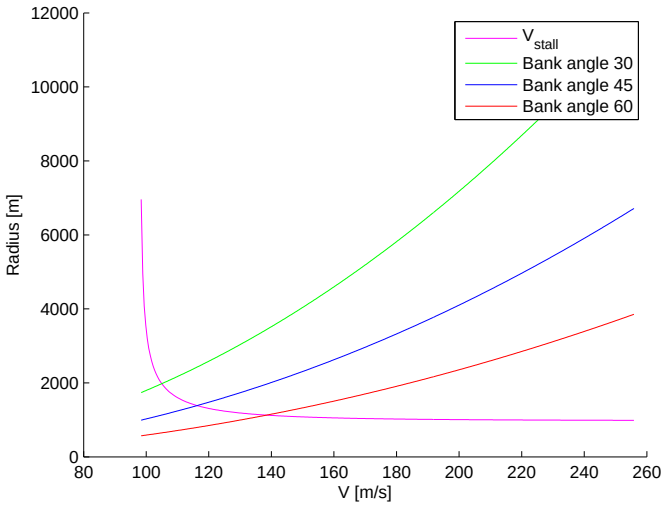

(b) Minimum Turn Radius for Different Speeds and Bank Angles

Figure 15.6: Turn Radius and Forces

15.5 Climb Performance

This section elaborates on the general climb performance of the EuroFlyer. First, the climb performance is determined, followed by the time to cruise altitude.

15.5.1 Rate of Climb

During the design process of the EuroFlyer, it was found that the optimum cruise altitude is 9000 m, resulting in a higher efficiency which is one of the main driving requirements. In addition, due to noise regulations, it is preferred that the EuroFlyer will reach this altitude in a short amount of time. In this section, the rate of climb, time to cruise and the service ceiling will be studied.

The maximum rate of climb can be found with Eq. 15.35 [100], however P_a changes with altitude as can be seen in Eq. 15.36 [100].

$$RoC = \frac{P_a}{W} - \sqrt{\frac{2 \cdot W \cdot C_d^2}{S \cdot \rho \cdot C_L^3}} \tag{15.35}$$

$$P_a = (\frac{\rho}{\rho_0})^{0.75} \cdot P_{a0} \tag{15.36}$$

By converting the altitude into a ratio of densities, the altitude versus RoC can be plotted as shown in Fig. 15.7. In this figure, it can be observed that the RoC decreases as the altitude increases. The theoretical ceiling can be found at an RoC of 0 m/s, the service ceiling is defined at an RoC equals to 0.5 m/s which is displayed with the dotted red line.

15.5.2 Time to Cruise Altitude

With the RoC known at every altitude, it is possible find the time to cruise with Eq. 15.37, where RoC_{avg} is the average rate of climb.

$$t = \frac{H}{RoC_{avg}} \tag{15.37}$$

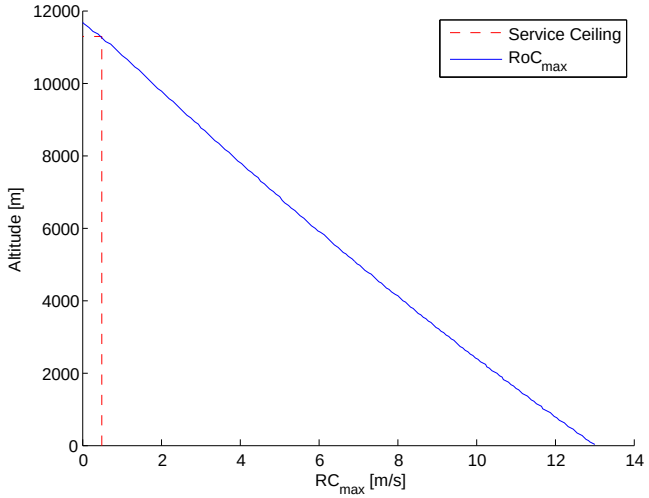

Figure 15.7: Rate of Climb at Different Altitudes

15.6 Loading Diagrams

A key design parameter contained in the structural design criteria is the load factor the structure must be able to bear. In the structural design of the EuroFlyer a maximum load factor of 2.5 and a minimum load factor of -1 have been taken into account, as required by the airworthiness regulations [32]. Here the airworthiness requirements also stipulate that an aircraft must be sufficiently strong to cope with all possible combinations of the flight velocity and load factors. This requirement must be satisfied at all possible altitudes, weights and weight configurations. The proof of strength is based on the critical points, in this case the corners of the diagrams. Since the aircraft will be most heavily loaded at the start of the cruise missions segment, the loading diagrams at this load state will be provided for the EuroFlyer.

The diagram found in Fig. 15.8a shows the loading diagram of the EuroFlyer at start of cruise conditions. The indicated equivalent airspeeds include the stall speed V_S, the minimum velocity at maximum load factor V_A, the cruise speed V_C and the dive speed V_D defined as 1.5 times the cruise speed. The two exponential represent the boundaries with and without high lift devices, where the limit load factor of the case with high lift devices is lower than in the case of a clean wing configuration.

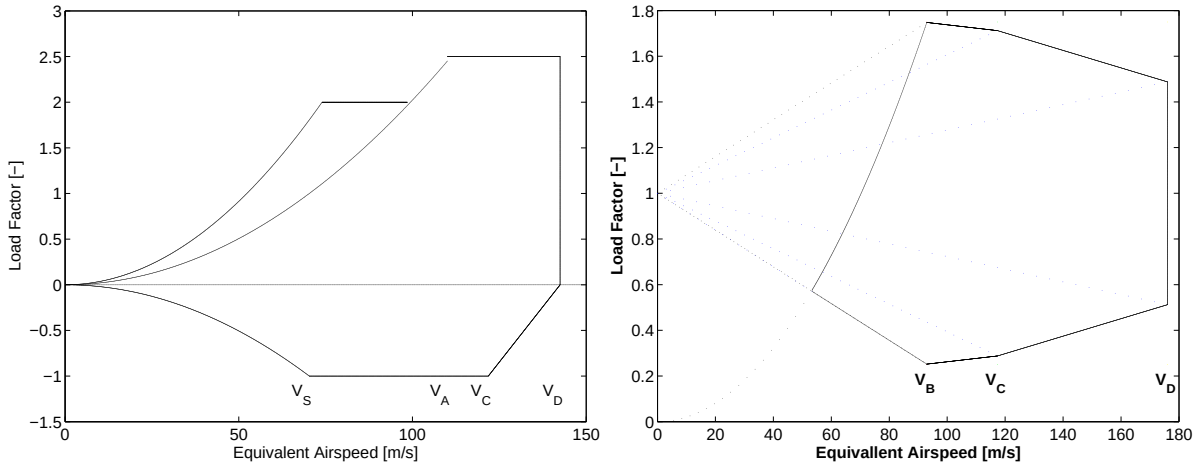

(a) Loading Diagram

(b) Gust Diagram

Figure 15.8: Loading and Gust Diagram at Start of Cruise at 9000 metres

To also assure that the aircraft is not crossing the load factor limits at bad weather conditions, a gust diagram is made and depicted in Fig. 15.8b. This diagram results from the aircraft flying through turbulent air. When an aircraft experiences a gust, the effect is an increase or decrease in the angle-of-attack, resulting in a change in lift and, consequently, a change in load factor [48]. The displayed gust lines are plotted for gust velocities of 58 ft/s, 46 ft/s and 21 ft/s as these are the respective relevant gust speeds at the cruise altitude of the EuroFlyer [48].

15.7 Payload-Range Diagram

To construct the payload-range diagram for the EuroFlyer, the design point was taken to be at a payload of 79 passengers with cargo (8137 kg) and 1500 km range to satisfy the emission requirements. In order to obtain the range with maximum payload and the maximum range with payload, the following method is used.
First, the maximum amount of energy that can be carried is related to a maximum range. Since the LNG tanks have been sized to reach 3000 km, the location of the maximum range with payload lies at this distance. To be able to fly even further, the payload has to be decreased in order to store more LNG. Since 1502 kg extra mass of LNG is required to reach a range of 3000 km, the payload should decrease by the same amount as the extra mass of LNG. Here, it is assumed that double the energy is required in order to reach double the range.

In order to determine the range which can be covered without transporting any payload, Eqs. 15.22 and 15.23 are used. By using these equations, the available energy on board, the required power, the aircraft drag and the maximum aircraft range can be determined. This value for the range was found to be 4140 km. To be able to compute the point on the payload-range diagram which represents the range with maximum payload, one has to set the range for this point. In Chapter 6 it was concluded that within the United States the average trip length

will be approximately 1300 km by the year 2030. With this in mind, the range for maximum payload has been set to this distance. By knowing this range, the corresponding value for the maximum payload is found to be 8337 kg.

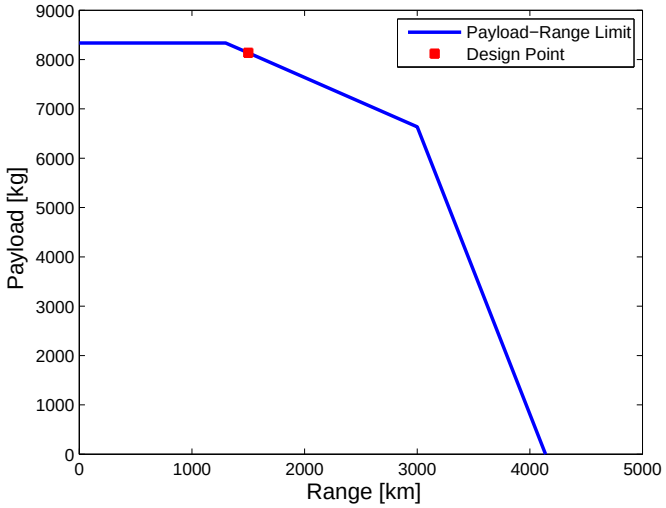

Figure 15.9: Payload-Range Diagram

With the help of these points, the payload-range diagram of the EuroFlyer can be constructed which is displayed in Fig. 15.9. The design point of the EuroFlyer is illustrated by the red dot and the blue line shows the payload as a function of range.

15.8 Results

The results found previously in this chapter are summarised in Table 15.1.

Table 15.1: Performance Analysis Results

Parameter	*Value*	*Unit*
Take-off Distance	1050.9	m
Landing Distance	936.1	m
Speed limits		
Stall Speed Sea Level	57.1	m/s
Stall Speed Cruise Altitude	114.0	m/s
Maximum Speed at Cruise Altitude	258.1	m/s
Speed for Maximum Range	129.7	m/s
Speed for Maximum Endurance	99	m/s
Engine Failure		
Maximum Range	203.58	km
Maximum Endurance	0.497	hr
Turn Performance		
Minimum Turn Radius 30 deg	1979	m
Minimum Turn Time 30 deg	118	s
Minimum Turn Radius 45 deg	1386	m
Minimum Turn Time 45 deg	75	s
Minimum Turn Radius 60 deg	1128	m
Minimum Turn Time 60 deg	51	s
Climb Performance		
Maximum Rate of Climb	13.01	m/s
Time to Cruise Altitude	1060	s
Service Ceiling	11250	m
Payload-Range Diagram		
Maximum Payload Range	1300	km
Maximum Zero-Payload Range	4140	km

CHAPTER 16

Concept Analysis

16.1 Overview

Summarising a ten week design process in a few dozen pages is quite an accomplishment, but the team realises that by this chapter readers might have lost a few details here and there. This chapter serves to refresh the memory and provides a concise overview of the designed aircraft.

16.1.1 Mission

Originally intended for a mission of 2000 km (excluding reserves), a market analysis has shown high potential for aircraft clearly oriented at regional travellers. The aircraft concept under development is therefore sized for a range of 1500 km. Of course, the aircraft will spend most of its time in the cruise phase at an altitude of 9000 m. Flying at Mach 0.65, a trip covering the full range takes approximately 2.65 hours. Which is the block time, which is defined as the time from gate to gate.

16.1.2 Fuselage

The fuselage is sized by the payload it is supposed to carry - 80 passengers and their luggage - and propulsion system. The boundary layer of the fuselage is ingested by the aft mounted propellers, increasing efficiency. Although it increases the wetted area and drag, it is due to this concept beneficial to have a wide fuselage, generating a large boundary layer. Due to the fuselage diameter of 4.7 m, the seats are configured in a 2x3x2 setting. For this diameter, a fuselage length of 20.37 m was selected. The number of seats varies from 79 to 81, depending on whether a single or twin-class configuration is preferred by the operating airline. Below the passenger floor, there is sufficient room for cargo of various shapes and sizes. With a maximum height of 1.62 m (excluding margins) and a usable volume of 54 m^3, more than just passengers' luggage can find a place on board. Appendix G shows all relevant dimensions in various planes and artist impressions of the EuroFlyer concept.

In the previous paragraph, the aerodynamic consequences of a wide fuselage were already touched upon. A total fuselage drag coefficient of 0.0106 is found. Based on a structural analysis performed, the team has selected Carbon Fibre Reinforced Plastics as the material of choice for the EuroFlyer airframe, yielding a skin thickness of 0.93 mm. The structure is further stiffened using 53 circumferential stringers. Due to the lightweight material and high structural efficiency, the fuselage weight is kept low at an approximated mass of only 3090.5 kg. This does not take into account the tricycle retractable landing gear, weighing 1142.3 kg.

16.1.3 Wing

The wing design team has taken off from the previously established design point, a combination of wing and power loading. With respect to the former parameter and the maximum take-off weight, a design lift coefficient of 0.4967 was computed. Based on this requirement and important aerodynamic qualities, the NACA $63_2 - 415$ was selected as the EuroFlyers aerofoil. Characteristics of the wing plan form are the wingspan of 36 m (set by the requirement to be able to operate on regional airports), the taper ratio of 0.3012 (chosen for the optimum

lift-to-drag ratio), the aspect ratio of 19.88 (based on a careful optimization between drag and climb performance on the one, and weight on the other hand) and a corresponding wing surface area of 65.18 m^2. Due to a relatively low cruise Mach number and the selected aerofoil, it was not necessary to apply sweep.

The wing configuration described above provides enough lift to keep the aircraft flying, but also creates drag. In terms of coefficients, the total drag is 0.0119, of which 0.0046 is induced by the lift force and 0.0073 is a result of the aerodynamic shape. Advanced spiroid winglets contribute to the low induced drag coefficient.

16.1.4 Propulsion

As the EuroFlyers propulsion system will be hybrid, it consists out of two engines - one turboprop operating on LNG and one electric engine - each connected to one of the two co-axial contra-rotating propellers. As explained in the next section on energy, the ratio between LNG and batteries is not equal. Hence, a generator coupled to an APU can be used to convert chemical energy (from the LNG) into electrical energy powering the electric engine. Although complexity is increased as compared to a conventional system, redundancy is too. The team cannot think of any event that can shut down both the chemical and electric system, which means that if one engine is inoperative, the aircraft can still make a safe emergency landing.

The propulsive system is placed in and mounted at the rear of the fuselage. This way, the boundary layer generated by the fuselage can be ingested by the propellers. With this technique, the aircraft wake is re-energized by the propeller. Rather than having a momentum deficit in this wake and a momentum excess behind the propellers, these two are now (partially) balancing each other, increasing efficiency and reducing energy consumption. To further increase efficiency, the two propellers are shrouded. This can be clearly seen in Appendix G.

The turboprop engine is sized based on the power requirements, following from the computed drag. Totalling 3.3 MW in cruise, the turboprop is needs to provide approximately half of that power, or 1.65 MW during cruise to be precise. A pressure ratio of 28 is selected, divided over an axial and a radial compressor. With a fuel flow of 0.075 kg/s and a turbine exit temperature of 1439.1 K, a total fuel efficiency of 43.2% is obtained. As mentioned, these specifications hold during cruise. During take-off, when more power is required, the fuel mass flow is increased to 0.095 kg/s, resulting in a shaft power output of 2.2 MW, on which the turboprop was sized

The APU sizing process is very similar to the turboprop sizing process. The pressure ratio is somewhat lower at 17, as well as the combustion temperature (1255.6 K). Due to this, the output power is 1.69 MW. The electrical engine is sized to deliver the other half of the total power.

It can be easily seen that this is a complex system. Many parts work together to guarantee optimal performance. This also comes at a price, not only in terms of cost, but also in weight.

16.1.5 Energy

The EuroFlyer draws its energy from a hybrid power source in which LNG and high-tech Lithium-air batteries are combined. The latter system provides 17.5% of the required energy, whereas the other 82.5% of the energy is stored in the LNG. The batteries are the heaviest component of this system, having a mass of 4159.35 kg, as opposed to 1248.18 kg reserved for LNG. The batteries will gain 119 kg of mass during flight. This is due to the nature of the batteries, which draw one of the reaction components (oxygen) from the ambient. The LNG is kept cool by means of evaporate-cooling, a process in which a total of 9.35 kg of LNG is evaporated to absorb the heat of the air surrounding the LNG tanks. A large tank is placed at the centre of the fuselage, a smaller tank is placed in the front to balance the increase in battery mass.

To keep turnaround time to a minimum, the batteries will be placed in a ULD. This facilitates easy loading and unloading, such that de-charged battery packs can be quickly replaced by charged ones.

16.1.6 Noise

Noise is analysed by means of the ESDU software package and the EuroFlyer concept is checked for compliance with the requirements (10 dB reduction with respect to ICAO Ch. 4 regulations). In these requirements, noise is measured at a lateral measurement point, a fly-over measurement point and an approach measurement point. Starting with the first, initial modelling a noise level of 90 $EPNLdB$ was found, which is six decibels too high to meet the requirements. The noise emissions are lowered by using serrated and slightly swept propeller blades, yielding a noise reduction of 6.11 $EPNLdB$, lowering the total noise at this measurement point to 83.9 $EPNLdB$. For fly-over, the EuroFlyer performs even better than required, only producing sound with an

intensity of 77.2 *EPNLdB* (whereas the requirement was set at 79 *EPNLdB*). The same conclusion holds for the approach measurement point. Emitting only 83 *EPNLdB*, the EuroFlyer is five decibels below the requirement.

16.1.7 Flight Performance

The flight performance of the EuroFlyer was analysed, elaborating on take-off, landing, climbing and turning performance. A short take-off distance is important to be able to successfully operate on regional airports, and with 1050.9 *m*, this performance can be classified excellent. The landing distance is lower, at 936.1 *m*. With a maximum rate of climb of 13.01 *m*/*s*, it takes 1060 *s* (almost 18 minutes) to reach the optimum cruise altitude of 9000 m. Turns were analysed for a set of three bank angles and corresponding load factors: 30, 45 and 60 degrees, or load factors of 1.15, 1.41 and 2. The minimum turn radii were found to be 1979 *m*, 1386 *m* and 1128 *m* respectively, with turns taking 118 *s*, 75 *s* and 51 *s* to complete.

Speeds at various points in the flight envelope have also been determined. At sea level, the stall speed is determined to be 57.1 *m*/*s*, increasing to 114 *m*/*s* at cruise altitude. At that same altitude, the maximum speed is 258.1 *m*/*s*. Optimising endurance or range, the team has found speeds of 99 *m*/*s* and 129.7 *m*/*s* to be most suitable, respectively. In normal operating conditions, the range with maximum payload is 1300 *km*, increasing to 4140 *km* if no payload is carried at all. For safety reasons, the maximum range and endurance for the one engine inoperative (OEI) condition are also important. These were computed to be 203.58 *km* and 30 *min*. Especially in the densely populated areas, the EuroFlyer will be operating in, this should be sufficient to safely get to an airport in time.

16.2 RAMS Characteristics

In order to make the EuroFlyer an attractive product, it should comply with the airliners' requirements. The requirements are covering several topics: Reliability, Availability, Maintainability, and Safety. In this section all these fields are touched upon. Starting with reliability which is the possibility that the EuroFlyer is able to readily perform its mission. Availability concerns the amount of time the EuroFlyer can be operative. Ease of access for maintenance is discussed and battery replacements are elaborated on in the maintainability section. Finally, the safety characteristics of the aircraft are defined. These subjects determine the effectiveness of the aircraft during its service life which forms an important aspect of the aircraft.

16.2.1 Reliability

Reliability is closely related with redundancy. For the EuroFlyer this is found in multiple subsystems which were designed to cope with various circumstances including single part or system failures. Due to the location of the propellers the length of the landing gear was increased to provide more clearance and an extra supporting strut was placed on the shroud. In addition, this strut also provides structural redundancy and limits propeller damage in case of a ground strike during landing or take-off, thereby increasing its reliability. The placement of the propellers also offers the advantage that they are shielded from objects coming from the front (such as birds), lowering the chance of taking damage on the blades during such an event. However, one of the disadvantages of this propulsive configuration is that the propellers are located behind the landing gear. As a consequence, dirt originating from the wheels might find its way into the propellers.

Another increase in reliability can be found in the powering the avionics and the electric engine. Their power is supplied by two separate batteries and a generator-APU combination. This results in systems with a very high redundancy, since the occurrence of simultaneous failure of all three sources is highly unlikely.

16.2.2 Availability

Purchasing an aircraft is not without any risk. It is a large investment and in order for the airliner to make a profit, it is important to return this investment as soon as possible. The aircraft therefore needs to be able to perform its mission and preferably as often as possible.

To achieve this, the EuroFlyer is designed to have a quick turnaround time. The cabin contains two aisles, therefore there are four aisle-seat rows, making it possible to load or unload passengers quicker. In addition, the batteries are stored in two different cargo containers. This contributes to easy loading and unloading operations regarding the battery system. And even though refuelling the EuroFlyer with LNG must be done carefully and may increase turnaround time, only a small amount of fuel is consumed during its mission compared to today's

aircraft and therefore the turn around time is expected to be shorter than it is today.

16.2.3 Maintainability

Part of the operational cost can be found in the maintenance of the EuroFlyer. Since most main systems are located inside the fuselage, all systems are centred and placed in easy accessible locations. This in turn leads to faster and more simple inspection procedures which reduce the maintenance cost and increase the availability of the aircraft. The battery packs however can be quickly replaced after they exceed the intended number of life cycles. Since they are replaced during every turnaround, used battery packs can be serviced while the aircraft remains operative.

A critical part of the EuroFlyer can be found at the end of the fuselage, here multiple subsystems are integrated. Both the tail, duct, propellers and shafts are joined in a complex architecture and will be subjected into high stresses. This means that this part of the EuroFlyer should be maintained with extreme caution and has to be checked frequently. The two gas turbines are located into the fuselage, as a result engine maintenance or replacement may cost more time and effort compared to today's maintenance procedures.

16.2.4 Safety

The EuroFlyer is designed to comfortably and safely transport passengers to their destination and even though the need for comfort may differ for some parties, safety standards will not. Strict regulations regarding safety apply, such as the Certification Specification (CS-25) [32]. These regulations have continuously influenced the design throughout the entire design process.

As mentioned in Section 16.2.1, the relation between the landing gear, shroud and propellers has been thoroughly considered and evaluated. The length of the landing gear was increased in order to have a take-off clearance angle of 14 degrees which is exceeds the requirement of 12 degrees. In addition an extra supporting strut was placed to both support the shroud and protect the propeller blades during take-off and landing procedures.

In the event of an accident six emergency exits are present, including the main entrances. These are spread throughout the cabin to effectively clear the cabin during emergencies. For an aircraft up to 79 passengers a total of four exits is required, but having six emergency exits leads to a quicker quicker and smoother evacuation.

The propulsive system of the EuroFlyer is designed in such a way that the electric engine is powered by multiple sources reducing the chance of a failure. And during the event of engine failure, one of the two propellers can still provided enough power to safely land the aircraft. Part of the energy is provided by LNG. Since the optimum size of the tanks was found to be spherical, they have to be placed inside the fuselage. It might sound more dangerous having the fuel close to the passengers, but it should be noted that LNG only explodes under certain conditions and is recognised to be less of a risk than kerosene in aircraft [101].

For all the structural aspects of the subsystems, a safety factor of 1.5 was taken into account. This should prevent failure during the event of a loading exceeding its maximum design load. This accounts for the situations that the EuroFlyer might experience due to a sudden movement during manoeuvres or other unexpected events.

16.3 Risk Assessment

In this section, a technical risk map is established. This is an crucial procedure in a product development project, such as effectuated in this DSE. Risk is defined as a "measure of uncertainty of attaining a goal, objective or requirement pertaining to technical performance, cost and schedule" [102]. From this definition, one can easily understand that risk is always present, as it is the interconnecting link between technical performance, cost and schedule, which characterise the Systems Engineering (SE) universe. One distinguishes technical, schedule and cost risk. The technical risk increases when the technical performance of the product is using state-of-the-art concepts, which have not proven their effect during operation. Schedule risk occurs when the product development and deployment is rushed in order to meet a given deadline. Finally, cost risk occurs when the available funds for the development project are limited. It is important to note that these different risk categories are not independent of each other, but the occurrence of one category might influence the magnitude of another.

It can easily be understood that in practical applications, risk can never be removed completely. However, in the context of industrial SE, risk management allows the design team to recognize, assess and control uncertainties that might result in schedule delays, cost overruns, performance problems or other undesired effects. More

specifically, Project Risk Management (PRM) concerns the management of technical risks associated with any development or production project, such that the product can meet the stipulated performance, cost and schedule objectives. It consists of the identification of potential risks, assessment of their probability of occurrence and seriousness of their impact on the product performance, schedule and cost, followed by ranking these risks. The PRM process is terminated with the indication of preferred measures to reduce the risk of these events. The main goal is to identify the areas where largest reductions in risk can be achieved, such that the limited resources in terms of persons, time and money can be optimally distributed.

Another definition of risk is the product of the likelihood of an event and the consequence of an event. This definition serves as the base for the creation of a risk map which is a graphical representation of risk simplifying the identification of the events involving a high risk. The risk map is shown in Fig. 16.1. On the x-axis the likelihood of an event is categorised as 'very low', 'low', 'medium', 'high' or 'very high'. The probability of occurrence is highly dependent on the current state of technology or technology maturity. Proven efficiencies and assumptions can be seen as synonym of 'very low' probability, while a theoretically feasibly concept suits better the 'very high' label. In other words, a 'very low' probability means the current design expectation will be most likely fulfilled, whereas a 'very high' probability implies it will be very hard to achieve the current design expectation. On the y-axis the consequence of an event is labelled as 'negligible', 'marginal', 'critical' or 'catastrophic', as the severity is expressed according to its influence on the design. The events with the highest risk are due to the definition of the events with the highest likelihood and severity of occurrence. This situation is illustrated in the upper right corner of Fig. 16.1. In the left under corner the events with lowest risk can be found and in between these regions the events with medium risk are indicated. The elements included in the risk map are the most important and influential novelties and assumptions for the Euroflyer design. The overall risks are not very high, as most assumptions and efficiencies were conservatively assumed in the design.

As can be observed in Fig. 16.1 and Table 16.1, there is one event resulting in high risk. More specifically, the EuroFlyer's performance expectation may be too demanding, as the drag estimations influences that to a great extent 16.4. The risk of not performing according to standard is very high due to its high likelihood of occurrence and high mission criticality. In order to reduce this high risk, risk mitigation offers the technical approach for risk minimization. High risks can be reduced by performing (pre-)development, which decreases the probability of occurrence. Another possibility is adapting the design. Both selecting different or additional technologies or adding margins for redundancy can be considered as tools to achieve these changes. Ultimately, the objective is to end up in the lower left corner of the risk map for each event.

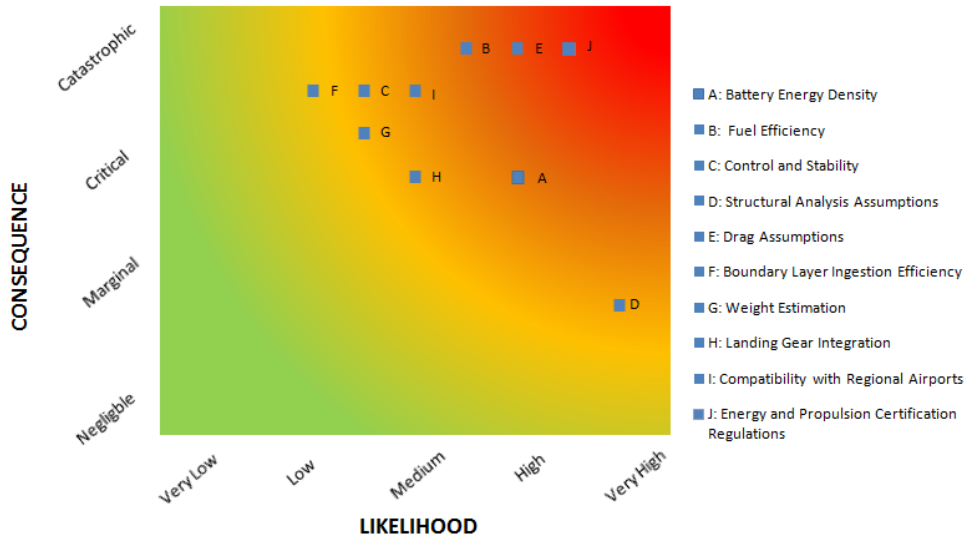

Figure 16.1: Risk Map

For each individual high risk element, a certain risk mitigation strategy will be selected to achieve this decrease. In this specific case, reducing the likelihood of an event is most likely to be achieved by careful selection, analysing and testing of the technologies and assumptions considered in the conceptual design phase, evaluation of current and addition of new sufficient margins in each subsystem. On a regular basis during the proceeding phases, risk item tracking will need to be executed. In other words, the status of the risks and mitigation strategies will have to be verified to ensure that the high risks are eliminated.

Table 16.1: Risk Ranking

Rank	*Event*	*Likelihood*	*Consequence*
1	Energy and Propulsion Certification Regulations	High	Catastrophic
2	Drag Assumptions	High	Catastrophic
3	Fuel Efficiency	Medium	Catastrophic
4	Battery Energy Density	High	Critical
5	Compatibility with Regional Airports	Medium	Critical
6	Control and Stability	Low	Critical
7	Structural Analysis Assumptions	Very High	Marginal
8	Landing Gear Integration	Medium	Critical
9	Weight Estimation	Medium	Critical
10	Boundary Layer Ingestion Efficiency	Low	Critical

16.4 Sensitivity Analysis

For a complete design of the EuroFlyer not only the final design parameters of the aircraft are necessary, but also how sensitive final values are when input parameters are changed. By means of this sensitivity analysis it is attempted to verify the impact of potential parameter changes, caused by possible over- or under estimations or model and calculation errors. Their influence is reflected on the change in MTOW, as this is a prominent driving factor in the design of the EuroFlyer.

During the design phase it was found that some variables had a more significant influence on the final design than others. To provide a proper outline of the sensitivity of the design, the impact of small changes in the variables with the most significant influence on the final weight are being quantitatively and qualitatively analysed. These parameters are the drag, battery energy density and the LNG fuel efficiency.

To quantify the results several iteration rounds are performed, only changing either one of the above mentioned variables while keeping the rest of the design variables constant. To provide a good impression of the individual effects of these three variables, all three are varied with the same percentage of 2%. This 2% is selected as a reasonable percentage to indicated the effects on the MTOW and a realistic error margin in the estimations that have been made on the above mentioned parameters.

16.4.1 Drag

The most dominant factors on the total aircraft drag are the fuselage form factor and the laminar flow percentages. In Chapters 8 and 9 a laminar flow of 10% over the wing chord and 5% over the fuselage length have been assumed, respectively. Despite that numerous articles predict a much higher possible percentage, a conservative approach is used as other articles predict a lower value. Similar, in the determination of the fuselage form factor an average of four different form factors has been taken to assure a realistic value. Since these important factors are based on assumptions, the total drag of the aircraft is able to vary slightly. Fig. 16.2 shows the result of a 2% increase and decrease in total aircraft drag after 25 iterations.
From Fig. 16.2 it becomes obvious that the design is very sensitive to variations in drag: a 2% increase results in a MTOW of 31788 kg whereas with a 2% reduction a MTOW of 25002 kg is found. These extreme numbers are mainly the result of the hybrid energy system utilised by the EuroFlyer. Here, because of the strict CO_2 emission limits the increase in required energy must be accounted for by the batteries. Since the addition of extra energy through the use of batteries does not follow a convergence pattern as steep as regular fossil fuels, the MTOW rapidly rises with addition of battery mass.

Furthermore it can be seen that in the case of a 2% drag reduction the trend converges faster than when the drag is increased by 2%. Referring back to Fig. 13.3, this behaviour can be explained by examining the black line, indicating the wing and energy system mass. This line provides a good impression on the trend followed by the total aircraft weight as in this design phase the energy system and the wing weight of the EuroFlyer are the two parameters which determine this trend. When the aspect ratio is increased, which in turn leads to a lower drag, the mass decreases. However, when the aspect ratio is decreased, leading to a higher drag, the mass of the aircraft increases exponentially. From Fig. 13.3 this behaviour can be explained: at the current aspect ratio of 19.88 the design point is still at a location where the battery and wing mass has not yet converged This explains the gap between the two results: the MTOW of the 2% increased total drag is 3949 kg higher and the MTOW of the 2% decreased total drag is 2838 kg than the original design.

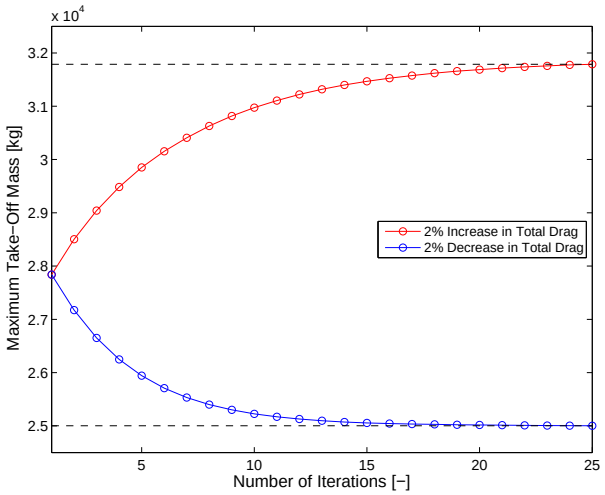

Figure 16.2: Drag Sensitivity

16.4.2 Battery Energy Density

The calculation of the expected battery energy density for the year 2035 has already been treated in Chapter 11. As the battery energy density of the EuroFlyer is not yet feasible as of this moment, it is necessary to analyse the sensitivity of the concept to changes in the battery energy density. Similar as before, the iterative process is repeated, but with changes of 2% in the energy density of the Lithium-air batteries. The result is depicted in Fig. 16.3.

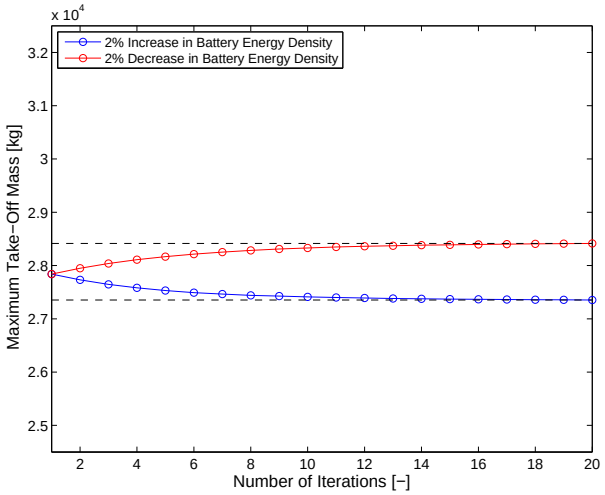

Figure 16.3: Battery Energy Density Sensitivity

With a 2% change in the energy density, the MTOW of the Euroflyer varies with approximately 2.0%. These variations simply originate from the additional battery mass required to still meet the required power. This mass increase, however, is not as significant as for the case where the drag is increased. This is due to a fact this change does not lead to large changes in the aspect ratio of the aircraft. Again referring to the aforementioned black line in Fig. 13.3, small changes an aspect ratio of 19-20 does not lead to large variations in the MTOW of the EuroFlyer.

16.4.3 Fuel Efficiency

The fuel efficiency of LNG set in Chapter 11 sets high requirements for the engine, specifically for the combustion chamber temperature. Current engines are limited in achieving higher efficiencies by the allowable limits of the combustion chamber temperature set by the thermal properties of materials. For 2035, it was obtained that a fuel efficiency of 43% is realisable. Fig. 16.4 provides the iteration results on the MTOW for the scenario where either a LNG fuel efficiency of 42.14 or 43.86% is achieved by 2035.

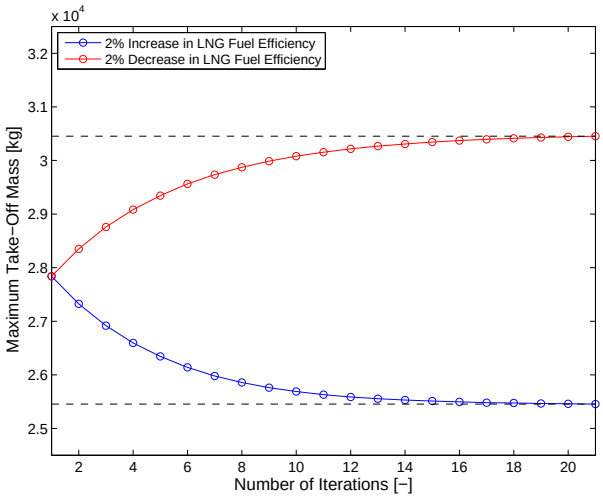

Figure 16.4: Fuel Efficiency Sensitivity

A similar profile as in Fig. 16.2 is found for the case where the LNG fuel efficiency is varied. The large variations can also be derived from the lower rate of convergence of the batteries. As can be seen, slightly varying the fuel efficiency has a significant influence on the MTOW. Therefore, during the iterations, this parameter should be closely monitored and its value confirmed.

16.4.4 Results

From the preceding sections it can be concluded that because of the implementation of an hybrid energy system the EuroFlyer is particularly sensitive to changes in certain prominent variables. Table 16.2 lists the exact values to changes of 2% in the total drag, battery energy density and LNG fuel efficiency. Since most parameters in the design are explicitly chosen conservatively, it is expected that the current MTOW will not be exceeded.

Table 16.2: Sensitivity Analysis Results on the Variation of Three Parameters

Parameter	*Initial Value*	*Direction*	*Aspect Ratio[-]*	*MTOW [kg]*	*Variation [%]*
Total Drag [N]	16714	2% Increase	17.41	31788	14.2
		2% Decrease	22.1	25002	11.4
Battery Energy Density [Wh/kg]	1350	2% Increase	20.24	27354	1.8
		2% Decrease	19.46	28414	2.1
Fuel Efficiency [%]	43	2% Increase	21.72	25455	9.4
		2% Decrease	18.18	30454	9.4

16.5 Family Concepts

The development cost of an aircraft contributes to the total Life Cycle Cost (LCC). However, this cost could be reduced as much as possible to generate a so called family concept. In such a case, an existing aircraft could be slightly modified so that the new design fulfils (its own) requirements. The idea of family concepts is quite established in the aviation industry. In this section, the capability for a EuroFlyer family is elaborated, by looking at different configurations of the aircraft. The first concepts' focus lies on transporting more passengers. The second concept turns the standard EuroFlyer from a short range to a long range aircraft. Finally the cargo transport capabilities of the EuroFlyer family are discussed.

16.5.1 Twin Deck

As was observed during the sensitivity analysis, the EuroFlyer is very sensitive to small changes in the design. This is partially due to the use of batteries, where their low energy density has a high influence on the total aircraft mass. The design team sees an opportunity - if the market shows a demand - for a higher passenger capacity aircraft. It was found that a short fat body was the most promising shape for the fuselage and this creates possibilities for a double deck. By adapting the passenger deck to a 3-3 configuration it can be moved upwards, creating enough space for another floor of seats on the lower deck.

Whereas the increased amount of passengers can be regarded as a benefit, there are also negative consequences. Due to the higher weight, a stronger structure is required and the control surfaces would have to be increased. Since the CO_2 emissions are determined per passenger kilometre, more LNG on board is allowed. However due to the large mass increase, more energy is needed which cannot be provided solely by the allowed amount of LNG. This could be solved by using a larger battery. However, less storage room is available due to the twin deck configuration.

Summarising, this family concept is feasible if the market shows a demand for a larger passenger capacity short range aircraft. However, it will not be as sustainable as the original EuroFlyer, because a larger brother will not be able to fully comply with these emission requirements. Next to that, due to the higher gross weight, the propulsive system has to provide more power, which leads to higher noise levels and with the small margins compared to ICAO Chapter 4, this concept might not fulfil the noise requirement.

16.5.2 Long Range

During the market analysis, a possibility to extend the EuroFlyer market was found in the USA. Here, the average flight was found to be around 1300 km, which is within the EuroFlyer range. However to really infiltrate in this market, this family concept would have to have an increase in range and in passengers: as the 1300 km is an average value, there are many flights longer than this. This result can be achieved by up scaling the completely aircraft. With this increase the fuselage dimensions has to be altered. As a result, the energy and propulsive system will also have to redesigned according to the fuselage and payload changes.

16.5.3 Cargo Transport

A completely different direction for the EuroFlyer could be as a cargo transporter, where the wide fuselage set-up offers large storage volume. Because cargo transport vehicles have a higher payload weight and different regulations for emissions, removing the batteries seems to be a reasonable option. Due to the configuration change, significant weight reduction can be achieved by removing furnishings. This, and removing the batteries, leads to an increased payload capacity for the transport family concept.

Concluding, there are some feasible possibilities for integrating the EuroFlyer into the different markets. These concepts will however not be able to exceed the level of sustainability of the current EuroFlyer, but will still be a great improvement compared to today's aircraft.

CHAPTER 17

Cost Analysis

An aircraft might perform perfectly, but if this comes at a huge cost, it will most definitely not be a best-seller. In this chapter, a cost analysis for the proposed EuroFlyer concept is presented. Section 17.1 deals with acquisition cost, Section 17.2 investigates the cost associated to operate the aircraft.

17.1 Acquisition Cost

To estimate the unit cost of an aircraft, comprised of Research, Development, Testing and Evaluation Cost (RDT&E) and Program Cost, two methods are well known. One of these is defined by Raymer [34]; the other by Roskam [31]. Seemingly different, both methods are based on the DAPCA IV model, developed by the Rand Corporation in 1987 [103]. This model might not give the most accurate Cost Estimating Relationship (CER) for a particular class of aircraft, but performs well over a wide design range. Also, and maybe even more important in this design phase, documentation is good and the number of design parameters that the method requires is low. Due to the more extended adaptation of Roskam, it is chosen to stick to that particular method.

The acquisition cost is split up in two parts. First, the RDT&E cost is determined, next the program cost is computed. In the following subsections, each of these steps is explained. Due to the fact that the method is fairly old, the total unit cost is scaled by a correction factor, based on the comparison of estimated and true cost for a set of reference aircraft. This is further explained in Section 17.1.3.

17.1.1 Research, Development, Testing and Evaluation Cost

This cost is split up in seven steps. For an extensive description, the reader is referred to the original work [31], but the most important steps are mentioned below. Please note that all costs are expressed in 1970 USD and that inflation is corrected afterwards [104] (one dollar in 1970 has about the same purchasing power as six dollars in 2013).

Airframe Engineering and Design Cost (C_{aed_r})

This cost is a function of AMPR weight (Aeronautical Manufacturers Planning Report), maximum speed, the number of aircraft produced for the RDT&E phase, a complexity factor, a factor accounting for the use of computer design, and the hourly engineering rate. The AMPR weight is statistically related to the take-off weight according to Eq. 17.1.

$$W_{ampr} = 10^{0.1936+0.8645 \cdot \log(W_{TO})} \tag{17.1}$$

For a take-off weight of 27840 kg, the AMPR weight is computed to be 10865 kg or 23952 lbs. The maximum speed is set at the Equivalent Air Speed in cruise conditions (200 m/s or 389 kts) and it is assumed that five test aircraft are produced. The complexity factor, F_{diff} is set at 2 (the highest value) due to the fact that the EuroFlyer design is innovative. F_{cad} is set at 0.8 (indicating that the aircraft manufacturer producing the EuroFlyer would have extensive experience with CAD-programs). The engineering rate, R_{aed_r} is set at a value of 18 USD per hour. These parameters are combined to yield C_{aed_r} in Eq. 17.2 below.

$$C_{aed_r} = 0.0396 \cdot W_{ampr}^{0.791} \cdot V_{max}^{1.526} \cdot N_{rdte}^{0.183} \cdot F_{diff} \cdot F_{cad} \cdot R_{aed_r} \tag{17.2}$$

Substituting the above values yields a value of 39, 896, 333 (1970 USD).

Development Support and Testing Cost C_{dst_r}

Much of the above parameters are also used to estimate the cost associated to the testing of various parts and subsystems, as can be seen from Eq. 17.3. The cost escalation factor (CEF) is set to 1, as the cost is computed in 1970 USD.

$$C_{dst_r} = 0.008325 \cdot W_{ampr}^{0.873} \cdot V_{max}^{1.890} \cdot N_{rdte}^{0.346} \cdot CEF \cdot F_{diff} \tag{17.3}$$

Substitution yields a value of 15, 168, 608 (1970 USD).

Flight Test Aeroplanes Cost C_{fta_r}

C_{fta_r} is quite a lot more complicated to compute than the above cost factors. The cost of test aircraft comprises engine and avionics cost, manufacturing cost (both material and labour), testing cost and quality control cost.

- **Engine and Avionics cost**
  Estimating the engine and especially the avionics cost has proven to be quite difficult. As the statistical relations for engine and propeller cost provided by Roskam are not very up-to-date, the team has chosen to work with more recent reference data for engine cost [20, 105], which is included in Appendix E. The corresponding relation is shown in Eq. 17.4. Please note that, contrary to most other values, this is expressed in 2013 USD.

  $$C_{e_r} = 1112.9 \cdot P_{sh}^{0.8786} \tag{17.4}$$

  Eq. 17.5 is used to obtain the propeller cost and stems from the original Roskam method. This computed cost is in 1989 USD.

  $$C_{p_r} = 10^{0.7746 + 1.1432 \cdot log(SHP_{TO})} \tag{17.5}$$

  Working with a shaft horsepower of 22313 SHP_{TO} (corresponding to a power output of 1.6504 MW per engine), the engine and propeller cost follow as 161, 422 and 12, 302 per engine or propeller in 1970 USD. For avionics, data were even scarcer and was therefore omitted. This is allowed as the final unit cost is corrected using reference aircraft, and this will also compensate for the left-out avionics. The battery cost has to be accounted for separately. It is expected that by 2030, the cost per unit of energy has decreased to a value between 200 and 250 USD/Wh [106, 107]. The more conservative latter value will be used in further calculations. Based on the energy requirement and the fact that batteries are only discharged 63%, the total battery cost is given as 104, 416 1970 USD. Given that only three of five aircraft will be used for flight testing, the total cost is 1, 355, 594 USD.

- **Manufacturing Labour Cost**
  The manufacturing labour cost depends on variables explained before and is based on a hourly labour rate of 11 USD. Eq. 17.6 shows the equation used.

  $$C_{man_r} = 28.984 \cdot W_{ampr}^{0.740} \cdot V_{max}^{0.543} \cdot (N_{rdte} - 2)^{0.524} \cdot F_{diff} \cdot R_{man_r} \tag{17.6}$$

  This yields a value of 65, 729, 821 USD in 1970.

- **Manufacturing Material Cost**
  The material cost associated with manufacturing the aircraft considered builds on many familiar variables, as Eq. 17.7 shows.

  $$C_{mat_r} = 37.632 \cdot F_{mat} \cdot W_{ampr}^{0.689} \cdot V_{max}^{0.624} \cdot N_{rdte}^{0.792} \cdot CEF \tag{17.7}$$

  F_{mat} is a factor that depends on the selected material. This value is set at 3 (for carbon composite airframes). Substituting the values, the material cost is computed to be 17, 362, 091 USD in 1970.

- **Tooling Cost**
  The tooling cost follows from AMPR weight, maximum speed, RDT&E production volume (N_{rdte}) and rate (N_{r_r}, set to 0.33 as advised by Roskam), complexity factor and a hourly rate of 13 USD. Adding and multiplying these factors as shown in Eq. 17.8 yields a tooling cost of 60, 954, 253 1970 USD.

  $$C_{tool_r} = 4.0127 \cdot W_{ampr}^{0.764} \cdot V_{max}^{0.899} \cdot N_{rdte}^{0.178} \cdot N_{r_r}^{0.066} \cdot F_{diff} \cdot R_{tool_r} \tag{17.8}$$

- **Quality Control Cost**
  Based on [31], the quality control cost is set at 13% of the manufacturing labour cost. This yields a total sum of 8, 544, 877 USD in 1970.

The total cost associated to (flight) test aircraft then equals 136, 584, 544 1970 USD.

Flight Test Operations Cost C_{fto_r}

Flight test operations cost can be estimated using Eq. 17.9. F_{obs} is a factor compensating for the possible importance of low visibility during testing. Since this is of no concern to the EuroFlyer team, this factor is set to its basis value of 1.

$$C_{fto_r} = 0.001244 \cdot W_{ampr}^{1.160} \cdot V_{max}^{1.371} \cdot (N_{rdte} - 2)^{1.281} \cdot CEF \cdot F_{diff} \cdot F_{obs} \tag{17.9}$$

Substituting the aforementioned values allows for finding a flight test operations cost of 4,340,650 USD.

Test and Simulation Facilities Cost C_{tsf_r}

Whereas the previously discussed Development Support and Testing Cost takes into account testing cost, it might sometimes be necessary to build new facilities. These expenses are accounted for, by applying a simple factor. The total RDT&E cost will be divided by this factor, F_{tsf_r}, which is set to 0.05 (corresponding to the situation where little new facilities are required).

Financing Cost C_{fin_r} and Profit C_{pro_r}

The most important driver for the financing cost for the entire RDT&E phase is the interest rate. This is estimated at 10% and applied using a factor (F_{fin_r}). An RDT&E profit is also accounted for by a factor, F_{pro_r}, of the total RDT&E cost. This is set to 10%.

Total RDT&E Cost

Logically, the total RDT&E cost sums the above cost, dividing by the various correction factors mentioned. This yields a total RDT&E cost of 261,320,181 1970 USD. Correcting for inflation over the period from 1970 to 2013 results in a present-day RDT&E cost of 1,565,307,881 USD. Table 17.1 summarizes the above results and shows how the RDT&E cost is built up.

Table 17.1: Research, Development, Testing & Evaluation Cost Breakdown

Cost factor	*Symbol*	*1970 USD*	*2013 USD*
Airframe Engineering and Design Cost	C_{aed_r}	39,893,333	238,979,037
Development Support and Testing Cost	C_{dst_r}	15,168,608	90,859,962
Flight Test Aeroplanes Cost	C_{fta_r}	136,584,544	818,141,420
Flight Test Operations Cost	C_{fto_r}	4,340,650	26,000,491
Test and Simulation Facilities Cost	C_{tsf_r}	13,066,009	78,265,394
Financing Cost	C_{fin_r}	26,132,018	156,530,788
Profit	C_{pro_r}	26,132,018	156,530,788
Total RDT&E Cost	C_{rdte}	261,320,181	1,565,307,881

17.1.2 Program Cost

Having spent the above total RDT&E cost does not result in an apron filled with aircraft that can be sold. During production, more costs are incurred because more aircraft are produced. This section summarizes the process used to compute this program cost.

Airframe Engineering and Design Cost C_{aed_m}

Most of the engineering and design cost is covered during the RDT&E phase, but some problems, iterations or analyses might only occur during the production run. These are computed using Eq. 17.10.

$$C_{aed_m} = 0.0396 \cdot W_{ampr}^{0.791} \cdot V_{max}^{1.526} \cdot N_{pr}^{0.183} \cdot F_{diff} \cdot F_{cad} \cdot R_{e_m} - C_{aed_r} \tag{17.10}$$

This equation is very similar to Eq. 17.2 presented above. The labour rate R_{e_m} for manufacturing is equal to the value used before, being 18 USD. A difference is found in the fact that the number of aircraft produced now comprises production rather than RDT&E aircraft. From the market analysis, presented in Chapter 6, it became clear that there exists a market for 1250 units. However, due to the influence of the production volume on the price, less positive estimates of 350 and 800 units are also considered. The total engineering and design cost therefore varies between 69,689,902 USD (1250 units), 61,095,659 USD (800 units) and 46,916,899 USD (350 units).

Aeroplane Production Cost C_{apc_m}

Contrary to before, now the interior cost is included. This is approximated to be 1,000 USD in 1990, which equals 310 1970 USD per passenger for regional transport aircraft. Multiplying with the number of passengers (79) yields an interior cost of 25,110 USD per aircraft. Summing engine and avionics cost, interior cost, manufacturing labour cost, manufacturing material cost, tooling cost and quality control cost yields production costs ranging from 2,446,464,701 USD (1250 units) to 1,800,327,319 USD (800 units) and 1,032,315,758 1970 USD (350 units).

Production Flight Test Operations Cost C_{fto_m}

Before aircraft are delivered, they undergo unit testing. The cost incurred in this phase can be found by the hourly operating cost (assumed to be 2,000 USD/hr), the number of flight test hours flown (assumed to be equal to eight) and an overhead factor. Lacking actual data, this is assumed to be equal to four. For the most optimistic production volumes, these costs are 80,000,000 USD. If only 800 units are produced, these reduce to 51,200,000 USD, to further lower to 22,400,000 USD for a production of 350 aircraft.

Financing Cost C_{fin_m} and Profit C_{pro_m}

A financing interest rate of 10% of the total program cost is assumed. Based on references [108], a profit of 16% of the total program is assumed.

Total Program Cost

The total program cost can be computed by summing engineering, design and production cost, and dividing by financing and profit rates. For the scenario in which 350 EuroFlyer aircraft are produced, the program cost can be computed to be 1,488,692,799 USD. The intermediate scenario of 800 units would result in program costs of 2,584,625,646 USD, further increasing to 3,508,317,030 USD if 1250 units are produced.

17.1.3 Total Acquisition Cost

The acquisition cost (list price) is computed by summing RDT&E and program cost, and dividing these by the number of aircraft produced. For the different scenarios, the acquisition cost then becomes 3,015,710 USD (1250 units), 3,557,432 USD (800 units) or 5,000,037 USD (350 units). Correcting for inflation over the period 1970 to 2013, these numbers change to 18,064,102 USD, 21,309,019 USD and 29,950,222 USD, respectively. Table 17.2 shows how this cost is broken down.

Table 17.2: Program Cost Breakdown

Cost factor	*Symbol*	350 units		800 units		1250 units	
		1970 USD	2013 USD	1970 USD	2013 USD	1970 USD	2013 USD
Airframe Engineering and Design Cost	C_{aed_m}	46,916,899	281,032,224	61,095,659	365,963,000	69,689,902	417,442,511
Aeroplane Production Cost	C_{apc_m}	1,032,315,758	6,183,571,388	1,800,327,319	10,783,960,638	2,446,464,701	14,654,323,557
Production Flight Test Operations Cost	C_{fto_m}	22,400,000	134,176,000	51,200,000	306,688,000	80,000,000	479,200,000
Financing Cost	C_{fin_m}	148,869,278	891,726,975	258,462,565	1,548,190,762	350,831,703	2,101,481,901
Profit	C_{pro_m}	238,190,845	1,426,763,159	413,540,103	2,477,105,219	561,330,725	3,362,371,042
Total Program Cost	$C_{program}$	1,488,692,799	8,917,269,745	2,584,625,646	15,481,907.618	3,508,317,030	21,014,819,011
Total RDT&E Cost	C_{rdte}	261,320,181	1,565,307,881	261,320,181	1,565,307.881	261,320,181	1,565,307,881
Total Cost		1,750,012,959	10,482,577,627	2,845,945,826	17,047,215.500	3,769,637,211	22,580,126,892
Acquisition Cos		5,000,037	29,950,222	3,557,432	21,309.019	3,015,710	18,064,102

As mentioned previously, in an effort to improve the quality of the estimation, the EuroFlyer design team has investigated the estimated cost of reference aircraft for which a list price is known. Due to the influence of the production volume of these aircraft, three scenarios have been investigated. The first has used the current production of the aircraft investigated, whereas the second uses the projected production (and, if not available, the total order backlog). A third scenario is based on the 1250 units estimated for the EuroFlyer and has normalized all aircraft production volumes against this value. Table 17.3 shows the results of the investigation [20, 109, 110, 31, 104]. Averaging all data yields a correction factor of 1.360. Applying this to the EuroFlyer cost estimated above results in a final (2013 USD) unit cost of 40.732.302 USD if 350 units are produced, 28.980.266 USD for 800 aircraft and 24.567.178 USD in case of 1250-unit case.

17.2 Operating Cost

Where the acquisition cost is just a one time expense, operation costs are a continuously returning cost. Therefore, the operating cost has a big influence on the profit made by airlines, which plays an important role in the success

Table 17.3: Comparison of Estimated and True Acquisition Cost, expressed in 2013 USD

Aircraft Model	True Cost	Current Production		Projected Production		Normalized Production		Average
		Projected Cost	Difference	Projected Cost	Difference	Projected Cost	Difference	
ATR 72-500	20,300,000	14,423,198		13,500,400		12,375,582		
Bombardier Dash-8	31,500,000	17,627,639		16,118,958		15,519,484		
XAC MA-600	14,420,000	22,818,036		15,729,961		8,869,993		
Average turboprop			1.207		1.460		1.801	1.489
COMAC ARJ21	30,240,000	36,475,628		30,223,153		24,166,930		
Embraer E170	36,600,000 [1]	27,425,159		23,879,853		23,496,170		
Embraer E190	44,240,000	32,282,969		28,965,903		29,442,796		
Average turbofan			1.155		1.338		1.393	1.295
Average			1.174		1.381		1.524	1.360

of the aircraft. This is the reason that a cost analysis of the operational cost cannot be forgotten. In this section, the operating cost will be elaborated, looking at the different aspects related to this cost. For this estimation, two different methods were used, therefore increasing the accuracy of the estimation. The two methods used are the ones provided by Roskam [31] and Liebeck [111].

First the Direct Operating Cost (DOC) are computed, followed by the Indirect Operating Cost (IOC). Note that the IOC will be a factor of 0.8 of the DOC, due to the fact that IOC strongly depends on the airline using the EuroFlyer. First all contributors to the DOC are elaborated and are shown later on in Table 17.4.

17.2.1 Crew Expenses

The crew expenses the contains the cost of wages, accommodation, transportation, meals and so on. The wages depend on standard starting wage plus some additional cost depending on the gross weight and the mission (international or domestic flights). Next to that, the wages are defined for the flight and cabin crew, where the flight crew have a fixed starting wage of 440 USD/hr and the cabin crew gets 78 USD/hr for international flights.

For the EuroFlyer it was found that a total of five crew members are required due to regulations. Two represent the flight crew and the other three the cabin crew. The only thing left to compute the cost of the crew per hour depends on the block time, which is the time from the moment the aircrafts' doors close till they open again at its destination and can be found with Eq. 17.11. This is found to be 2.65 hr. At last one can simply multiply the cost per hour with the corresponding number of crew members to find its total crew expenses of 1274 USD/hr.

$$T_{block} = 0.0021 \cdot Range + 0.94 \tag{17.11}$$

17.2.2 Fuel Cost

Where the cost of kerosene is expected to rise over the following years and the EuroFlyer is switching to LNG, the fuel costs are expected to drop compared to current day aircraft. The fuel cost per hour depends on a few variables, where the largest contribution is the cost of the main energy source. However, since the EuroFlyer will use both LNG and electricity it has to be computed slightly different.
By dividing the total cost of the 1248 kg LNG, $\pm 6GJ$ energy and an extra factor (0.08 of the LNG cost) for oil, by the total block time. For the EuroFlyer this results in a cost of 1022 USD/hr, which is around 12.5% of the TOC. Note that this is lower then the conventional aircraft, since the concept aircraft considered will consume less fuel, and use a different energy source.

17.2.3 Maintenance Cost

Maintenance cost exist out of two different groups, which can be found in cost due to maintenance of the airframe and engine. Both groups can be subdivided even further, looking at the cost due to labour, materials and an extra burden. Here the labour cost depends on the weight of the airframe or engine, the block time, number of yearly flights and the wage. From these variables, in combination with regulations, it is possible to define the amount of time needed to perform a maintenance. Next to that it represents the number of checks during it operating life. Maintenance cost can be found using the same variables and the cost of the airframe and engine. While the extra burden can be found multiplying the labour cost with a factor two. For the wages 66 USD/hr was taken as was found in Section. 17.1 (now corrected for 2013 USD). This results in a total maintenance cost, both engine and airframe of 750 USD/hr

17.2.4 Depreciation, Insurance and Interest

These three factors are affected by many variables, starting with depreciation. This can be found using the acquisition cost of the subsystems found in Section 17.1, the operating life of the subsystems and the spares of the systems. The interest can be found looking at the unit cost of both present and future values and the interest rate. For the interest rate a percentage of 5.54% was taken, which is the interest rate for 18 years [112] plus an extra rate of 2% [113]. Insurance only takes up a small contribution and is solely depending on the unit cost. Adding all these values result in extra cost of 1075 USD/hr

17.2.5 Airport Fees

Airport fees may vary in Europe, due to additional cost for emissions and noise produced. Luckily, the EuroFlyer is quite promising in reducing these emissions which should result in lower fees. However a baseline cost cannot be prevented. These depend on the gross weight of the aircraft. In addition, extra costs can be found in navigating fee. This result in a total fee cost of 436 USD/hr.

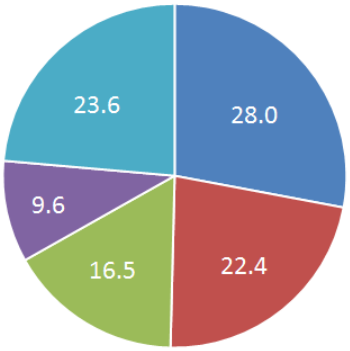

Figure 17.1: Direct Operating Cost Breakdown

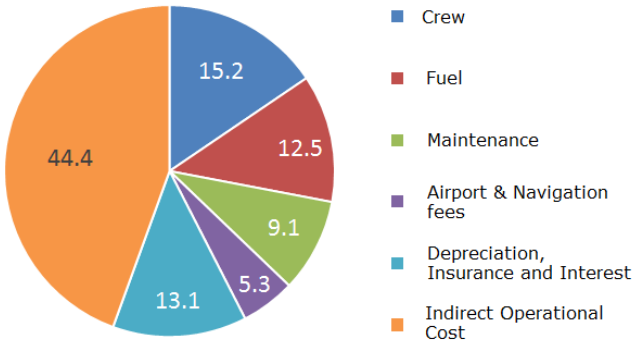

Figure 17.2: Total Operating Cost Breakdown

All calculated costs can be found in Table 17.4, where the cost are shown as an hourly rate and the total cost for its Operating Life (OL). Here, it was taken that the EuroFlyer will be operational nine hours a day on average, where the market analysis shows an operating life of 18 years. It was found that the hourly operating cost will be around 8,201 USD/hr which results in a total unit operational cost of 484.9 million in 18 years. At last, this it multiplied by 800 units, taken from the market analysis and results in a cost of 387,958,120,810 USD. In order to give a clear overview the contribution of each subgroup, two pie charts are shown, in Fig. 17.1. The left shows the percentages of the DOC and the right one, Fig. 17.2 of the total operation cost.

Table 17.4: Subsystem Operating Cost Breakdown

	USD/hr	$10^6 \cdot USD/OL$
Crew	1274	75.32
Fuel	1022	60.42
Maintenance	750	44.33
Airport Fees	436	25.76
Depreciation, Insurance and Interest	1075	63.59
Total Direect Operating Cost	4556	269.4
Indirect Operating Cost	3645	215.5
Total Operating Cost	8201	484.9

CHAPTER 18

Verification and Validation

This section elaborates on the verification and validation procedures for the EuroFlyer. The main question to be answered is whether this concept can guarantee the design team that the product is able to meet all the relevant requirements, as found in the RDT and list of requirements. First the general outline will be discussed and after that the wind tunnel will be elaborated

18.1 Verification and Validation Outline

Verification yields as proof of compliance with design solution specifications and descriptive documents. Put differently, it can be understood as an objective evidence that the specified requirements have been fulfilled. Validation is in turn the proof that the product accomplishes the intended purpose based on stakeholder requirements. In other words, the design team can confirm by means of examination and provision of objective evidence that the particular requirements for a specific intended use are fulfilled.

There are different approaches to verify a design. Depending on risks related to the operation of the system, technology maturity, experience with technologies used in the concept and verification requirements from the customer, the design team can select a verification method for the different subsystems. The most frequently used verification methods are tests, analysis, simulation, inspection, and demonstration. As verification procedures need to be executed for each requirement, to show the product's compliance with that specific requirement, each verification effort needs to be carefully specified. A compliance matrix for the EuroFlyer, listing each requirement and whether this is met at the current stage of the design, can be found in Section 19.1.

In a first preparation phase, the requirement needs to be validated according to the Verifiable, Achievable, Logical, Integral and Definitive (VALID) standards. In this case a (numerical) are used in the verification procedure. The models need to be defined in advance and validated for the specific requirement. Secondly, the verification activity needs to be planned. The objectives of the verification task needs to be established, as well as the most suitable verification type. One can certainly not forget about the given budget, in terms of time, people, facilities and the determination of the required inputs and outputs. In addition, the potential risks associated to partial or non-fulfilment of a requirement should be assessed and a back-up plan should be present. Finally, the planning phase is concluded with the actual planning of the verification activities, which include number of runs and duration in case of a test, and documenting the verification plan. Once all these steps have successfully been completed, the actual verification procedures can be executed and documented.

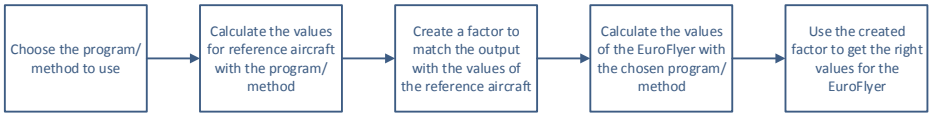

Figure 18.1: Verification Process for the EuroFlyer

For the EuroFlyer, several subsystems are be verified by means of simulation and analysis, given the limited time and budget of this project. Examples include the use of Computational Fluid Dynamics (CFD) and other computational tools such as XFLR5 to verify the aerodynamic properties used in the design process. Moreover, another approach was used both in the cost estimation and determination of aerofoil properties. The process is schematically represented in Fig. 18.1. The method uses reference data as input to a model to define comparison factors for more accurate and reliable prediction. Furthermore, a wind tunnel test will be conducted in one of the coming weeks to verify the predicted efficiency increase due to the implementation of the propulsive fuselage concept. The experiment aims to obtain actual measure for the reduction in energy consumption due to BLI. A more detailed description of the test can be found in Section 18.2.

Validation procedures for passenger aircraft include the development and construction of several prototypes, including the Qualification Model (QM) and Flight Model (FM). Within the given scope of this project, it is most likely that no validation procedures are performed and therefore these are not treated in more detail.

18.2 Windtunnel Experiments

Next to the design of the EuroFlyer, the team co-operated intensively with wind tunnel experiments conducted in the low wind speed tunnel lab at the Faculty of Aerospace Engineering at the TU Delft. With these tests, the benefit of Boundary Layer Ingestion (BLI) is investigated and compared to the theoretical expectations. Despite the fact that the results of these tests are not directly implementable into the design of the EuroFlyer, the BLI experiments are an extension of the DSE, with the goal of validating the efficiency gains expected from BLI.

18.2.1 Set-Up

To demonstrate the effect of BLI, three cases are tested: a drag estimation case, a BLI case and a free stream propeller case. This need in order to finally compute the efficiency difference between the latter two tests. The layout of the tests are shown in Fig. 18.2. The test setup consists of the following facilities:

1. Windtunnel (400 x 400 mm, V_∞= 0-32 m/s)
2. Detachable Axis-Symmetric Body
3. Air Bearing / Connection / Struts
4. Drag Sensor (KD 40S-2N)
5. Propeller Test Rig: DC Motor (Maxon 310007 60W) Thrust Balances RPM Meter
6. Propellers (APC 4.1X4.1 / GRAUPNER 4.7X4.7 / 4.75X4.75 / 5X5 / 5.5X5.5)
7. DC Power (30V, 2A)

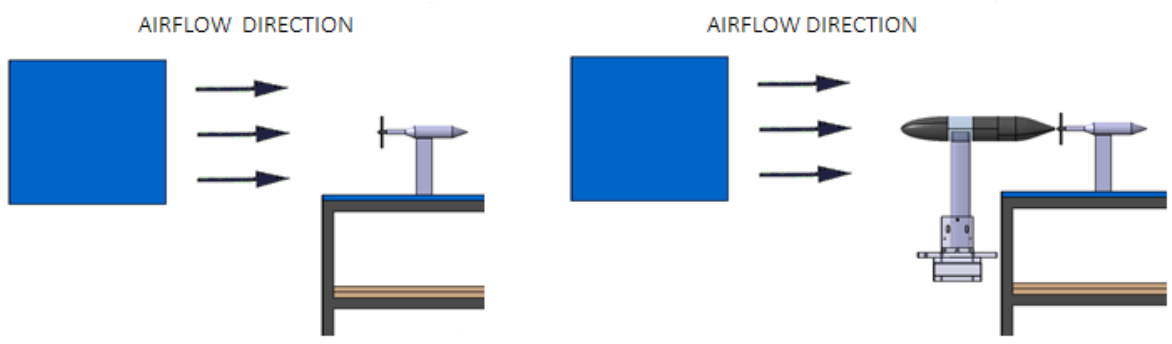

Figure 18.2: Test Set-up without (left) and with BLI (right)

Both the body and the propeller are set to an angle of attack of 0 *deg*. This implies that only the zero-lift drag (profile drag) and the energy related are investigated. In the two propelled scenarios thrust is set so that the $T = D$ condition is satisfied. Before testing begins the ambient temperature and pressure are noted. In every case, drag is measured for every integer increment in air speed velocity. In the two propelled scenarios, the thrust, power setting, voltage and amperage of the propeller is noted.

18.2.2 Data Processing

Between every case and before the results can be considered, the data needs to be processed. From the drag estimation case a strut drag, hub with strut drag and fixed total drag including body drag are observed. In the BLI scenario, the total drag is constantly measured as the suction of the propeller influences the body drag. To determine the thrust required some simple computations are required. In the BLI case, thrust is equal to the total constantly measured total drag subtracted by the fixed hub with strut drag. In the free stream propeller case, the thrust is set to be equal to the fixed total drag subtracted by the hub with strut drag.

18.2.3 Results

As the main goal of the experiment was to validate the effect of BLI, this is the aspect which is assessed from the results. In Fig.18.3 a plot shows the absolute difference in power and drag for every speed increment which are linked. The plot clearly indicates an increase in drag for the BLI case. Although the drag increases, power is notably reduced. This means that the BLI scenario is significantly more efficient and validates the theoretical results in our design.

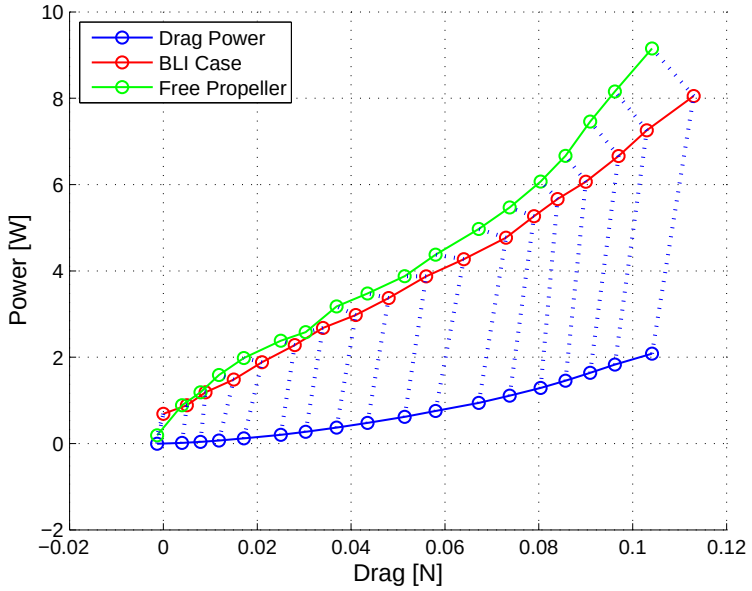

Figure 18.3: Results of the Experiment

18.2.4 Discussion

The efficiency gain of BLI proved significant (12%), however the experiment has quite a few differences with respect to the EuroFlyer. First of all, scalability is an issue as the Reynolds number of the test model and the EuroFlyer design differ significantly. The second discrepancy is the low mechanical efficiency of the motor used in the test. This influences the amount of efficiency gain found in the test. As to how much the real efficiency gain would be a scaled model has to be tested. Another point of interest for future experiments are the blade profiles which can be tested. Currently the same profile was tested in all cases. However the blade implemented in the test is optimised for a freesteam scenario. If in the BLI case an optimised profile would be used, the BLI gains would be even more pronounced. Furthermore, a point of discussion for the EuroFlyer design is that the drag increase of the fuselage is assumed to be negligible as the modelling of this was assumed out of the scope of the project. The experiment shows that the influence of the increased drag is a point which definitely has to be investigated in the future. Nevertheless, the goal of the experiment to validate the expected effects of BLI was successful.

CHAPTER 19

Compliance Matrix and Feasibility

As the design process has been concluded and the performance and specifications of the EuroFlyer are established, it is now possible to verify if the requirements mentioned in the project guide were met. In order to do so, a so called compliance matrix is made which contains the requirements and the indication of if it was met, partially met or not met. The basic structure of this chapter is divided into two sections, where Section 19.1 provides the compliance matrix and the feasibility analysis in Section 19.2 provides the background information to certain requirements from the compliance matrix.

19.1 Compliance Matrix

In Table 19.1, the requirements from the project guide are listed and the corresponding outcome is shown. As all requirements are derived from those specified in the initial project outline, the compliance of the final design is also analysed with reference to the original requirements.

Table 19.1: Requirements Compliance Matrix

#	*Requirement*	*Compliance*
	Key Requirements	
1	A minimum of 80 passengers, including 23 kg of luggage each, shall be transported.	✓
2	The aircraft shall have a range of at least 2000 km.	-
3	The aircraft shall have the ability to use alternative fuels.	-
4	The aircraft shall be available on the market before 2035.	✓
5	A minimal cruise speed of 0.65 Mach at cruising altitude shall be achieved.	✓
6	The CO_2 emissions per passenger km should be reduced by 50% when compared to the Embraer E170 on the same mission, without making use of biofuels.	✓
7	Safe and comfortable travel within regulations (FAR/CS-25).	✓
8	The aircraft needs to comply with the standard infrastructure at regional airports.	✓
9	The aircraft needs to be able to land and take-off on the regional airports in Europe.	✓
10	The noise emission should be around 10dB less than ICAO Chapter 4.	✓
11	Design has to comply with CS-25 regulations.	✓

19.2 Feasibility Analysis

In Table 19.1, the key requirements of the EuroFlyer are specified. By means of a feasibility analysis, the reasoning behind the compliance of some highlighted requirements is provided.

The second requirement is marked as partially met since this requirement has been restated in consultation with the complete EuroFlyer team, lowering the design range of the EuroFlyer to 1500 km. This range followed from the results of the market analysis conducted in the initial phase of the design process. As discussed in Chapter 6, the average flight distance is much lower than the 2000 km specified in the initial requirements. To ensure a competitive design of the EuroFlyer on most of the European flight routes, the initial design range of 2000 km is lowered to 1500 km to avoid an over designed aircraft. The range of 1500 km was pinpointed as one of the maximum flight route lengths in Europe.

Since the year 1941, kerosene has been the primary jet fuel that powers the world's aircraft [114]. With LNG being the main power source of the EuroFlyer, a new era of jet fuel has been defined. The third requirement of the EuroFlyer states that the aircraft shall have the ability to utilise alternative fuel sources. Since using LNG as an energy source brings more difficulties than kerosene, such as cooling, it is expected that the EuroFlyer is able to operate on kerosine as well with slight modifications to the fuel system. The same goes for using alternative biofuels. The requirement has been marked as partially met as only small changes are necessary, however these changes have not been looked at into much detail.

The sixth requirement in the compliance matrix regarding the CO_2 emissions has the outcome that it is met. However, it is important to mention that this requirement was changed by the supervisor of the design team, as flying at a lower Mach number would imply that the original requirement could almost be met without any other major design changes. Therefore, the requirement was changed to 75% reduction in CO_2 emissions when compared to the Embraer, in order to make the design process more challenging for the EuroFlyer team.

Although met, the eighth requirement in Table 19.1 needs more explanation. As the EuroFlyer utilizes a hybrid energy system, which implies more complicated refuelling during loading and unloading manoeuvres, additional infrastructure at regional airports may be required. This is due to the design choice that the batteries are not recharged after one mission, but being completely replaced which could require special equipment and operations at regional airports. However, as the electrical mobility is expected to increase in the upcoming years, it is safe to assume that the airports are getting more prepared for electrical powered aircraft.

CHAPTER 20

Conclusion

In order to meet the set requirements, revolutionary design changes were made and a new type of aircraft is born. The propulsive system, consisting out of contra-rotating propeller, has been located at the aft of the aircraft. With this drastic configuration change, it is possible to make use of the propulsive fuselage concept. Boundary layer generated by the fuselage is ingested into the propellers resulting in a propulsive efficiency of 99.8%.

In addition, the EuroFlyer is one of the first aircraft which makes uses of a hybrid energy system. This system combines both Liquefied Natural Gas and batteries to create an environmentally friendly form of air transportation. The EuroFlyer makes use of new technologies such as spiriod winglets, trialling edge blowing, serrated blades and a chevron shaped shroud to further decrease emissions and noise pollution. During the iteration, the sensitivity to specific design parameters has been identified. From this analysis, it can be concluded that the implementation of a hybrid energy system leads to a particularly sensitive design.

The presented design satisfies almost all key requirements and even exceeds the goals set by ACARE since the EuroFlyer achieves an impressive 92% reduction in NO_x emissions. From a market perspective, the EuroFlyer acquisition cost ranges from 24 to 40 million current day USD, depending on the units produced. To attract airlines, the EuroFlyer is compatible with different seating configurations and energy system compositions. As a result, the aircraft can also be used as cargo transport or as long range aircraft, thereby extending its market and capabilities.

This project has proven that it is possible to design a new generation of environmentally friendly aircraft, even when subjected to strict regulations. Liquefied Natural Gas, just as a partially electrical propulsive system, is feasible and leads to significant advantages regarding fuel consumption and emissions.

CHAPTER 21

Recommendations

As stated in the preface of this report, it was not the team's goal to attain a flawless final result, able to compete with contemporary standard in industrial practice. It is not without reason that many years are spent before an idea of an aircraft can be transformed into a product that can be ready for production and performs according to its specifications. In the course of the project, the EuroFlyer design team has identified various areas in which more research could greatly benefit the design. In this chapter, these recommendations are discussed, to hopefully be picked up later and to contribute to a more refined design.

21.1 Conservative Design

Not entirely convinced or simply not knowledgeable enough, the team has chosen to design certain elements of the aircraft in a fairly conservative way. A prime example of this is the design of the distinguishing spiroid winglets that are mounted on the tips of the wings. Estimates by Guerrero et al. [46] have shown a decrease in induced drag that varies between 28 and 35%, whereas the team assumed a decrease of only 10%. Investigating this further might confirm the earlier results, or validate the more conservative assumption made.

Another recommendation is to further optimise the fuselage nose design as it is currently driven by visibility requirements. Even in the scope of these requirements, the selected shape might not be the one most optimal in terms of aerodynamics, cockpit layout and room for the installation of avionics systems.

Rather time consuming is the structural optimisation of wing and fuselage. In the former, the skin thickness is assumed constant over the entire length of the wing. This might be necessary to ensure safe flight, but it just might as well be a design that is too heavy. This also holds for the stiffening elements placed in the wings and the fuselage of the aircraft.

21.2 Energy Storage

The EuroFlyer is revolutionary in the fact that it uses a hybrid system to store the required energy. Based on a number of research projects, the performance of Lithium-air batteries was estimated, but tests are necessary to confirm these assumptions. Even harder to predict is battery cost. When the design progresses, this parameter should be under constant evaluation. Also lacking are safety regulations for the use of batteries in the propulsive system of an aircraft, but these regulations are only set up when aircraft manufacturers are considering using these solutions in their designs. With this conceptual study, the EuroFlyer design team has shown that these regulations are needed. The operations aspect closely touches upon this. Many questions are still remaining: are airlines or airports willing to invest into battery charging stations? Would these facilities be cheap enough to indeed guarantee the operating cost advantage over traditional fuels?

Working with the assumptions presented in this report, an APU and generator are required to convert part of the LNG into electrical energy, driving the electric engine. Currently, a gas generator is selected for this task, but the team sees a large potential for a fuel cell powered system. To further reduce emissions and increase

the energy efficiency, as compared to combustion engines, changing to fuel cells would allow for further design optimisation.

21.3 Propulsion

In theory, much progress can be made concerning engine performance. In an ideal case the turboprop engine would always run at its most efficient power setting, with another engine with a wider range of efficient performance assisting in cases where more power is needed. The energy required for this engine can be extracted from the turboprop engine, given that the power output is higher than the power required for propulsion. However, this is only possible in an ideal case. Currently, regulations do not permit such systems. Rather than giving up at that notion, the EuroFlyer design team would like to encourage policy makers to see if current regulations are still applicable or should be altered to allow for new and efficient technology to be utilized to their full extent.

A discipline that the team is lacking in is propeller blade design. The propellers have now been sized based on actuator disk theory and blade element theory, but a proper aerofoil selection was deemed out of the scope of this design project. The same goes for carefully determining the blade pitch and twist angles. In conjunction with verifying and altering the currently proposed design, research into new technologies can be performed. Various methods, such as serrated or swept blades, seem promising ways to reduce noise. Although the EuroFlyer already is a very quiet aircraft, further optimisation is necessary to ensure a small audible footprint in the further future of aviation.

The current design was assessed versus all existing safety regulations. However the novel propeller with shroud design is not categorized in current regulations. Therefore in following design stages, it is essential to certify this propulsive system.

Balancing on the verge between propulsion and aerodynamics is the technique of boundary layer ingestion. Theoretically proving significant reductions in fuel burn, these claims have to be verified and validated before the idea can be used on a large scale. In a later addendum to this Final Report, the team hopes to share some preliminary test results of research investigating the true effectiveness of BLI, partially fulfilling the recommendation made here.

21.4 Shroud

The shroud surrounding the propellers, is closely related to the propulsive system. Lacking time to design this part in more detail, the team has chosen an aerofoil that does not interfere with the interior shroud aerodynamics. However, it might be more efficient to use an aerofoil that generates lift towards the propeller. This configuration has been investigated and proven beneficial in high cruise speed situations. The principle is that the pressure inside the shroud is augmented with the result that the propeller energizes a larger volume of air. To validate whether this concept is beneficial for the EuroFlyer design, tests have to be conducted.

21.5 Operations

This DSE focusses on the design of an environmentally friendly aircraft, in addition, research can be extended to design an environmentally friendly aircraft operating system. For this, the component of operations would be an important addition. Only touching upon this aspect in selected parts, the effects of ground assisted taxiing or Continuous Descent Approaches (CDA) were unfortunately not investigated. Similarly, it is not taken into account that the definition of regional airport might change in the next two decades, due to the continued growth of the air transport market. Larger airports might not limit the wingspan to 36, which would possibly allow to further increase aspect ratio.

Continuous descent approaches were already mentioned in the previous paragraph, but even if these protocols would not be applicable to the EuroFlyer mission, the mission characteristics can be further analysed. Checking the power requirements in the various flight phases would be a first step. Seeing how these can be lowered would yield optimisation in a different field.

Bibliography

[1] AGAPE, "ACARE Goals Progress Evaluation." **http://ec.europa.eu/research/transport/projects/items/agape_en.htm**, 2013. Consulted 25-04-2013.

[2] Bombardier, "Commercial Aircraft Market Forecast 2012 - 2031." Report, 2012.

[3] A. Gangoli Rao, "Project Guide Design Synthesis Exercise - EUROFLYER." Project Guide, 2013. Internal Publication.

[4] United Nations, "Report of the World Commission on Environment and Deveopment." **http://www.un.org/documents/ga/res/42/ares42-187.htm**, 1987. Consulted 02-05-2013.

[5] Sustainable Aviation, "CO_2 Roadmap," 2008.

[6] C. Droney, D. Paisley, B. Roth, S. Gowda, and M. Kirby, "Subsonic Ultra Green Aircraft Research – SUGAR." Final Review, 2010.

[7] J. Penner, D. Lister, D. Griggs, D. Dokken, and M. McFarland, "Aviation and the Global Atmosphere." GRID-Arendal, 2000. Internal Publication.

[8] "Questions, Answers on Aviation, Climate Change." European Union Press Release, 2005. Internal Publication.

[9] B. Owen, D. Lee, and L. Ling, "Flying into the Future: Aviation Emissions Scenarios to 2050." Dalton Research Institute, 2009. Internal Publication.

[10] S. Putt del Pino and P. Bhatia, "Working 9 to 5 on Climate Change: An Office Guide," tech. rep., World Resources Institute, 2002.

[11] R. S. D. Casalino, F. Diozzi and A. Paonessa, "Aircraft noise reduciton technologies: A blibliographic review," *ScienceDirect*, 2008.

[12] Airbus, "Global Market Forecast 2012 - 2031 – "Navigating the Future"." Report, 2012.

[13] ATR, "Regional Market Outlook - Turboprop Perspectives 2010 - 2029." Report, 2010.

[14] Boeing, "Current Market Outlook 2012 - 2031." Report, 2012.

[15] Embraer, "Market Outlook 2010 - 2029." Report, 2010.

[16] S. Bosma, A. Eggermont, R. Heuijerjans, F. Kruijssen, S. Leest, M. Meijburg, K. Morias, F. van den Oudenalder, B. Peerlings, and K. van Zomeren, "Mid-Term Report," tech. rep., Delft University of Technology, 2013.

[17] International Air Transport Association, "Airline Fuel and Labour Cost Share," 2010.

[18] R. Babikian, S. Lukachko, and I. Waitz, "The Historical Fuel Efficiency Characteristics of Regional Aircraft from Technological, Operational and Cost Perspectives," *Journal of Air Transport Management*, 2002.

[19] US Energy Information Administration, "Petroleum , Other Liquids." Review, 2013.

[20] P. Jackson, *Jane's All the World's Aircraft*. IHS Jane's, 2012-2013.

[21] Airfleets.net, "Airfleets Aviation – Production List." **http://www.airfleets.net/home/**, 2013. Consulted 02-05-2013.

[22] Avolon, "Aircraft Retirement Trends, Outlook." Report, 2012.

[23] Embraer, "E-Jets Family." **http://www.flyswedish.eu/press/E-170.pdf**, 2007. Consulted 02-06-2013.

[24] G. La Rocca, "Aerospace Design and Systems Engineering Elements II." Lecture Slides, 2011. Internal Publication.

[25] T. C. Corke, "Design of Aircraft," 2013. Consulted 12-06-2013.

[26] M. Isidoro, "Aircraft Environmental Control," 2013. Consulted 12-06-2013.

[27] R. Vos and B. Zandbergen, "Aerospace Design and Systems Engineering Elements I." Lecture Slides, 2011. Internal Publication.

[28] C. Tang and J. D. Zimmerman, "Managing New Product Development and Supply Chain Risks: The Boeing 787 Case," 2013. Consulted 12-06-2013.

[29] R. Vos and B. Zardbergen, "Fuselage Design Part II," 2010. Consulted 12-06-2013.

[30] O. Gur, W. Mason, and J. Schetz, "Full-Configuration Drag Estimation," tech. rep., Virginia Polytechnic Institute and State University, 2010.

[31] J. Roskam, *Aircraft Design*. Roskam Aviation and Engineering Corporation, 1985.

[32] European Aviation Safety Agency, "Certification Specifications and Acceptable Means of Compliance for Large Aeroplanes CS-25," 2012.

[33] M. C. Niu, *Airframe Structural Design*. Hong Kong Conmilit Press Ltd., 1988.

[34] D. Raymer, *Aircraft Design: A Conceptual Approach*. American institute for Aeronautics and Astronautics, 3 ed., 1999.

[35] N. S. Currey, *Aircraft Landing Gear Design: Principles and Practices*. AIAA Education Series, 2004.

[36] Airliners.net, "The British Aerospace BAe-146." **http://www.airliners.net/aircraft-data/stats.main?id=45**, 2013. Consulted 20-06-2013.

[37] L. Rosa, "Landing Gear of WDL BAe 146." **http://www.flickriver.com/photos/lrosa/528118438/**, 2007.

[38] A. Deperrois, "XFLR5." Program.

[39] I. Abbott and A. Von Doenhoff, *Theory of Wing Sections*. Dover Publications Inc., 1958.

[40] Airbus, *A320 Aircraft Characteristics Airport and Maintenance Planning*. Airbus, 1985.

[41] International Civil Aviation Organization, "Aerodrome Standards," tech. rep., ICAO, 1999.

[42] G. La Rocca, "Wing Design Part II," 2011. Internal Publication.

[43] E. Gill and G. La Rocca, "Aerospace Design and Systems Engineering Elements II." Lecture Slides, 2012. Internal Publication.

[44] S. F. Hoerner, *Fluid-Dynamic Drag*. Hoerner Fluid Dynamics, 1965.

[45] D. Howe, *Aircraft Conceptual Design Synthesis*. ESDU, 2000.

[46] J. Guerrero, D. Maestro, and A. Bottaro, "Biomimetic Spiroid Winglets for Lift and Drag Control," tech. rep., University of Genoa, 2011.

[47] R. L. Bisplinghoff, H. Ashley, and R. L. Halfman, *Aeroelasticity*. Addison-Wesley Publishing Company, 1983.

[48] L. Nicolai and G. Carichner, *Fundamentals of Aircraft and Airship Design*. American Institue of Aeronautics and Astronautics, 2010.

[49] G. Rogers, "Propeller Efficiency - Rule of Thumb," tech. rep., American Bonanza Society, 2010.

[50] D. Howe, *Aircraft Conceptual Design Synthesis*. Professional Engineering Publishing, 2000.

[51] G. Ruijgrok, *Elements of Airplane Performance*. VSSD, 2009.

[52] Z. Spakovsky, "Unified: Thermodynamics and Propulsion," tech. rep., Massachusetts Institute of Technology, 2007.

[53] J. Roskam and E. Lan, *Aircraft Conceptual Design Synthesis*. Roskam Design, Anlysis and Research Corporation, 1997.

[54] S. Slavìk, "Preliminary Determination of Propeller Aerodynamic Characteristics for Small Aeroplanes," tech. rep., Acta Polytechnical, 2004.

[55] B. Zandbergen, "Power and Propulsion Course." Lecture Slides, 2012. Internal Publication.

[56] J. Frauenhofer, "Erste Prüfergebnisse 4-MW-HTS-Motor." Braunschweiger Supraleitersseminars, 2010.

[57] P. J. Masson, "HTS Machines for Applications in All-Electric Aircraft." PES General Meeting, 2007.

[58] J. Banke, "NASA Helps Create a More Silent Night." Directorate, 2010.

[59] M. Lazzereff, "Aerodynamics of Shrouded Propellers." Reasearch Report, 1968. Internal Publication.

[60] Embraer, "E-Jets Family." **http://www.flyswedish.eu/press/E-170.pdf**, 2007. Consulted 02-06-2013.

[61] R. L. Martin, "Method 2 for Computing In-Flight Aircraft Engine Emissions," in *Scheduled Civil Aircraft Emission Inventories for 1992: Database Development and Analysis*, 1992.

[62] The Engineering Toolbox, "Fuels Combustion - Nitrogen Oxides Emission." **http://www.engineeringtoolbox.com/nox-emission-combustion-fuels-d_1086.html**, 2013. Consulted 07-06-2013.

[63] G. Girishkumar, B. McCloskey, A. C. Luntz, S. Swanson, and W. Wilcke, "Lithium-Air Battery: Promise and Challenges," *Journal of Physical Chemistry Letters*, pp. 2193–2203, 2010.

[64] S. Visco, E. Nimon, B. K. en Lutgard De Jonghe, and M.-Y. Chu., "High Energy Density Lithium-Air Batteries with No Self Discharge," in *Proceedings of the 42nd Power Sources Conference*, pp. 201–203, 2012.

[65] L. Johnson, "The Viability of High Specific Energy Lithium-Air Batteries," in *Symposium on Research Opportunities in Electrochemical Energy Storage - Beyond Lithium Ion: Materials Perspectives*, 10 2010.

[66] PolyPlus Battery Company, "Lithium-Air." **http://www.polyplus.com/liair.html**, 2013. Consulted 05-06-2013.

[67] J. Zheng, R. Lang, M. Hendrickson, and E. Plichta, "Theoretical Energy Density of Li-Air Batteries," *Journal of The Electrochemical Society*, vol. 155, no. 6, pp. A432 – A437, 2008.

[68] S. St'uckl, J. van Toor, and H. Lobentanzer, "VoltAir - The All-Electric Propulsion Concept Platform," in *Proceedings of the 28th International Congress of the Aeronautical Sciences*, 2012.

[69] A. Friedrich, N. Wagner, and W. Bessler, "Entwicklungsperspektiven von Li-Schwefel- und Li-Luft-Batterien," in *Energie Speicher Symposium*, (Stuttgart, Germany), DLR, 2012.

[70] F.P. Incropera and D.P. De Witt and T.L. Bergman and A.S. Lavine, *Fundamentals of Heat and Mass Transfer*. Wiley, 2006.

[71] Shippipedia, "GAS Carrier." **http://www.shippipedia.com/ships/ship-types/tanker/gas-carrier/**, 2013. Consulted 11-06-2013.

[72] R. Doganis, *Flying Off Course*. Routledge, 1985.

[73] C. Halasz, "Advanced Trailing Edge Blowing Concept for Fan Noise Control: Experimental Validation," tech. rep., Virginia Polytechnic Institute, 2005.

[74] E. Gill and G. La Rocca, "Systems Engineering and Aerospace Design." Lecture Slides, 2013. Internal Publication.

[75] Stanford, "Tail Design and Sizing." **adg.stanford.edu/aa241/stability/taildesign.html**.

[76] M. H. Sadraey, *Aircraft Design; A Systems Engineering Approach*. Wiley, 2012.

[77] J. D. Anderson, *Introduction to Flight*. McGraw-Hill, 2008.

[78] D. Casalino, F. Diozzi, R. Sannino, and A. Paonessa, "Aircraft Noise Reduction Technologies: A Bibliographic Review," tech. rep., Rotocraft Aerodynamics and Aeroacoustic Department, 2008.

[79] Airframe Noise Working Party, "Airframe Noise Prediction," tech. rep., ESDU International, 2008.

[80] Propeller Noise Working Party, "Prediction of Near-Field and Far-Field Harmonic Noise from Subsonic Propellers with Non-Axial Inflow," tech. rep., ESDU International, 2011.

[81] D. Hanson and D. Parzych, *Theory for Noise of Propellers in Angular Inflow with Parametric Studies and Experimental Verification*. NASA, 1993.

[82] J. Böttcher, "Noise Certification Workshop," 2004.

[83] M. Fink, *Airframe Noise Prediction Method*. NTIS, 1997.

[84] R. Rathgeber and D. Sipes, "The Influence of Design Parameters on Light Propeller Aircraft Noise," *SAE Technical Paper 770444*, 1977.

[85] W. Dobrzynski, "Almost 40 Years of Airframe Noise Research - What did we achieve?," 2008.

[86] J. I. Hileman, Z. Sparkovsky, M. Drela, M. Sargeant, and A. Jones, "Airframe Design for Silent Fuel-Efficient Aircraft," *Journal of Aircraft*, 2010.

[87] M. Herr, "Experimental Study on Noise Reduction through Trailing Edge Brushes," tech. rep., Institut für Aerodynamik und Strömungstechnik, 2005.

[88] W. Dobrzynski, K. Nagakura, B. Gehlhar, and A. Buschbaum, "Airframe Noise Studies on Wings with Deployed High-Lift Devices," *4th AIAA/CEAS Aeroacoustic Conference*, 1998.

[89] Y. Guo, "On Noise Reduction by Flap Side Edge Fences," *Journal of Sound and Vibration*, vol. 227, 2003.

[90] L. Lopes, "Prediction of Landing Gear Noise Reduction and Comparison to Measurements," tech. rep., NASA Langley Research Center, 2010.

[91] J. Lieser, D. Lohmnn, and C. Rohardt, "Aeroacoustic Design of a 60-Bladed Propeller," tech. rep., Aerospace Science and Technology, 1997.

[92] F. Metzger, "An Assessment of Propeller Aircraft Noise Reduction Technology," tech. rep., National Aeronautics and Space Administration Langley Research Center, 1995.

[93] W. Dobrzynski, "Propeller Noise Reduction by Means of Unsymmetrical Blade-Spacing," *Journal of Sound and Vibration*, 1993.

[94] C. Arce-Léon, "Modelling of Serrated Trailing Edges to Reduce Aerodynamic Noise in Wind Turbines Using Computational Fluid Dynamics," tech. rep., Department of Information Technology, 2010.

[95] S. G. C. Weckm'uller, "On the Influence of Trailing-Edge Serrations on Open-Rotor Tonal Noise," tech. rep., German Aerospace Center, Institue of Propulsion Technology, 2012.

[96] J. Anderson, *Aircraft Performance and Design*. McGraw-Hill, 1999.

[97] M. W. Austyn, *Aircraft Performance*. Cambridge Univeristy Press, 1992.

[98] B. W. MacCormick, *Aerodynamics, Aeronautics and Flight Mechanics*. Wiley, 1994.

[99] M. Voskuijl, "Flight Mechanics." Lecture Slides, 2013. Internal Publication.

[100] J. Ruijgrok, *Elements of Airplane Performance*. VSSD, 2009.

[101] NGSA, "Liquified Natural Gas." **http://www.naturalgas.org**, 2004. Consulted 08-06-2013.

[102] E. Gill, "System Engineering Methods." Lecture Slides, 2013. Internal Publication.

[103] R. Hess and H. Romanoff, "Aircraft Airframe Cost Estimating Relationships," tech. rep., Rand Corporation, 1987.

[104] InflationData, "Inflation Calculator." **http://inflationdata.com/Inflation/Inflation_Calculators/Inflation_Calculator.asp**, 2013. Consulted 06-2013.

[105] Deagel, "Powerplants." **http://www.deagel.com/Powerplants.htm**, 2012. Consulted 17-06-2013.

[106] EVsRoll, "Electric Car Battery Cost." **http://www.evsroll.com/Electric_Car_Battery_Cost.html**, 2012. Consulted 21-06-2013.

[107] C. Cluzel and C. Douglas, "Cost and Performance of EV Batteries," tech. rep., Element Energy Ltd., 2012.

[108] D. Visser, "Air Transportation." Lecture Slides, 2012. Internal Publication.

[109] Aircraft Compare, "Embraer E170." **http://www.aircraftcompare.com/helicopter-airplane/Embraer-170/118**, 2013. Consulted 17-06-2013.

[110] Aircraft Compare, "Embraer 190." **http://www.aircraftcompare.com/helicopter-airplane/Embraer-190/116**, 2013. Consulted 17-06-2013.

[111] R. H. Liebeck, *Advanced Subsonic Airplane*. NASA, 1995.

[112] Bankrate, "Mortgage Ratet." **http://www.bankrate.com/**, 2007. Consulted 16-06-2013.

[113] K. Zolotusky, "Boeing Capital Corporation," tech. rep., Boeing, 2009.

[114] Air BP Limited, "The History of Jet Fuel." **http://www.bp.com/sectiongenericarticle.do?categoryId=4503664&contentId=57733**. 26-6-2013.

[115] C. Bradshaw, "Blue Sky." **http://christopherbradshawphotography.com/?attachment_id=188**, 2012.

APPENDIX A

Functional Breakdown Structure

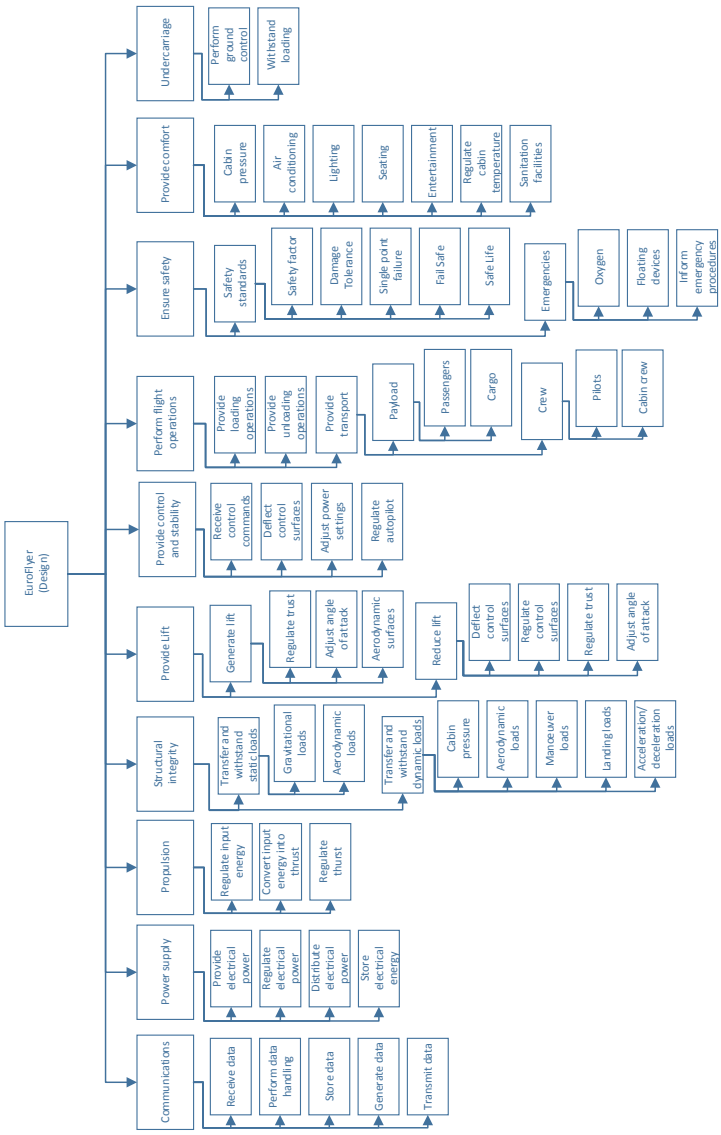

Figure A.1: Functional Breakdown Structure – Design

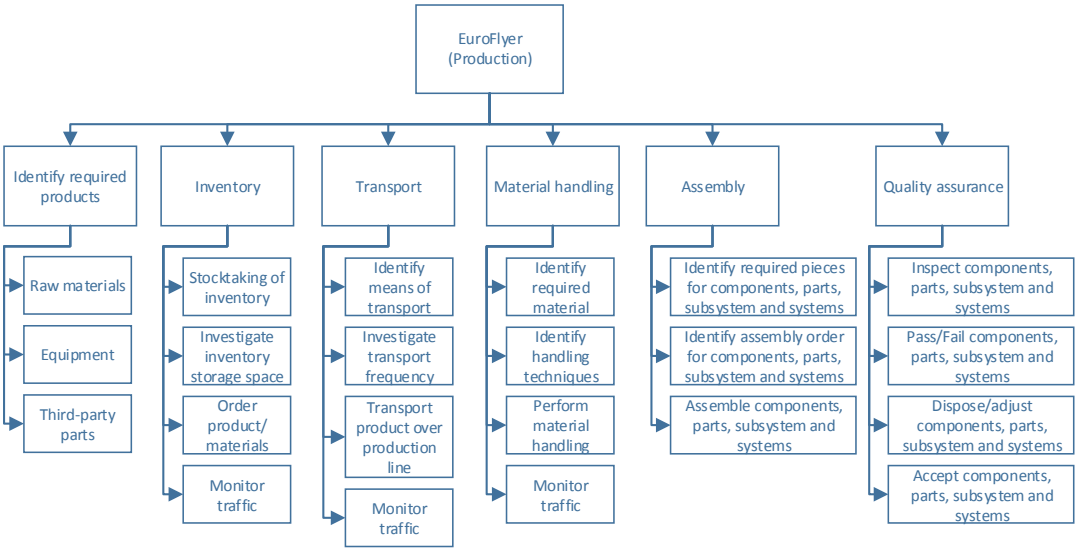

Figure A.2: Functional Breakdown Structure – Production

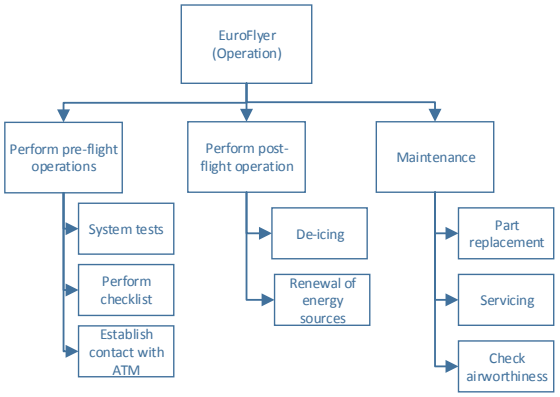

Figure A.3: Functional Breakdown Structure – Operation

APPENDIX B

Functional Flow Block Diagram

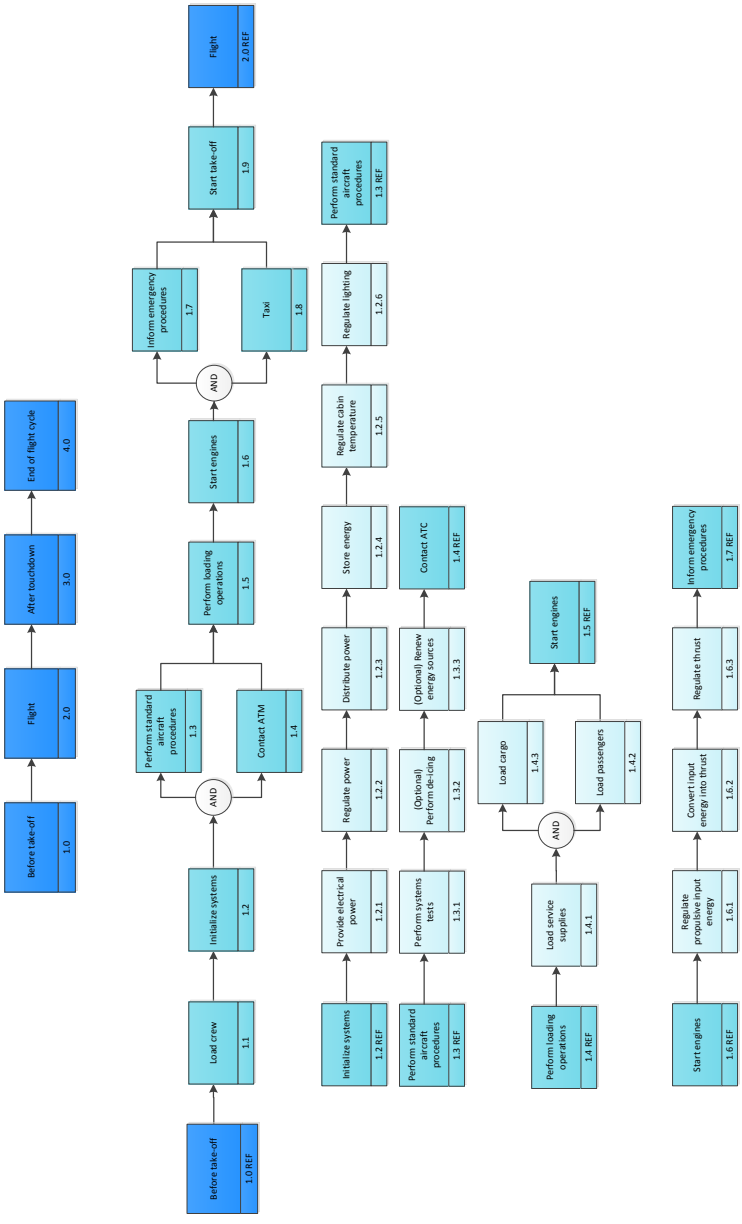

Figure B.1: Functional Flow Block Diagram of Lift-Off Stage

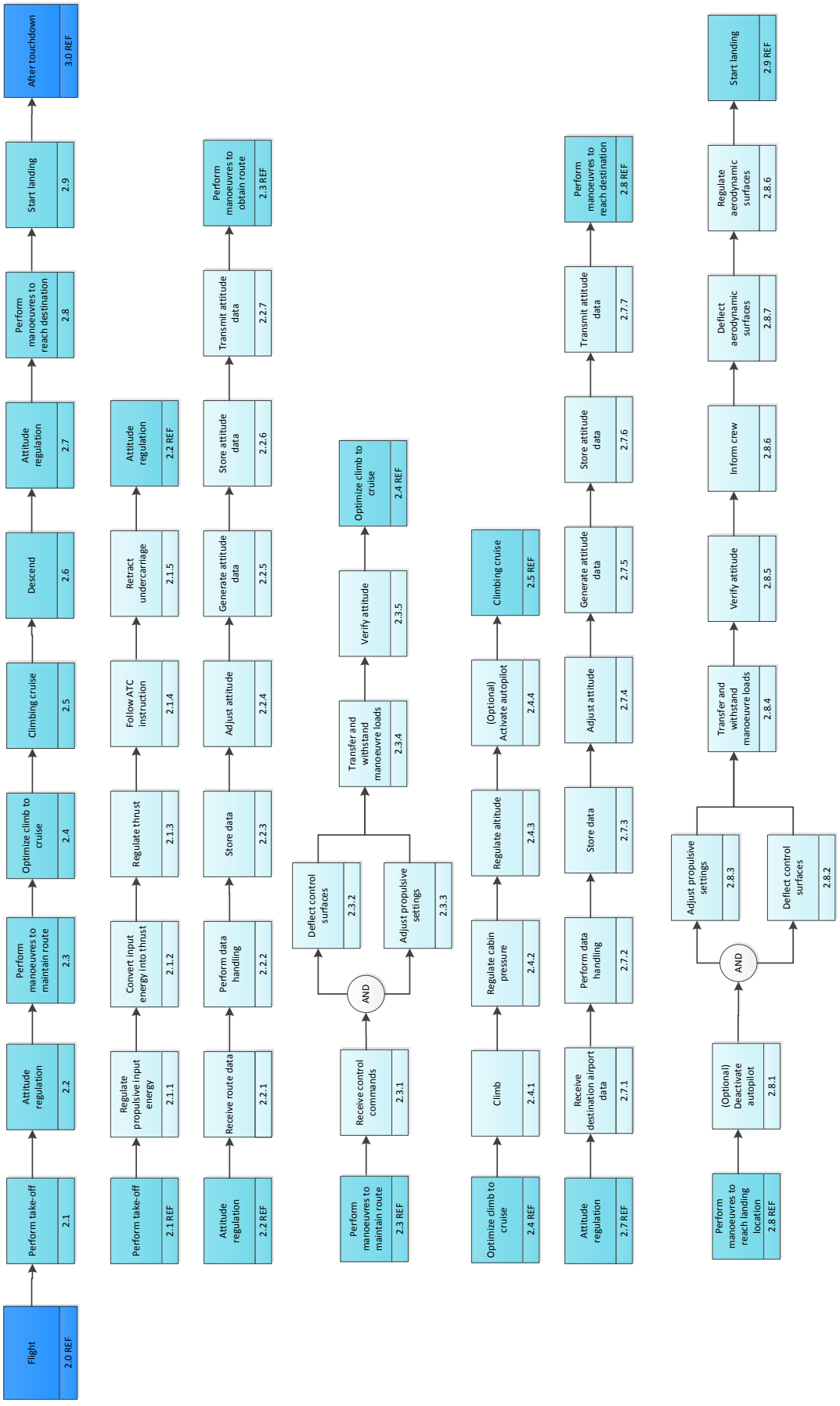

Figure B.2: Functional Flow Block Diagram of Flight Stage

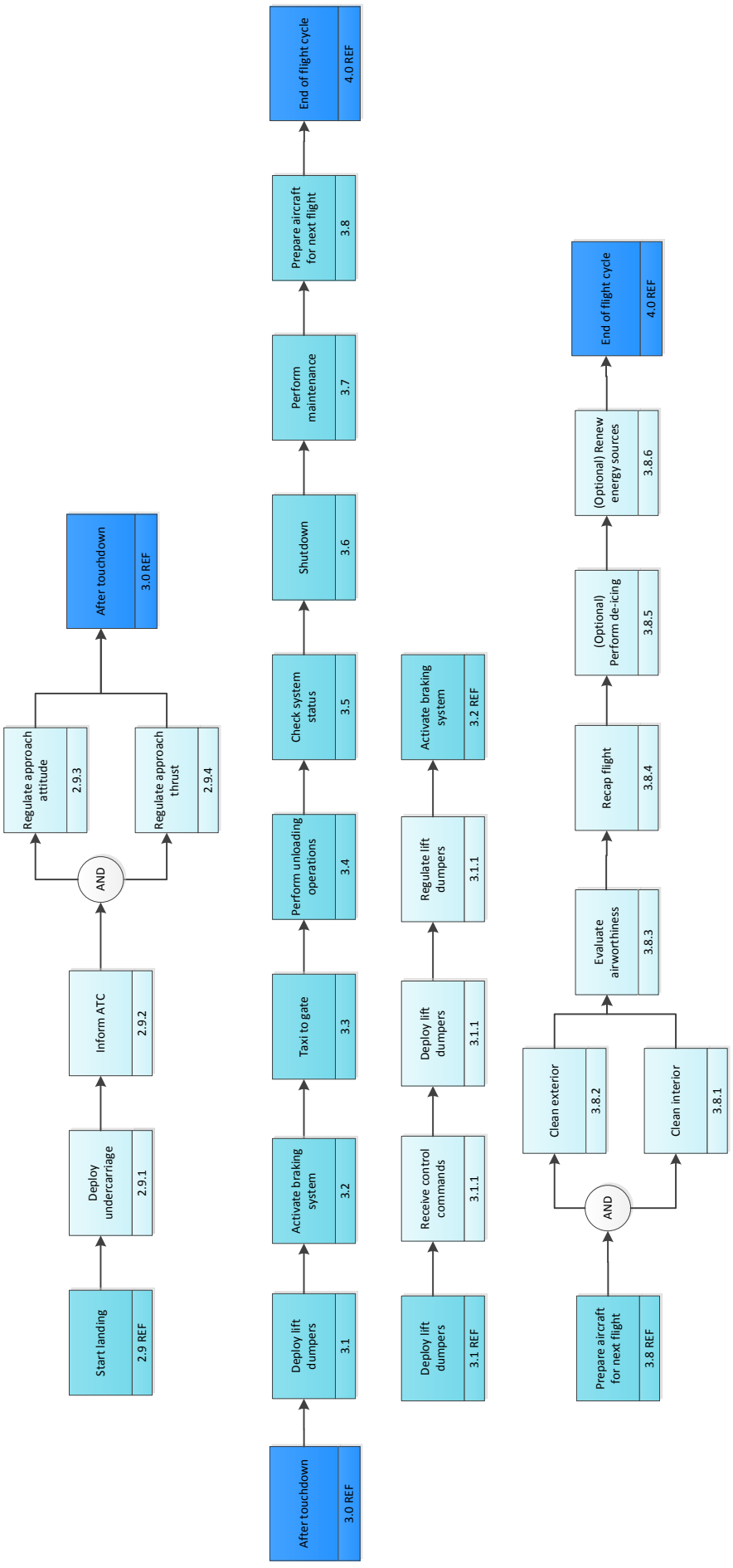

Figure B.3: Functional Flow Block Diagram of After Touchdown Stage

APPENDIX C

Gantt Chart

ID	Task Name	Duration	Work	Start	Finish	Estimate
1	**Project start-up**	40 hrs	378 hrs	Mon 22/04/13	Fri 26/04/13	No
2	Project introduction	1,5 hrs	15 hrs	Mon 22/04/13	Mon 22/04/13	No
3	Team management	20,5 hrs	46 hrs	Mon 22/04/13	Wed 24/04/13	No
4	*Team organisation*	1 hr	10 hrs	Mon 22/04/13	Mon 22/04/13	No
5	*Belbin test*	1 hr	10 hrs	Mon 22/04/13	Mon 22/04/13	No
6	*Task division*	1 hr	10 hrs	Mon 22/04/13	Mon 22/04/13	No
7	*Task responsibilities*	1 hr	10 hrs	Mon 22/04/13	Mon 22/04/13	No
8	*Communication method*	0,5 hrs	5 hrs	Mon 22/04/13	Mon 22/04/13	No
9	*Develop OBS, DTD, RT*	4 hrs	8 hrs	Mon 22/04/13	Tue 23/04/13	No
10	*Update OBS*	3 hrs	3 hrs	Wed 24/04/13	Wed 24/04/13	No
11	Documenting and template definition	22,98 hrs	23 hrs	Tue 23/04/13	Thu 25/04/13	No
12	*DID inventarisation*	4 hrs	4 hrs	Tue 23/04/13	Tue 23/04/13	No
13	*LaTeX setup*	11 hrs	11 hrs	Tue 23/04/13	Thu 25/04/13	No
14	*AIAA reference guidelines*	8 hrs	8 hrs	Thu 25/04/13	Thu 25/04/13	No
15	Set-up planning	27 hrs	134 hrs	Mon 22/04/13	Fri 26/04/13	No
16	*Develop WFD*	26,92 hrs	35 hrs	Mon 22/04/13	Thu 25/04/13	No
17	*Set-up WFD*	4 hrs	8 hrs	Mon 22/04/13	Tue 23/04/13	No
18	*Visualize WFD*	1 hr	1 hr	Tue 23/04/13	Tue 23/04/13	No
19	*Revise WFD*	13 hrs	26 hrs	Wed 24/04/13	Thu 25/04/13	No
20	*Develop WBS*	22,98 hrs	42 hrs	Tue 23/04/13	Thu 25/04/13	No
21	*Set-up WBS*	5 hrs	10 hrs	Tue 23/04/13	Tue 23/04/13	No
22	*Visualize WBS*	16 hrs	32 hrs	Wed 24/04/13	Thu 25/04/13	No
23	*Develop Gantt chart*	27 hrs	57 hrs	Mon 22/04/13	Fri 26/04/13	No
24	*Set-up Gantt software*	3 hrs	9 hrs	Mon 22/04/13	Tue 23/04/13	No
25	*Fill Gantt*	24 hrs	48 hrs	Tue 23/04/13	Fri 26/04/13	No
26	Draft project plan	16 hrs	160 hrs	Thu 25/04/13	Fri 26/04/13	No
27	*Write draft*	8 hrs	80 hrs	Thu 25/04/13	Thu 25/04/13	No
28	*Review draft*	7 hrs	70 hrs	Fri 26/04/13	Fri 26/04/13	No
29	*Approve draft*	1 hr	10 hrs	Fri 26/04/13	Fri 26/04/13	No
30	Hand-in project plan	0 hrs	0 hrs	Fri 26/04/13	Fri 26/04/13	No

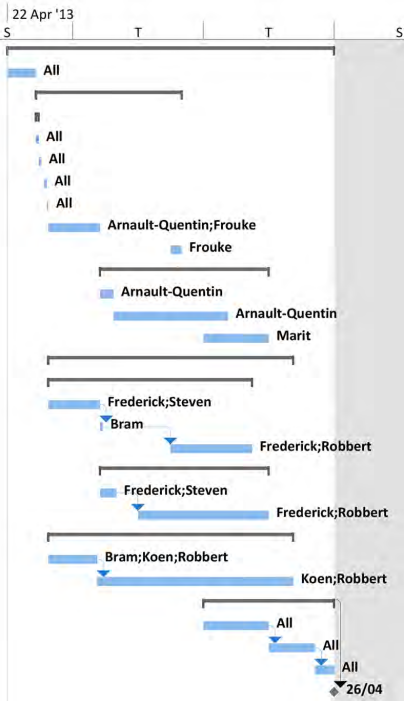

Figure C.1: Project Gantt Chart – Project Start-Up

ID	Task Name	Duration	Work	Start	Finish	Estimate
32	**Project definition**	74,98 hrs	871 hrs	Mon 22/04/13	Tue 07/05/13	No
33	Define mission	24,98 hrs	16 hrs	Tue 23/04/13	Fri 26/04/13	No
34	*Mission statement*	5 hrs	5 hrs	Tue 23/04/13	Tue 23/04/13	No
35	*Revise mission statement*	2 hrs	2 hrs	Wed 24/04/13	Wed 24/04/13	No
36	*Need statement*	5 hrs	5 hrs	Tue 23/04/13	Tue 23/04/13	No
37	*Revise need statement*	2 hrs	2 hrs	Wed 24/04/13	Wed 24/04/13	No
38	*Project objective statement*	2 hrs	2 hrs	Fri 26/04/13	Fri 26/04/13	No
39	*Literature study*	12 hrs	36 hrs	Thu 25/04/13	Fri 26/04/13	No
40	Stakeholder analysis	4 hrs	12 hrs	Tue 23/04/13	Tue 23/04/13	No
41	Establish design space	74,98 hrs	383 hrs	Mon 22/04/13	Tue 07/05/13	No
42	*Requirements discovery tree*	58,98 hrs	96 hrs	Mon 22/04/13	Fri 03/05/13	No
43	*Top level requirements*	5 hrs	15 hrs	Mon 22/04/13	Tue 23/04/13	No
44	*CS-25*	3 hrs	3 hrs	Wed 24/04/13	Wed 24/04/13	No
45	*Approach I*	14 hrs	14 hrs	Fri 26/04/13	Wed 01/05/13	No
46	*Approach II*	16 hrs	32 hrs	Wed 01/05/13	Thu 02/05/13	No
47	*Requirements list*	16 hrs	32 hrs	Thu 02/05/13	Fri 03/05/13	No
48	*Functional analysis*	47 hrs	58 hrs	Wed 24/04/13	Fri 03/05/13	No
49	*FBS*	3 hrs	6 hrs	Wed 24/04/13	Wed 24/04/13	No
50	*Revise FBS*	6 hrs	12 hrs	Wed 01/05/13	Wed 01/05/13	No
51	*FFD*	16 hrs	32 hrs	Wed 01/05/13	Thu 02/05/13	No
52	*Adapt functional analysis*	8 hrs	8 hrs	Fri 03/05/13	Fri 03/05/13	No
53	*Market analysis*	53,98 hrs	98 hrs	Tue 23/04/13	Fri 03/05/13	No
54	*Set up*	4 hrs	8 hrs	Tue 23/04/13	Tue 23/04/13	No
55	*Update*	8 hrs	16 hrs	Thu 25/04/13	Thu 25/04/13	No
56	*Update*	24 hrs	48 hrs	Wed 01/05/13	Fri 03/05/13	No
57	*Cost analysis*	13 hrs	26 hrs	Thu 02/05/13	Fri 03/05/13	No
58	*DOT*	40 hrs	91 hrs	Wed 01/05/13	Tue 07/05/13	No
59	*Start*	11 hrs	11 hrs	Wed 01/05/13	Thu 02/05/13	No
60	*Continue*	8 hrs	48 hrs	Mon 06/05/13	Mon 06/05/13	No
61	*Finish*	8 hrs	32 hrs	Tue 07/05/13	Tue 07/05/13	No
62	*Brainstorm I*	2 hrs	20 hrs	Tue 23/04/13	Tue 23/04/13	No
63	*Brainstorm II*	2 hrs	20 hrs	Wed 01/05/13	Wed 01/05/13	No
64	Sustainable development strategy	24 hrs	24 hrs	Wed 01/05/13	Fri 03/05/13	No
65	Risk planning	45,98 hrs	40 hrs	Tue 23/04/13	Thu 02/05/13	No
66	*Risk management plan*	4 hrs	8 hrs	Tue 23/04/13	Tue 23/04/13	No
67	*Technical risk assessment*	16 hrs	32 hrs	Wed 01/05/13	Thu 02/05/13	No
68	Baseline review	5,5 hrs	27 hrs	Mon 06/05/13	Mon 06/05/13	No
69	*Prepare baseline review presentation*	3,5 hrs	7 hrs	Mon 06/05/13	Mon 06/05/13	No
70	*Baseline review*	2 hrs	20 hrs	Mon 06/05/13	Mon 06/05/13	No
71	Draft Baseline report	27,5 hrs	333 hrs	Wed 01/05/13	Mon 06/05/13	No
72	*LaTeX setup*	6 hrs	6 hrs	Wed 01/05/13	Wed 01/05/13	No
73	*Write draft*	16 hrs	160 hrs	Thu 02/05/13	Fri 03/05/13	No
74	*Review draft*	16 hrs	160 hrs	Thu 02/05/13	Fri 03/05/13	No
75	*Approve draft*	3,5 hrs	7 hrs	Mon 06/05/13	Mon 06/05/13	No
76	Hand-in baseline report	0 hrs	0 hrs	Mon 06/05/13	Mon 06/05/13	No

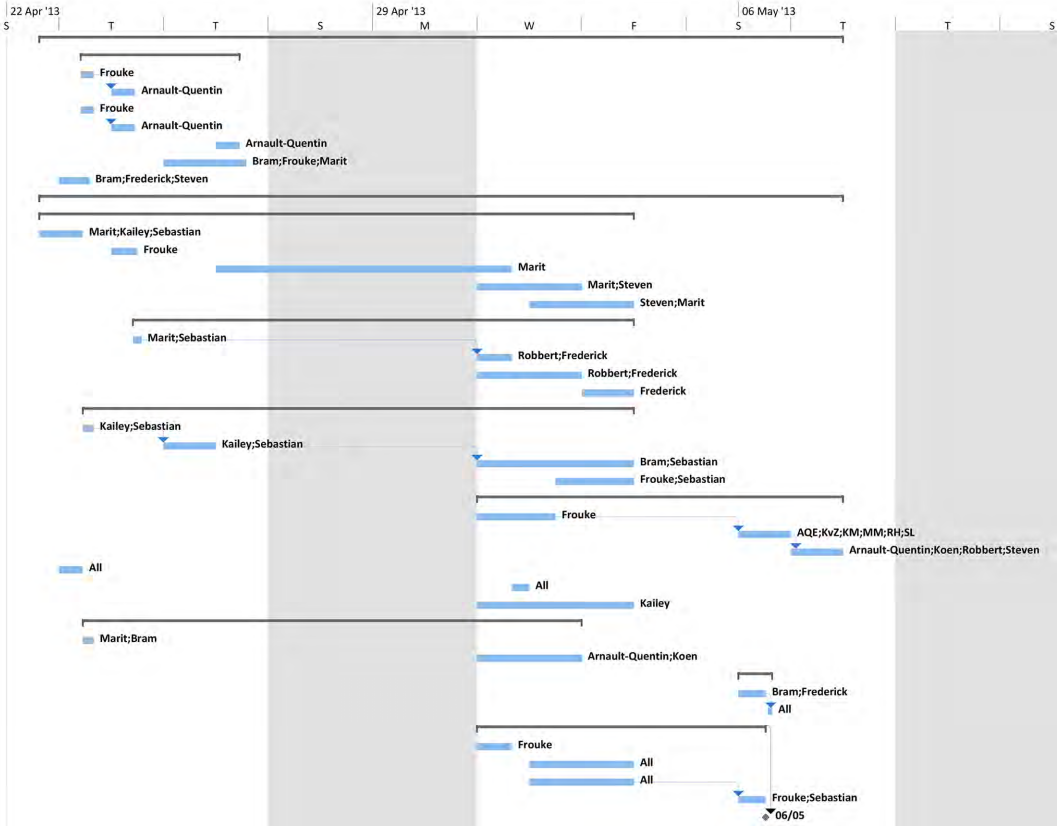

Figure C.2: Project Gantt Chart – Project Definition

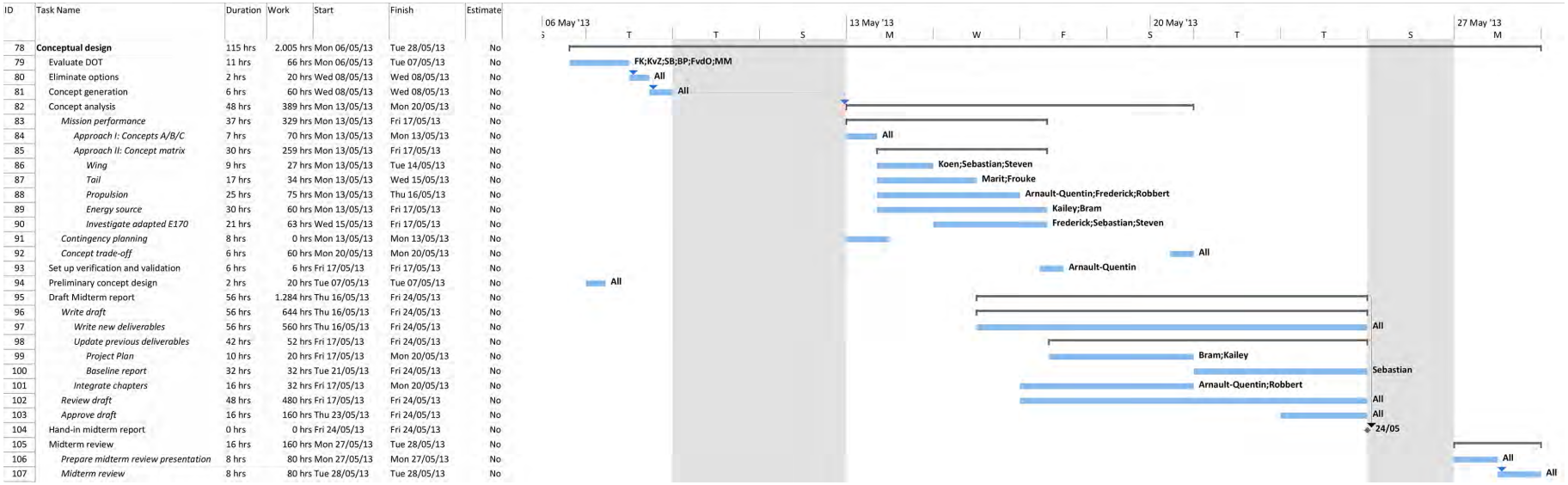

ID	Task Name	Duration	Work	Start	Finish	Estimate
78	**Conceptual design**	115 hrs	2.005 hrs	Mon 06/05/13	Tue 28/05/13	No
79	Evaluate DOT	11 hrs	66 hrs	Mon 06/05/13	Tue 07/05/13	No
80	Eliminate options	2 hrs	20 hrs	Wed 08/05/13	Wed 08/05/13	No
81	Concept generation	6 hrs	60 hrs	Wed 08/05/13	Wed 08/05/13	No
82	Concept analysis	48 hrs	389 hrs	Mon 13/05/13	Mon 20/05/13	No
83	*Mission performance*	37 hrs	329 hrs	Mon 13/05/13	Fri 17/05/13	No
84	*Approach I: Concepts A/B/C*	7 hrs	70 hrs	Mon 13/05/13	Mon 13/05/13	No
85	*Approach II: Concept matrix*	30 hrs	259 hrs	Mon 13/05/13	Fri 17/05/13	No
86	*Wing*	9 hrs	27 hrs	Mon 13/05/13	Tue 14/05/13	No
87	*Tail*	17 hrs	34 hrs	Mon 13/05/13	Wed 15/05/13	No
88	*Propulsion*	25 hrs	75 hrs	Mon 13/05/13	Thu 16/05/13	No
89	*Energy source*	30 hrs	60 hrs	Mon 13/05/13	Fri 17/05/13	No
90	*Investigate adapted E170*	21 hrs	63 hrs	Wed 15/05/13	Fri 17/05/13	No
91	*Contingency planning*	8 hrs	0 hrs	Mon 13/05/13	Mon 13/05/13	No
92	*Concept trade-off*	6 hrs	60 hrs	Mon 20/05/13	Mon 20/05/13	No
93	Set up verification and validation	6 hrs	6 hrs	Fri 17/05/13	Fri 17/05/13	No
94	Preliminary concept design	2 hrs	20 hrs	Tue 07/05/13	Tue 07/05/13	No
95	Draft Midterm report	56 hrs	1.284 hrs	Thu 16/05/13	Fri 24/05/13	No
96	*Write draft*	56 hrs	644 hrs	Thu 16/05/13	Fri 24/05/13	No
97	*Write new deliverables*	56 hrs	560 hrs	Thu 16/05/13	Fri 24/05/13	No
98	*Update previous deliverables*	42 hrs	52 hrs	Fri 17/05/13	Fri 24/05/13	No
99	*Project Plan*	10 hrs	20 hrs	Fri 17/05/13	Mon 20/05/13	No
100	*Baseline report*	32 hrs	32 hrs	Tue 21/05/13	Fri 24/05/13	No
101	*Integrate chapters*	16 hrs	32 hrs	Fri 17/05/13	Mon 20/05/13	No
102	*Review draft*	48 hrs	480 hrs	Fri 17/05/13	Fri 24/05/13	No
103	*Approve draft*	16 hrs	160 hrs	Thu 23/05/13	Fri 24/05/13	No
104	Hand-in midterm report	0 hrs	0 hrs	Fri 24/05/13	Fri 24/05/13	No
105	Midterm review	16 hrs	160 hrs	Mon 27/05/13	Tue 28/05/13	No
106	*Prepare midterm review presentation*	8 hrs	80 hrs	Mon 27/05/13	Mon 27/05/13	No
107	*Midterm review*	8 hrs	80 hrs	Tue 28/05/13	Tue 28/05/13	No

Figure C.3: Project Gantt Chart – Conceptual Design

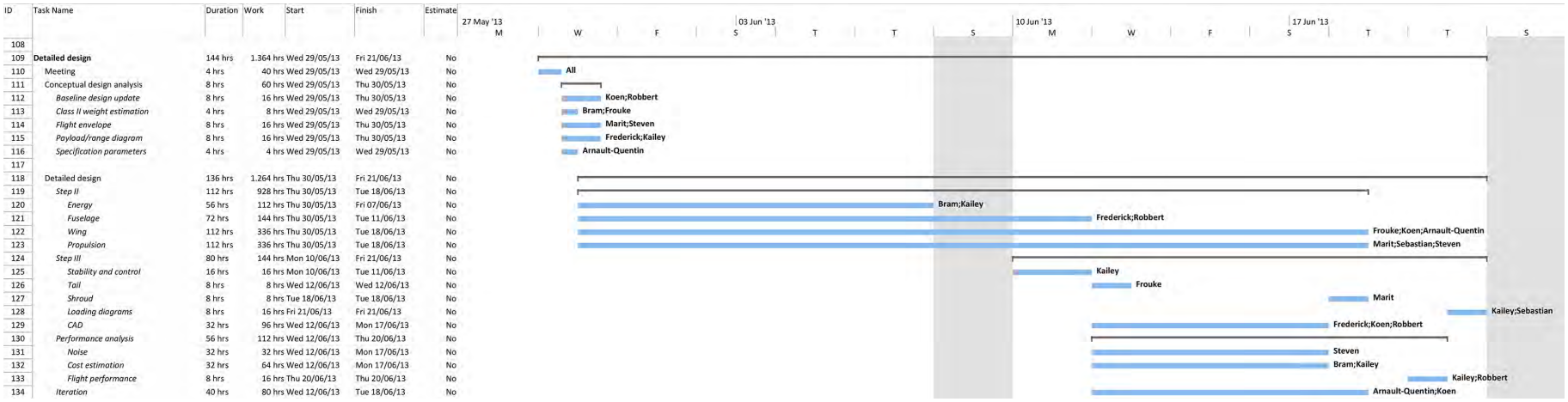

ID	Task Name	Duration	Work	Start	Finish	Estimate
108						
109	**Detailed design**	144 hrs	1.364 hrs	Wed 29/05/13	Fri 21/06/13	No
110	Meeting	4 hrs	40 hrs	Wed 29/05/13	Wed 29/05/13	No
111	Conceptual design analysis	8 hrs	60 hrs	Wed 29/05/13	Thu 30/05/13	No
112	*Baseline design update*	8 hrs	16 hrs	Wed 29/05/13	Thu 30/05/13	No
113	*Class II weight estimation*	4 hrs	8 hrs	Wed 29/05/13	Wed 29/05/13	No
114	*Flight envelope*	8 hrs	16 hrs	Wed 29/05/13	Thu 30/05/13	No
115	*Payload/range diagram*	8 hrs	16 hrs	Wed 29/05/13	Thu 30/05/13	No
116	*Specification parameters*	4 hrs	4 hrs	Wed 29/05/13	Wed 29/05/13	No
117						
118	Detailed design	136 hrs	1.264 hrs	Thu 30/05/13	Fri 21/06/13	No
119	*Step II*	112 hrs	928 hrs	Thu 30/05/13	Tue 18/06/13	No
120	*Energy*	56 hrs	112 hrs	Thu 30/05/13	Fri 07/06/13	No
121	*Fuselage*	72 hrs	144 hrs	Thu 30/05/13	Tue 11/06/13	No
122	*Wing*	112 hrs	336 hrs	Thu 30/05/13	Tue 18/06/13	No
123	*Propulsion*	112 hrs	336 hrs	Thu 30/05/13	Tue 18/06/13	No
124	*Step III*	80 hrs	144 hrs	Mon 10/06/13	Fri 21/06/13	No
125	*Stability and control*	16 hrs	16 hrs	Mon 10/06/13	Tue 11/06/13	No
126	*Tail*	8 hrs	8 hrs	Wed 12/06/13	Wed 12/06/13	No
127	*Shroud*	8 hrs	8 hrs	Tue 18/06/13	Tue 18/06/13	No
128	*Loading diagrams*	8 hrs	16 hrs	Fri 21/06/13	Fri 21/06/13	No
129	*CAD*	32 hrs	96 hrs	Wed 12/06/13	Mon 17/06/13	No
130	*Performance analysis*	56 hrs	112 hrs	Wed 12/06/13	Thu 20/06/13	No
131	*Noise*	32 hrs	32 hrs	Wed 12/06/13	Mon 17/06/13	No
132	*Cost estimation*	32 hrs	64 hrs	Wed 12/06/13	Mon 17/06/13	No
133	*Flight performance*	8 hrs	16 hrs	Thu 20/06/13	Thu 20/06/13	No
134	*Iteration*	40 hrs	80 hrs	Wed 12/06/13	Tue 18/06/13	No

Figure C.4: Project Gantt Chart – Detailed Design

ID	Task Name	Duration	Work	Start	Finish	Estimate
135						
136	**Project completion**	187 hrs?	2.092 hrs	Mon 03/06/13	Thu 04/07/13	Yes
137	Draft Final report	136 hrs	1.534 hrs	Mon 03/06/13	Tue 25/06/13	No
138	*Write draft*	136 hrs	1.424 hrs	Mon 03/06/13	Tue 25/06/13	No
139	*Write new deliverables*	136 hrs	1.360 hrs	Mon 03/06/13	Tue 25/06/13	No
140	*Update previous deliverables*	56 hrs	40 hrs	Thu 13/06/13	Fri 21/06/13	No
141	*Project Plan*	16 hrs	16 hrs	Thu 20/06/13	Fri 21/06/13	No
142	*Baseline report*	16 hrs	16 hrs	Thu 13/06/13	Fri 14/06/13	No
143	*Midterm report*	8 hrs	8 hrs	Tue 18/06/13	Tue 18/06/13	No
144	*Integrate chapters*	24 hrs	24 hrs	Thu 20/06/13	Mon 24/06/13	No
145	*Review draft*	9 hrs	90 hrs	Mon 24/06/13	Tue 25/06/13	No
146	*Approve draft*	2 hrs	20 hrs	Tue 25/06/13	Tue 25/06/13	No
147	Hand-in final report	0 hrs	0 hrs	Tue 25/06/13	Tue 25/06/13	No
148	Draft Final review presentation	24 hrs?	240 hrs	Wed 26/06/13	Fri 28/06/13	Yes
149	*Create draft*	8 hrs?	80 hrs	Wed 26/06/13	Wed 26/06/13	Yes
150	*Review draft*	8 hrs?	80 hrs	Thu 27/06/13	Thu 27/06/13	Yes
151	*Approve draft*	8 hrs?	80 hrs	Fri 28/06/13	Fri 28/06/13	Yes
152	Final review presentation	0 hrs	0 hrs	Fri 28/06/13	Fri 28/06/13	No
153	DSE symposium	99 hrs?	318 hrs	Tue 18/06/13	Thu 04/07/13	Yes
154	*Create poster*	48 hrs?	48 hrs	Tue 18/06/13	Tue 25/06/13	Yes
155	*Preparation*	24 hrs?	240 hrs	Mon 01/07/13	Wed 03/07/13	Yes
156	*DSE symposium*	3 hrs?	30 hrs	Thu 04/07/13	Thu 04/07/13	Yes

Figure C.5: Project Gantt Chart – Project Completion

APPENDIX D

Fleet Analysis

Table D.1: Fleet Analysis for 61-90 Seater Regional Aircraft – ATR 72, CRJ700, CRJ900 DHC-8 400, E170, E175, F70 [21]

Aircraft	*Status*	*Number*	*Oldest*	*Newest*	*Average*
61-90 seats	Active	1843	25	11	7.429572
	On Order	17			
	Stored	161	24	2	10.87
	Scrapped	8	22	8	16.13
	Written off	18	22	5	15.67

Table D.2: Fleet Analysis for 60+ Seater Regional Turboprop Aircraft – ATR 72, DHC-8 400 [21]

Aircraft	*Status*	*Number*	*Oldest*	*Newest*	*Average*
Turboprops (60+ seats)	Active	900	25	0	7.65
	On order	15			
	Stored	124	24	2	12.23
	Scrapped	5	22	8	16.8
	Written off	17	22	5	15.94

Table D.3: Fleet Analysis for 61-90 Seater Regional Jets – CRJ700, CRJ900, E170, E175, F70 [21]

Aircraft	*Status*	*Number*	*Oldest*	*Newest*	*Average*
Jets (61 - 90 seats)	Active	943	19	0	7.21
	On order	2			
	Stored	37	18	2	6.30
	Scrapped	3	22	11	15
	Written off	1	11	11	11

APPENDIX E

Engine Cost

Table E.1 shows the reference used to determine Eq. 17.4 in Chapter 17 on Cost Analysis. Due to a fairly limited amount of reference turboprops (indicated TP), turbofan (TF) engines rated up to 70.000 pounds of thrust were also included in the analysis. Thrust was converted to power using Eq. E.1.

$$P_{sh}[hp] = \frac{T}{1000} \cdot 1.36 \cdot V \tag{E.1}$$

For V, a value of 200 m/s has been substituted, corresponding to the approximate cruising speed of the EuroFlyer aircraft.

Table E.1: Engine Cost Analysis Reference Data [20, 105, 104]

Type	*Engine*	Thrust		*Power*	Cost		*Application*
		[lb]	[N]	[hp]	[USD]	[2013 USD]	
TP	Klimov VK-800			1000	210,000 (2007)	236,000	
TP	RR AE2100			4395	2,450,000 (2002)	3,167,000	C130, S2000
TP	RR AE 2100D3			4590	1,900,000 (1990)	3,380,000	C130
TP	RR Allison T56			4672	2,150,000 (2000)	2,903,000	C130
TP	RR AE 1107C			6150	2,200,000 (2007)	2,470,000	CV-22 Osprey
TF	RR AE 3007	7580	33729	9174	1,400,000 (1996)	2,070,000	ERJ-145
TF	GE CF34-3BI	9220	41027	11159	2,000,000 (2001)	2,630,000	CRJ-200
TF	GE CF-34-10E	18820	83744	22778	3,570,000 (2004)	4,395,000	E-190
TF	RR BR715	22000	97894	26627	7,000,000 (1999)	9,770,000	B717
TF	CFM56-7	27300	121478	33042	11,000,000 (1997)	15,940,000	B737NG
TF	CM56-5B	33000	146841	39941	10,000,000 (1994)	15,690,000	A320
TF	IAE V2500	33000	146841	39941	9,700,000 (1989)	18,190,000	A320
TF	PW F117-PW-100	41700	185554	50471	8,400,000 (1995)	12,820,000	C-17A
TF	PW PW4062	62000	275884	75040	14,000,000 (2004)	19,700,000	A300, B747, B767
TF	GE CF6-80C2	63500	282558	76856	10,000,000 (1985)	21,610,000	A300, B747, B767
TF	GE GEnx 2B	66500	295908	80487	12,000,000 (2011)	12,410,000	B747-8
TF	PW PW4168	68600	305252	83029	20,000,000 (2000)	27,010,000	A330

APPENDIX F

Propulsion Specifications

Turboprop

All standard constants and efficiencies originate from the AE2203 course [55] and the atmospheric values are ISA.

Table F.1: Turboprop Parameters

Parameter	*Unit*	*Value*
Work free turbine	1.66	MW
Mass flow fuel	0.075	kg/s
Mass flow air	5	kg/s
Fuel efficiency	0.432	—
Thermal efficiency	0.385	—

Table F.2: Temperature and Pressure values Throughout the Turboprop

Point	*Location*	*Temperature [K]*	*Pressure [Pa]*
0	Ambient	229.65	30742
2	Before compressor	249.15	38692
3	After compressor	689.59	1083376
4	Before turbine	1439.1	1004041
5	Before free turbine	1007.9	203487
6	After free turbine	686.67	34939
7	Before nozzle	686.67	34939
8	After nozzle	596.06	40888

Table F.3: Turboprop Efficiencies

Efficiencies		
$\eta_{is,in}$	Intake isentropic	0.8
$\eta_{is,comp}$	Compressor	0.9
η_c	Combustion	0.99
η_{mech}	Mechanic	0.99
$\eta_{is,turb1}$	Turbine isentropic	0.9
$\eta_{is,turb2}$	Free turbine isentropic	0.9
$\eta_{p,cc}$	Combustion chamber pressure ratio	0.96
$\eta_{is,n}$	Nozzle isentropic	0.97

APU

All standard constants and efficiencies originate from the AE2203 course [55] and the atmospheric values are ISA.

Table F.4: APU Parameters

Parameter	*Unit*	*Value*
Work free turbine	1.69	MW
Mass flow fuel	0.075	kg/s
Mass flow air	5	kg/s
Fuel efficiency	0.439	–
Thermal efficiency	0.444	–

Table F.5: Temperature and Pressure values Throughout the APU

Point	*Location*	*Temperature [K]*	*Pressure [Pa]*
0	Ambient	229.65	30742
2	Before compressor	249.15	38692
3	After compressor	594.29	657762
4	Before turbine	1255.6	631451
5	Before free turbine	956.89	183264
6	After free turbine	667.81	35256
7	Before nozzle	667.81	35256
8	After nozzle	586.28	40888

Table F.6: APU Efficiencies

Efficiencies		
$\eta_{is,in}$	Intake isentropic	0.8
$\eta_{is,comp}$	Compressor	0.9
η_c	Combustion	0.99
η_{mech}	Mechanic	0.99
$\eta_{is,turb1}$	Turbine isentropic	0.9
$\eta_{is,turb2}$	Free turbine isentropic	0.9
$\eta_{p,cc}$	Combustion chamber pressure ratio	0.96
$\eta_{is,n}$	Nozzle isentropic	0.97

APPENDIX G

CAD Drawings

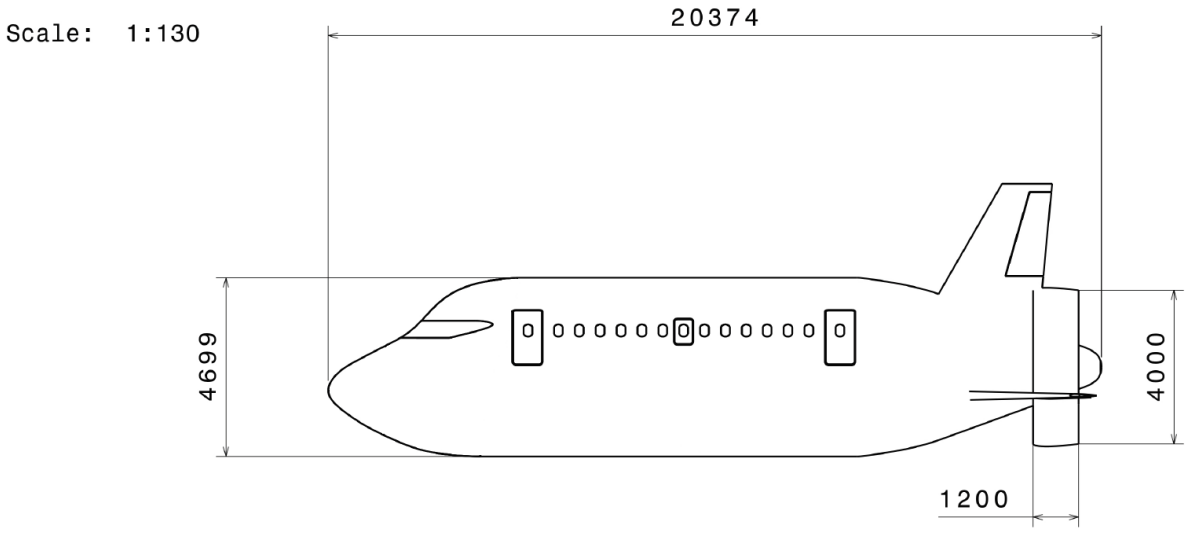

Figure G.1: Side View

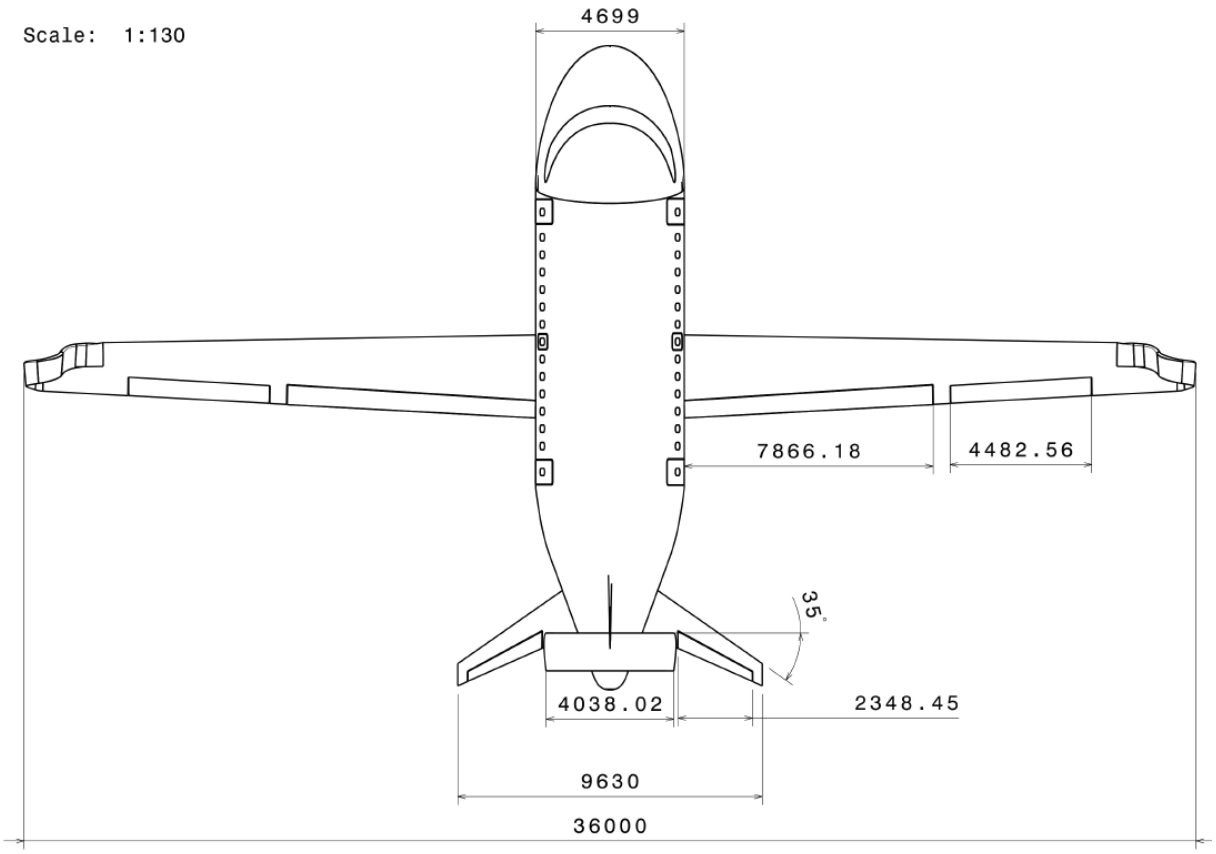

Figure G.2: Top View

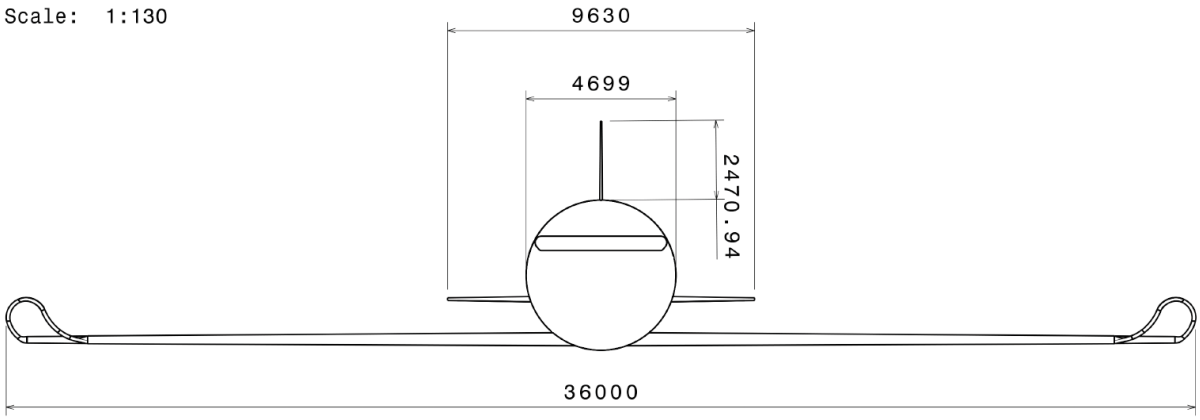

Figure G.3: Front View